DOUBLE POPULATION CASCADED LATTICE BOLTZMANN METHOD

Keerti Vardhan Sharma

Tese de Doutorado apresentada ao Programa de Pós-graduação em Engenharia Química, COPPE, da Universidade Federal do Rio de Janeiro, como parte dos requisitos necessários à obtenção do título de Doutor em Engenharia Química.

Orientadores: Frederico Wanderley Tavares
Robert Straka

Rio de Janeiro
Novembro de 2018

DOUBLE POPULATION CASCADED LATTICE BOLTZMANN METHOD

Keerti Vardhan Sharma

TESE SUBMETIDA AO CORPO DOCENTE DO INSTITUTO ALBERTO LUIZ
COIMBRA DE PÓS-GRADUAÇÃO E PESQUISA DE ENGENHARIA (COPPE)
DA UNIVERSIDADE FEDERAL DO RIO DE JANEIRO COMO PARTE DOS
REQUISITOS NECESSÁRIOS PARA A OBTENÇÃO DO GRAU DE DOUTOR
EM CIÊNCIAS EM ENGENHARIA QUÍMICA.

Examinada por:

_____
Prof. Frederico Wanderley Tavares, D.Sc.

_____
Prof. Paulo Laranjeira de Cunha Lage, D.Sc.

_____
Prof. Amaro Gomes Barreto Junior, D.Sc.

_____
Prof. Luca Moriconi, Ph.D.

_____
Prof. Eduardo Rocha de Almeida Lima, D.Sc.

RIO DE JANEIRO, RJ – BRASIL
NOVEMBRO DE 2018

To my parents Sh. Kamlesh Chandra Sharma and Smt. Sushma Sharma for all the love and blessings.
To Prof. Frederico Tavares for always supporting me and having faith in me
To Prof. Robert Straka (the best mathematician I know) for all the unconditional support

Acknowledgements

I deeply thank my supervisor Prof. Frederico W. Tavares for providing me the opportunity to work with him, and for all the support you provided me during this research. I thank you immensely for having faith in me and guiding me. Your trust in me is my driving force.

I immensely thank my co-supervisor Prof. Robert Straka for always being there for me. There is not a single moment in the last two years when you were not available to help me and for our Skype meetings to discuss LBM. Your guidance and support provide me the energy, motivation, and inspiration to do my best. Thank you very much for everything.

I also thank Prof. Paulo Lage for his constructive comments and important suggestions about my research work provided during the Ph.D. seminars. I also thank Prof. Amaro Barreto Jr. and Prof. Luca Moriconi for their important feedback. I thank Prof. Helen C. Ferraz and Prof. Ricardo Tadeu Lopes for giving me full freedom to use their laboratories. I also thank Olga de Araujo and Joao Victor Nicolini for their excellent support during the course of the experiments.

I thank Nathalia Ribeiro at ATOMS for support with the administrative stuff. I also thank my fellow colleagues at ATOMS for the support and providing me an excellent research atmosphere. I thank CNPq and Petrobras for research fellowship and support.

I thank Vera S. Cruz and Luciana S. Damasceno from PEQ-COPPE office. They are two excellent people who are always ready to help you in any kind of bureaucratic challenge.

I thank my family for all the love and patience. I thank my wife for finding LBM interesting enough, as she now knows how to draw a lattice model in 2-D with all the microscopic velocities indicated. And especially my daughter Karolina for bringing the smile to my face.

MÉTODO DE "LATTICE" BOLTZMANN EM CASCATA COM DUPLA POPULAÇÃO

Keerti Vardhan Sharma

Novembro/2018

Os métodos de "Lattice" Boltzmann (LBM) são potentes ferrementas numéricas
para simular problemas de transferência de massa e calor. Ao invés de integrar dire-
tamente as equações de Navier-Stokes, o método LBM resolve, de forma discretizada,
a equação de transporte de Boltzmann, acompanhando a descrição microscópica dos
sistemas. O método LBM pode solucionar fluxo de fluidos com grande estabilidade
e eficiência computacional, especialmente fluxos em geometrias complexas. Para
fluxos térmicos, o esquema LBM de dupla função de distribuição (DDF) é a abor-
dagem mais popular e bem sucedida. Mas é evidente, a partir da literatura, que
as abordagens LBM de dupla função de distribuição (DDF), as quais utilizam dois
operadores de colisão, envolvem esquemas de colisão que violam a invariância de
Galileu, produzindo instabilidades para fluxos com números Re e Ra altos. Nesta
tese, o método de "Lattice" Boltzmann em cascata de dupla população em cascata
é desenvolvido para corrigir o esquema DDF LBM. O método proposto reduz o
grau de violação da invariância de Galileu, aumentando a estabilidade e acurácia
do método LBM. O método foi implementado para simular problemas de advecção-
difusão, convecções natural e forçada típicos de transferências de calor. O esquema
proposto foi também bem sucedido em regimes de fluxo turbulento e em escoamen-
tos 3-D em meios porosos. Os resultados obtidos neste trabalho estão fortemente de
acordo com experimentos e métodos numéricos disponíveis na literatura.

Abstract of Thesis presented to COPPE/UFRJ as a partial fulfillment of the requirements for the degree of Doctor of Science (D.Sc.)

DOUBLE POPULATION CASCADED LATTICE BOLTZMANN METHOD

Keerti Vardhan Sharma

November/2018

Advisors: Frederico Wanderley Tavares
                Robert Straka

Department: Chemical Engineering

Lattice Boltzmann Methods (LBM) are powerful numerical tools to simulate heat and mass transfer problems. Instead of directly integrating the N-S equations, LBM solves the discretized form of the Boltzmann Transport Equation (BTE), keeping track of the microscopic description of the systems. Therefore, LBM can solve fluid flows with great stability and computational efficiency, especially complex geometry fluid flows. For thermal flows, double distribution function (DDF) LBM scheme is the most popular and successful approach. But it is evident from the literature that existing double distribution function (DDF) LBM approaches, which use two collision operators, involve collision schemes which violate Galilean invariance, therefore producing instabilities for flows with high Re and Ra numbers. In this thesis, a double population cascaded lattice Boltzmann method is developed to improve the DDF LBM scheme from this drawback. The proposed method reduces the degree of violation of Galilean invariance, increasing the stability and accuracy of the LBM scheme. The scheme was implemented to simulate advection-diffusion, forced convection and natural convection heat transfer problems. The proposed scheme was also successfully tested for turbulent flow regimes and 3-D fluid flow in porous media. The results obtained from this work are in strong agreement with those available in the literature obtained through other numerical methods and experiments.

Sumário

Lista de Figuras

Lista de Tabelas

Nomenclature

a	CTLBM free parameter
$\vec{c}$	characteristic lattice velocity
c_s	lattice speed of sound
D	diffusivity coefficient, diameter of cylinder
E_1	error measured in L_1 norm
E_2	error measured in L_2 norm
E_∞	error measured in L_∞ norm
f	DF for velocity and density fields
g	DF for a temperature field
$\vec{k}$	cascaded collision vector
K	wave mode
L	characteristic length
L_1	L_1 norm
L_2	L_2 norm
L_∞	L_∞ norm
m	raw moment of DF
$\vec{n}$	outer normal
N	number of lattice sites
Pe	Peclet number
Pr	Prandtl number
Re	Reynolds number
Ra	Rayleigh number
Nu	Nusselt number
Gr	Grashof number
t	time
T	temperature
$\vec{u}$	macroscopic velocity
U	characteristic velocity
w_i	i-th weight factor
$\vec{x}$	position vector
α	thermal diffusivity
Δt	time step
ϵ	small perturbation parameter

κ	central moment of DF
ν	kinematic viscosity
ϕ	scalar quantity
ρ	fluid density
τ	relaxation time for fluid flow
ω	relaxation frequency
Ω	cascaded collision operator
$\mathbb{A}$	general collision matrix
$\mathbb{K}$	orthogonal transformation matrix
$\mathbb{M}$	transformation matrix
$\mathbb{R}$	relaxation matrix
$\mathbb{S}$	shift matrix
F	forcing term
Subscripts	
0	inlet, characteristic
b	boundary
c	cold
C	characteristic
d	Dirichlet, spatial dimension
f	related to flow DF, fluid
g	related to temperature DF
h	hot
i	i-th component, related to i-th DF
in	inlet
lb	lattice units
out	outlet
p	physical units
s	solid
x	component in x direction
y	component in y direction
Superscripts	
c	post-collision state
eq	equilibrium
Abbreviations	
BGK-SRT	Bhatnagar-Gross-Krook Single Relaxation Time
BTE	Boltzmann Transport Equation
CFD	Computational Fluid Dynamics

CFL	Courant-Friedrichs-Levy
CLBM	Cascaded Lattice Boltzmann Method
CTLBM	Cascaded Thermal Lattice Boltzmann Method
CUDA	Compute Unified Device Architecture
$DdQq$	d-dimensional q-velocity lattice
DDF	Double Distribution Function
DF	Distribution Function
N-S	Navier-Stokes
F-K	Fourier-Kirchhoff
EDF	Equilibrium Distribution Function
ELBM	Entropic Lattice Boltzmann Method
EOC	Experimental Order of Convergence
EPDE	Equivalent Partial Differential Equation
GPU	Graphic Processing Unit
KBC	Karlin Bösch Chikatamarla
LBE	Lattice Boltzmann Equation
LBM	Lattice Boltzmann Method
MD	Molecular Dynamics
MRT	Multiple Relaxation Times
MS	Multi Speed
PDE	Partial Differential Equation

Capítulo 1

Introduction

Computational Fluid Dynamics (CFD) is the stream in which physical and physico-chemical systems with heat and mass transfer are studied. Conventional numerical approaches such as finite difference methods (FDM), finite volume methods (FVM) and finite element methods (FEM) have been frequently and successfully used to numerically solve heat and mass transfer problems for many decades. These techniques directly solve the conservation equations governing a thermal (energy conservation along with mass and momentum conservation) and athermal (mass and momentum conservation) systems. This approach known as Navier-Stokes model (system of N-S equations, i.e. mass, momentum, and energy conservation), which considers fluid as a continuum, solves the hydrodynamic (macroscopic) description of the systems. Microscopic developments, i.e. molecule-molecule interactions are generally overlooked in such a model. Therefore, the N-S approach struggle in solving phenomena which are dictated by fluid-fluid, fluid-solid interactions, i.e. with interfacial phenomena and phase transition and produce unstable and inaccurate numerical results. These direct approach N-S model solve the Poisson equation to determine pressure, which is exhaustive and difficult. As a result, the data communication is global making it difficult to parallelize the codes, directly increasing the computation cost. Another drawback of these numerical solvers using N-S models is their inefficiency in dealing with complex boundary conditions and pore-scale analysis of fluid flow in rocks. Flows through porous media is an example of complex geometry fluid flows, and an effort to solve such flows using N-S models requires an enormous amount of grid-refining which makes the computation very expensive. Wettability, a phenomenon present in such flows, poses serious challenges in these models.

Lattice Boltzmann Methods (LBM) considers fluid as an ensemble of virtual particles which follow the dynamics of an ideal gas. Boltzmann Transport Equation (BTE) describes the kinetic behavior of these particles. The collisions in the LBM scheme also obey mass, momentum, and energy conservation. BTE describes the mesoscopic and microscopic nature of the system. Therefore, the LBM approach

efficiently captures the microscopic developments and molecule interactions taking place in the system. Particle collisions, responsible for mass, momentum and energy conservation, are local. The pressure can be calculated using an equation of state, instead of solving the Poisson equation. The local nature of particle collisions makes the data communication local, what makes LBM a better candidate for code parallelization. The dynamics of the virtual particles in LBM is governed by the probability distribution function. The local nature of these particles makes LBM naturally fit to deal with complex boundary conditions. Therefore, the LBM approach can solve efficiently the flow problems with phase separation, phase transition, fluid-fluid and fluid-solid interactions, reactive flows and flows through porous media.

LBM is an indirect approach, in which solving BTE on a lattice model which has a finite number of degree of freedom, leads to the lattice Boltzmann equations (LBE). The LBE consists of advection and collision terms. There exist many collision schemes such as single relaxation time-Bhatnagar-Gross-Krook (SRT-BGK), Multiple Relaxation Times (MRT), Cascaded scheme, etc. BGK produces errors in fluid flows with very low viscosity and is unstable in complex problems. BGK also does not preserve the Galilean invariance which is required to fulfill the closure relation in solving Navier-Stokes equations in its hydrodynamic limits and produces numerical artifacts as a result. To increase the stability and accuracy of the LBM schemes multiple relaxation times (MRT) method was developed. MRT showed better performance compared to BGK providing higher stability and accuracy. But MRT, as well as BGK, do not preserve the Galilean invariance, as a result, numerical artifacts and errors are present especially for turbulent flows. In order to correct the problem regarding Galilean invariance central moment, the LBM scheme also known as cascaded LBM was proposed. This scheme not only corrected the Galilean invariance problem up to a great extent but also introduced a unique relaxation scheme, making the collision scheme semi-implicit. This scheme presented results with even higher stability and accuracy compared to SRT-BGK and MRT methods and easily solved the turbulent fluid flows.

In LBM, there exist three approaches to solve heat transfer problems e.g. Multispeed approach, double distribution function (DDF) approach, and hybrid approach. For incompressible conjugate heat transfer, the multispeed approach is not suitable because the Prandtl number is fixed and it produces erroneous viscosity value. A hybrid approach is an efficient approach which solve fluid flow by LBM and use a conventional CFD method to solve the energy equation. This usage of conventional CFD method poses a serious challenge in the parallelization of the codes, and become computationally expensive and unattractive. The third one is the DDF approach, which uses LBM methods to solve both the fluid flow and energy equation simultaneously. Due to its purity, DDF approach is the most successful LBM

tool to solve thermal flows and is ideal for parallelization. Double population BGK schemes, double population MRT schemes, Cascaded-MRT, and BGK-MRT LBM schemes have been developed by different groups to address thermal problems. To cure the existing DDF schemes from the violation of Galilean invariance and numerical instabilities for complex and turbulent flows, we propose a double population Cascaded LBM model.

In the proposed double population cascaded LBM, flow field equations (mass and momentum) are solved on one lattice model using cascaded collision scheme and energy equation or temperature equation is solved on another lattice again using cascaded collision scheme. In Chapter 2, evolutionary advancement of the thermal LBM schemes are presented. In this chapter major thermal LBM schemes and their implementations are reviewed. Chapter 3 provides an insight into the recovery of hydrodynamic (N-S) equations recovered using different collision schemes. The approach of Equivalent Partial Differential Equation and its application in LBM have been reviewed extensively and detailed recovery of equivalent N-S equations and thermal Fourier-Kirchhoff equations are presented. Double population cascaded LBM scheme is developed in Chapter 4 for problems of advection-diffusion and forced convective heat transfer. The consistency, stability, and accuracy of the proposed LBM scheme are tested against others LBM methods and many benchmarking problems existing in the literature. Chapter 5 extends the proposed double population cascaded LBM to solve natural convection heat transfer in a square cavity. To solve natural convection, an extra force term is introduced to the LBE and a large range of Rayleigh numbers have been considered. In chapter 6 we simulate forced and natural convection heat transfer through an array of hot tube banks. Chapter 7 presents the implementation of cascaded LBM to study fluid flows in porous media with microscopic alterations. The main conclusions drawn from this work have been presented in Chapter 8, along with suggestions for future extension of the developed double population cascaded LBM.

Appendix section consists of additional research works also developed during the D.Sc. Appendix A presents the accuracy analysis of the cascaded lattice Boltzmann method. Extending the work presented in Chapter 7, wettability analysis of laser-treated limestone rocks is presented in Appendix B. Appendix C presents the imaging methodology of limestone rocks and provides quantitative analysis to define a reliable representative elementary volume (REV) for future fluid flow simulations using cascaded LBM.

The analysis and results presented here clearly show that the proposed double population cascaded LBM scheme produces reliable numerical results for complex flow conditions, i.e. turbulent flows. The numerical results showed good agreement with results obtained by Direct Numerical Solvers (DNS) and experiments by other

authors. The proposed scheme can now be implemented to solve complex thermal flows such as multicomponent, multiphase flows with temperature variations.

Capítulo 2

Evolutionary Advancement of Thermal Lattice Boltzmann Methods

2.1 Abstract

Here, we present a comprehensive review of the evolutionary advancement of the thermal lattice Boltzmann methods along with detailed implementations. We develop a comparative study of various LBM frameworks, methodologies, and thermal boundary conditions since the time of Lattice Gas Automata (LGA) to recently developed advanced LBM methods used to model numerous simple and complex thermal flow problems.

The material of this chapter has been submitted for publication as a review paper in **Progress in Aerospace Sciences**

2.2 Introduction

Lattice Boltzmann Methods (LBM) have been important and successful numerical tools for solving various fluid flow and heat transfer problems for the last two decades [30, 44, 154, 159, 168, 169, 194, 195]. Initially, LBM was used to solve fluid flow problems, and based on the success it achieved, was used to deal with thermal problems but with many challenges [41, 156, 190, 273, 285]. But prior to the development of statistical lattice Boltzmann equation approaches fully based on Boltzmann Transport Equation (BTE) and their implementation in thermal-fluid flow problems, Lattice Gas Automata (LGA) was used to solve fluid flow and thermal problems [22, 49, 91, 108, 315]. Numerical simulations by direct integration of the partial differential equations, known as direct numerical simulations mostly solve

the macroscopic description of the fluid flow. LGA can be considered as the indirect approach which solves the microscopic and mesoscopic description of the systems. The Lattice Gas Automata (LGA) was developed to solve fluid flow problems at the microscopic level using the Boolean approach [91].

The first alternative to the LGA was described by McNamara, where the author used Boltzmann equation [201]. The very first effort to use LGA to solve the thermal problem was made by Chen et al. [47]. But due to its Boolean nature, this approach was neither free from statistical noise and instability nor it could be used to simulate large regions. The LGA was also computationally costly and extending it to the hydrodynamic limit posed serious problems. Remarkable efforts were then adopted to cure the LGA of these drawbacks [42, 47, 131, 201]. Further improvements in the performance of LGA were carried out by Chen et al., where they derived the Navier-Stokes equation using an improved Lattice Gas Boltzmann approach [42]. The lattice-gas Boltzmann method removed the numerical artifacts due to the non-Galilean invariance and velocity dependent equation of state. The lattice Boltzmann equation used real numbers and Maxwell equilibrium distribution function unlike LGA which uses Boolean numbers and Fermi-Dirac equilibrium distribution function rule which cause the statistical noise and non-Galilean invariance [42, 48, 163]. In 1993, Alexander et al. [8], Bartolini et al. [17], and Qian et al. [235] made the earliest contributions to solve thermohydrodynamics using the lattice Boltzmann equations. Afterward, numerous lattice Boltzmann schemes and frameworks have been developed over the years which can provide efficient numerical solutions for complex thermal-fluid flow problems.

To address a thermal flow, the system of equations must contain mass, momentum, and energy conservation equations. These equations can be recovered successfully by using Chapman-Enskog (C-E) expansion of the continuous Boltzmann equations using appropriate collision rules. In LBM, there are three frameworks which deal with the fluid flow with heat transfer, which is (1) Multispeed model, (2) Hybrid model and (3) Double Distribution Function (DDF) model or Multi-Distribution Function (MDF) model. In LBM, fluid is treated as an ensemble of fictitious particles. The state of the particles in certain space and time is defined by the local velocity distribution functions [44]. These particles exist on a Cartesian grid, a finite set of admissible speeds which particles can take. The streaming of the particles from one node to another is possible via links connecting these nodes. The collisions among the particles take place at lattice nodes only and conserve the quantities such as mass, momentum, and energy. In LBM, there exist numerous schemes such as Bhatnagar-Gross-Krook (BGK) (also known as single relaxation time; SRT), Multiple Relaxation Times (MRT), Cascaded collision operator, En-

tropic LBM, Cumulant LBM and Karlin-Bosch-Chikatamarala (KBC), which have been frequently used to define these collisions. These collision operators have been studied in great depth and their advantages and relevance in dealing with specific problems have also been well established in the literature. Therefore, in-depth comparisons among these collision schemes are not necessary here because the scope of the present work is to study thermal LBM approaches.

Multispeed (MS) model deals with single distribution function. Mass, momentum, and energy conservation rules are defined using velocity distribution function f. These models consider energy (or temperature) as an additional velocity component. Some most notable implementations of MS models to solve thermal flows can be found in Refs. [8, 31, 51, 149, 202, 235, 253, 280, 297, 298, 316]. Hybrid thermal lattice Boltzmann models, as clearly suggested by the name, use a hybrid approach to treat thermal flows. The mass and momentum equations are solved by using athermal lattice Boltzmann methods and temperature equation (or energy equation) is solved by the conventional computational fluid dynamics methods such as finite volume method (FVM) and finite difference method (FDM). These models perform efficiently and are accurate and stable in solving the thermal flows. The major drawback with such models is that this approach deviates from the very essence of using LBM in the first place. LBM is well known for easy and efficient parallelization of the algorithms due to the fact that the data communication are local. Some notable implementations of hybrid models can be found in Refs. [33, 88, 146, 172, 173, 187, 203, 209, 211, 272, 279].

The double distribution function (DDF) models are considered to be the most successful LBM framework to solve thermal problems. In this model, two distribution functions have been used, one distribution function to address mass and momentum conservation and another to address energy conservation (temperature). Inside DDF framework itself, there exist two approaches, one approach is when the temperature is considered as a passive scalar, in which the compressive work and heat dissipation are considered to be negligible [17, 81, 256]. And another approach is internal energy approach, which simulates the evolution of internal energy and allows incorporation of compressive work and heat dissipation. The lattice Boltzmann equation (LBE) is derived by discretizing the continuous Boltzmann equation in time, space and velocity spaces [127]. The internal energy DDF approach is similar to the passive scalar DDF approach in the sense that in both cases separated distribution functions are used to simulate temperature evolution. The DDF models improve the stability and accuracy of the LB schemes significantly and due to their better performance compared to Multispeed methods, the DDF models have drawn much attention of various research groups [29, 39, 40, 50, 74–76, 82, 97, 112–

114, 127, 141, 147, 148, 155, 160, 167, 204, 214, 216, 221, 225, 228, 229, 259, 262, 277, 278, 283, 291].

A large variety of thermal problems have been solved using the LBM frameworks and schemes described earlier. Chen et al. made the first attempt to apply a lattice gas model to study thermal flow. The authors implemented lattice gas automata to solve thermal Poiseuille flow and heat conduction [47]. Bartoloni et al. used the enhanced collision scheme of the LGA and solved Rayleigh-Bénard convection [17]. Alexander et al. and Qian et al. presented the first implementations of the BGK collision operators to solve Rayleigh-Bénard convection [8, 235]. Massaioli et al. presented the exponential tails in two-dimensional Rayleigh-Bénard convection using LGA [197]. Chen et al. presented one of the first implementations of the MRT collision scheme for variable Prandtl number flow [52]. In BGK thermal LBM schemes, the ratio of viscosity and thermal conductivity depends only on one relaxation parameter which fixes the Prandtl number limiting the performance of the numerical scheme. MRT collision scheme deals with more than one relaxation parameter giving birth to variable Prandtl number thermal flows. Soe et al. provided an improved BGK collision scheme and extended the application of variable Prandtl number flows to turbulent thermal flows [263]. Shan et al. implemented the DDF BGK thermal LBM scheme to solve Rayleigh-Bénard convection, in which the temperature was solved using the passive scalar approach, i.e. in incompressible limit without heat dissipation and compressive work [256]. He et al. adopted a different DDF LBM approach to deal with temperature, using internal energy distribution function instead of using passive scalar approach [127]. Ihle et al. adopted the DDF LBM scheme using BGK operators to simulate non-ideal gases with potential energy [141]. Palmer et al. implemented the DDF framework for compressible fluids, in which the authors considered the internal energy to be passive scalar [225].

Multispeed models are generally unstable due to insufficient Galilean Invariance [225, 280]. And due to fixed Prandtl number, they are also inadequate when solving flows with large temperature variations. Therefore MS model was not suitable for solving non-ideal gas flows. Teixeira et al. identified the temperature dependent term in the equilibrium distribution function leading to the Galilean invariance violation and improved the performance of the MS model by introducing under-relaxed collision scheme [280]. Jiaung et al. incorporated the enthalpy formation into the thermal LBM scheme to solve heat conduction with phase change [149]. Guo et al. demonstrated the first implementation of DDF LBM scheme where two separate lattice models were adopted to solve mass and momentum, and temperature [113]. LBM for the mixture of two immiscible fluids was developed by Inamuro et al. and used to solve Rayleigh-Bénard convection [144]. Heat transfer in the multi-layered

structure using dual phase lag heat conduction model was studied using BGK-LBM [134]. For flows with considerable density variation and temperature dependent transport coefficient, Lallemand et al. proposed the use of a hybrid scheme, where finite difference method (FDM) was used to solve temperature and MRT-LBM was used to solve flow field [172]. Therefore, the stability of the LBM scheme was improved significantly. For thermal flows, the coupling between shear and energy modes is extremely important, for energy conservation approach. Lallemand et al. suggested that spurious algebraic coupling between shear and energy modes plagued the energy conserving LBM. The authors proposed an improved coupling in Ref. [173]. Ansumali and Karlin suggested that thermal LBM models did not fully conserve the energy thus giving rise to absurdly high bulk viscosity values. The authors proposed the "Consistent Lattice Boltzmann Method" to solve energy conservation [10].

Convective heat transfer in porous media was also solved by using DDF LBM schemes [29, 112, 254]. Gao et al. implemented local thermal non-equilibrium conditions into the LBM scheme to model natural convection in porous media [93]. Phenomena such as interfacial tension and its dependence on temperature were studied by Chang et al. and two-phase Rayleigh-Bénard convection with a deformable interface was solved using BGK-LBM [37]. Zhang et al. developed the LBM scheme for simulations of liquid-vapor thermal flows using BGK-LBM under MS model framework [316]. The similar MS LBM formulation was applied to solve liquid-gas two-phase flow in 2D by Seta et al. [253]. Enthalpy based hybrid LBM was proposed by Chakraborty et al. to simulate solid-liquid phase transition in presence of convective transport using BGK-LBM to solve the flow field [33]. Safari et al. presented an extended version of the LBM to study phase change for two-phase fluid flow [247]. The authors provide a great in-depth insight into efficient modeling of phase interface, and the impact of evaporation, boiling, and condensation. Huang and Wu adopted the DDF framework to develop immersed boundary thermal LBM to simulate solid-liquid phase change [139]. Gonnela et al. solved the non-ideal fluid flows using finite difference LBM approach for application in phase separation [103].

Enthalpy based DDF-LBM scheme was developed by Chatterjee et al., in which the authors replaced the internal energy distribution function by enthalpy distribution function and simulated phase transition [39]. LBM has also been used to solve backward facing steps flows using the BGK collision scheme under DDF framework [40]. Escobar et al. simulated multi-length and multi-time scale heat transfer in crystalline semiconductor [82]. The authors adopted the DDF BGK approach to solving the Boltzmann transport equation for phonons. Radiative and conductive heat transfer simulations using hybrid LBM were studied by Mishra et al. and

Gupta et al. [115, 209, 211]. Combustion simulations for low Mach number were performed by Chen et al. using a coupled LBM [50]. Microfluidic analysis of bubble dynamics of CO_2 was simulated by Fei et al. using thermal BGK LBM scheme [83]. Watari used the BGK-FDLBM scheme to simulate temperature jump and velocity slip in 3D [296]. Thermal fluctuations were introduced by Gross et al. to the LBM scheme for non-ideal gas flows to increase the numerical accuracy for thermal flows [106]. The LBM scheme with Langmuir slip model to solve thermal microflows was developed by Chen et al. [45]. Compressible Rayleigh-Taylor fluid flows were solved by Scagliarini et al. [250]. Natural convection heat transfer in closed enclosures and square cavity have been studied extensively using thermal LBM frameworks by many groups [74, 114, 160, 172, 187, 203, 204, 214, 216, 228, 229]. Delouei et al. presented DDF thermal LBM scheme using direct forcing immersed boundary to simulate non-Newtonian fluid flow [69].

In the next Sections, we discuss and describe various thermal LBM models separated based on MS, Hybrid and DDF approaches, followed by a presentation of various types of thermal boundary conditions. And finally, we show diverse applications of thermal LBM schemes in solving thermal fluid flows, e.g. natural convection, forced convection, phase transition and separation, thermal flows in porous media and in micro and nano-channels.

2.3 Lattice Gas Automata

Lattice Gas (LGA) approach with discrete Boolean elements was applied to solve Navier-Stokes equations by Frisch et al. [91]. Due to the local nature of the particle collision, these LGA models were suitable for massively parallel computing machines. In LGA models, the fluid is described as an ensemble of Boolean particles, signifying a complete discrete phase space and discrete time. The model by Hardy, de Pazzis and Pomeau (HPP model) [119–121] can simulate these Boolean nature particles flow on an underlying regular square 2D lattice. The thermodynamic equilibria of the HPP model have free continuous parameters, e.g. average density and momentum. It should be noted that each particle which is not in rest must follow a pre-determined path called link and it must reach the equilibrium state after colliding with other particles at the resting nodes. For these models, the macroscopic equation, recovered by slowly varying density and momentum in space and time, deviate from the non-linear N-S equation due to lack of Galilean invariance, lack of isotropy and crossover dimension problem [91]. HPP model is invariant under $\pi/2$ rotation (square lattice) and unable to guarantee the isotropy. The momentum flux

tensor, for the HPP model is given by

$$P_{\alpha\beta} = p_{\alpha\beta} + T_{\alpha\beta\gamma\epsilon}u_\gamma u_\epsilon + O(u^4),$$

where p is pressure, $\mathbb{T}$ is a tensor. The momentum flux tensor is different from the N-S equation due to the lack of isotropy. Using Hexagonal Lattice Gas (HLG) model, which is invariant under $\pi/3$ rotation, one recovers the isotropy of the tensor T and provides correct momentum flux tensor

$$P_{\alpha\beta} \sim (p + u^2) + u_\alpha u_\beta + O(u^4)$$

for the N-S equation at low Mach numbers. The corrected HLG model suffers from statistical noise and serious stability problems due to the Boolean approach and Fermi-Dirac distribution rules for equilibrium. The fact that very small subregion can be used for simulations in LGA models, contribute heavily to the numerical inaccuracy and instability when the microscopic details are extended to their macroscopic description. Therefore, it is necessary to average the microscopic quantities over large subregions, for longer times and different initial conditions [201]. McNamara and Zanetti, therefore, suggested transferring the LGA into a Boltzmann model. The Boolean site populations were replaced by real numbers and the Boltzmann equation was adopted to govern the time evolution of those particles. Higuera et al. proposed a scheme with enhanced collision along with lattice gas Boltzmann equation, migrating from LGA's Boolean numbers towards probability distribution functions [131]. The lattice gas Boltzmann equation reads

$$N_i(x + c_i, t + 1) = N_i(x, t) - \Omega(N_i - N_i^{eq}), \tag{2.1}$$

where N_i is the lattice gas particle distribution function, c_i is the lattice gas particle velocity in i^{th} direction, Ω is the collision operator and N_i^{eq} is the equilibrium distribution function. The conservation rules, i.e. mass and momentum are given by

$$\rho = \sum_i N_i$$

and

$$\rho u = \sum_i c_i N_i,$$

respectively. The equation of state of the LGA models differs from the equation of state of ideal gases, $p = p(n, T)$. In LGA models, pressure depends on the macroscopic velocity

$$p = p_0(n, T) - p_1(n, T)nu^2,$$

11

which causes spurious currents [47]. The relation between pressure and density for LGA can be written as $p_0 = c_s^2 \rho$, where c_s is the sound velocity and can be given by c^2/D, D is the lattice model dimension [42, 47]. Therefore,

$$p_0(n, T) = \rho c_s^2$$

and

$$p_1(n, T) = \rho C(\rho) u^2/D,$$

where $C(\rho)$ is the convection coefficient. The insufficient degree of Galilean invariance is due to the fact that convection coefficient depends on the density, strictly limiting the LGA to an incompressible scenario. And the term $p_1(n, T)$ is the root cause of the kinetic energy fluctuations in LGA simulations due to the direct velocity dependence of pressure [46, 62]. Dealing with thermal flows using LGA models had been a serious issue, as there was no theoretical development to study temperature gradient in LGA models. Chen et al. suggested that multi-speed particles could conserve the energy [47]. But the authors again retained the root cause of numerical instabilities and inaccuracy, i.e. Fermi-Dirac equilibrium rules.

2.4   Lattice Boltzmann Equations

Lattice Boltzmann Equations (LBE) were emerged from the lattice gas Boltzmann equation with some much needed improvements [42, 201]. Boltzmann transport equation (BTE) reads

$$\frac{\partial f(\mathbf{x}, \xi, t)}{\partial t} + \xi \cdot \nabla f(\mathbf{x}, \xi, t) = \Omega(f, f), \tag{2.2}$$

where f is the velocity distribution function, ξ is the microscopic velocity and Ω is the collision operator. Discretization of BTE on a lattice model leads to the lattice Boltzmann equation (LBE). The basic kinetic equation (LBE) reads

$$f_i(x + c_i \triangle t, t + \triangle t) - f_i(x, t) = \Omega_i, \tag{2.3}$$

where f_i is the one particle distribution function, c_i is the microscopic (characteristic) velocity of fluid particle in i^{th} direction, and Ω_i is the collision operator, proportional to $(f_i^{eq} - f_i)$. A particle in LBE approach can be considered as an ensemble of infinite subparticles which are infinitely separable, thus giving freedom to define collisions in infinite ways satisfying conservation rules. The Fermi-Dirac distribution equilibrium rule is no longer required in LBE [42]. The Galilean invariance problem can be

corrected by adopting the following equilibrium distribution function defined by

$$f_i^{eq} = \frac{\rho}{b} + \frac{\rho}{c_s^2 b}\hat{c}_i \cdot u + \rho\left(\frac{1}{2c_s^4 b} + \frac{1}{c_s^4 Db}\right)Q_{i\alpha\beta}u_\alpha u_\beta, \tag{2.4}$$

where $Q_{i\alpha\beta} = \hat{c}_{i\alpha}\hat{c}_{i\beta} - (1/D)\delta_{\alpha\beta}$, $c_{i\alpha}$ and $c_{i\beta}$ are microscopic velocities in α and β directions, u_α, u_β are macroscopic velocities. Eq. (2.4) removes the dependency of convection coefficient C on density ρ, recovering Galilean invariance. Therefore, at this stage, the LBE is with improved Galilean invariance and is valid for any particle density distribution. But one speed LBE is not enough to correct the direct relation between pressure and velocity. By introducing the rest particles, new general form of equilibrium distribution function for moving particles can be given such that

$$f_i^{eq} = d + \frac{\rho}{c_s^2 b}\hat{c}_i \cdot u + \rho\left(\frac{1}{2c_s^4 b} + \frac{1}{c_s^4 Db}\right)\hat{c}_{i\alpha}\hat{c}_{i\beta}u_\alpha u_\beta + \gamma u^2, \tag{2.5}$$

The coefficient d, γ, and those derived from equilibrium expression of rest particles can be assigned appropriate values to attain the correct ideal gas equation of state, $p = c_s^2 \rho$, which does not explicitly depends on velocity. In the LBE model, the fluid is considered as a collection of fictitious particles and their evolution in space and time can be described by the velocity distribution function. Maxwell Boltzmann distribution function is the most popular to define the equlibrium distribution. The Maxwellian equilibrium for velocity distribution function f_i^{eq} reads

$$f_i^{eq} = \rho w_i\left(1 + \frac{\vec{u} \cdot \vec{c}_i}{c_s^2} + \frac{(\vec{u} \cdot \vec{c}_i)^2}{2c_s^4} - \frac{\vec{u} \cdot \vec{u}}{2c_s^2}\right), \tag{2.6}$$

where w_i is the weight for characteristic velocity for i^{th} lattice node. Use of square lattice models in 2D and 3D has been a common practice in LBM. There exist numerous square lattice models, the most popular ones are D_2Q_5, D_2Q_9, D_3Q_{15}, D_3Q_{19}, and D_3Q_{27}. The subscript of Q denotes the number of velocities, i.e. number of lattice nodes existing in a unit lattice cell. The LBEs are discretized on a chosen lattice model, and their implementation and properties are available in the literature [165].

Here we discuss two 2D lattice models which can be used for successfull thermal simulations in 2D. For D_2Q_9 lattice model $c_i = (c_{i,x}, c_{i,y})$ $(i = 1, \ldots, 9)$ are

$$\{(0,0), (-1,1), (-1,0), (-1,-1), (0,-1), (1,-1), (1,0), (1,1), (0,1)\}.$$

The weight factors for D_2Q_9 lattice model are

$$[w_1, \ldots, w_9] = \left(\frac{4}{9}, \; \frac{1}{36}, \; \frac{1}{9}, \; \frac{1}{36}, \; \frac{1}{9}, \; \frac{1}{36}, \; \frac{1}{9}, \; \frac{1}{36}, \; \frac{1}{9}\right).$$

13
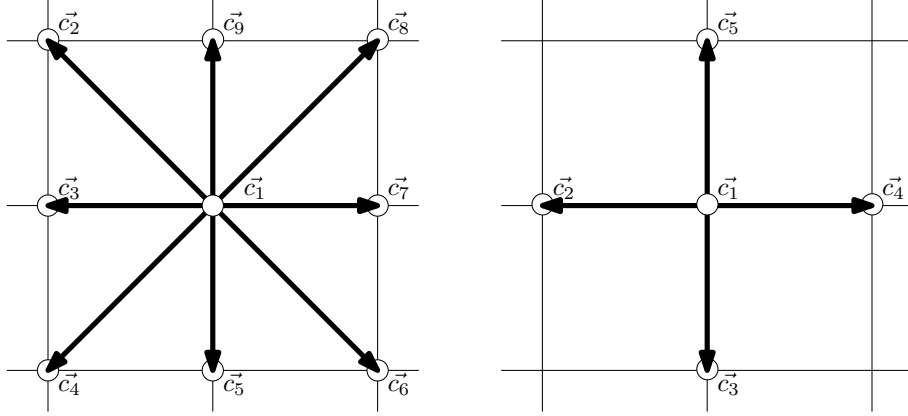
Figura 2.1: D_2Q_9 lattice model(left) and D_2Q_5 lattice model (right).

For D_2Q_5 lattice model $c_i = (c_{i,x}, c_{i,y})$ $(i = 1, \ldots, 5)$ are

$$\{(0,0), (-1,0), (0,-1), (1,0), (0,1)\}.$$

The weight factors for D_2Q_5 lattice model are

$$[w_1, \ldots, w_5] = \left(\frac{1}{3}, \quad \frac{1}{6}, \quad \frac{1}{6}, \quad \frac{1}{6}, \quad \frac{1}{6} \right).$$

The conservation rules are obeyed at the lattice models, and conserved and non-conserved moments are defined for each lattice before proceeding with the numerical simulations. These moments are of the form of Hermite polynomials which satisfy the isotropy conditions to recover correct macroscopic equations [165]. For D_2Q_9 model, nine moments must be defined, and for D_2Q_5 model five moments must be defined. Therefore, the total number of moments defined on a lattice model is equal to the total number of velocities of the lattice model.

2.5 Thermal Lattice Boltzmann Methods

The initial approaches to solve thermal hydrodynamics involved LGA models [48]. But the use of Fermi-Dirac equilibrium distribution prevented from recovering the correct form of energy equation. The LBM approach adopts Maxwellian equilibrium distribution and solve mass, momentum and energy conservation equations. The system of mass, momentum and energy conservation equations with viscous, compressible and heat conducting flows reads [8]

$$\frac{\partial \rho}{\partial t} + \frac{\partial (\rho u_\alpha)}{\partial x} = 0, \tag{2.7}$$

14

$$\rho \frac{\partial u_\alpha}{\partial t} + \rho u_\beta \frac{\partial u_\alpha}{\partial x_\beta} = -\frac{\partial p}{\partial x_\alpha} + \frac{\partial}{\partial x_\alpha} \left[\lambda \frac{\partial u_\gamma}{\partial x_\gamma} \right]$$
$$+ \frac{\partial}{\partial x_\beta} \left[\mu \left[\frac{\partial u_\beta}{\partial x_\alpha} + \frac{\partial u_\alpha}{\partial x_\beta} \right] \right], \tag{2.8}$$

$$\rho \frac{\partial E}{\partial t} + \rho u_\alpha \frac{\partial E}{\partial x_\alpha} = -p \frac{\partial u_\gamma}{\partial x_\gamma} + \frac{\partial}{\partial x_\beta} \left[\kappa \frac{\partial T}{\partial x_\beta} \right]$$
$$+ \mu \left[\frac{\partial u_\beta}{\partial x_\alpha} + \frac{\partial u_\alpha}{\partial x_\beta} \right] \frac{\partial u_\beta}{\partial x_\alpha} + \lambda \left[\frac{\partial u_\gamma}{\partial x_\gamma} \right]^2, \tag{2.9}$$

where E is the internal energy per unit mass, u is the macroscopic velocity, λ is the bulk viscosity, μ is the dynamic viscosity, and κ is the thermal conductivity. The macroscopic conserved quantities can be calculated from the LBE Eq. (2.3), such that,

$$\rho = \sum_i f_i,$$

$$\rho u = \sum_i c_i f_i,$$

and

$$\rho E = \sum_i f_i (c_i - u)^2 / 2.$$

Some initial approaches considered internal energy as a moment of velocity distribution function [8, 17, 235]. The single relaxation time collision operator, also known as the BGK collision operator was used, where

$$\Omega = -\frac{1}{\tau} \left(f_i - f_i^{eq} \right), \tag{2.10}$$

where τ is the relaxation time for f_i to reach its local equilibrium state f_i^{eq}. Since in these approaches, the flow and thermal coefficients depend on single parameter τ, the Prandtl number is fixed and therefore induces limitations and instabilities in the numerical scheme. These initial approaches can be classified under the multi-speed thermal LBM framework, which we will discuss in next Section. Therefore, to deal with the thermal flows with high accuracy and stability, different frameworks and approaches were adopted, and as discussed in the introduction, are classified into three framework categories. Different collision schemes have been implemented to obtain variable Prandtl number to increase the stability of the LBM scheme.

2.6 Multi-Speed Thermal LBM

Initially, LGA and LBE were used to solve athermal fluid flow problems. The extension of these LB techniques was then made to simulate thermal problems [8, 17, 47, 51, 235]. These approaches were called Multi-speed models in which the energy was considered as an additional moment of the velocity. As described in the previous section, only one set of distribution functions is needed to describe mass, momentum and energy conservation. From Eq. (2.3 and 2.10), BGK-LBE reads

$$f_i(x + c_i \triangle t, t + \triangle t) - f_i(x, t) = -\frac{1}{\tau}(f_i - f_i^{eq}). \tag{2.11}$$

There are two important steps in LBM numerical approach, one is advection (the propagation of fluid particles along the links connecting nodes), and second is the collision, which is local and occur only at nodes. The term

$$f_i(x + c_i \triangle t, t + \triangle t)$$

is the advection (or streaming) step, and

$$f_i(x, t) - \frac{1}{\tau}(f_i - f_i^{eq})$$

is the collision step. In order to recover the N-S equations from the LBE scheme, f^{eq} taken as the Maxwellian equilibrium distribution depends only on the conserved quantities ρ, u and E. The equilibrium distribution also depends on the lattice structure models. But the general form of the equilibrium distribution can be given by [8, 51]

$$\begin{aligned} f_i^{eq} = A + Bc_i \cdot u + C(c_i \cdot u)^2 + Du^2 \\ + E(c_i \cdot u)^3 + F(c_i \cdot u)u^2, \end{aligned} \tag{2.12}$$

A, B, C, D, E and F are coefficients, which are functions of ρ and internal energy E. These coefficients depend on the lattice structure. Now to recover the hydrodynamic equations, we Taylor expand the LBE; Eq. (2.11) to second order. Now the Chapman-Enskog (C-E) multiscale expansion is adopted, where time derivative and distribution functions are expanded and used in the Taylor expanded LBE. Then, continuity, momentum, and energy equations are recovered [8]. The correct form of Euler and N-S equations are then identified from the three equations after fulfilling few conditions, described in the paper [8]. The above described LBM is the multi-speed approach. This LBM can now be implemented on a 2D or 3D lattice geometry. The isotropy of the momentum flux tensor directly depends on the lattice structure

and the coefficients from the equilibrium distribution Eq. (2.12) can be determined by fulfilling these conditions. A direct identification of the transport coefficients is done by comparing the corrected N-S equations recovered through C-E expansion with the real continuity, moment and energy equations, Eq. (2.7, 2.8, 2.9). The shear viscosity

$$\mu = \rho E \big(\tau - \frac{1}{2} \big)$$

and thermal conductivity

$$\kappa = 2\rho E \big(\tau - \frac{1}{2} \big).$$

Transport coefficient depend on a single parameter τ, which results in a fixed Prandtl number.

2.6.1   Improvements in Multi-Speed Models

The M-S model described earlier was used by many groups to simulate thermal flows [17, 51, 81, 235]. But these implementations were not very stable and accurate [202]. The one way to remove the dependency of transport coefficients on a single relaxation parameter is to introduce two relaxation parameters collision operator. In this way, the problem of fixed Prandtl number can also be solved. The LBE Eq.(2.11) can be rewritten after modifying the collision operator such that [52]

$$f_i(x + c_i \triangle t, t + \triangle t) - f_i(x, t) = -\frac{1}{\tau_1} \big(f_i - f_i^{eq} \big) - \frac{1}{\tau_2} \big(f_{i'} - f_{i'}^{eq} \big), \qquad (2.13)$$

where τ_1 and τ_2 are two relaxation parameters, and $i' = i + Q/2$. To recover N-S equations, C-E expansion is required where first the distribution function should be expanded such that

$$f_i = f_i^{(0)} + \epsilon f_i^{(1)} + \epsilon^2 f_i^{(2)} + ...,$$

similar expansion is applied for $f_{i'}$, where ϵ is a small parameter proportional to Knudsen number. It should be noted that $f^{(0)} = f^{eq}$, since the contributions from high order distribution functions $f^{1,2,3\cdots}$ are considered negligible in the local macroscopic mass density, momentum and energy density. Therefore the conservation equations are

$$\rho = \sum_i f_i = \sum_i f_i^{eq}$$

$$\rho u = \sum_i c_i f_i = \sum_i c_i f_i^{eq} \qquad (2.14)$$

$$\rho E = \sum_i f_i (c_i - u)^2/2 = \sum_i f_i^{eq} (c_i - u)^2/2,$$

and

$$\sum_i f_i^{(1)} = 0$$

$$\sum_i c_i f_i^{(1)} = 0 \qquad (2.15)$$

$$\sum_i f_i^{(1)}(c_i - u)^2/2 = 0,$$

similarly, conservation rules can be established for $f_{i'}$, where the contributions from $f_{i'}^{(1)}$ and so on, would be negligible, where $\sum_i f_i^{(1)} = \sum_i f_{i'}^{(1)} = 0$. In a real physical dynamic system, different phenomena occur at different time scales, therefore to recover correct dynamics of the system the time derivative is also expanded, $\partial_t = \partial_{t(1)} + \epsilon \partial_{t(2)}$. Now the LBE for the two relaxation parameters can be Taylor expanded and using the expansion of f and ∂_t, different equations for the various order of ϵ can be recovered [52]. After following typical C-E procedure, continuity, momentum, and energy equations are recovered, see Eq. (2.10), Eq. (2.11) and Eq. (2.12) in [52]. After a direct comparison between these equations and the set of equations Eq. (2.7, 2.8 and 2.9), the transport coefficients values are determined. For two relaxation BGK LB scheme, an inconsistency was observed since two type of viscosity is defined unlike the case of single relaxation BGK LBM. The momentum and energy equation provide different viscosity, see [52]. The momentum equation is considered to determine fluid flow related transport coefficients, the shear viscosity

$$\mu = \frac{2}{D}\rho E\left(\frac{\tau_2 \tau_1}{\tau_2 + \tau_1} - \frac{1}{2}\right)$$

and bulk viscosity

$$\lambda = -\frac{4}{D^2}\rho E\left(\frac{\tau_2 \tau_1}{\tau_2 + \tau_1} - \frac{1}{2}\right).$$

Thermal conductivity κ can be evaluated from the energy equation as the coefficient of the heat conductive term in the energy equation. It reads,

$$\kappa = \frac{D+2}{D}\rho E\left(\frac{\tau_2 \tau_1}{\tau_2 - \tau_1} - \frac{1}{2}\right).$$

The Prandtl number Pr, the ratio of viscous diffusion rate and thermal diffusion rate, reads

$$Pr = \frac{2}{D+2} \cdot \frac{2\frac{\tau_2 \tau_1}{\tau_2 + \tau_1} - 1}{2\frac{\tau_2 \tau_1}{\tau_2 - \tau_1} - 1}.$$

Therefore, it is evident that two relaxation BGK LB scheme eliminates the single

relaxation parameter dependence of Prandtl number. This improves the stability of the LBM scheme for large temperature variations. But it must be noted as well that this two-parameter scheme suffers from the inconsistency in defining viscous dissipation correctly. The BGK single relaxation parameter scheme can define the viscous dissipation better as it does not generate different viscosity in momentum and energy equations. But due to fixed Prandtl number in this LB scheme, it can only be used to simulate thermal flows with small temperature variations. Chen et al. and Texeira et al. proposed a new improved definition for the collision operator that can lead to flexible Prandtl number [43, 280]. The equilibrium distribution was then computed by minimizing the local H- function [43]. The equilibrium distribution for the small number of degrees of freedom contributes to the numerical instability in continuum dynamics. The authors suggested increasing the degree of freedom by increasing speed.

Teixeira et al. [280] proposed an under-relaxed equilibrium which slowed down the evolution of a temperature dependent term present in the equilibrium distribution. In this work the authors provide the development of this equilibrium under relaxation approach and an in-depth analysis of the stability enhancement of the M-S LBM model. Zhang et al. [316] extended the M-S model to simulate liquid-vapor thermal flows but with a single relaxation parameter BGK scheme. Watari et al. [297] proposed the use of finite difference LBM (FDLBM) [31] to increase the accuracy of the M-S model. The correct form of fluid and energy equations can be recovered by retaining higher order velocity terms (up to 4th order) in the equilibrium distribution and by increasing the degree of freedom by increasing the rank of the isotropic velocity tensors (up to 7th rank). The accuracy of the M-S model was further improved by introducing global coefficients in the local equilibrium distribution [298]. In Ref. [298], Watari et al. presented an in-depth analysis of appropriate lattice models to produce high-rank isotropy for deriving the correct form of N-S equations.

2.7   Hybrid Thermal LBM

Hybrid thermal LBM model consists of combining two different numerical approaches to deal with thermal flows. Generally, such models solve continuity and momentum equations using LBM approach and solve temperature evolution by directly solving the macroscopic temperature equation using a conventional computational fluid dynamics approach such as finite volume methods (FVM) or finite difference methods (FDM) [172]. Contrary to the M-S models, in hybrid models, there exists decoupling between LBE simulation and finite difference type simulation to solve the

temperature. It was believed that an inefficient coupling between flow and energy modes is the source of the numerical instabilities in all LBM thermal methods. Therefore, to avoid such inefficient coupling, hybrid models were developed [172, 173]. To further increase the stability of the LBM scheme, an improved collision operator called multiple relaxation times (MRT) was developed [70, 71, 171]. In MRT operator, streaming is described in velocity space, but the collision operator is defined in moment space. The problems such as fixed Prandtl number and fixed kinematic and bulk viscosities can be removed by using MRT collision scheme. The two relaxation parameter scheme used in some of the M-S thermal models is also a form of MRT collision scheme [71, 202]. The MRT LBE reads

$$
\begin{aligned}
& f_i(\vec{x} + \vec{c}_i \triangle t, t + \triangle t) - f_i(\vec{x}, t) \\
& = -\mathbb{M}^{-1}\mathbb{R}\bigg(m_i(\vec{x}, t) - m_i^{eq}(\vec{x}, t) \bigg),
\end{aligned}
\tag{2.16}
$$

where $\mathbb{R}$ is a diagonal matrix with different relaxation times for non-conserved quantities, $\mathbb{M}$ is the transformation matrix $\vec{m} = \mathbb{M}\vec{f}$. Raw moment m and velocity distribution function f are related through the microscopic velocity of the lattice model, such that $m_{x^m y^n} = \sum_i c_{i,x}^m c_{i,y}^n f_i$. See [70, 71] for an in-depth discussion on MRT collision scheme. And advection-diffusion equation can be solved for temperature evolution using a finite difference scheme [172],

$$
\begin{aligned}
T_i(\vec{x}, t + \triangle t) - T_i(\vec{x}, t) = & -\mathbf{j} \cdot \nabla_h T + \kappa \Delta_h T \\
& + q_2(\gamma - 1)c_{s_0}^2 \nabla_h \cdot \mathbf{j},
\end{aligned}
\tag{2.17}
$$

where T is the temperature, ∇_h and Δ_h are finite difference gradient and finite difference operator, respectively, q_2 is a coefficient. Then the coupling between temperature and momentum is established by adopting the proper definition of equilibrium distribution. As an equilibrium depends on conserved quantities ρ, $\mathbf{j} \cdot \mathbf{j}$ and T (specific internal energy proportional to T), therefore, the coefficients of conserved quantities can be determined by first order solution of the dispersion equation. One of the benefits of using the hybrid model is that this model does not use Boussinesq approximation explicitly, therefore, can be a good numerical tool to study thermal flows like combustions, compressible flows, etc. See Ref. [172] for detailed implementation.

For convective heat transfer where Boussinesq approximation stands valid, i.e. low Ma number flows, flows with a very small variation in density with respect to temperature, the coupling between T and velocity field is done through the buoyancy force [203]. The buoyancy force $g\beta T$ (where g is gravitational constant, β is linear isobaric thermal expansion coefficient) can be added to the R.H.S. of Eq.

(2.16). In such flows, it is generally considered that velocity field does not depend on the temperature, that means that the flow is incompressible with negligible heat dissipation, and an advection-diffusion temperature equation

$$\frac{\partial T}{\partial t} + u \cdot \nabla T = \alpha \nabla^2 T$$

is solved directly using FDM. The macroscopic velocity u in the advection-diffusion equation is determined by the relation $\rho u = \sum_i c_i f_i$.

Problems with conductive and radiative heat transfer can also be solved using LBM and FVM methods [208, 211]. A benchmark problem for transient conduction and radiation heat transfer in 2-D enclosed geometry filled with absorbing, emitting and scattering medium is presented in [208, 303, 314]. The energy equation was solved by BGK-LBM scheme. For radiative heat transfer, the source term added in the energy equation can be addressed by various methods such as discrete ordinate method, the discrete transfer method, finite volume method, and the collapsed dimension method [161, 208, 210]. The heat flow equation for the present problem with zero advection is

$$\left(\partial T / \partial t \right) = \alpha \nabla^2 T + \mathbb{Q},$$

α is the thermal diffusivity, $\mathbb{Q}$ is the radiative heat source, which can be calculated from any of the four techniques described earlier to solve radiation transfer equation. An appropriate lattice model must be chosen to solve the problem in 2D or 3D. The generalized discretized BGK-LBE for radiative heat conduction,

$$f_i(x + c_i \triangle t, t + \triangle t) - f_i(x, t) = -\frac{1}{\tau} \left(f_i - f_i^{eq} \right) + \mathbb{Q}$$

is extended to hydrodynamic limit using C-E expansion and transport coefficients are determined by comparing the original heat flow equation given earlier, with the recovered heat equation. Temperature is defined such that, $T = \sum_i f_i$. The hybrid LBM model can also be extended to simulate phase transition problems [66, 205–207]. In these implementations of LBM, the phase field approach was used to determine the evolution of each phase fraction. But there exists drawback with this technique which makes modeling of solidifications with small undercooling effects difficult. This problem can be addressed by using adaptive mesh refinement, which again increases the computation cost, rendering the phase field model ineffective. Therefore to make phase transition LBM approach more effective, an enthalpy based, thermodynamically consistent, hybrid LBM model was constructed to model solid-liquid phase transition in the presence of advection transport [33]. As previously for mass and momentum conservation, a simple athermal LBM approach can be adopted to address flow equations (mass and momentum), and a fixed-grid enthalpy-

21

porosity approach [28, 287] is used to couple the fluid moments with macroscopic temperature field which is obtained by directly solving coupled scalar transport equations. The term "enthalpy-porosity" means that in such models, the morphology of the phase-changing domain can be considered as a porous medium creating a frictional resistance towards fluid flow in phase interface regions [33, 287]. The macroscopic conservation equation for mass for each phase remains similar to Eq. (2.7). But momentum and energy equation for each phase for incompressible and laminar flows are

$$
\rho \frac{\partial u_\alpha}{\partial t} + \rho u_\beta \frac{\partial u_\alpha}{\partial x_\beta} = -\frac{\partial p}{\partial x_\alpha} + \frac{\partial}{\partial x_\beta}\left[\mu\left[\frac{\partial u_\beta}{\partial x_\alpha} + \frac{\partial u_\alpha}{\partial x_\beta}\right]\right]
$$
$$
+ \rho G + \rho S, \tag{2.18}
$$

$$
\frac{\partial\big(C_p T\big)}{\partial t} + u \cdot \nabla C_p T = \kappa \Delta T + \mathbb{Q}, \tag{2.19}
$$

where G and S are the external body force $g\beta(T - T_{ref})$ (Boussinesq approximation) and equivalent frictional resistance force, respectively. The term $\mathbb{Q}$ in Eq.(2.19) describes the latent-heat evolution,

$$
\mathbb{Q} = -\frac{\partial \Delta H}{\partial t} - \nabla \cdot (u \Delta H),
$$

for pure material phase change $\nabla \cdot (u \Delta H) = 0$. For phase changing system, an additional forcing term $\mathbf{F}_i$ (consisting of body force G, frictional force S and interaction force F^{int}) is added to the collision operator in a BGK-LBE,

$$
f_i(x + c_i \triangle t, t + \triangle t) - f_i(x, t) = -\frac{1}{\tau}\big(f_i - f_i^{eq}\big) + \mathbf{F}_i.
$$

Mass and momentum conservation rules are given by

$$
\rho = \sum_i f_i
$$

and

$$
\rho u = \sum_i c_i f_i + \frac{1}{2}\sum_i \mathbf{F}_i,
$$

respectively. The interaction force can be calculated by using Shan-Chen type interaction potential V,

$$
F^{int} = -\nabla V
$$

[257]. The similar steps must be followed to recover macroscopic equations using C-E expansion and identify the transport coefficients. Heat transfer in a differentially

heated square enclosure with a conducting cylindrical body inside (see Fig.1 in Ref. [146]) was also solved by using hybrid models. MRT collision operator was used to solve the fluid flow fields and temperature equation was solved using a finite difference method [146]. In many body problems like this, implementation of accurate boundary conditions are essential to maintain the stability and accuracy of the numerical schemes, which we shall discuss in Section 2.9, devoted to the boundary conditions.

2.8 Double Distribution Function (DDF) LBM

The last and most successful LBM framework to deal with thermal flows is the double distribution function (DDF) thermal LBM. In which, two separate distribution functions are used, one to address mass and momentum, and another to solve energy (temperature field). Generally, as always, velocity distribution function to describe macroscopic density and momentum, and an internal energy distribution function to describe the evolution of temperature field. Thermal flows can be classified into two categories for convenience, first is when the temperature is considered as a passive scalar (flows with negligible heat dissipation and compressive work; incompressible thermal flows), and second is when velocity profile depends on the temperature (flows with heat dissipation and compressive work; compressible thermal flows). In the first case, temperature field obeys the advection-diffusion equation, and in second case temperature field is drawn by tracking the internal energy evolution; energy equation. DDF LBM scheme to address the first case type of flows consists of two distribution function, one to address flow field (like in all athermal LBM discussed earlier), and another distribution function to define temperature which is independent of the density ρ [17, 256]. For the second type of thermal flows, fluid flow approach is the same but the temperature is not independent of the density anymore.

One of the plus points of using DDF scheme is that it is easy to implement and highly parallelizable as other pure LBM schemes and due to the liberty of choosing two separate collision operators, Prandtl number is not fixed (allowing simulations of a higher range of temperature compared to M-S model). It also provides the liberty to choose two different (or the same) collision operators to address flow field and thermal field. The passive scalar DDF approach has been tested against the M-S models and showed better stability compared to the latter [17, 127, 256]. The accuracy of the passive scalar DDF LBM was proven to be better than the M-S models as well [81]. It should be noted here that the passive scalar approach is stable and accurate only for small Mach number flows (incompressible limits). The

LBE for flow field is

$$f_i(x + c_i \triangle t, t + \triangle t) - f_i(x, t) = \Omega_i(f_i, f_i), \qquad (2.20)$$

and LBE for temperature is

$$g_i(x + c_i \triangle t, t + \triangle t) - g_i(x, t) = \Omega_i(g_i, g_i), \qquad (2.21)$$

where f_i and g_i are velocity and temperature (or energy) distribution function, respectively, and $\Omega_i(f, f)$ and $\Omega_i(g, g)$ are collision operators used for fluid flow and temperature evolution, respectively. The macroscopic conserved quantities are given by $\rho = \sum_i f_i$, $\rho u = \sum_i c_i f_i$ and temperature $T = \sum_i g_i$. It must be noted that temperature is not the conserved quantity, internal specific energy is the conserved quantity and is proportional to temperature. These two LBEs can be implemented on two separate lattice models, simultaneously. For 2-D, D_2Q_9 is very popular to solve mass and momentum conservation, and D_2Q_5 to solve for temperature field [147, 204, 259, 262].

The lattice models' properties are widely available in the literature. Since DDF passive scalar approach is stable and accurate in solving incompressible thermal flows (low Mach number), therefore, the equilibrium distribution contains terms just up to the second order in velocity, see Eq. (2.6). The equilibrium distribution for temperature can be left with second order terms only due to just one conserved quantity. It requires less number of velocities to produce correct temperature equation, therefore

$$g_i^{eq} = T w_i \left(1 + \frac{\vec{u} \cdot \vec{c_i}}{c_s^2} \right),$$

w_i is the weight factor for the D_2Q_5 lattice model. Now similarly as all previous LBM cases, the C-E expansion can be performed to the two LBEs to separately recover N-S and Fourier-Kirchhoff (temperature equation), respectively. The relaxation of non-conserved fluid moments and temperature moments must occur at different times, therefore even if the BGK collision scheme is adopted for both LBEs, they must have different relaxation parameters. Say,

$$\Omega_i(f_i, f_i) = -\frac{1}{\tau_f} \left(f_i - f_i^{eq} \right)$$

and

$$\Omega_i(g_i, g_i) = -\frac{1}{\tau_g} \left(g_i - g_i^{eq} \right),$$

where τ_f and τ_g are relaxation times for non-conserved flow moments and thermal

moments, respectively. The kinematic viscosity ($\nu = \mu/\rho$) is

$$\nu = c_{s_f}^2 \left(\tau_f - \frac{1}{2} \right)$$

and thermal diffusivity ($\alpha = \kappa/\rho$); for ideal gas like situation,

$$\alpha = c_{s_g}^2 \left(\tau_g - \frac{1}{2} \right),$$

where c_{s_f} is the speed of sound for the lattice model used to solve flow field and c_{s_g} is the speed of sound for lattice model used for temperature. The DDF model produces flexible Prandtl number. The limitation of the passive scalar DDF approach is that it is unstable and inaccurate when heat dissipation and compressive work are taken into account [113, 127].

2.8.1 DDF LBM with heat dissipation and compressive work

Based on the studies [2, 123], in which it was shown that isothermal LBM models can be directly derived from continuous Boltzmann equation with velocity distribution function, in the similar manner an isothermal LBM model can also be derived from the continuous Boltzmann equation with internal energy distribution function [127, 171]. Therefore, to increase the scope of DDF LBM approach, the focus has been shifted from temperature evolution to internal energy evolution, which naturally incorporates heat dissipation and compressive work. He et al. [127] extended their previous work [123] and introduced a forcing scheme to address compressibility and develop a model for arbitrary Prandtl numbers. The used external force is,

$$F = \frac{G \cdot (c_i - u)}{RT} f^{eq}$$

[128]. In one important paper on the stability of LBM schemes [267], Sterling and Chen showed that considering the collision operator in BGK-LBE constant in each time step leads towards second order truncation error. This error is non-destructive in solving for mass and momentum flow equations, but it creates a discrepancy in the viscosity terms present in momentum and energy equations while solving a thermal fluid flow model (also seen in our discussions on M-S models). The viscous heat dissipation comes from the first order C-E expansion, therefore is not affected by the second order truncation error. The discrepancy in viscous terms in heat dissipation and momentum equation is persistent and He et al. proposed a second order strategy to integrate the Boltzmann transport equation (which is discretized

to attain LBE). The second order LBE reads

$$f_i(x + c_i \triangle t, t + \triangle t) - f_i(x, t) = \frac{1}{2}\Omega_i(f(x + c_i \triangle t, t + \triangle t)$$
$$+ \frac{1}{2}\Omega_i(f(x, t)) + \frac{1}{2}F(x + c_i \triangle t, t + \triangle t) + \frac{1}{2}F(x, t),$$

(2.22)

where Ω is any collision operator. For a simple BGK collision scheme,

$$\Omega_i(f(x + c_i \triangle t, t + \triangle t) = -\frac{1}{\tau_f}\big(f_i(x + c_i \triangle t, t + \triangle t)$$
$$-f_i^{eq}(x + c_i \triangle t, t + \triangle t)\big).$$

Any lattice model with sufficient velocities to preserve isotropy of moment stress tensors can be used to solve for mass and momentum conservation such that

$$\rho = \sum_i \big(f_i - \frac{1}{2}\Omega_i(f(x, t)) - \frac{1}{2}F\big),$$

$$\rho u = \sum_i c_i \big(f_i + \frac{1}{2}\Omega(f(x, t)) - \frac{1}{2}F\big) + \frac{\rho G}{2}.$$

The similar second-order temporal integration approach can be adopted for the internal energy distribution function, let's say g.

$$g_i(x + c_i \triangle t, t + \triangle t) - g_i(x, t) = \frac{1}{2}\Omega_i(g(x + c_i \triangle t, t + \triangle t)$$
$$+ \frac{1}{2}\Omega_i(g(x, t)) + \frac{1}{2}f(x + c_i \triangle t, t + \triangle t)\mathbb{Q}(x + c_i \triangle t, t + \triangle t)$$
$$+ \frac{1}{2}f(x, t)\mathbb{Q}(x, t),$$

(2.23)

where internal energy is given by

$$\rho E = \sum_i \big(g_i - \frac{1}{2}\Omega(g(x, t))\big).$$

The proper definitions for the equilibrium of velocity distribution and internal energy distribution functions are provided with in-depth details in the papers [75, 127]. The coupling between the flow field and energy field is done through the definition of internal energy. Though the internal energy distribution DDF scheme discussed above was designed to address compressive work and heat dissipation, but in practice, it delivered stability only in incompressible limit. Incorporating compressive work and dissipation terms, it still produced some errors. Guo et al. identified and discussed few of the drawbacks in their paper [114]. One of the serious concerns was about the term $f\mathbb{Q}$ appearing in Eq. (2.23), causing density and velocity derivatives ap-

26

pearing in the final LBE. These derivatives induce numerical instability and make the computation difficult and costly [114, 228].

In order to improve the stability of the DDF scheme with compressive work and dissipation term included, the authors adopted total energy to be the conserved quantity instead of internal energy. Therefore, a total energy distribution function was proposed. The detailed procedure for developing the total energy DDF scheme has been provided in the paper [114]. Due to the decoupling between momentum and energy equations caused by the definition of the equilibrium distribution, the model was implemented only for thermal flows with small temperature variations. Chatterjee proposed an enthalpy based thermal LBM to address strongly coupled momentum and energy equations system, e.g. phase transition or solidification [39]. The author replaced the internal energy distribution function by He et al. with an enthalpy distribution function because the previous was inefficient in addressing the source terms. And the author also pressed upon the fact that enthalpy represented energy equation escapes from the source terms explicitly appearing in the LBM model.

2.8.2 Further Implementations of thermal DDF LBM

Palmer et al. [225] adopted similar internal energy distribution-DDF LBM approach used in [127] to study compressible flows. Ihle and Kroll extended the idea of double distribution function to even three distribution functions to simulate thermal flows for non-ideal gas with potential energy [141]. The authors introduced a distribution function to define the non-ideal part of the pressure, and a distribution function to define potential energy evolution along with a distribution to define mass and momentum evolution. The scheme above for compressible flows by He et al. [127] can be simplified for incompressible flows by simply dropping out the viscous heat dissipation and compressive work term $f\mathbb{Q}$ [228]. The authors present the implementation of the two LBEs on 2-D nine velocities (D_2Q_9) lattice model. The C-E expansion performed for the two LBEs recovers correct incompressible N-S, energy equation and transport coefficients [137]. It should be noted that the LBE for fluid flow (with f) and LBE for temperature field can be solved on same lattice model or two separate and different lattice models can be chosen to solve flow field and temperature. One another plus point of using DDF thermal LBM schemes is that implementation of pressure and temperature boundary conditions is very straightforward [75, 76, 277].

Simulating fluid flow in complex porous media has been a very hot topic for long and continue to be so. These types of simulations become even more tricky

when fluid flow is accompanied by heat transfer. The initial applications of lattice Boltzmann method to simulate fluid flow in porous media go back to the time of LGA [15, 245]. Later on, after the development of LBM, they were instantly applied to solve fluid flow in porous media by many groups [3, 271]. In LBM, there exist two approaches to simulate porous media fluid flow, (1) pore scale approach and (2) representative elementary volume (REV) approach [112, 113]. The easy and natural implementation of the boundary conditions (bounce-back or no-slip boundary conditions) in complex geometry made the LBM an ideal numerical tool to simulate fluid flows in porous media.

For flows in porous media, there might exist phenomena which are strongly dictated by the microscopic fluid-rock interactions and fluid-fluid interactions. Reactive flows, multiphase flows, flows in tight capillaries or channels are some of the examples where these microscopic phenomena occur. The conventional approaches (FDM, FVM, FEM) solve macroscopic description of the system and often lack the microscopic details of the flows in porous media such as wettability, interface effects, etc. [53, 220, 284]. Therefore, to take into consideration these microscopic effects, LBM serves as a perfect tool to predict these kinds of flows with better micro-meso scale understandings of the system. At the pore scale, the implementation of LBM is simpler as the effect of porosity are only implemented into the LBM formulation for REV scale modeling. The Darcy and Brinkmann model have been used frequently to address porosity in LBM simulations in the past [63, 266]. These models suffer from some intrinsic limitations [112]. An N-S model based on generalized porosity model proposed in [220] was then used with the generalized lattice Boltzmann equation for fluid flow in porous media [111] to better address the porosity and further improve the LBM numerical scheme initially marred by the limitations of Darcy and Brinkmann models. Therefore, to simulate heat transfer in the porous medium in the incompressible limit, we need to have an efficient athermal LBM (with porosity included in the equilibrium distribution and a force term to address the linear and non-linear drag) and a thermal LBM approach. The macroscopic equation

$$\frac{\partial u}{\partial t} + \left(u \cdot \nabla \right) \left(\frac{u}{\phi} \right) = -\frac{1}{\rho} \nabla(\phi p) + \nu \nabla^2 u + F \tag{2.24}$$

governs the incompressible fluid flow in porous media, where ϕ is the porosity, ν is the effective viscosity and F is the force term. In order to solve the above macroscopic system, a LBE with a force term is needed to address flow field conservation equations,

$$f_i(x + c_i \triangle t, t + \triangle t) - f_i(x, t) = \Omega_i(f, f) + \triangle t F_i.$$

The simplest approach is to use BGK as the collision operator as done in [111, 112].

The force term must address efficiently the force exerted by the porous medium and any other existing force. It is quite essential as well to define the porosity factor's contribution to the equilibrium of the fluid particles after collisions. Guo et al. defined the force term (for a BGK single relaxation parameter τ),

$$F_i = w_i \rho \left(1 - \frac{1}{2\tau} \right) \left[\frac{\vec{c}_i \cdot \vec{F}}{c_{s_f}^2} + \frac{(\vec{c}_i \cdot \vec{u})(\vec{c}_i \cdot \vec{F})}{\phi c_{s_f}^4} + \frac{\vec{u} \cdot \vec{F}}{\phi c_{s_f}^4} \right]$$

and equilibrium distribution with porosity ϕ is,

$$f_i^{eq} = \rho w_i \left(1 + \frac{\vec{u} \cdot \vec{c}_i}{c_{s_f}^2} + \frac{(\vec{u} \cdot \vec{c}_i)^2}{2\phi c_{s_f}^4} - \frac{\vec{u} \cdot \vec{u}}{2\phi c_{s_f}^2} \right).$$

The values of weight factors w_i, the speed of sound for flow field c_{s_f} are the characteristics of a particular lattice model and can be defined once the lattice model has been chosen to solve fluid flow LBE. As a normal practice, C-E expansion of the LBE above can be performed to recover generalized N-S equations and effective viscosity. Next, the temperature field is solved. The temperature equation for heat transfer in porous media [112] reads

$$\sigma \frac{\partial T}{\partial t} + u \cdot \nabla T = \nabla \cdot \left(\alpha_m \nabla T \right), \tag{2.25}$$

where

$$\sigma = \phi + \left(1 - \phi \right) \frac{\rho_s c_{p_s}}{\rho c_p},$$

ρ_s is the density of porous solid, α_m is the effective thermal diffusivity, c_p and c_{p_s} are the specific heat of fluid and porous solid, respectively. The Eq. (2.21) can be solved further using an appropriate collision scheme and one can use C-E expansion to recover the temperature equation using the standard procedure. The conservation rule now will have the form $\sigma T = \sum_i g_i$ and g_i^{eq} as defined earlier in the text. The $D_2 Q_9$ and $D_2 Q_5$ lattice models can be used to solve the flow field and temperature field, respectively.

Thermal flows such as natural convection and Rayleigh-Bénard convection have also been solved by many groups using LBM scheme for small/moderate Ra numbers (laminar flows) [8, 75, 81, 197, 214, 229, 256]. Turbulent flows simulations generally need special turbulence models and are computationally costly due to large grid requirement. Dixit and Babu developed the first implementation of the DDF scheme to study turbulent (Ra > 10^8) thermal flows. The authors used interpolation supplemented lattice Boltzmann method [125] with non-uniform grids to simulate turbulent flows [74]. The authors simulated the natural convection heat

transfer in a square cavity for Ra up to 10^{10} using BGK collision scheme for flow field and temperature field, using internal energy distribution function. Kuznik et al. used Taylor expansion-Least square LBM to simulate natural convection in a differentially heated cavity on non-uniform grid [167]. But the simulations were kept limited to the transitional limit of the Rayleigh number ($10^6 < Ra < 10^8$). Mohamad et al. simulated natural convection in an open-ended cavity for laminar flow limit but used D_2Q_4 lattice model to simulate temperature field [214]. The same system of lattice models was used to simulate natural convection in an open enclosure filled with nanofluid [160]. Mezrhab et al. used MRT collision schemes for fluid flow on a D_2Q_9 lattice model and temperature field on D_2Q_5 [204]. Je-ong et al. [148] combined immersed boundary conditions with DDF thermal LBM scheme using equilibrium velocity approach proposed in [257]. This approach is very useful to simulate heat flows with immersed boundary problems, i.e. the problem with different body shapes. Ghazanfarian and Abbassi implemented internal energy distribution DDF thermal LBM (by He et al. [127]) to simulate heat transfer in micro and mini-channels [97]. Dubois et al. implemented MRT collision operator on two D_2Q_9 lattice models to simulate anisotropic heat transfer in a square cavity for different lattice resolutions [80].

Cascaded collision operator, developed to enhance the stability and accuracy of the BGK and MRT LBM scheme [94, 95], was first applied to simulate thermal flows by the authors in recent publications [259, 262, 269]. Straka has previously used cascaded collision scheme to solve the flow field and MRT collision scheme to solve temperature field [268]. In cascaded LBM scheme streaming step is defined in velocity space like BGK and MRT schemes, and collision is defined in central moment space. The central moments κ are given by

$$\kappa_{x^m y^n} = \sum_i (c_{ix} - c_{iy})^m (c_{ix} - c_{iy})^n f_i.$$

The cascaded LBE is given by

$$f_i(x + c_i \triangle t, t + \triangle t) - f_i(x, t) = \mathbb{K} \cdot \vec{k},$$

where $\mathbb{K}$ is the transformation matrix and $\vec{k}$ is the collision vector. A similar LBE can be written for the temperature field, using temperature distribution function. The authors simulated a variety of heat transfer problems, e.g. forced convection, advection-diffusion, rotational flows and natural convection in the square cavity using a passive scalar cascaded DDF scheme. Advection-diffusion of the sine wave was simulated using CTLBM [259] and the results were compared with MRT collision schemes developed by Mezrhab et al. and Yoshida et al. [204, 309]. The performance

of the CTLBM for natural convection simulations in square cavity for a large range of Rayleigh numbers [262] was compared against various other LBM works [58, 75, 167, 292], DNS works from Lé Quéré [238], Markatos and Pericleous [193], Barakos et al. [16], and experimental works from Tian and Karayiannis [282] and King [162]. The results obtained by CTLBM for a large range of Ra number ($10^3 - 10^{10}$) presented in [262] were found to be in strong agreement with those obtained by DNS and experiments. Fei et al. also implemented cascaded collision scheme in the same year to address thermal flows [84, 85]. It can be seen from the previous implementations that cascaded collision scheme enhanced numerical stability by reducing the degree of Galilean invariance insufficiency. Conjugate heat transfer simulations depend on the material properties, which affect the fluid-solid interface properties differently [150]. Numerical implementation of interface boundaries is crucial for efficient numerical stability and accuracy for fluid-solid heat transfer. There exists an LBM numerical scheme called as "half lattice division scheme"by Wang et al. [291] which develop boundary implementation of an interface and characterizes the properties of solid materials [278, 293]. Cai and Huai used passive scalar DDF approach to simulate fluid-solid conjugate heat transfer in a fractal porous medium and presented the qualitative comparison between FVM and LBM approach [29].

2.9 Thermal Boundary Conditions

The implementation of boundary conditions is very problem specific and there exist some standard frameworks in LBM to address various types of problems. No-slip boundary conditions, also known as bounce-back boundary conditions of the non-linear distributions are the most used in LBM applications [126, 256, 264, 321]. The bounce-back boundary conditions are first order accurate, and initial implementations of no-slip conditions were found to be the source of error [126, 175, 256]. Athermal boundary conditions applied in LBM can be classified as periodic, velocity and pressure boundary conditions. Maier et al. presented a detailed overview of the boundary conditions and their implementation for simulations of different fluid flow problems using different lattice models [191]. Improved no-slip and local second-order velocity boundary methods improved the accuracy of the LBM schemes [98, 142]. Isothermal no-slip boundary conditions ensure zero velocity at the boundary for fluid flow components and fixed density for the temperature component [256]. Further improvements in isothermal boundary conditions were made by Chang et al. where the authors proposed a scheme called consistent boundary condition in which unknown components become functions of the known components [36]. The heat flux must be permitted through the boundaries. D'Orazio and

Succi [75] presented in-depth analyses of the counter-slip approach proposed by Inamuro et al. [142] applied to the internal energy and its implementations for thermal Couette flow and thermal Poiseuille flow. D'Orazio further extended the counter slip approach used in thermal Poiseuille and Couette flows previously, to general purpose boundary conditions to simulate imposed wall temperature and imposed wall heat fluxes [76]. The authors present a quantitative analysis of internal energy DDF scheme using Dirichlet and Neumann type thermal boundary conditions for simulations of natural convection in a square cavity and compared the results with the literature. Simulations' accuracy of thermal flows with extremely high velocity and sharp fluctuations in temperature strongly depends on the boundary conditions. Simple no-slip boundary conditions are inefficient in addressing such problems due to the fact that unknown components of the fluid and temperature are computed at the boundary itself as in such cases the solid nodes exist on the wall itself, imposing the fluid and solid to have similar velocity and temperature at the boundary. Due to this fact temperature jump and velocity slip, phenomena that often occur in rarefied aerodynamics cases and in micro and nanodevices cannot be addressed.

Sofonea and Sekerka suggested the application of diffuse-reflection thermal boundary conditions for such high Knudsen number (K_n) flow [264]. This approach assumes the existence of the wall (solid nodes) half lattice cell spacing outside the physical wall. The detailed implementation of this diffuse-reflection boundary conditions approach has been provided in the paper and the authors simulated thermal flows in microchannels and flow with temperature jumps using a finite difference LBM (FDLBM) approach. Liu et al. extended the consistent boundary condition by Chang et al. to thermal flow problems. The authors made the unknown components of the energy distribution function of the known energy distribution components and correctors [186]. Li et al. noted that the previously used consistent boundary condition by Liu et al., Chang et al., He et al. were defined for specified boundary conditions and Neumann boundary conditions were transformed into the specified or fixed boundary conditions by using finite difference schemes [180]. In the case of flows with mixed boundaries where previous approaches are inadequate, Li et al. recommended the use of a direct boundary condition with specified derivatives. Li et al. developed a second-order accurate boundary condition approach for Dirichlet (specified boundary) and Neumann (specified derivative) conditions [180].

2.10 Critical Summary of Thermal LBM

The overall motivation of using LBM to solve thermal problems was completely based upon the success it achieved in solving athermal problems. It is quite evident

from the review that initial implementations of LGA (which were LGA) to simulate thermal problems were full of inaccuracies and instabilities due to the Boolean nature of the fluid and pressure explicitly depending on velocity. LGA were replaced with improved lattice Boltzmann equation models which used real numbers and a statistical average over a large region. The overall accuracy and stability of athermal LBM were improved heavily due to the development of more sophisticated collision schemes such as MRT along with the appropriate definition of the equilibrium distribution. The "as it is" extension of the athermal model to solve isothermal or non-isothermal problems was full of inaccuracy, instabilities and other challenges such that how to address compressible or other non-linear behaviors of energy equations. It can be understood that the most popular collision scheme "Single Relaxation Time (BGK)" was initially used to deal with thermal problems altogether. This application was unstable due to the fact that all non-conserved quantities were depending on just one relaxation parameter, which in true sense must be relaxing towards their equilibrium at different time scales. This approach fixed the Prandtl number, limiting the use of LBM just for problems with a very narrow temperature variation range. In order to make LBM free from this disease, MRT collision schemes were used and a variable Prandtl number was achieved, and also different non-conserved quantities of flow field and energy could be relaxed on different time scales.

The source of numerical error and instabilities were not only limited to the collision schemes, considering energy as an additional moment or component of the velocity (see MS models) was also problematic, as it required up to fourth order velocity terms appearing in the equilibrium distribution, though it increased the potential of LBM to deal with compressible problems through its ability to incorporate compressive work, it still produced great instability and low accuracy, and fixed Prandtl number. Though some improved versions of the MS model have been developed, with a tremendously high number of extra velocities. Therefore to establish LBM as a credible tool to simulate incompressible flows with high stability, temperature fields were solved by assigning a separate LBE for temperature distribution function, internal energy distribution function or total energy distribution function. This approach was called DDF approach, with its two subordinates, one is a passive scalar approach which was developed to simulate thermal flows where the temperature is advected by the velocity but it does not affect it anyway, therefore for temperature, solving the advection-diffusion equation (obeyed by temperature) was sufficient. The second subordinate was proposed and developed by He et al. in which internal energy was considered to be the conserved quantity directly derived from the continuous Boltzmann equation, which also could incorporate compressive

work and heat dissipation conveniently, in the incompressible limit. These terms cannot be included in the passive scalar DDF framework. The equilibrium distribution was simply Maxwellian and its Taylor expansion could be truncated at second order of velocity to produce stable results with this DDF schemes. Hybrid LBM models exploit the benefits of already well established conventional CFD techniques to simulate advection-diffusion equations or radiative heat transfer problems. Recently, a trend has been seen in which various groups have used advanced collision schemes such as cascaded LBM and have achieved greater stability and robustness.

2.11   Conclusion

This paper works as an ensemble of existing thermal LBM frameworks and a large number of LBM approaches by different groups dealing with numerous thermal flow problems such as natural convection, forced convection, phase transition, radiative heat transfer, thermal flows through porous media, conductive heat transfer, etc. Instead of flying by various important steps in thermal LBM such as theoretical development, choosing collision schemes, discretization and numerical results superficially (as it was not possible to account all parts with numerous notable works done by different groups in the last three decades in just one article), we have focused intensively on an evolutionary advancement of thermal LBM. We have studied and analyzed different approaches adopted by different groups falling under three categories of thermal LBM frameworks and have left the reader with all the freedom to select the collision schemes, lattice models and other important stuff such as boundary condition, for efficient simulations of the problems of their interest.

It can be understood from the discussions that stability and accuracy of LBM scheme mostly depend on the structure of the collision operator and applied boundary conditions. Cascaded collision scheme, gradually becoming more popular, can produce better stability and accuracy. Recent trends shows that cascaded-cascaded DDF scheme, with sophisticated boundary conditions can be a powerful numerical tool to simulate a diverse range of thermal flow problems.

We do believe that the present study is a rich source of information that can be of great interest to the scientists and engineers dealing with heat and mass transfer simulation using LBM and conventional CFD tools for diverse industrial and academic applications.

Capítulo 3

Recovering Equivalent Partial Differential Equations from the BGK, MRT, and Cascaded Lattice Boltzmann Methods

3.1 Abstract

Recovery of Navier-Stokes equations from Lattice Boltzmann Methods is an essential practice to evidence the consistency and stability of numerical schemes. Here, we discuss and show techniques for recovery of the Navier-Stokes (N-S) and Fourier-Kirchhoff (F-K) equations from various lattice Boltzmann methods in a rather simple and systematic manner. Originating from the concept of the modified equation and non-centered schemes for equivalent non-linear equation used to recover Navier-Stokes equations, the Equivalent Partial Differential Equation (EPDE) approach is adopted here to recover these macroscopic equations. Bhatnagar-Gross-Krook; Single Relaxation Time (BGK-SRT), Multiple Relaxation Times (MRT), and Cascaded collision schemes have been discussed in details and the corresponding lattice Boltzmann equations are taken to their hydrodynamic limit using Taylor expansion and diffusive scaling to recover macroscopic Navier-Stokes and Fourier-Kirchhoff equations in the incompressible limit.

3.2 Introduction

Lattice Boltzmann Methods (LBM) are recent but very reliable and powerful tools for solving complex computational fluid dynamics problems. It is proven that LBM can solve complicated fluid flow and heat transfer problems efficiently with great stability and accuracy [19, 95, 123, 171, 317]. It has been also shown that complex fluid flow problem e.g., turbulence flows, flows in porous media, phase transitions, and many other phenomena can be solved by LBM [12, 18, 68, 89, 95, 113, 164, 172, 182, 199, 217]. But LBM has been subjected to extensive scrutiny and put under intensive investigations. The one thing beyond stability and accuracy that interests the most is the consistency of the LBM schemes. The consistency of the LBM can be established by recovering the Navier-Stokes and Fourier-Kirchhoff equations by rescaling and Taylor expansion of the lattice Boltzmann equation. Chapman-Enskog expansion and asymptotic analysis techniques have been the most popular way to recover the macroscopic equations [12, 152, 171, 234, 304]. But there exist methods like (1) Hilbert expansion, (2) Equivalent Partial Differential Equations (EPDE), and very recently reported (3) Maxwell iteration method that can also recover the hydrodynamic limits of the lattice Boltzmann schemes [79, 80, 153, 308, 319].

In 1986, Frisch et. al. presented the lattice gas automata for the Navier-Stokes equations [91]. The N-S equations obey the conservation rules. The motivation behind this work was to provide a model which could efficiently solve fluid flow with high Reynolds number with massively parallel algorithms. It can be argued that the authors followed the similar concept as of the modified equations to approximate various field equations governing different fluid flow systems by using cellular automata instead of difference schemes [91] but with an intention of extending the microscopic description to its macroscopic description (the continuum level). In lattice gas automata the fluid particles are described at the kinetic level with the irreversible low-density Boltzmann approximation. In order to describe the behavior of this kinetic level lattice gas system at the macroscopic level in the continuum approximation Chapman-Enskog (C-E) expansion technique was used. The authors used the lattice gas models with complete discrete phase space and time describing the fluid as it was made of Boolean molecules. The term lattice is a model which dictates the propagation and existence of fluid particles distributed over the spatial domain of interest or simply grid. Similar to the approximated equations in the case of partial differential equations using finite difference schemes, macroscopic equations recovered by the Chapman-Enskog expansion technique are N-S equations. A direct comparison between the original N-S equation and the lattice gas approximated N-S equation reflects the stability, consistency, and accuracy of the lattice

gas scheme. The HPP model named after authors Hardy, de Pazzis and Pomeau was implemented on a two-dimensional square grid to constrain the propagation of Boolean fluid particles [119–121]. But the N-S equation recovered by this scheme did not possess dissipative terms and nonlinear terms of the N-S equation. This was attributed to the lack of isotropy of the lattice model used by HPP. This drawback associated with the HPP scheme was removed by Frisch et al. as they used a hexagonal lattice model preserving the symmetry of the lattice [91]. Modified collision rule by Harris was incorporated with discrete Boltzmann model fulfilling Fermi distribution rule [122].

The special features, importance and various applications of the lattice gas models have been described in great detail in the literature [22, 42, 48, 90, 108, 315]. The lattice gas models possess some statistical noise due to the Boolean nature of the system variables. This statistical noise was because of the average over a very small space-time region of the considered system. Therefore, to remove the statistical noise, the concept of the lattice Boltzmann equation was proposed. A very systematic study of the journey from Boolean microdynamics to the lattice Boltzmann equation has been presented by Benzi et al. [19]. Qian et al. used the BGK collision scheme [21] to recover the 2nd order approximated N-S equation using Chapman-Enskog expansion technique [236]. In the new formulation of the lattice Boltzmann equation, the velocity distribution function was used to describe the probabilistic population of the fluid particles in larger space-time region, the collision rules were improved using Maxwell-Boltzmann distributions and the symmetry of the lattice was assured. Therefore, the recovered N-S equations possessed non-linear terms and dissipative terms. It should be noted that the collision scheme must obey the mass, momentum, and energy conservation rules. The derivation of the macroscopic equations from the generalized lattice Boltzmann equations is given in Ref.[72]. The author showed that using Chapman-Enskog expansion and BGK collision scheme on a generalized lattice Boltzmann equations one can recover macroscopic equation containing more complex information compared to the lattice gas equations. BGK collision scheme states that all non-conserved quantities associated with the fluid flow reach to the equilibrium state with identical relaxation frequency. He and Luo stated that Lattice Boltzmann equation is used to recover the N-S equation for low Mach number only, i.e. for incompressible limit [123, 126]. The authors showed that removing the terms of higher order Mach number can provide an accurate solution for the incompressible limit. The authors used the two dimensional nine velocity lattice model and BGK collision scheme to describe the lattice Boltzmann equation and afterward used the Chapman-Enskog expansion to recover the N-S equation.

The lattice Boltzmann equations studied by various authors above were defi-

ned in discrete velocity space. In 2000, Lallemand and Luo proposed a new form of lattice Boltzmann equation defined in moment space [171]. Dellar proposed a modified lattice Boltzmann scheme with BGK collision operator to recover compressible Navier-Stokes equations. The motivation behind this work was to control bulk viscosity [68]. Tuning bulk viscosity can provide accurate solutions for the compressible flows. It should be noted that LBE's inherently designed to solve compressible flows. Truncation of the equilibrium distribution function to second order limits the performance of LBM making it suitable for small Mach number flows only. The authors redefined the equilibrium distribution function by inducing new bulk viscosity coefficient to attain N-S equations with adjustable bulk viscosity. Later, Guo et al. incorporated forcing term in the lattice Boltzmann equation [113]. The forcing term can be simply added to the LBE. The inclusion of forcing terms becomes essential when solving multiphase or multicomponent flows, and the problems which involve external or internal forces. The authors added the forcing terms into the lattice Boltzmann equation and used the BGK collision scheme and Chapman Enskog expansion technique to derive the N-S equation. In 2003, Lallemand and Luo developed a hybrid thermal lattice Boltzmann scheme called HTLBE which was used to study the acoustic and thermal properties of the system with energy conservation [172]. Interestingly, instead of BGK, the authors adopted a special collision scheme called Multiple relaxation times (MRT) by d'Humieres, well known for increasing the stability of the LBM scheme, to solve the flow field equations. The energy equation in terms of temperature equation was solved separately using a finite difference scheme. Again, the Chapman-Enskog technique was used to derive the hydrodynamic equations and analyze the numerical stability of the HTLBE scheme.

Therefore, it can be understood that the Chapman-Enskog (C-E) expansion technique was the most used technique to recover the N-S equations to study the consistency, stability, and accuracy of the various lattice Boltzmann schemes. The one important characteristic of the C-E expansion techniques is that it considers convective scaling in which the spatial and temporal steps are considered to be approximately equal combined with two-time-scale expansion [188, 310]. As discussed earlier, the N-S equation recovered using C-E expansion represents a compressible system and the incompressible limit of these N-S equations can be achieved by setting Mach number low [101, 102, 151, 185, 196]. To free the LBM schemes from this drawback, Junk et al. proposed use of asymptotic analysis with diffusive scaling to study the consistency and stability of the purely incompressible N-S equations [152]. McCracken and Abraham derived the hydrodynamic equations for multiphase flows using C-E expansion for the MRT collision schemes [199]. As it is well established

that MRT improves the stability of the LBM schemes, N-S equations recovered by the C-E expansion contain terms which establish the improved consistency and stability of the method and shows how to adjust the bulk viscosity to zero for small Mach number cases.

Actually, LBM is known to solve ideal fluids leading to an ideal-gas equation of state. But LBM simulations of multiphase fluid flows, e.g. non-ideal cases caused by the forcing term such as phase transition or separation, fail to sufficiently maintain the thermodynamic equilibrium. Wagner investigated this problem by studying the equilibrium behavior of the original N-S equation for non-ideal gas [288], and afterward, the authors formulated the lattice Boltzmann equation with the forcing term inducing non-ideal terms to recover the N-S equation by means of the Taylor expansion. Matching the original N-S equation for non-ideal gas with the N-S equation recovered by the lattice Boltzmann approach with forcing term for non-ideal gas can help in identifying the terms which can later be incorporated into the LBM formulation [182]. In 2007, Li and Abraham developed the lattice Boltzmann formulation for a multicomponent system with free energy with application in the formation of polymer membranes through immersion precipitation [182]. In LBM, there exist few kinds of approaches to solve multicomponent and multiphase systems: (1) Rothman Keller approach, (2) Shan-Chen method and (3) free energy approach [11, 34, 35, 107, 129, 138, 143, 182, 194, 320]. We already discussed the role of N-S equations for the multiphase system above with thermodynamic inefficiency. When the thermodynamic equilibrium of non-ideal gases is of interest, free energy approach seems to be the favorite choice [182, 288]. The chemical potential of each component and pressure of the system were incorporated in the multicomponent lattice Boltzmann model [182]. The authors then followed the standard procedure as discussed above, the N-S equation (hydrodynamic limits) governing the overall system was recovered using the Taylor expansion techniques (similar concept as of equivalent equation which is described in next sections). The authors also provided numerical solutions for binary and ternary systems deriving a convection-diffusion equation for each component. Li et al. later in the same year obtained compressible N-S equations using C-E expansion technique for double distribution function (DDF) LBM scheme with BGK collision operator [183].

In 2008, P. Asinari published a paper which provided the detailed asymptotic analysis of MRT LBM scheme for systems of ideal mixture [12]. The analysis of the recovered macroscopic equation for MRT collision schemes showed that MRT schemes can tune the diffusivity conveniently. Asymptotic analysis by the diffusive scaling, the Euler integration rule, and the modified mid-point integration rule was derived in detail. The authors showed that asymptotic analysis has an edge over

the classical C-E expansion technique due to its ability to deal with high order non-Maxwellian terms. Finally, Francois Dubois published papers in which he derived the equivalent partial differential equations of lattice Boltzmann scheme [79, 80]. It was the first time that the method of equivalent equations was applied to lattice Boltzmann equations. The benefit of this scheme is that two-time multiple scaling is not necessary here to recover N-S equations from the lattice Boltzmann equations. The equivalent equations provided by the author could be generalized for BGK or MRT collision operator. Premnath and Banerjee incorporated the forcing term in the cascaded lattice Boltzmann method and recovered the hydrodynamic equations using C-E expansion techniques [234]. In 2015, Yand and Yong presented a magnificent analysis of the C-E expansion technique for a class of hyperbolic relaxation systems. Actually, the authors studied the validity of using C-E expansion technique to describe the viscous characteristics of the hyperbolic relaxation systems [304]. In 2016, entropic lattice Boltzmann method, based on double distribution function framework, was developed for turbulent and conjugate heat transfer flows. The authors incorporated entropic MRT collision operator and recovered hydrodynamic equations for turbulent flows and flow with complex boundaries [226]. In 2017, a new class of recovery scheme, Maxwell iteration method was developed to recover macroscopic equations. The proposed technique is a single parameter expansion and does not require multiscale expansion and Hilbert expansion which are required in C-E expansion and asymptotic analysis techniques, respectively [308, 319].

As we have seen so far from the literature, techniques such as C-E expansion and asymptotic analysis have been used quite significantly to recover the hydrodynamic equations from various LBM schemes. The Maxwell iteration method is a relatively new method, especially for LBM framework. The equivalent partial differential equation method has been used in the LBM framework by a small number of authors [79, 80, 96, 147]. C-E expansion and asymptotic analyses are multiscale expansion techniques and rather complicated compared to the equivalent PDE method which is simply the Taylor expansion method. Due to its simplicity and straightforwardness, we have adopted the equivalent PDE method and have presented the recovery process of the N-S equations for BGK, MRT, and Cascaded collision schemes. We have used the double distribution function framework to solve fluid flow and heat transfer simultaneously. For flow field, the mass and momentum conservation rules are obeyed, while for temperature field internal energy conservation was considered without taking into consideration the viscous dissipation and compressive work. Therefore temperature can be considered as a passive scalar. The present study solves the incompressible fluid flow problems and the Navier-Stokes equations are recovered by rescaling the LB equations in the incompressible limit. Mass and mo-

mentum conservation rules are implemented on the D_2Q_9 lattice model for the fluid flow, the specific internal energy of the fluid is considered as the conserved quantity and has been solved using a D_2Q_5 lattice model.

3.3 Origin and Methodology of Equivalent Equations

Most of the real world physical systems are governed by non-linear equations or equations with nonconstant coefficients [133]. The Fourier method proposed by Von Neuman in 1950 was fit for linear difference equations with constant coefficients. In 1960, Lax and Wendroff presented a very detailed study of a broad range of a class of difference equation to approximate discontinuous time-dependent solutions of hyperbolic systems of nonlinear conservation laws. The authors suggested that the best class of difference equations were to have the smallest truncation error with narrowly confined discontinuities [177]. Strang suggested that the convergence of such approximations depend on the stability of the linearized difference equation [270], where he studied the scheme proposed by Lax and Wendroff [178] and the Runge-Kutta method. For non-linear equations or equations with nonconstant coefficients, in 1968, Hirt proposed a heuristic method called the truncation-error method to study the computational stability of the finite difference schemes [133]. In this scheme, the author proposed to reduce a finite difference equation into a differential equation by Taylor expansion. The author claimed that stability of a difference scheme can be determined by investigating the truncation error terms which are nothing but the higher-order terms generated in the Taylor expansion. A one-dimensional compressible fluid flow problem was solved using the truncation error method to estimate the numerical instabilities, that was not possible with the Fourier stability analysis. In 1973, McGuire and Morris [200] derived the two-step Richtmyer method [242, 243] to solve first-order systems of conservation laws. The authors considered the generalized two-step Richtmyer form of the previously mentioned Lax-Wendroff method. The second order correct, Taylor series expansion of $u_i^{m+1} = u(ih, (m+1)K)$ reads

$$u_i^{m+1} = u_i^m + K\partial_t u_i^m + \frac{K^2}{2}\partial_{tt}u_i^m + O(K^3). \tag{3.1}$$

Conservation laws, i.e. $\partial_t u + \partial_x f = 0$, can be used to replace the time derivatives by space derivatives in different manners giving birth to different schemes. The generalized two-step Richtmyer scheme was defined by choosing an intermediate approximation $u_i^{m+1} = u(ih, (m+2a)K)$, and with Taylor series expansion

$$u_i^{m+1} = u_i^m + K\left(1 - \frac{1}{4a}\right)\partial_t u_i^m + \frac{K}{4a}\partial_t u_i^{m+2a} + O(K^3). \tag{3.2}$$

From the conservation rule, replacing time derivatives by space derivatives gives

$$u_i^{m+1} = u_i^m - K\left(1 - \frac{1}{4a}\right)\partial_x f_i^m - \frac{K}{4a}\partial_x f_i^{m+2a} + O(K^3). \tag{3.3}$$

The space derivatives in the above equations are replaced by differences to achieve the finite difference scheme, i.e. approximation to u_i^m and $u(ih, (m+2a)K)$. Authors also showed that different difference schemes can be recovered by assigning different values to a. In the same year, Lerat and Peyret studied theoretically Mac Cormack's noncentered difference scheme to solve the gas dynamics equations [179]. This study was an extension of a scheme developed by Mac Cormack in 1969, in which the author replaced the spatial derivatives by noncentered differences, giving birth to the so-called "noncentered scheme". The scheme was proven to be second-order correct in space. It was claimed by the authors that noncentered schemes were easy to implement computationally, moreover, these schemes dealt with non-linearities present in the system more efficiently. The choice of direction of the noncentered difference has a direct influence on spurious effects. Therefore, at this stage, there were schemes developed by Lax Wendroff, Mac Cormack, Richtmyer, which could solve the non-linear problems, conservative form of the gas dynamics equations, i.e. shock propagation. The most importantly, in the same paper, Lerat and Peyret elaborated more on the idea of Equivalent Equation for the case of a linear system. The scheme 'equivalent equations' were used to study the discretized differential equations to describe the properties, e.g. stability, accuracy, consistency of a scheme [133, 305]. The stability and the dissipative properties of the schemes were studied using the concept of first differential approximation. The viscosity which appears due to the approximation of the hyperbolic systems was also studied. Lerat and Peyret described equivalent equation formulations for linear and non-linear systems [179]. The hyperbolic linear system reads

$$\partial_t f + A\partial_x f = 0. \tag{3.4}$$

Using the Mac Cormack scheme for the linear system, the equivalent equation can be written as

$$\partial_t f + A\partial_x f + A_3\partial_{x^3} f + A_4\partial_{x^4} f = 0, \tag{3.5}$$

where A_3, A_4 are matrix polynomials such that $A_3 = P_3(A) = O(\triangle x^2)$, $A_4 = P_4(A) = O(\triangle x^3)$. From Eq.(3.4, 3.5), the dispersive and dissipative error can be characterized. The polynomials P_3, P_4, for the Mac Cormack's scheme, can be

written as function of the eigenvalue of A, spatial step $\triangle x$ and temporal step $\triangle t$. Therefore, the stability conditions, dispersive error, dissipative error of the scheme can be set in relation to the polynomials characteristics. If λ is the eigenvalues of the matrix A, the scheme is stable for $P_4(\lambda) \geqslant 0$, the dispersive error arises when $P_3(\lambda) \neq 0$ and the dispersive error can contribute to the dissipative error if $P_4(\lambda) > 0$.

To attain higher stability of the equivalent equation of linear systems, the authors suggested condition $\eta = max|\lambda|\frac{\triangle t}{\triangle x} \leq 1$. The origin of spurious oscillations is attributed to the condition when $\eta < 1$, which suggests that the magnitude of dispersive errors are greater than the dissipative errors. Next, the author presented [179] the equivalent equation for the nonlinear system

$$\partial_t f + \partial_x g(f) = 0, \ g(f) = \frac{1}{2}f^2 \qquad (3.6)$$

The Mac Cormack scheme was then used to discretize the above system of equation followed by Taylor expansion to replace time derivatives by spatial derivatives. The third order equivalent equation was derived. The analysis of the equivalent equation resulted in the conclusion that the numerical stability of the scheme is greatly influenced by the choice of the direction of differences. Unsteady shock profiles were then solved numerically using the equivalent equation. Warming and Hyett (1974) presented a very detailed analysis of the accuracy and stability of the modified equations using finite difference scheme [295]. A critical analysis of this scheme has been presented by Chang [38]. The authors carried out a stability analysis on the truncated partial differential equation. The stability analysis of error terms present in the modified equation was named 'Heuristic'. The authors also studied the connection between the Von Neumann method and the modified equation method. It was already established by Richtmyer's version of the Lax-Wendroff method that large wave number Fourier components were dampened. Phase error analysis was presented for convective flows using the modified equations. We present here one example presented by the authors to closely understand the concept. The partial differential equation chosen by the authors was a scalar convection equation:

$$\partial_t \widetilde{u} + c\partial_x \widetilde{u} = 0, \qquad (3.7)$$

where c is a real constant and $\widetilde{u}$ is obviously the exact solution of the original differential equation. To describe the difference analog of the original equation, a difference scheme along with Taylor expansion is necessary which will transform the above equation into a modified one. The second-order difference scheme algorithm

43

for u_i^{n+1} proposed by Crowley was analyzed [60]. The explicit algorithm reads:

$$u_i^{n+1} = u_i^n - \nu(\mu\delta)u_i^n + \frac{\nu^2}{2}(\mu^2\delta^2)u_i^n - \frac{1}{8}\nu^3(\mu\delta^3)u_i^n, \qquad (3.8)$$

where $\nu = c\frac{\triangle t}{\triangle x}$, μ and δ are difference operators such that $\mu u_i = \frac{u_{i+1/2}^n + u_{i-1/2}^n}{2}$ and $\delta u_i = u_{i+1/2}^n - u_{i-1/2}^n$. Using the above-mentioned difference scheme and Taylor expansion, the corresponding modified or equivalent equation of Eq.(3.7) reads

$$\partial_t u + c\partial_x u = -C(3)\partial_{x^3}u - C(4)\partial_{x^4}u - C(5)\partial_{x^5}u + ... \qquad (3.9)$$

where $C(t)$ is the coefficient of tth order spatial derivative and u is the solution of the difference analog. To perform a detailed analysis of the truncated partial differential equation (modified equation) one needs to closely examine the coefficients (C) of the spatial derivatives of a different order. One should note that new terms appearing in the equivalent or modified equations are the error terms. For example, all the terms on the right-hand side of the above-mentioned equation are error terms, and conclusion regarding the dissipative error, dispersive error, consistency, and accuracy can be drawn by carefully analyzing these terms. The lowest order error term is dictated by $C(3)$, which is, $C(3) = \frac{c\triangle x^2}{24}(4 - \nu^2)$. In temporal and spatial steps, $C(3) = \frac{c}{24}(4 \triangle x^2 - c^2 \triangle t^2)$. The quadratic terms $\triangle x$ and $\triangle t$ appearing in the error term renders the scheme second-order correct in space and time. To ascertain the consistency of the scheme with the convective equation, the terms $C(t)$ must be zero when spatial and temporal spacing approach zero. The authors stated that $C(3), C(4), ...$ tend to zero when $\triangle x$ and $\triangle t$ tends to zero which established the consistency of the difference scheme adopted with the scalar convective equation. The further analysis of the stability of the Crowley scheme was also discussed in great detail by the authors and can be found in the paper [295]. It is very clear that the principal objective of the studies we discussed is to solve different type of partial differential equations using various difference approximations and schemes. The original partial differential equation is transformed into a truncated equivalent partial differential equation having infinite numbers of error terms using finite difference schemes. The basic process is very simple, (1) the partial differential equation is discretized by using an appropriate difference scheme; (2) the time derivatives are eliminated using the Taylor expansion and conservation rules; (3) various orders of error terms (i.e. higher order derivatives) in the modified or equivalent partial differential equation are then recovered. Finally, the stability and accuracy analysis of these difference schemes can be made on these truncated equivalents or modified equations [105] by carefully examining the coefficient of the high order spatial derivatives. The similar equivalent equation methodology was ap-

plied to the Boltzmann transport equation by Francois Dubois [79, 80]. Boltzmann transport equation (BTE), which is, of course, a conditionally linear partial differential equation, can be written as the difference equation by adopting a suitable difference scheme. Using Taylor expansion, the BTE can be approximated as the equivalent partial differential equation which can be used to study the characteristics and behavior of the physical systems governed by the original BTE equation. In the next section, we introduce and discuss the lattice models used in the present study, definitions of moments, lattice Boltzmann equation, detailed collision schemes, lattice Boltzmann difference schemes, and finally the recovery of equivalent partial differential equations.

3.4 Lattice Models and Moments Definition

3.4.1 D_2Q_9 Lattice model for the velocity field

In LBM, fluid is considered as the fictitious particles. Probability distribution function f contains the information regarding the positions of the particles at certain time in the flow domain on the lattice, see Fig. (2.1). The D_2Q_9 lattice model is called the nine velocity model, this model contains nine nodes, and on this lattice model we define three conserved quantities e.g, mass conservation and momentum conservation in x and y directions respectively, and six non-conserved moments or quantities. The speed of sound c_s is such that $c_s^2 = 1/3$ for all lattice models used here. The nine fluid flow moments defined on this lattice model read m_{00}, m_x, m_y, m_{xx}, m_{yy}, m_{xy}, m_{xxy}, m_{xyy}, m_{xxyy}, where m_{00}, m_x, m_y are the conserved quantities. For the sake of simplicity we denote the previous moments such as m_{00}, m_{10}, m_{01}, m_{20}, m_{02}, m_{11}, m_{21}, m_{12}, m_{22}. The characteristic velocities $\mathbf{c}_i = (c_{i,x}, c_{i,y})$ for D_2Q_9 lattice ($i = 0, \ldots, 8$) are

$$\{(0,0), (-1,1), (-1,0), (-1,-1), (0,-1), (1,-1), (1,0), (1,1), (0,1)\},$$

The conserved fluid flow moments reads

$$m_{00} = \sum_i f_i = \rho$$

$$m_{10} = \sum_i c_{ix} f_i = \rho u_x \tag{3.10}$$

$$m_{01} = \sum_i c_{iy} f_i = \rho u_y,$$

where ρ is the macroscopic density, u_x and u_y are the macroscopic velocities of the fluid in x and y directions.

Other six non-conserved fluid flow moments are given as follows

$$
\begin{aligned}
m_{xx} = m_{20} &= \sum_i c_{ix}^2 f_i \\
m_{yy} = m_{02} &= \sum_i c_{iy}^2 f_i \\
m_{xy} = m_{11} &= \sum_i c_{ix} c_{iy} f_i \\
m_{xxy} = m_{21} &= \sum_i c_{ix}^2 c_{iy} f_i \\
m_{xyy} = m_{12} &= \sum_i c_{ix} c_{iy}^2 f_i \\
m_{xxyy} = m_{22} &= \sum_i c_{ix}^2 c_{iy}^2 f_i
\end{aligned}
\tag{3.11}
$$

3.4.2 D_2Q_5 Lattice model for energy balance

As discussed earlier, specific internal energy conservation is implemented on the D_2Q_5 lattice model to solve the temperature field. This lattice model contains five nodes thus five sets of characteristic velocities c_{ix}, c_{iy} where $i = 1...5$ are given by

$$
\{(0,0), (-1,0), (0,-1), (1,0), (0,1)\}.
$$

For the thermal case, we have one conservation rule to be obliged which is the specific internal energy. For this lattice we have one conserved moment and four non-conserved moments. Temperature distribution function is denoted by g and the five moments valid on this lattice model are $m_{00}, m_{10}, m_{01}, m_{20}, m_{02}$. The specific internal energy conservation rule for incompressible fluids

$$
m_{00} = \sum_i g_i = T.
\tag{3.12}
$$

The non-conserved moments

$$m_{10} = \sum_i c_{ix} g_i$$
$$m_{01} = \sum_i c_{iy} g_i$$
$$m_{20} = \sum_i c_{ix}^2 g_i \qquad (3.13)$$
$$m_{02} = \sum_i c_{iy}^2 g_i.$$

3.5 Lattice Boltzmann Equation

The general discretized form of the lattice Boltzmann equation reads

$$f_i(x + c_{ix} \triangle t, y + c_{iy} \triangle t, t + \triangle t) - f_i(x, y, t) = \Omega_i(f, f) + F_i(x, y), \qquad (3.14)$$

where $\Omega(f, f)$ is the non-linear integral term that can also be understood as the generalized form of the collision operator, and $F_i(x, y)$ is the forcing term. The streaming step reads

$$f_i(x + c_{ix} \triangle t, y + c_{iy} \triangle t, t + \triangle t),$$

and the collision term reads

$$f_i(x, y, t) + \Omega_i(f, f) + F_i(x, y).$$

In present study $F_i(x, y) = 0$. The collision step can also be assigned to the post collision distribution function f^c.

$$f_i^c = f_i(x, y, t) + \Omega_i(f, f). \qquad (3.15)$$

From above equations we can write down the following form of the lattice Boltzmann equation

$$f_i(x + c_{ix} \triangle t, y + c_{iy} \triangle t, t + \triangle t) - f_i^c(x, y, t) = 0. \qquad (3.16)$$

3.6 Bhatnagar-Gross-Krook (BGK) LBM

BGK collision scheme is the simplest and the most used scheme to solve lattice Boltzmann equations [8, 50, 111, 114, 124, 144, 149, 189, 209, 214, 235, 263, 290]. In BGK the highly non-linear integral collision operator $\Omega(f, f)$ is linearized and

simplified such that

$$\Omega_{i(BGK)}(f, f) = -\omega\big(f_i - f_i^{eq}\big), \tag{3.17}$$

where f^{eq} is the equilibrium distribution function, ω is the relaxation frequency with which a distribution function of the ith node f_i relaxes to its equilibria f_i^{eq}. In BGK, all non-conserved quantities relax to their equilibria with an identical relaxation frequency. Therefore the lattice Boltzmann equation Eq. (3.14) for the BGK collision operator reads

$$\begin{aligned} f_i(x + c_{ix} \triangle t, y + c_{iy} \triangle t, t + \triangle t) - f_i(x, y, t) = \\ -\omega\big(f_i(x, y, t) - f_i^{eq}(x, y, t)\big). \end{aligned} \tag{3.18}$$

From Eq. (3.16), (3.18), we have

$$f_i^c(x, y, t) = f_i(x, y, t) - \omega\big(f_i(x, y, t) - f_i^{eq}(x, y, t)\big). \tag{3.19}$$

It is evident from the above equations that streaming and collision steps are performed in the velocity space. Eq. (3.19) will be used in future to calculate the post collision distribution function f^c and corresponding moments $m_{x^\alpha y^\beta}$. The time and space shifted form of the lattice Boltzmann equation, Eq. (3.16) reads

$$\begin{aligned} f(x + c_{ix} \triangle t/2, y + c_{iy} \triangle t/2, t + \triangle t/2) \\ - f^c(x - c_{ix} \triangle t/2, y - c_{iy} \triangle t/2, t - \triangle t/2) = 0. \end{aligned} \tag{3.20}$$

To recover the Navier-Stokes equations, the very first step to be taken is the Taylor expansion of the lattice Boltzmann equation, Eq. (3.20). Afterwards we will apply the diffusive scaling to the asymptotic expansion of the moments m. The diffusive scaling for the LBM reads $\triangle x^2/\triangle t = \epsilon$. The asymptotic expansion of the moments m reads

$$m_{x^m y^n} = \sum_{l=0}^{\infty} \epsilon^l m_{x^m y^n}^{(l)}. \tag{3.21}$$

Now by definitions provided in Eq. (3.11), f_i can be transformed into the moments generally such that

$$m_{x^m y^n} = \sum_i c_{ix}^m c_{iy}^n f_i. \tag{3.22}$$

Using above relation Eq. (3.22), transforming the f into m in Eq. (3.20), and later on applying the asymptotic expansion provided in Eq. (4.29), The Taylor expansion

of the lattice Boltzmann equation reads

$$\sum_{p=0}^{\infty} \frac{\epsilon^{2p}}{p!} \partial_t^p \left(\sum_{q=0}^{\infty} \epsilon^q m_{\alpha\beta}^{(q)} \right)$$
$$= \sum_{m,n=0}^{\infty} \frac{-\epsilon^{(m+n)}}{m!n!} \partial x^m y^n \left(\sum_{q=0}^{\infty} m_{(\alpha+m)(\beta+n)}^{(c)} \right). \tag{3.23}$$

Now our next objective will be to expand the above expression for various orders of ϵ. For ϵ^0, we have

$$m_{\alpha\beta}^{(0)} = m_{\alpha\beta}^{c(0)} = m_{\alpha\beta}^{(eq)}. \tag{3.24}$$

For ϵ^1, we have

$$m_{\alpha\beta}^{(1)} = m_{\alpha\beta}^{(c)(1)} - \partial_x m_{(\alpha+1)\beta}^{(c)(0)} - \partial_y m_{\alpha(\beta+1)}^{(c)(0)}. \tag{3.25}$$

For ϵ^2, we have

$$m_{\alpha\beta}^{(2)} + \partial_t m_{\alpha\beta}^{(eq)(0)} = m_{\alpha\beta}^{(c)(2)} - \partial_x m_{(\alpha+1)\beta}^{(c)(1)} - \partial_y m_{\alpha(\beta+1)}^{(c)(1)}$$
$$+ \partial_{xy} m_{(\alpha+1)(\beta+1)}^{(c)(0)} + \frac{1}{2} \left(\partial_{xx} m_{(\alpha+2)\beta}^{(c)(0)} + \partial_{yy} m_{\alpha(\beta+2)}^{(c)(0)} \right). \tag{3.26}$$

For ϵ^3,

$$m_{\alpha\beta}^{(3)} + \partial_t m_{\alpha\beta}^{(1)} = m_{\alpha\beta}^{(c)(3)} - \partial_x m_{(\alpha+1)\beta}^{(c)(2)} - \partial_y m_{\alpha(\beta+1)}^{(c)(2)}$$
$$+ \partial_{xy} m_{(\alpha+1)(\beta+1)}^{(c)(1)} + \frac{1}{2} \left(\partial_{xx} m_{(\alpha+2)\beta}^{(c)(1)} + \partial_{yy} m_{\alpha(\beta+2)}^{(c)(1)} \right.$$
$$\left. - \partial_{x^2 y} m_{(\alpha+2)(\beta+1)}^{(c)(0)} - \partial_{xy^2} m_{(\alpha+1)(\beta+2)}^{(c)(0)} \right) - \frac{1}{6} \left(\partial_{x^3} m_{(\alpha+3)\beta}^{(c)(0)} \right.$$
$$\left. + \partial_{y^3} m_{\alpha(\beta+3)}^{(c)(0)} \right). \tag{3.27}$$

We must now set some conditions for the conserved moments in terms of moments and their post collision values. As mentioned earlier we have three conserved moments, one mass conservation rule and two momentum conservation rules to be obeyed on the D_2Q_9 lattice model. The terms m_{00}, m_{10}, m_{01} are the conserved moments, therefore they also obey the collisional invariance. That means that for these moments their post collision values are equal to their equilibrium values, therefore $m_{00}^{c()} = m_{00} = m_{00}^{eq}$, $m_{10}^{c()} = m_{10} = m_{10}^{eq}$, $m_{01}^{c()} = m_{01} = m_{01}^{eq}$. From relation for ϵ^0, it is evident that all the post collision moments of zeroth order elevation; $c(0)$, are equal to the equilibria of that corresponding moment. For example, for

any valid values of α, β, lets say $\alpha = (1, 2)$, $\beta = (1, 2)$, $m^{c(0)}_{(1or2)(1or2)} = m^{eq(0)}_{(1or2)(1or2)}$.

3.6.1 Navier-Stokes Equations Recovery for Fluid Flow from BGK-LBM

The very first macroscopic equation we choose to recover is the continuity equation or the divergence free condition for the incompressible flows. To recover the continuity equation or the divergence free condition for the fluid flow we choose the equivalent partial differential equation for ϵ^1. We set $\alpha = 0$, $\beta = 0$, Eq. (3.25) reads

$$m^{(1)}_{00} = m^{(c)(1)}_{00} - \partial_x m^{(c)(0)}_{10} - \partial_y m^{(c)(0)}_{01}. \tag{3.28}$$

From the conservation rule and collisional invariance for the mass conservation rule, we have $m^{(1)}_{00} = m^{c(1)}_{00}$, therefore

$$\partial_x m^{(c)(0)}_{10} + \partial_y m^{(c)(0)}_{01} = 0. \tag{3.29}$$

As discussed above, m_{10}, m_{01} are collisional invariant, we have $m^{(c)(0)}_{01} = m^{eq}_{01}$ and $m^{(c)(0)}_{10} = m^{eq}_{10}$, therefore

$$\partial_x m^{eq}_{10} + \partial_y m^{eq}_{01} = 0. \tag{3.30}$$

In LBM, the equilibrium values of the moments are calculated by the second order truncation of the Taylor expansion of the Maxwell-Boltzmann distributions. In future we shall apply this theory to calculate the equilibria for the non-conserved moments. But m_{10}, m_{01} are the conserved moments, momentum in x and y directions respectively, therefore $m^{eq}_{10} = \rho u_x$, $m^{eq}_{01} = \rho u_y$. Substituting these equilibrium values of the moments in the above equation

$$\partial_x(\rho u_x) + \partial_y(\rho u_y) = 0, \tag{3.31}$$

this equation is the well known divergence free condition for the fluid flow.

The Navier-Stokes momentum equations for the velocities u_x, u_y contain terms of variations of momentum ρu_x, ρu_y with respect to time and space. Therefore after having a look at the Eq. (3.27), to end up with a terms such that $\frac{\partial(\rho u_x)}{\partial t}$ we need to

assign $\alpha = 1, \beta = 0$ in Eq. (3.26). For $\alpha = 1, \beta = 0$ the ϵ^2 equation reads

$$m_{10}^{(2)} + \partial_t m_{10}^{(eq)(0)} = m_{10}^{(c)(2)} - \partial_x m_{20}^{(c)(1)} - \partial_y m_{11}^{(c)(1)}$$
$$+ \partial_{xy} m_{21}^{(c)(0)} + \frac{1}{2} \left(\partial_{xx} m_{30}^{(c)(0)} + \partial_{yy} m_{12}^{(c)(0)} \right). \tag{3.32}$$

The contribution of the moments which are not defined on the lattice model we are working with is null and void given the condition that these moments are not subjected to aliasing. Due to aliasing we can write $m_{30} = m_{10}, m_{13} = m_{11}, m_{31} = m_{11}$. Therefore after applying aliasing for moment m_{30}

$$m_{10}^{(2)} + \partial_t m_{10}^{(eq)(0)} = m_{10}^{(c)(2)} - \partial_x m_{20}^{(c)(1)} - \partial_y m_{11}^{(c)(1)}$$
$$+ \partial_{xy} m_{21}^{(c)(0)} + \frac{1}{2} \left(\partial_{xx} m_{10}^{(c)(0)} + \partial_{yy} m_{12}^{(c)(0)} \right). \tag{3.33}$$

From the relations for ϵ^0 and collisional invariance of the conserved moments, for the above equation we already can write that $m_{10}^{(1)} = m_{10}^{(c)(1)} = m_{10}^{eq}$. The forcing term in the x direction $F_x = m_{10}^{(2)} - m_{10}^{(c)(2)}$. In the present study $F_x = 0$. The unknown moments are $m_{20}^{(c)(1)}, m_{11}^{(c)(1)}$. To calculate first order post collision moments $m_{20}^{(c)(1)}, m_{11}^{(c)(1)}$ we need ϵ^1 equation and the BGK collision scheme to calculate the post collision moments (unknown) in all equilibrium (known) terms. To calculate the post collision moment $m_{20}^{c(1)}$, first we assign $\alpha = 2, \beta = 0$ in Eq. (3.25) and use aliasing for the moment $m_{30} = m_{10}$

$$m_{20}^{(1)} = m_{20}^{(c)(1)} - \partial_x m_{10}^{(c)(0)} - \partial_y m_{21}^{(c)(0)}. \tag{3.34}$$

We have $m_{10}^{(c)(0)} = m_{10}^{eq}, m_{21}^{(c)(0)} = m_{21}^{eq}$, therefore $m_{20}^{(1)}$ reads

$$m_{20}^{(1)} = m_{20}^{(c)(1)} - \partial_x m_{10}^{eq} - \partial_y m_{21}^{eq}. \tag{3.35}$$

It is evident from the above equation that there exists one unknown $m_{20}^{(1)}$. Now transforming the distribution function f into moments $m_{20}^{(1)}$ in the collision scheme Eq. (3.19), we multiply both sides by $\sum_i c_{ix}^2$ because $m_{20}^{(1)} = \sum_i c_{ix}^2 f_i^{(1)}$. Moment transformed form of the Eq. (3.19) reads

$$m_{20}^{(c)(1)} = m_{20}^{(1)} - \omega \left(m_{20}^{(1)} - m_{20}^{eq(1)} \right). \tag{3.36}$$

Solving Eq. (3.35) and Eq. (3.36),

$$m_{20}^{(c)(1)} = m_{20}^{eq(1)} + \left(1 - \frac{1}{\omega} \right) \partial_x m_{10}^{eq(0)} + \left(1 - \frac{1}{\omega} \right) \partial_y m_{21}^{eq(0)}. \tag{3.37}$$

Now to calculate the term $m_{11}^{(c)(1)}$, we put $\alpha = 1, \beta = 1$ in Eq. (3.25) and transform f into m_{11} in the collision scheme by multiplying both sides by $\sum_i c_{ix} c_{iy}$, the ϵ^1 equation reads

$$m_{11}^{(1)} = m_{11}^{(c)(1)} - \partial_x m_{21}^{(c)(0)} - \partial_y m_{12}^{(c)(0)}. \tag{3.38}$$

The moment transformed collision scheme reads

$$m_{11}^{(c)(1)} = m_{11}^{(1)} - \omega\left(m_{11}^{(1)} - m_{11}^{eq(1)}\right). \tag{3.39}$$

From above equations we have the final expression for the moment $m_{11}^{(c)(1)}$

$$m_{11}^{(c)(1)} = m_{11}^{eq(1)} + \left(1 - \frac{1}{\omega}\right)\partial_x m_{21}^{eq(0)} + \left(1 - \frac{1}{\omega}\right)\partial_y m_{12}^{eq(0)}. \tag{3.40}$$

Now substituting $m_{20}^{(c)(1)}, m_{11}^{(c)(1)}$ into Eq. (3.33) and using relations $m_{\alpha\beta}^{(c)(0)} = m_{\alpha\beta}^{eq(0)}$, for $F_x^{(2)} = 0$

$$\partial_t m_{10}^{eq(0)} + \partial_x m_{20}^{eq(1)} + \partial_y m_{11}^{eq(1)}$$
$$= \left(\frac{1}{\omega} - \frac{1}{2}\right)\left(\partial_{xx} m_{10}^{eq(0)} + \partial_{yy} m_{12}^{eq(0)} + 2\partial_{xy} m_{21}^{eq(0)}\right). \tag{3.41}$$

All the non-conserved moment terms in the above equation are in their equilibria, these moments are known and reads (up to required order)

$$\begin{aligned} m_{20}^{eq} &= \rho c_s^2 + \rho u_x^2 \\ m_{02}^{eq} &= \rho c_s^2 + \rho u_y^2 \\ m_{11}^{eq} &= \rho u_x u_y \\ m_{12}^{eq} &= \rho c_s^2 u_x \\ m_{21}^{eq} &= \rho c_s^2 u_y. \end{aligned} \tag{3.42}$$

Now substituting the equilibria of the moments we have

$$\partial_t\left(\rho u_x\right) + \partial_x\left(\rho c_s^2 + \rho u_x^2\right) + \partial_y\left(\rho u_x u_y\right)$$
$$= \left(\frac{1}{\omega} - \frac{1}{2}\right)\left(\partial_{xx}\left(\rho u_x\right) + \partial_{yy}\left(\rho c_s^2 u_x\right) + 2\partial_{xy}\left(\rho c_s^2 u_y\right)\right). \tag{3.43}$$

Pressure is given by $p = \rho c_s^2$, therefore the much resolved equation reads

$$\partial_t\left(\rho u_x\right) + \partial_x\left(p + \rho u_x^2\right) + \partial_y\left(\rho u_x u_y\right)$$
$$= \left(\frac{1}{\omega} - \frac{1}{2}\right)\left(\partial_{xx}\left(\rho u_x\right) + c_s^2 \partial_{yy}\left(\rho u_x\right) + 2c_s^2 \partial_{xy}\left(\rho u_y\right)\right). \tag{3.44}$$

The above equation is the well known Navier-Stokes moment equation for u_x recovered from the BGK-LBM scheme.

Recovery of N-S equations using Taylor expansion method by Wagner

The Taylor expansion method was adopted by Wagner to achieve the generalized N-S equations for BGK collision scheme [288]. The lattice Boltzmann equation for a non-ideal fluid used by Wagner reads

$$
\begin{aligned}
f_i(x + v_i \triangle t, t+1) &= f_i(x,t) + F_i(x,t) \\
&+ \frac{1}{\tau}\big[f_i^0(x,t) + A(x,t) - f_i(x,t)\big],
\end{aligned}
\tag{3.45}
$$

where F is the forcing term giving birth to the non-ideal behavior, τ is the relaxation time used in the BGK collision scheme and A is the non-ideal contribution in the pressure tensor [276]. Please see the mass and momentum conservation conditions for f, A and F, which are defined in details in the paper. Wagner defined the Taylor expansion of the advection step of the LBE, which reads

$$
f_i(x + v_i \triangle t, t+\triangle t) = \sum_k \frac{(\triangle t)^k}{k!} D^k f_i(x,t),
\tag{3.46}
$$

where v_i is equivalent to c_i in our case; the microscopic velocity, $D = \frac{\partial}{\partial t} + v_i \frac{\partial}{\partial x}$ is the convective derivative. The second order Taylor expansion of the above equation reads

$$
D_i f_i + \frac{1}{2} D_i^2 f_i + F_i + O(D^3) = \frac{1}{\tau}(f_i^0 + A - f_i),
\tag{3.47}
$$

where $\tau(= 1/\omega)$ is the relaxation time. To attain the lattice Boltzmann difference equation in all known variables, the unknown variable, e.g. distribution function f_i can be expressed as the known (equilibrium distribution function f^0) such that

$$
\begin{aligned}
f_i &= f_i^0 + A - \tau F_i - \tau D_i f_i + O(\partial^2) \\
&= f_i^0 + A - \tau F_i - \tau D_i(f_i^0 + A - \tau F_i) + O(\partial^2).
\end{aligned}
\tag{3.48}
$$

Substituting f_i into Eq. (3.47), the difference equation for the BGK lattice Boltzmann equation reads

$$
\begin{aligned}
F_i + D_i(f_i^0 + A - \tau F_i) &- \left(\tau - \frac{1}{2}\right) D_i^2(f_i^0 + A - \tau F_i) \\
&= \frac{1}{\tau}(f_i^0 + A - f_i) + O(\partial^3).
\end{aligned}
\tag{3.49}
$$

Now applying the conservation rules for mass $\sum_i f_i^0 = \rho$ on the above equation, the zeroth order moment $\sum_i$ of the above equation leads to the continuity equation,

which reads

$$\partial_t \rho + \partial_x(\rho u) - \frac{1}{2}\partial_x F = O(\partial^3). \tag{3.50}$$

For an ideal fluid case, where $A = 0, F = 0$, the standard continuity, i.e. Euler equation is recovered. The first order moment of the Eq. (3.49) $\sum_i v_i$ leads to the momentum N-S equation

$$
\begin{aligned}
&\rho \partial_t \left(u - \frac{1}{2\rho} \right) + \rho \left(u - \frac{1}{2\rho} \right) \cdot \bigtriangledown \left(u - \frac{1}{2\rho} \right) = - \bigtriangledown (\rho \theta + A) \\
&+ F + \bigtriangledown \nu \rho \Big[\bigtriangledown \left(u - \frac{1}{2\rho} \right) + \bigtriangledown \left(u - \frac{1}{2\rho} \right)^T \Big] + \bigtriangledown R + O(\partial^3),
\end{aligned}
\tag{3.51}
$$

where kinematic viscosity $\nu = \left(\tau - \frac{1}{2} \right)\theta$, and $\theta = c_s^2$. The term $\bigtriangledown R$ is the collection of the nonphysical contributions arising due to the difference scheme. Wagner studied the forcing and pressure methods for non-ideal gas and extended this analysis to the higher orders. Li and Wagner, a year later, derived the N-S equations for a free energy based multi-component system. The detailed derivations of multi component N-S equations using Taylor expansion method can be found in Ref. [182]. In 2012 Kaehler and Wagner developed the moment based methodology to recover the hydrodynamic equations by using MRT scheme with BGK collision operator. That means that the non-conserved moments relax to the equilibrium with different relaxation time but collision operator is written in velocity space. The moment based approach can be found in the Ref. [153]

Recovery of equivalent partial differential equations by Dubois

Francois Dubois was the first to apply the equivalent equation methodology to the LBM framework to recover hydrodynamic equations, e.g. N-S equations. The developed methodology is applicable to the linear collision schemes, e.g. BGK and MRT collision operator. We have extended that and applied it to non-linear semi implicit collision operator, e.g. cascaded LBM, presented in Cascaded LBM section. The advection step, i.e. streaming step of any general LBM scheme reads

$$f(x + v_i \bigtriangleup t, t + \bigtriangleup t), \tag{3.52}$$

where v_i is the microscopic velocity of the fluid particles, which is equivalent to the characteristic velocity c_i used in previous sections. Dubois rewrote the advection step considering the fact that the distribution function at $(x + v_i \bigtriangleup t, t + \bigtriangleup t)$ is equal to the distribution function after collision at (x, t). That reads $f_i(x + v_i \bigtriangleup t, t + \bigtriangleup t) = f_i^c(x, t)$. The equivalent difference equation of the previous equation reads

$$f_i(x, t + \bigtriangleup t) = f_i^c(x - v_i \bigtriangleup t, t). \tag{3.53}$$

The above equation is the explicit upwind scheme for the advection equation

$$\partial_t f_i + v_i \cdot \triangledown f_i = 0 \qquad (3.54)$$

From the first order Taylor expansions of both sides of Eq. (3.53), the post collision derivative reads

$$\partial_{x_\alpha} f_i^c = \partial_{x_\alpha} f_i^{eq}$$

$$- \triangle t \sum_k^J \left(\frac{1}{\tau_k} - 1 \right) M^{-1}{}_k^i \partial_{x_\alpha} \sum_{i=0}^J M_i^k (\partial_t f_i^{eq} + v_i^\alpha \partial_{x_\alpha} f_i^{eq}) \qquad (3.55)$$

$$+ O(\triangle t^2).$$

From the the second order Taylor expansion of the Eq. (3.53) and using the conservation rules we can write the equivalent equation

$$\partial_t m^l + \sum_{\alpha=1}^d \sum_{i=0}^J M_i^l v_i^\alpha \partial_{x_\alpha} f_i^{eq} =$$

$$\triangle t \sum_{\alpha=1}^d \sum_{i=0}^J \sum_{k \le d+1} M_i^l v_i^\alpha \left(\frac{1}{\tau_k} - 1 \right) M^{-1}{}_k^i$$

$$\times \partial_{x_\alpha} \sum_{i=0}^J M_i^k (\partial_t f_i^{eq} + v_i^\alpha \partial_{x_\alpha} f_i^{eq}) + \frac{\triangle t}{2} \Bigg(- \partial_{tt} m^l$$

$$+ \sum_{\alpha=1}^d \sum_{i=0}^J M_i^l v_i^\alpha v_i^\beta \partial_{x_\alpha x_\beta} f_i^{eq} \Bigg) + O(\triangle t^2)$$

$$(3.56)$$

where d is the lattice model dimension, i.e. for two dimensional lattice, $d = 2$, m is the raw moment, M is the transformation matrix which transforms velocity distribution function f into raw moment m, and τ_k is the relaxation frequency for the kth non-conserved moment. The mass conservation equation, i.e. the continuity equation can be recovered by assigning $l = 0$. As from the definition of the raw moment m given in the moment section, for conserved quantities, $m_0 = \rho, m_{10} = m_{10}^{eq} = \rho u_x, m_{01} = m_{01}^{eq} = \rho u_y$. Here in Dubois notations, $m^0 = m_0, m^1 = m_{10}, m^2 = m_{01}$. The principal attraction of the previous steps was to eliminate the post collision terms by solving the first and second order Taylor expansion and applying the collision scheme. The momentum equations can be recovered for conditions $l = \gamma, 1 \le \gamma \le d$. For two dimensional model, $d = 2$, $\gamma = 1, 2$, the N-S equations for ρu_x and ρu_y can be obtained after some complex algebra. Dubois et al. presented a paper in which the authors have used MRT DDF LBM scheme, in which the N-S equations were derived for mass and momentum conservation laws and thermal hydrodynamic equations were recovered for

advection-diffusion and total energy conservation rules [80]. The thermal equations have been presented in the sections dedicated to thermal flows.

3.6.2 Equivalent Thermal Macroscopic Equations (Fourier-Kirchhoff Equations) Recovery from BGK-LBM

To recover macroscopic equations for the thermal field, we use the D_2Q_5 lattice model and moments described in section 2.2. This is a one conservation rule problem, where only one moment is the conserved quantity and rest four moments are the non-conserved quantities. These non-conserved thermal moments do relax to their equilibria with an identical relaxation frequency ω_g. To recover the Fourier-Kirchhoff equations, there must exist terms such as $\frac{\partial T}{\partial t}$ and temperature T variations in x, y directions. Therefore, we assign $\alpha = 0$, $\beta = 0$ in Eq. (3.26)

$$m_{00}^{(2)} + \partial_t m_{00}^{(eq)(0)} = m_{00}^{(c)(2)} - \partial_x m_{10}^{(c)(1)} - \partial_y m_{01}^{(c)(1)}$$
$$+ \partial_{xy} m_{11}^{(c)(0)} + \frac{1}{2}\left(\partial_{xx} m_{20}^{(c)(0)} + \partial_{yy} m_{02}^{(c)(0)}\right). \tag{3.57}$$

The forcing term $F_{00}^{(2)} = m_{00}^{(2)} - m_{00}^{(c)(2)} = 0$. It should be noted that moment m_{11} is non-existent on the D_2Q_5 lattice model. Therefore m_{11} will be dropped out from all the equations. In above equation non-conserved thermal moments $m_{10}^{(c)(1)}, m_{01}^{(c)(1)}$ are unknowns and must be calculated from ϵ^1 equation. Now, to calculate $m_{10}^{(c)(1)}$, we assign $\alpha = 1, \beta = 0$ in Eq. (3.25) and drop the non-existent moment m_{11}

$$m_{10}^{(1)} = m_{10}^{(c)(1)} - \partial_x m_{20}^{(c)(0)}. \tag{3.58}$$

From the BGK collision scheme for temperature distribution function g, from $m_{x^\alpha y^\beta} = \sum_i c_{ix}^\alpha c_{iy}^\beta g_i$, we have the moment transformed form

$$m_{10}^{(c)(1)} = m_{10}^{(1)} - \omega_g\left(m_{10}^{(1)} - m_{10}^{eq(1)}\right). \tag{3.59}$$

From the above equations we have

$$m_{10}^{(c)(1)} = m_{10}^{eq(1)} + \left(1 - \frac{1}{\omega_g}\right)\partial_x m_{20}^{eq(0)}. \tag{3.60}$$

Now calculating moment $m_{01}^{(c)(1)}$

$$m_{01}^{(1)} = m_{01}^{(c)(1)} - \partial_y m_{02}^{(c)(0)}. \tag{3.61}$$

From the BGK collision scheme, moment transforming it for $m_{01}^{(c)(1)}$

$$m_{01}^{(c)(1)} = m_{01}^{(1)} - \omega_g \big(m_{01}^{(1)} - m_{01}^{eq(1)} \big). \tag{3.62}$$

From the above equations we have

$$m_{01}^{(c)(1)} = m_{01}^{eq(1)} + \left(1 - \frac{1}{\omega_g}\right) \partial_y m_{02}^{eq(0)}. \tag{3.63}$$

Substituting the above calculated post collision thermal moments in Eq. (3.57), and using relation $m_{\alpha\beta}^{(c)(0)} = m_{\alpha\beta}^{eq(0)}$

$$\partial_t m_{00}^{(eq)(0)} + \partial_x m_{10}^{eq(1)} + \partial_y m_{01}^{eq(1)}$$
$$= \left(\frac{1}{\omega_g} - \frac{1}{2}\right) \left(\partial_{xx} m_{20}^{eq(0)} + \partial_{yy} m_{02}^{eq(0)} \right). \tag{3.64}$$

For thermal case, the equilibrium values for the non-conserved higher order thermal moments are defined with a free parameter a, used to tune the thermal diffusivity. The equilibria for the non-conserved thermal moments reads

$$\begin{aligned}
m_{10}^{eq} &= T u_x, \\
m_{01}^{eq} &= T u_y, \\
m_{20}^{eq} &= \frac{a}{2} T, \\
m_{02}^{eq} &= \frac{a}{2} T.
\end{aligned} \tag{3.65}$$

Substituting the value of the conserved thermal moment and equilibria of the non-conserved thermal moments given above into the Eq. (3.64)

$$\partial_t T + \partial_x \big(T u_x \big) + \partial_y \big(T u_y \big) = \frac{a}{2} \left(\frac{1}{\omega_g} - \frac{1}{2} \right) \left(\partial_{xx} T + \partial_{yy} T \right). \tag{3.66}$$

The above equation is the well known and desired thermal macroscopic equation also known as the Fourier-Kirchhoff equation recovered from the BGK LBM. The term $\frac{a}{2}\left(\frac{1}{\omega_g} - \frac{1}{2}\right)$ is the thermal diffusivity. Therefore in this section we have established the consistency of the BGK LBM by successfully recovering Navier-Stokes and Fourier-Kirchhoff equations.

3.7 Multiple Relaxation Times (MRT)- LBM

Multiple relaxation times lattice Boltzmann methods (MRT-LBM) contrary to BGK LBM use multiple relaxation times for the relaxation of the non-conserved moments.

Each non-conserved moment can be relaxed to its equilibrium with a unique relaxation time. Sometimes some specific non-conserved moments have been chosen to be relaxed with different relaxation times while rest of the moments can be relaxed with different or identical relaxation time [52, 73, 110, 146, 147, 172–174, 180, 204, 309]. Another principal difference between BGK and MRT LBM scheme is that the collision operation is performed in the moment space. As earlier section, the lattice Boltzmann equation for the MRT LBM reads

$$
\begin{aligned}
f(x + c_{ix} \bigtriangleup t, y + c_{iy} \bigtriangleup t, t + \bigtriangleup t) - f(x, y, t) \\
= \Omega_{MRT}(m, m) + F(x, y),
\end{aligned} \tag{3.67}
$$

again $F(x, y) = 0$. The MRT collision operator reads

$$
\Omega_{i(MRT)}(m, m) = -\mathbb{A}(m_i - m_i^{eq}), \tag{3.68}
$$

where $\mathbb{A}$ is the collision matrix. Therefore the MRT lattice Boltzmann equation reads

$$
\begin{aligned}
m_i(x + c_{ix} \bigtriangleup t, y + c_{iy} \bigtriangleup t, t + \bigtriangleup t) - m_i(x, y, t) = \\
-\mathbb{A}(m_i(x, y, t) - m_i^{eq}(x, y, t)).
\end{aligned} \tag{3.69}
$$

For the D_2Q_9 lattice model for our fluid flow case, we have three conserved moments and six non-conserved moments which relax to their equilibria with a unique relaxation time, therefore $\mathbb{A} = diag(0, 0, 0, \omega_1, \omega_2, \omega_3, \omega_4, \omega_5, \omega_6)$. We define

$$
m_i^{(c)} = m_i(x, y, t) - \mathbb{A}(m_i(x, y, t) - m_i^{eq}(x, y, t)), \tag{3.70}
$$

The lattice Boltzmann equation for MRT reads

$$
m_i(x + c_{ix} \bigtriangleup t, y + c_{iy} \bigtriangleup t, t + \bigtriangleup t) - m_i^{(c)}(x, y, t) = 0. \tag{3.71}
$$

The above equation can be written in time and space shifted form and similarly as before Taylor expansion and diffusive scaling is applied to it. The only thing that will distinct MRT from BGK is the relaxation scheme of the non-conserved moments. The moments relations, collision invariance, conservation rules, and generalized EPDE Eq. (3.25, 3.26, 3.27) recovered in previous section for $\epsilon^0, \epsilon^1, \epsilon^2, \epsilon^3$ stand valid for the MRT LBM study as well.

3.7.1 Equivalent Navier-Stokes Equations Recovery for Fluid Flow from MRT-LBM

The conserved moments m_{00}, m_{10}, m_{01} do not associate with the collision scheme as they are collisional invariant, therefore relations and equality of these conserved quantities remain identical for both BGK and MRT LBM. As a result, divergence free condition remains identical and can be proven as earlier. The Navier-Stokes equations for the momentum can be recovered in the similar manner as before. We assign $\alpha = 1, \beta = 0$ in Eq. (3.26), the ϵ^2 equation reads

$$
\begin{aligned}
m_{10}^{(2)} + \partial_t m_{10}^{(eq)(0)} = {} & m_{10}^{(c)(2)} - \partial_x m_{20}^{(c)(1)} - \partial_y m_{11}^{(c)(1)} \\
& + \partial_{xy} m_{21}^{(c)(0)} + \frac{1}{2}\left(\partial_{xx} m_{30}^{(c)(0)} + \partial_{yy} m_{12}^{(c)(0)} \right).
\end{aligned}
\tag{3.72}
$$

Due to aliasing, $m_{30} = m_{10}$,

$$
\begin{aligned}
m_{10}^{(2)} + \partial_t m_{10}^{(eq)(0)} = {} & m_{10}^{(c)(2)} - \partial_x m_{20}^{(c)(1)} - \partial_y m_{11}^{(c)(1)} \\
& + \partial_{xy} m_{21}^{(c)(0)} + \frac{1}{2}\left(\partial_{xx} m_{10}^{(c)(0)} + \partial_{yy} m_{12}^{(c)(0)} \right).
\end{aligned}
\tag{3.73}
$$

The forcing term $F_x^{(2)} = m_{10}^{(2)} - m_{10}^{(c)(2)} = 0$. Now we need to calculate the unknowns non-conserved post collision moments $m_{20}^{(c)(1)}, m_{11}^{(c)(1)}$ from Eq. (3.25) and the MRT collision scheme. For $m_{20}^{(c)(1)}$, we assign $\alpha = 2, \beta = 0$ in Eq. (3.25) and due to aliasing $m_{30} = m_{10}$,

$$
m_{20}^{(1)} = m_{20}^{(c)(1)} - \partial_x m_{10}^{eq} - \partial_y m_{21}^{eq}.
\tag{3.74}
$$

From the collision matrix $\mathbb{A}$ it is evident that moment m_{20} relaxes to its equilibria with ω_1 relaxation frequency. Therefore the collision scheme for the moment $m_{20}^{(1)}$ reads

$$
m_{20}^{(c)(1)} = m_{20}^{(1)} - \omega_1 \left(m_{20}^{(1)} - m_{20}^{eq(1)} \right).
\tag{3.75}
$$

Solving above equations for $m_{20}^{(c)(1)}$

$$
m_{20}^{(c)(1)} = m_{20}^{eq(1)} + \left(1 - \frac{1}{\omega_1} \right) \partial_x m_{10}^{eq(0)} + \left(1 - \frac{1}{\omega_1} \right) \partial_y m_{21}^{eq(0)}.
\tag{3.76}
$$

Similarly for the moment $m_{11}^{(c)(1)}$,

$$
m_{11}^{(1)} = m_{11}^{(c)(1)} - \partial_x m_{21}^{(c)(0)} - \partial_y m_{12}^{(c)(0)}.
\tag{3.77}
$$

From collision matrix $\mathbb{A}$, moment m_{11} relaxes to its equilibria with frequency ω_3. The collision scheme for m_{11} reads

$$m_{11}^{(c)(1)} = m_{11}^{(1)} - \omega_3\big(m_{11}^{(1)} - m_{11}^{eq(1)}\big). \tag{3.78}$$

The final expression for the $m_{11}^{(c)(1)}$ reads

$$m_{11}^{(c)(1)} = m_{11}^{eq(1)} + \left(1 - \frac{1}{\omega_3}\right)\partial_x m_{21}^{eq(0)} + \left(1 - \frac{1}{\omega_3}\right)\partial_y m_{12}^{eq(0)}. \tag{3.79}$$

Now substituting moments $m_{20}^{(c)(1)}, m_{11}^{(c)(1)}$ into Eq. (3.73) and using relations $m_{12}^{(c)(0)} = m_{12}^{eq(0)}, m_{21}^{(c)(0)} = m_{21}^{eq(0)}$,

$$
\begin{aligned}
\partial_t m_{10}^{eq(0)} + \partial_x m_{20}^{eq(1)} + \partial_y m_{11}^{eq(1)} &= \left(\frac{1}{\omega_1} - \frac{1}{2}\right)\partial_{xx} m_{10}^{eq(0)} \\
&+ \left(\frac{1}{\omega_3} - \frac{1}{2}\right)\partial_{yy} m_{12}^{eq(0)} + \left(\frac{1}{\omega_1} - \frac{1}{2} + \frac{1}{\omega_3} - \frac{1}{2}\right)\partial_{xy} m_{21}^{eq(0)}.
\end{aligned}
\tag{3.80}
$$

Using Eq. (3.42) we have,

$$
\begin{aligned}
\partial_t\big(\rho u_x\big) + \partial_x\big(\rho c_s^2 + \rho u_x^2\big) + \partial_y\big(\rho u_x u_y\big) &= \left(\frac{1}{\omega_1} - \frac{1}{2}\right)\partial_{xx}\big(\rho u_x\big) \\
&+ \left(\frac{1}{\omega_3} - \frac{1}{2}\right)\partial_{yy}\big(\rho c_s^2 u_x\big) + \left(\frac{1}{\omega_1} - \frac{1}{2} + \frac{1}{\omega_3} - \frac{1}{2}\right)\partial_{xy}\big(\rho c_s^2 u_y\big).
\end{aligned}
\tag{3.81}
$$

The above equation is the Navier-Stokes momentum equation for u_x recovered from the MRT LBM. It must be noted that N-S equations recovered from the BGK LBM is the special case of the N-S equation recovered from the MRT. If only one relaxation frequency is considered for the MRT case i.e. $(\omega_1 = \omega_3 = \omega)$ the recovered equation is the N-S equation of the BGK Eq. (3.44).

3.7.2 Equivalent Thermal Macroscopic Equations (Fourier-Kirchhoff Equations) Recovery from MRT-LBM

Recovering of the Fourier-Kirchhoff equation from MRT LBM is done in the similar manner in Section 4.2 for the BGK. Again, the D_2Q_5 lattice model have been used for a one conservation rule problem. The conserved and non-conserved moments remain identical to that of BGK. The ϵ^2 equation is selected where $\alpha = 0, \beta = 0$, we have

$$
\begin{aligned}
m_{00}^{(2)} + \partial_t m_{00}^{(eq)(0)} &= m_{00}^{(c)(2)} - \partial_x m_{10}^{(c)(1)} - \partial_y m_{01}^{(c)(1)} \\
&+ \partial_{xy} m_{11}^{(c)(0)} + \frac{1}{2}\bigg(\partial_{xx} m_{20}^{(c)(0)} + \partial_{yy} m_{02}^{(c)(0)}\bigg).
\end{aligned}
\tag{3.82}
$$

Adopting similar steps as before, we calculate the unknowns $m_{01}^{(c)(1)}, m_{10}^{(c)(1)}$. For one conservation rule, in our case, the collision matrix for the thermal moments $m_{00}, m_{10}, m_{01}, m_{20}, m_{02}$ is $\mathbb{A} = diag\left(0, \omega_{g_1}, \omega_{g_2}, \omega_{g_3}, \omega_{g_4}\right)$. From ϵ^1 equation, Eq. (3.25), for $\alpha = 1, \beta = 0$

$$m_{10}^{(1)} = m_{10}^{(c)(1)} - \partial_x m_{20}^{(c)(0)}. \tag{3.83}$$

The MRT collision scheme for the thermal moment m_{10} reads

$$m_{10}^{(c)(1)} = m_{10}^{(1)} - \omega_{g_1}\left(m_{10}^{(1)} - m_{10}^{eq(1)}\right). \tag{3.84}$$

From above equations

$$m_{10}^{(c)(1)} = m_{10}^{eq(1)} + \left(1 - \frac{1}{\omega_{g_1}}\right)\partial_x m_{20}^{eq(0)}. \tag{3.85}$$

For the moment $m_{01}^{(c)(1)}$, setting $\alpha = 0, \beta = 1$ in Eq. (3.25)

$$m_{01}^{(1)} = m_{01}^{(c)(1)} - \partial_y m_{02}^{(c)(0)}. \tag{3.86}$$

From the MRT collision scheme for m_{01}

$$m_{01}^{(c)(1)} = m_{01}^{(1)} - \omega_{g_2}\left(m_{01}^{(1)} - m_{01}^{eq(1)}\right). \tag{3.87}$$

From the above equations we have

$$m_{01}^{(c)(1)} = m_{01}^{eq(1)} + \left(1 - \frac{1}{\omega_{g_2}}\right)\partial_y m_{02}^{eq(0)}. \tag{3.88}$$

Substituting $m_{10}^{(c)(1)}, m_{01}^{(c)(1)}$ into the Eq. (3.82)

$$\partial_t m_{00}^{(eq)(0)} + \partial_x m_{10}^{eq(1)} + \partial_y m_{01}^{eq(1)}$$
$$= \left(\frac{1}{\omega_{g_1}} - \frac{1}{2}\right)\partial_{xx} m_{20}^{eq(0)} + \left(\frac{1}{\omega_{g_2}} - \frac{1}{2}\right)\partial_{yy} m_{02}^{eq(0)}. \tag{3.89}$$

Substituting equilibria of the thermal moments from Eq. (3.65), the final form of the thermal macroscopic equation reads

$$\partial_t T + \partial_x\left(Tu_x\right) + \partial_y\left(Tu_y\right)$$
$$= \frac{a}{2}\left(\frac{1}{\omega_{g_1}} - \frac{1}{2}\right)\partial_{xx} T + \frac{a}{2}\left(\frac{1}{\omega_{g_2}} - \frac{1}{2}\right)\partial_{yy} T. \tag{3.90}$$

The above equation is the Fourier-Kirchhoff equation recovered from the MRT LBM. The multiples of the double derivatives terms on the right hand side $\frac{a}{2}\left(\frac{1}{\omega_{g_1}} - \frac{1}{2}\right)$ and $\frac{a}{2}\left(\frac{1}{\omega_{g_2}} - \frac{1}{2}\right)$ can be recognized as the thermal diffusivities in x and y direction. The F-K equation for the BGK case can be recovered from the above F-K equation once we set $\omega_{g_1} = \omega_{g_2}$.

Equivalent thermal macroscopic equation by Dubois et al.

In 2016, Dubois et al. developed the Taylor expansion methodology to recover various thermal macroscopic equations [80]. The authors solved the advection-diffusion equation with an MRT collision scheme on a one-dimensional lattice D_1Q_3. In such models, as described above, the temperature is considered as a passive scalar and it follows the similar procedure as ours for thermal flows. To solve for energy equation, a coupling has been made between the mass and momentum conservation and volumic energy conservation on different lattice model of the DDF scheme. The total energy distribution function is denoted by "g", the conservation rule reads

$$\sum g_i = \sum g_i^{eq} = \rho E = \rho\left(e + \frac{1}{2}u^2\right), \tag{3.91}$$

where e is the internal energy, $\frac{1}{2}u^2$ is the specific kinetic energy. The recovered thermal equation for total energy reads

$$\partial_t \rho E + \partial_x(\rho E u + pu) - \partial_x(\rho \nu u \partial_x u) - \partial_x(\kappa \partial_x T) = 0, \tag{3.92}$$

where $\kappa = \triangle t\left(\frac{1}{\tau_k} - \frac{1}{2}\right)\left(\frac{2+\alpha}{3}\lambda^2 - u_0^2\right)$, $p = \left(\frac{c_p}{c_v} - 1\right)\rho i$, $Pr = \frac{\rho \nu c_p}{\kappa}$

Equivalent advection-diffusion equations by Jami et al.

Jami et al. proposed a modified DDF MRT LBM scheme to solve convective flows [147]. The authors solved mass and momentum conservation on a standard D_2Q_9 lattice model and the internal energy conservation for thermal flows on a cross D_2Q_5 lattice model. As a standard procedure of the DDF scheme, velocity distribution function f was used to solve mass and momentum conservation rules and thermal distribution function g to solve the temperature. The thermal LBE reads

$$g_i(x_i + c_i\delta t, t + \delta t) = g_i^*, \tag{3.93}$$

g_i^* is the post-collision distribution function. MRT collision scheme has been used which follows the similar collision scheme as defined in the previous section. For D_2Q_5 lattice model, Jami et al. defined the equilibrium moments such that $m_0 =$

$m_0^{eq} = T, m_1^{eq} = 0, m_2^{eq} = 0, m_3^{eq} = aT, m_4^{eq} = bT$. The difference between the present and the scheme described in Section 6.2 are the definition of the equilibrium moments and the cross lattice model. The authors applied the same Taylor expansion method to derive the equivalent anisotropic diffusion equation up to order three in δt, using the MRT collision scheme, which reads

$$
\begin{aligned}
\partial_t T - \frac{c^2 \delta t}{5}(4 + a)&\left(\frac{1}{\tau_1} - \frac{1}{2}\right)\partial_{xx}T \\
&-c^2 \delta t b\left(\frac{1}{\tau_1} + \frac{1}{\tau_2} - \frac{1}{2}\right)\partial_{xy}T \\
-\frac{c^2 \delta t}{5}(4 + a)\left(\frac{1}{\tau_2} - \frac{1}{2}\right)&\partial_{yy}T = O(\delta t^3).
\end{aligned}
\tag{3.94}
$$

For the standard isotropic diffusion equation, $b = 0, \tau_1 = \tau_2 = \tau, \delta x = \delta t = 1, a = -2$.

3.8 Cascaded Lattice Boltzmann Method (CLBM)

To attain higher stability and accuracy for the lattice Boltzmann schemes beyond BGK and MRT for fluid flow and thermal transport problems, cascaded lattice Boltzmann method was formulated [13, 84, 94, 95, 116, 234, 244, 259, 262]. For CLBM, collision are performed in the central moment space, which are simply raw moment shifted by the macroscopic velocity components of the fluid flow system under consideration. This central moment approach helps reducing the Galilean invariancy violation caused by adopting the limited velocity lattice models. Putting a constraint of finite velocity set induces this Galilean invariancy. The term cascaded implies the cascaded operation implemented in the relaxation process. This represents the semi implicitness of the collision operator. The lower order non-conserved moments effect the relaxation process of the higher order non-conserved moments. For a two dimensional lattice system central moment can be defined as follows

$$
\kappa_{x^m y^n} = \sum_i \left(c_{ix} - u_x\right)^m \left(c_{iy} - u_y\right)^n f_i,
\tag{3.95}
$$

where κ is the central moment, f_i is the velocity distribution function, u_x, u_y are the component of the macroscopic velocity, c_{ix}, c_{iy} are the characteristic lattice velocities in x and y directions, respectively. There exist two ways to deal with the raw moments, using non-orthogonal moments and using orthogonal raw moments. The Gram-Schmidt orthogonalization process is used to orthogonalize these raw

moments. Similarly, dealing with the central moment cascaded lattice Boltzmann scheme, non-orthogonal or orthogonal processes can be chosen. In our case we chose orthogonalised central moments, giving birth to an orthogonal transformation matrix which transform velocity distribution functions into orthogonalized raw moments. The streaming step of cascaded LB scheme is performed in central moment space. The collision step of cascaded LB differs severely from the BGK and MRT collision schemes. For CLBM, collisions are performed in central moment space and moreover there exists the semi-implicitness. The lattice Boltzmann equation for the cascaded case reads

$$f_i(x + c_{ix} \triangle t, y + c_{iy} \triangle t, t + \triangle t) - f_i(x, y, t) = \mathbb{K} \cdot k \tag{3.96}$$

Therefore from Eq. (3.95) and (3.96), we have

$$
\begin{aligned}
\kappa_{x^m y^n}(x + c_{ix} \triangle t, y + c_{iy} \triangle t, t + \triangle t) - \kappa_{x^m y^n}(x, y, t) \\
= \left(\sum_i \left(c_{ix} - u_x \right)^m \left(c_{iy} - u_y \right)^n \right) \mathbb{K} \cdot k.
\end{aligned}
\tag{3.97}
$$

For simplicity let us denote the term $\kappa_{x^m y^n}(x + c_{ix} \triangle t, y + c_{iy} \triangle t, t + \triangle t) = \kappa^{(c)}_{x^m y^n}(x, y, t)$, which represents the post collision in central moment space. Therefore the cascaded lattice Boltzmann equation in complete central moment space that we will be dealing with all along the study reads

$$
\begin{aligned}
\kappa^{(c)}_{x^m y^n}(x, y, t) - \kappa_{x^m y^n}(x, y, t) \\
= \left(\sum_i \left(c_{ix} - u_x \right)^m \left(c_{iy} - u_y \right)^n \right) \mathbb{K} \cdot k.
\end{aligned}
\tag{3.98}
$$

3.8.1 Navier-Stokes Equations Recovery for Fluid Flow from Central Moment CLBM

It is essential here to describe the central moment cascaded collision scheme as it is drastically different from the previously stated BGK, MRT collision schemes. Unlike BGK and MRT collision schemes, the cascaded collision vector k is relaxed towards its equilibrium. k_0, k_1 and $k_2 = 0$ because they correspond to the conserved quantities. Similarly as raw moments, the central moments corresponding to these conserved quantities are collisional invariant as well, that means

$$
\begin{aligned}
\kappa_{00} &= \kappa_{00}^{eq} = \kappa_{00}^{(c)} \\
\kappa_{10} &= \kappa_{10}^{eq} = \kappa_{10}^{(c)} \\
\kappa_{01} &= \kappa_{01}^{eq} = \kappa_{01}^{(c)}
\end{aligned}
\tag{3.99}
$$

To recover the N-S equation for momentum, we need to assign α and β to 1 and 0, respectively in Eq. (3.26). The ϵ^2 equation for negligible forcing term and after aliasing reads

$$\partial_t m_{10}^{(eq)(0)} = -\partial_x m_{20}^{(c)(1)} - \partial_y m_{11}^{(c)(1)} + \partial_{xy} m_{21}^{(c)(0)} \\ + \frac{1}{2}\left(\partial_{xx} m_{10}^{(c)(0)} + \partial_{yy} m_{12}^{(c)(0)}\right).$$

(3.100)

The unknown post collision moments in the above equations are $m_{20}^{(c)(1)}$ and $m_{11}^{(c)(1)}$. To calculate these post collision moments we need to define the cascaded collision scheme. The cascaded collision scheme reads

$$k_3 = \frac{\omega_3}{12}\left(\rho(u_x^2 + u_y^2) - f_6 - f_8 - f_4 - f_2 \\ -2(f_5 + f_3 + f_7 + f_1 - \rho c_s^2)\right)$$

(3.101)

$$k_4 = \frac{\omega_4}{4}\left[f_8 + f_4 - f_6 - f_2 + \rho(u_x^2 - u_y^2)\right]$$

(3.102)

$$k_5 = \frac{\omega_5}{4}(f_7 + f_3 - f_1 - f_5 - u_x u_y \rho)$$

(3.103)

$$k_6 = -\omega_6\Big(\big(f_5 + f_3 - f_7 - f_1 - 2u_x^2 u_y \rho \\ +u_y(\rho - f_8 - f_4 - f_0)\big)/4 + \frac{u_x}{2}(f_7 - f_1 - f_5 + f_3)\Big) \\ + \frac{u_y}{2}(-3k_4 - k_5) + 2u_x k_6$$

(3.104)

$$k_7 = -\omega_7\Big(\big(f_3 + f_1 - f_5 - f_7 - 2u_y^2 u_x \rho \\ +u_x(\rho - f_2 - f_6 - f_0)\big)/4 + \frac{u_y}{2}(f_7 - f_1 - f_5 + f_3)\Big) \\ + \frac{u_x}{2}(-3k_4 + k_5) + 2u_y k_6$$

(3.105)

$$k_8 = \frac{1}{4}\Big[\omega_8\left(\rho c_s^4 - \kappa_{22}\right) - 8k_4 - 6k_5(u_x^2 + u_y^2) \\ -2k_5(u_y^2 - u_x^2) + 16k_6 u_x u_y - 8k_7 u_y - 8k_8 u_x\Big],$$

(3.106)

where $\omega_4....\omega_9$ are the relaxation frequencies of the moments corresponding to $(xx, yy, xy, xxy, xyy, xxyy)$, respectively. The relations between the collision vector k and central moments $\kappa_{x^m y^n}$ can be obtained by solving Eq. (3.98)) on the D_2Q_9 lattice model. Central moments $\kappa_{xx}, \kappa_{yy}, \kappa_{xy}$ reads

$$
\begin{aligned}
\kappa_{20}^{(c)} - \kappa_{20} &= 6k_3 + 2k_4 \\
\kappa_{02}^{(c)} - \kappa_{02} &= 6k_3 - k_4 \\
\kappa_{11}^{(c)} - \kappa_{11} &= -4k_5.
\end{aligned}
\tag{3.107}
$$

The momentum N-S equation shown above contains terms in raw moment space. But the above system of equations is in the central moment space and cascaded collision scheme clearly expresses the semi-implicitness of the collision operator. Therefore, for the sake of simplicity and comparability, we intend to recover the N-S equation from cascaded central moment scheme in raw moment space as done in previous cases. In order to do that we need to first calculate $\kappa_{xx}, \kappa_{yy}, \kappa_{xy}$ by replacing the k values in Eq. (3.107). Thereafter we will transform κ and node-specific velocity distribution functions f_i appearing in the collision scheme into raw moments m using Eq. (3.11, 3.95). From Eq. (3.107, 3.106), for κ_{xx} we have

$$
\begin{aligned}
\kappa_{20}^{(c)} - \kappa_{20} = \frac{\omega_3}{2}\big(\rho(u_x^2 + u_y^2) - f_6 - f_8 - f_4 - f_2 \\
-2(f_5 + f_3 + f_7 + f_1 - \rho c_s^2)\big) + \frac{\omega_4}{2}\big(f_8 + f_4 - f_6 - f_2 \\
+\rho(u_x^2 - u_y^2)\big)
\end{aligned}
\tag{3.108}
$$

$$
\begin{aligned}
\kappa_{02}^{(c)} - \kappa_{02} = \frac{\omega_3}{2}\big(\rho(u_x^2 + u_y^2) - f_6 - f_8 - f_4 - f_2 \\
-2(f_5 + f_3 + f_7 + f_1 - \rho c_s^2)\big) - \frac{\omega_4}{2}\big(f_8 + f_4 - f_6 - f_2 \\
+\rho(u_x^2 - u_y^2)\big)
\end{aligned}
\tag{3.109}
$$

$$
\kappa_{11}^{(c)} - \kappa_{11} = \frac{\omega_5}{4}(f_7 + f_3 - f_1 - f_5 - u_x u_y \rho)
\tag{3.110}
$$

The raw moment $m_{20} = \sum_i c_{ix}^2 f_i$ calculated on the D_2Q_9 lattice model reads

$$
m_{20} = f_1 + f_2 + f_3 + f_5 + f_6 + f_7,
\tag{3.111}
$$

where f_1 is the velocity distribution function of the particle at node 1, f_2 at node 2

and so on. Similarly, $m_{02} = \sum_i c_{iy}^2 f_i$ and $m_{11} = \sum_i c_{ix} c_{iy} f_i$ reads

$$m_{02} = f_1 + f_3 + f_4 + f_5 + f_7 + f_8,$$
$$m_{11} = -f_1 + f_3 - f_5 + f_7. \tag{3.112}$$

Solving Eq. (3.11) and Eq. (3.95), and applying the conservation laws for mass and momentum, the relations between the central moment and raw moment can be established.

$$\kappa_{20}^{(c)} - \kappa_{20} = m_{20}^{(c)} - m_{20},$$
$$\kappa_{02}^{(c)} - \kappa_{02} = m_{02}^{(c)} - m_{02}, \tag{3.113}$$
$$\kappa_{11}^{(c)} - \kappa_{11} = m_{11}^{(c)} - m_{11}.$$

From Eq. (3.108, 3.111, 3.112, 3.113) we have

$$m_{20}^{(c)} - m_{20} = \frac{\omega_3}{2} \left[\rho(u_x^2 + u_y^2) - (m_{xx} + m_{yy}) + 2\rho c_s^2) \right]$$
$$+ \frac{\omega_4}{2} \left[m_{yy} - m_{xx} + \rho(u_x^2 - u_y^2) \right].$$
$$m_{02}^{(c)} - m_{02} = \frac{\omega_3}{2} \left[\rho(u_x^2 + u_y^2) - (m_{xx} + m_{yy}) + 2\rho c_s^2) \right] \tag{3.114}$$
$$- \frac{\omega_4}{2} \left[m_{yy} - m_{xx} + \rho(u_x^2 - u_y^2) \right].$$
$$m_{11}^{(c)} - m_{11} = -\omega_5(m_{xy} - \rho u_x u_y).$$

After defining the cascaded collision scheme, we must turn our attention back to the equivalent partial differential equations; Eq. (3.24, 3.25, 3.26) to recover the desired N-S equations. From Eq. (3.24), we can write that $m_{21}^{(c)(0)} = m_{21}^{eq(0)}, m_{10}^{(c)(0)} = m_{10}^{eq(0)}$ and $m_{12}^{(c)(0)} = m_{12}^{eq(0)}$. These equilibria moments can directly be put in Eq. (3.100) replacing the post collision moments. The two post collision moments in the equivalent PDE must be expressed in equilibria moments. As it can be seen in Eq. (3.114), there exist unknown moments such as m_{20}, m_{02} and m_{11}. In order to have expression for post collision moments completely in equilibria moments we will need to perform some algebra using Eq. (3.25) and Eq. (3.114). From Eq. (3.25), we have

$$m_{20}^{(1)} = m_{20}^{(c)(1)} - \partial_x m_{10}^{(c)(0)} - \partial_y m_{21}^{(c)(0)}.$$
$$m_{02}^{(1)} = m_{20}^{(c)(1)} - \partial_x m_{12}^{(c)(0)} - \partial_y m_{01}^{(c)(0)}. \tag{3.115}$$
$$m_{11}^{(1)} = m_{11}^{(c)(1)} - \partial_x m_{21}^{(c)(0)} - \partial_y m_{12}^{(c)(0)}.$$

From above system of equations (3.114) and (3.115), calculating $m^{(c)}$ in terms of

m^{eq}, and substituting the value of equilibria moments (from Eq. (3.42)) in (3.100), we have

$$\partial_t\big(\rho u_x\big) + \partial_x\bigg(\rho\big(u_x^2 + \chi_{\omega_3}c_s^2\big)\bigg) + \partial_y\big(\rho u_x u_y\big)$$
$$-\partial_{xx}\bigg(\big(\tfrac{1}{2} + \chi_{\omega_1}\big)\rho u_x - \chi_{\omega_2}\rho c_s^2 u_x\bigg) - \partial_{yy}\bigg(\big(\tfrac{1}{\omega_5} - \tfrac{1}{2}\big)\rho c_s^2 u_x\bigg) \qquad (3.116)$$
$$-\partial_{xy}\bigg(\big(\tfrac{1}{\omega_5} + \chi_{\omega_1}\big)\rho c_s^2 u_y - \chi_{\omega_2}\rho u_y\bigg) = 0,$$

where

$$\chi_{\omega_1} = \frac{1 - \tfrac{\omega_3}{2} - \tfrac{\omega_4}{2} + \big(\tfrac{\omega_3}{2} - \tfrac{\omega_4}{2}\big)^2 \tfrac{2}{(\omega_3+\omega_4)}}{\tfrac{\omega_3}{2} + \tfrac{\omega_4}{2} - \big(\tfrac{\omega_3}{2} - \tfrac{\omega_4}{2}\big)^2 \tfrac{2}{(\omega_3+\omega_4)}} \qquad (3.117)$$

$$\chi_{\omega_2} = \frac{\big(\tfrac{\omega_3}{2} - \tfrac{\omega_4}{2}\big)\tfrac{2}{(\omega_3+\omega_4)}}{\tfrac{\omega_3}{2} + \tfrac{\omega_4}{2} - \big(\tfrac{\omega_3}{2} - \tfrac{\omega_4}{2}\big)^2 \tfrac{2}{(\omega_3+\omega_4)}} \qquad (3.118)$$

$$\chi_{\omega_3} = \frac{\omega_3\big(1 - \big(\tfrac{\omega_3}{2} - \tfrac{\omega_4}{2}\big)\tfrac{2}{(\omega_3+\omega_4)}\big)}{\tfrac{\omega_3}{2} + \tfrac{\omega_4}{2} - \big(\tfrac{\omega_3}{2} - \tfrac{\omega_4}{2}\big)^2 \tfrac{2}{(\omega_3+\omega_4)}} \qquad (3.119)$$

The Eq. (3.116) is the desired Navier-Stokes momentum equation for ρu_x recovered by pure central moment based cascaded lattice Boltzmann method. It can be easily verified that N-S equation for a two relaxation times (TRT) collision scheme can be recovered from the cascaded scheme by assigning $\omega_3 = \omega_4$. The BGK N-S scheme can be recovered when all the non-conserved moments are assigned identical relaxation frequency such as; $\omega_3 = \omega_4 = \omega_5$. Now, similar steps with appropriate choice of moment for $\frac{\partial m_{01}}{\partial t}$ term in the equivalent partial differential equation must be taken to recover the N-S equation for the y component of the momentum.

3.8.2 Thermal Macroscopic Equations (Fourier-Kirchhoff Equations) Recovery from Central Moment CLBM

The thermal macroscopic equations from cascaded LBM was recently derived in the paper by the authors in Ref. [259]. The EPDE reads

$$
\begin{aligned}
m_0^{(3)} - m_0^{c(3)} = -\partial_t m_0^{eq(1)} - \partial_x m_x^{eq(2)} - \partial_y m_y^{eq(2)} \\
+ \left(\frac{1}{\omega_2} + \frac{1}{\omega_3} - 1 \right) \partial_{xy} m_{xy}^{eq(1)} \\
+ \left(\frac{1}{\omega_2} - \frac{1}{2} \right) \partial_{xx} m_{xx}^{eq(1)} + \left(\frac{1}{\omega_3} - \frac{1}{2} \right) \partial_{yy} m_{yy}^{eq(1)}.
\end{aligned}
\tag{3.120}
$$

For negligible forcing term, and after inserting the equilibrium values of the moments we attain the following

$$
\begin{aligned}
\partial_t T + \partial_x T u_x + \partial_y T u_y = \frac{a}{2} \left(\frac{1}{\omega_2} - \frac{1}{2} \right) \partial_{xx} T \\
+ \frac{a}{2} \left(\frac{1}{\omega_3} - \frac{1}{2} \right) \partial_{yy} T + O(\Delta t^3).
\end{aligned}
\tag{3.121}
$$

The above equation is the desired F-K equations for incompressible fluids.

3.9 Conclusion

A comprehensive study discussing LBM consistency and stability has been presented in a simple and systematic manner with complete derivations of hydrodynamic equations for mass, momentum and energy conservation. The method of equivalent (or modified) partial differential equation was used to recover the hydrodynamic limits, i.e. Navier-Stokes and Fourier-Kirchhoff equations, for various lattice Boltzmann schemes. It was shown that Taylor expansion method can be used to accurately study the consistency and stability of various lattice Boltzmann methods. Multi-scale expansion technique, i.e. Chapman-Enskog expansion and asymptotic analysis technique are rather complex techniques compared to equivalent partial differential equation method. We believe that the present study will be very useful for new readers willing to use LBM for research and applications.

Capítulo 4

Double Population Cascaded Lattice Boltzmann Method for Convective Heat Transfer

4.1 Abstract

A Cascaded Thermal Lattice Boltzmann Method (CTLBM) is presented for efficient simulations of fluid flow and heat transfer problems. Contrary to the Bhatnagar-Gross-Krook Single Relaxation Time (BGK-SRT or just BGK) and Multiple Relaxation Times (MRT) methods of the LBM used for thermal problems, the proposed CTLBM improves Galilean invariancy of the method. The cascaded collision scheme was proved to increase the stability of the LBM in the case of fluid flow. Here we prove the enhanced stability and accuracy of the CTLBM scheme for thermal problems by comparing our results to traditional thermal MRT lattice Boltzmann methods. The proposed numerical scheme employs cascaded D_2Q_9 model for fluid flow and cascaded D_2Q_5 model for the temperature to study advection diffusion of sine wave and forced convection phenomena in forced cooling of a cylinder with heated core. To validate the proposed scheme, we compare our numerical results to the exact solutions of the sine wave advection-diffusion in 1D system for Peclet numbers between 10^2 and 10^6. We also present comparisons of our CTLBM with BGK and two widely used MRT lattice Boltzmann methods for several lattice resolutions. For 2D case, we present numerical validation of forced cooling of a cylinder with heated core. To show the stability of the proposed CTLBM even for moderate lattice resolutions, we also present numerical simulations of forced convection across the row of hot tubes and double shear layer flow. The numerical simulations are faster and numerical results are in strong agreements with those available in the literature. The enhanced stability and accuracy of the cascaded scheme are clearly

evident in the numerical results. Therefore, we show that the proposed CTLBM possesses higher stability and good accuracy with faster computation speed when compared to the other thermal MRT LBMs.

This work has been published in the ***International Journal of Thermal Sciences*** as an original research paper [259].

4.2 Introduction

Heat and mass transfer is one of the most occurring natural phenomenon in our daily lives. We see conjugate heat transfer taking place between solids and fluids in various domestic appliances, engineering, medical, and scientific applications such as furnaces [246], electronic circuitry devices, heat exchangers, nuclear reactors, surgeries, chemical reactions, etc. [32]. There are various numerical methods to tackle heat transfer problems. Computational fluid dynamics (CFD) is one of the most conventional framework used to solve heat transfer and fluid flow problems [56, 226]. Conventional solvers for the Navier-Stokes equations (based on e.g., finite difference method, finite element method or finite volume method) may have problems when it comes to dealing with fluid flow or heat and mass transfer problems in complex geometries [54] like e.g., fluid flow in porous media [44] or turbulent flows, mixing and combustion [312]. These conventional algorithms are usually computationally expensive and are hard to implement all along the complex fluid-solid interfaces which leaves us to search for an efficient alternative to conventional CFD solvers [181, 226, 310].

Numerical solvers for heat transfer problems are based on microscopic approaches (Molecular Dynamics methods - MD), mesoscopic approaches (LBM) and macroscopic approaches (Navier-Stokes-Fourier equations). Different kind of problem in heat transfer is the inverse problem [192] when one want to determine heat transfer coefficients from known temperature fields. Molecular dynamics has its own limitations due to its lack of capacity to simulate large number of molecules for long timescale [281]. Therefore, a significant quantity of fluid can not be simulated and the bigger picture regarding the fluid flow on large scales always remains uncertain. On the other hand, Navier-Stokes-Fourier solvers are macroscopic in nature and often lack information regarding microscopic developments occurring in the system during the fluid flow and heat transfer. Therefore the natural approach in LBM is to incorporate microscopic properties of the system to its mesoscopic description and then examine the hydrodynamic limit, or in other words to check if it can reproduce governing equations (in case of incompressible flow – the Navier Stokes equations). This is carried out here by the Lattice Boltzmann Method. LBM numerical schemes, kinetic in nature, incorporate microscopic laws of the flow characteristics and

solve Lattice Boltzmann Equations. Navier-Stokes equations can be recovered from the Lattice Boltzmann Equation e.g. by Chapman-Enskog expansion [44]. A wide range of research has been performed establishing the fact that LBM functions as a kinetic link between microscopic and macroscopic approaches. A physical system is described at a mesoscopic level through the LBM. The dynamics of the fluid is described by "virtual" fluid particles obeying the Boltzmann's Transport Equation (BTE). Using BTE we can describe the dynamics of the system by the particle density distribution functions (DF). These DFs contain a microscopic level information on particles' position and momentum together with collisions between the particles or particles and solid walls [302]. Due to this virtue of the LBM, complex boundary conditions, wettability, phase separation, etc. can be naturally incorporated into the numerical schemes. Therefore we state that LBM is deemed as one of the most reliable and viable alternative as the numerical solver among the microscopic and macroscopic methods.

Massive efforts have been made by the scientists and engineers to solve thermal problems utilizing LBM in the last two decades [226, 230]. There exist three principal categories to solve thermal flows using LBM [110], named as Multi-Speed methods (MS) [8], Double Distribution Function methods (DDF) [268], and hybrid methods [212]. Hybrid methods use LBM as a solver for the fluid flow and some other conventional numerical method for the heat transfer. Due to the fact that they are sandwich models, they could be more computationally costly compared to DDF models. DDF models have gained tremendous popularity among researchers due to their simplicity and higher stability compared to the other mentioned methods. First MS methods have Prandtl number fixed when using the simple collision operator [8] and the viscosity is erroneous in the viscous dissipation in the energy equation [202]. These shortcomings were later improved but MS methods still suffer from instabilities. These shortcomings are very well removed in the DDF models [157] and numerical stability is enhanced drastically.

In DDF models, two DF sets are used, one to define velocity and pressure fields and the other to define a temperature field. Two separate lattices are used to simulate fluid flow and temperature fields respectively. On the first lattice, the mass and momentum are the conserved quantities and on the second lattice, the temperature[1] field is solved[2]. Any standard lattice topology model can be chosen to simulate these fields according to one's convenience and they do not need to be the same. For example in 2D, the fluid flow field can be simulated on a D_2Q_9 lattice and the temperature field can be simulated on D_2Q_5 lattice simultaneously (where

---

[1] The conserved quantity here is the specific internal energy of the fluid.

[2] Obviously it is possible to use this approach for any scalar quantity that obeys advection-diffusion-reaction equation.

D_2 means 2D and Q_9 and Q_5 stand for nine and five speeds model respectively).

BGK-SRT[3] collision operator is the most used collision scheme in the LBM. The reason behind this is because this collision operator can simulate simple isothermal and incompressible flows. The simplicity of the SRT lies in the fact that all non-conserved quantities are relaxed with identical relaxation frequency or relaxation time. Numerical schemes based on the SRT operator are generally unstable for large Reynolds number and small lattice resolution. To solve this stability problem and also to increase the accuracy of the LBM, MRT collision schemes were constructed, in which DF are transformed to appropriate moments and the relaxation is done in this moment space with different relaxation times for each of the moments [73]. MRT schemes are mostly unstable for high Reynolds number flows. The reason behind this instability is related to violations of the Galilean invariancy [96]. This insufficient degree of preserving Galilean invariancy in MRT schemes was corrected by relaxing the central moments (i.e. shifted by the macroscopic velocity) in the moving frame rather than relaxing raw moments in a stationary frame as done in MRT [13, 94]. Another improvement was cascaded collision scheme canceling the influence between different orders of moments. This LBM scheme is known as the Cascaded Lattice Boltzmann Method (CLBM) [94, 95]. Cascaded schemes are more stable compared to raw moment MRT schemes and can simulate high Reynolds number flows in complex geometries with higher stability than MRT schemes. Apart from SRT, MRT and CLBM a class of Entropic Lattice Boltzmann Method (ELBM) emerged [156]. Both CLBM and ELBM were further developed and recently Cumulant method [96] and KBC method [23] appeared. In Cumulant method, a new statistically independent observable quantity of the distribution is defined called cumulants. In this model, cumulants are relaxed unlike in cascaded and MRT models where central and raw moments are relaxed respectively. Cumulants claim to eliminate numerical error unlike MRT methods in the hyper viscosity problems[96]. Cumulant method is claimed to be as numerically stable as cascaded LBM method[96]. KBC method is applied to only fluid flow problems, while the thermal problems are solved by quasi-equilibrium approach using SRT-BGK. KBC method is still being improved in various LBM aspects and was successfully applied in different fluid flow simulations and thermal problems [77, 226]. KBC and Cumulant methods are very recent methods that have been used to solve only fluid flow field(2015, 2016 respectively), and are under investigation by the LBM community. Since the main aim of this article is to compare DDF cascaded and MRT thermal schemes, these methods were mentioned here for the sake of completeness. We suggest that the interested readers will check the references [77, 96, 156, 226], and citations within these references for more information on these methods. Recently,

---

[3]Abbreviated simply as SRT or BGK in LBM literature.

the cascaded model for the fluid flow and the SRT-BGK model for the temperature field appeared [86]. In this model, a total energy approach is used to determine the temperature field, which is then incorporated into the flow field through the forcing term. Viscous dissipation and compression work are also modeled by this approach. Our approach described in this article is different in the sense that we have two cascaded collisional operators, one for the fluid flow (derived for the first time by Geier [94]) and one for the temperature field (derived for the first time by the authors and presented here).

A very important ingredient of the LBM is the definition of the equilibrium distribution function (EDF). Application of the Taylor expansion to the Maxwell-Boltzmann DF for ideal gases yields the required expression for the EDF [302]. Navier-Stokes equations could be recovered as a hydrodynamic limit of the system employing the Chapman-Enskog expansion applied to BGK-SRT lattice Boltzmann equation [302]. Actually, Chapman-Enskog expansion or Hilbert expansion techniques [132] are frequently applied to LBE to recover Navier-Stokes equations from LBE for fluid flow and the Fourier-Kirchhoff equation from LBE for temperature field. Other possibility to recover hydrodynamic limits of LBE is the method of equivalent partial differential equations (EPDEs) [79]. These expansion techniques also serve to establish a relation between diffusivity coefficients (i.e. viscosity or thermal diffusivity) and the relaxation time.

The previously mentioned SRT LBM suffers from severe numerical instability for flows with small kinematic viscosity or thermal diffusivity and moderate lattice resolution (i.e. when relaxation time is close to 0.5). In order to improve the performance of the LBM schemes, MRT schemes were proposed in which moments of velocity and temperature DFs are relaxed with different relaxation times. In MRT LBM schemes, collisions are performed in moment space while streaming is performed in the velocity space. The MRT is the LBM method with general collision matrix and the SRT is the special case of MRT. Cascaded LBM goes further and can be seen as LBM with general collision matrix and modified EDF [13].

In this article, we will present the 2D implementation of our cascaded scheme for one conservation law with the D_2Q_5 lattice model. To our best knowledge, this is the first time the cascaded scheme is used to simulate the temperature field. In Sec. 4.3 we develop the Cascaded Double Distribution Function Lattice Boltzmann Method for problems with one conservation law, i.e., in our case we consider temperature as the passive scalar. In Sec. 4.3.1 and 4.3.2 we develop theory of the CTLBM and CLBM for thermal and fluid flows, respectively. In Sec. 4.3.3 we discuss implementation of boundary conditions applied in our cases and in 4.3.4 we show physical and lattice units conversions. In Sec. 4.4 the theory which is developed in Sec. 2 is validated numerically. In Sec. 4.4.1 we numerically solve 1D advection-diffusion

equation using sine wave as an initial condition. In Sec. 4.4.2 we solve 2D forced convection problem of cooling a cylinder with heated core. In Sec. 4.4.3 we show the stability of the CTLBM using the forced convection across the row of hot tubes as a benchmark. In Sec. 4.4.4 the numerical stability of BGK and CTLBM are further investigated for the double shear layer flow. Sec. 4.5 contains discussion and Sec. 4.6 conclusions.

4.3 Cascaded lattice Boltzmann method for heat transfer and fluid flow

The fluid in LBM is considered as collection of fictitious particles living on the lattice and their behavior is described by the density DFs. These particles do stream with their respective characteristic velocity along the fixed links and collide on the nodes.

Here we show the characteristics of lattice models which will be used in this article. Here we use D_2Q_9 model for the fluid flow and D_2Q_5 model for heat transfer (Fig. 2.1). For the D_2Q_9 lattice, the characteristic velocities and weight factors are

$$[\vec{c_1}, \ldots, \vec{c_9}] = \begin{pmatrix} 0 & 1 & -1 & -1 & 0 & -1 & 1 & 1 & 0 \\ 0 & -1 & 0 & -1 & -1 & 1 & 0 & 1 & 1 \end{pmatrix},$$

$$[w_1, \ldots, w_9] = \left(\frac{4}{9}, \quad \frac{1}{36}, \quad \frac{1}{9}, \quad \frac{1}{36}, \quad \frac{1}{9}, \quad \frac{1}{36}, \quad \frac{1}{9}, \quad \frac{1}{36}, \quad \frac{1}{9} \right).$$

The speed of sound c_s for the D_2Q_9 model is $c_s^2 = \frac{1}{3}$. For the D_2Q_5 lattice, the characteristic velocities and weight factors are

$$[\vec{c_1}, \ldots, \vec{c_5}] = \begin{pmatrix} 0 & -1 & 0 & 1 & 0 \\ 0 & 0 & -1 & 0 & 1 \end{pmatrix},$$

$$[w_1, \ldots, w_5] = \left(\frac{1}{3}, \quad \frac{1}{6}, \quad \frac{1}{6}, \quad \frac{1}{6}, \quad \frac{1}{6} \right).$$

For D_2Q_5 lattice model the speed of sound $c_{s,g}$ is the same as for the D_2Q_9 model. The Lattice Boltzmann Equation for D_dQ_q model, which is solved by LBM, in its simplest form (BGK-SRT) reads

$$f_i(\vec{x} + \vec{c_i}, t+1) = f_i^c(\vec{x}, t) = f_i(\vec{x}, t) + \frac{1}{\tau_f} [f_i^{\mathrm{eq}}(\vec{x}, t) - f_i(\vec{x}, t)], \qquad (4.1)$$

where $\vec{x} = (x_1, \ldots, x_d)$ is a position vector, t is time, $i \in [1, q]$, f_i is the i-th distribution function, $f_i^c(\vec{x}, t)$ is the post-collision distribution function, τ_f is the relaxation time ($1/\tau_f = \omega_f$ where ω_f is called relaxation frequency), f_i^{eq} is the i-th equilibrium distribution function and $\vec{c_i}$ is the i-th characteristic velocity. Note that

all quantities here are in lattice units so the appropriate scaling must be done in order to simulate equivalent phenomena in physical units. The "streaming step" and "collision step" are defined as $f_i(\vec{x} + \vec{c}_i, t + 1) = f_i^c(\vec{x}, t)$ and $f_i^c(\vec{x}, t) = f_i(\vec{x}, t) + \frac{1}{\tau_f}[f_i^{\text{eq}}(\vec{x}, t) - f_i(\vec{x}, t)]$ respectively. In case of DDF LBM we have another set of DFs g_i obeying the same equation but with different τ_g and possibly different vectors $\vec{c}_i$

$$g_i(\vec{x} + \vec{c}_i, t + 1) = g_i^c(\vec{x}, t) = g_i(\vec{x}, t) + \frac{1}{\tau_g}[g_i^{\text{eq}}(\vec{x}, t) - g_i(\vec{x}, t)], \qquad (4.2)$$

Navier Stokes equations could be recovered as a hydrodynamic limit of the system employing the Chapman-Enskog expansion applied to (4.1) [302]. The Chapman-Enskog expansion or Hilbert expansion techniques [132] can be applied to LBE to recover Navier-Stokes equations and the Fourier-Kirchhoff equation from (4.2). In Eq. (4.1) we can see that collisions are performed in velocity space (i.e. we relax f_i towards f_i^{eq}).

The previously mentioned SRT LBM suffers from severe numerical instability for flows with small kinematic viscosity or thermal diffusivity (i.e. when τ is close to 0.5 [267]) and moderate lattice resolution. In order to improve the performance of the LBM schemes, MRT schemes were proposed in which moments of f_i or g_i are relaxed with different relaxation times τ_i [174]. In MRT LBM schemes, collisions are performed in the moment space while streaming is performed in the velocity space. The MRT LBM reads

$$f_i(\vec{x} + \vec{c}_i, t + 1) = f_i(\vec{x}, t) + \mathbb{M}^{-1}\mathbb{R}(m_i^{\text{eq}}(\vec{x}, t) - m_i(\vec{x}, t)), \qquad (4.3)$$

where $\mathbb{R} = \text{diag}(\frac{1}{\tau_1}, \ldots, \frac{1}{\tau_q})$ is a diagonal matrix with relaxation times τ_i, $\mathbb{M}$ is the moment transformation matrix $\vec{m} = \mathbb{M}\vec{f}$. It is possible to write the Eq. (4.3) in the following form

$$f_i(\vec{x} + \vec{c}_i, t + 1) = f_i(\vec{x}, t) + \mathbb{M}^{-1}\mathbb{R}\mathbb{M}(f_i^{\text{eq}}(\vec{x}, t) - f_i(\vec{x}, t)), \qquad (4.4)$$

so the MRT is the LBM method with general collision matrix $\mathbb{A} = \mathbb{M}^{-1}\mathbb{R}\mathbb{M}$ and the SRT is the special case with $\mathbb{A} = \mathbb{R} = \text{diag}(\frac{1}{\tau}, \ldots, \frac{1}{\tau})$.

The LBM algorithm itself consists of several steps. The first step is to calculate f_i^{eq} from the known initial conserved macroscopic quantities i.e. density ρ, velocity $\vec{u}$ and the scalar quantity ϕ (e.g. temperature) and initialize every lattice node with EDFs, then streaming is performed along the fixed links between the lattice nodes, then boundary conditions are applied. Next we calculate the new macroscopic

quantities from [110]

$$\rho = \sum_i f_i, \qquad \rho\vec{u} = \sum_i f_i \vec{c}_i, \qquad \phi = T = \sum_i g_i, \tag{4.5}$$

where f_i is the velocity DF for i^{th} lattice node. At this stage collision is performed and the algorithm is repeated from the streaming step until convergence of solution occurs or desired time step is reached. The EDFs for fluid flow (f_i^{eq}) on D_2Q_9 lattice model and for temperature (g_i^{eq}) on D_2Q_5 lattice model reads

$$f_i^{eq} = \rho w_i \left(1 + \frac{\vec{u} \cdot \vec{c}_i}{c_s^2} + \frac{(\vec{u} \cdot \vec{c}_i)^2}{2c_s^4} - \frac{\vec{u} \cdot \vec{u}}{2c_s^2} \right)$$
$$g_i^{eq} = T w_i \left(1 + \frac{\vec{u} \cdot \vec{c}_i}{c_s^2} \right) \tag{4.6}$$

where ρ is the density, w_i is the weight factor, and c_s is the speed of sound, and T is the temperature. From the Chapman-Enskog expansion we have the following relation for the kinematic viscosity (or the thermal diffusivity) and the relaxation time in the case of SRT LBM [110, 302]

$$\nu = c_s^2 \left(\tau_f - \frac{1}{2} \right), \tag{4.7}$$

$$\alpha = c_{s,g}^2 \left(\tau_g - \frac{1}{2} \right), \tag{4.8}$$

where c_s, $c_{s,g}$ are the speeds of sound and depend on the lattice model used.

In order to improve the stability of the thermal SRT and MRT schemes we apply the cascaded technique to the LBM with one conservation law. It is important and necessary to mention here that cascaded schemes perform collision in central moment space, unlike MRT where raw moments are relaxed, and both could use different relaxation times.

4.3.1 Cascaded Thermal Lattice Boltzmann Method (CTLBM) for Heat Transfer

In this section, the cascaded version of LBM for D_2Q_5 and one conservation law is derived with temperature being the scalar quantity obeying the conservation law. The LBM is a method which solves the velocity-spatial discretized Boltzmann's Transport Equation on a regular lattice. Here the discretized Boltzmann equation governing temperature field reads

$$g_i(\vec{x} + \vec{c}_i, t + 1) = \vec{g} + \mathbb{K} \cdot \vec{k}(\vec{g}, \vec{g}^{\text{eq}}, \omega_1, \ldots, \omega_5), \tag{4.9}$$

where g is the temperature DF, $\vec{c_i}$ is the characteristic lattice velocity, and $\mathbb{K} \cdot \vec{k}$ is the cascaded collision scheme depending on the relaxation frequencies ω.

In order to transform the temperature DF g_i into the moment m_i we need a transformation matrix $\mathbb{M}$ such that $\vec{m} = \mathbb{M}\vec{g}$. This transformation matrix is not unique and is chosen considering the condition that $\mathbb{M}$ must involve proper combinations of lattice characteristic velocities in all dimensions [13]. In our case we have chosen our non-orthogonal transformation matrix $\mathbb{M}$ such that

$$\mathbb{M} = \left[\vec{M}_0, \vec{M}_x, \vec{M}_y, \vec{M}_{xx+yy}, \vec{M}_{yy-xx} \right],$$

where $\vec{M}_0 = [1, 1, 1, 1, 1]^{\mathrm{T}}$, $M_{x,i} = c_{i,x}$, $M_{y,i} = c_{i,y}$, $M_{xx+yy,i} = c_{i,x}^2 + c_{i,y}^2$, $M_{yy-xx,i} = c_{i,y}^2 - c_{i,x}^2$, where c_{ix}, c_{iy} are i^{th} characteristic lattice velocities' components in x and y directions respectively. Afterward, we calculate the transformation matrix $\mathbb{K}$ by performing the Gram-Schmidt orthogonalization process on $\mathbb{M}$. The matrix $\mathbb{K}$ reads

$$\mathbb{K}^{\mathrm{T}} = \begin{bmatrix} 1 & 1 & 1 & 1 & 1 \\ 0 & -1 & 0 & 1 & 0 \\ 0 & 0 & -1 & 0 & 1 \\ 4 & -1 & -1 & -1 & -1 \\ 0 & -1 & 1 & -1 & 1 \end{bmatrix}. \tag{4.10}$$

The collision step for our CTLBM reads

$$\vec{g}^c = \vec{g} + \mathbb{K} \cdot \vec{k}(\vec{g}, \vec{g}^{\mathrm{eq}}, \omega_1, \ldots, \omega_5), \tag{4.11}$$

where $\vec{g}^c$ is the vector of post collision temperature DFs, $\vec{g}^{eq}$ is the EDFs for temperature, ω's are the relaxation frequencies of the non-conserved moments, $\vec{k}$ is the special collision vector that should be determined [13]. The streaming step is

$$g_i(\vec{x} + \vec{c_i}, t+1) = \vec{g}^c. \tag{4.12}$$

The collisions are performed in moment space, therefore let us define the raw moment $m_{x^m y^n}$ and central moment $\kappa_{x^m y^n}$ of order $m+n$

$$m_{x^m y^n} = \sum_i c_{i,x}^m c_{i,y}^n g_i, \quad m_{x^m y^n}^{\mathrm{eq}} = \sum_i c_{i,x}^m c_{i,y}^n g_i^{\mathrm{eq}} \tag{4.13}$$

$$\kappa_{x^m y^n} = \sum_i (c_{i,x} - u_x)^m (c_{i,y} - u_y)^n g_i, \quad \kappa_{x^m y^n}^{\mathrm{eq}} = \sum_i (c_{i,x} - u_x)^m (c_{i,y} - u_y)^n g_i^{\mathrm{eq}}, \tag{4.14}$$

where u_x and u_y are the macroscopic velocity components in x and y directions, respectively. The new set of moments for central moment space reads

$[\vec{\kappa}_0, \vec{\kappa}_x, \vec{\kappa}_y, \vec{\kappa}_{xx+yy}, \vec{\kappa}_{yy-xx}]$. The first moment is the conserved quantity, here T, i.e. $T = \sum_{i=1}^{5} g_i = \sum_{i=1}^{5} g_i^{eq}$. From the above we can see that

$$T = m_0 = m_0^{\text{eq}} = \kappa_0 = \kappa_0^{\text{eq}}.$$

In order to obtain the shift matrix $\mathbb{S}$, we take central moments from both sides of the (4.11) and assume that the post-collision state is in the equilibrium, we get [13]

$$\mathbb{S} \begin{bmatrix} k_1 \\ k_2 \\ k_3 \\ k_4 \\ k_5 \end{bmatrix} = \begin{bmatrix} 0 \\ \kappa_x^{eq} - \kappa_x \\ \kappa_y^{eq} - \kappa_y \\ \kappa_{xx+yy}^{eq} - \kappa_{xx+yy} \\ \kappa_{yy-xx}^{eq} - \kappa_{yy-xx} \end{bmatrix}. \tag{4.15}$$

The shift matrix $\mathbb{S}$ is as follows

$$\mathbb{S} = \begin{bmatrix} 0 & 0 & 0 & 0 & 0 \\ 0 & 2 & 0 & 0 & 0 \\ 0 & 0 & 2 & 0 & 0 \\ 0 & -4u_x & 0 & -2 & -2 \\ 0 & 0 & -4u_y & -2 & 2 \end{bmatrix}. \tag{4.16}$$

It is to be noted here that k_1 is zero as it corresponds to the conserved quantity (collisional invariant) i.e. $(\kappa_0^{\text{eq}} - \kappa_0) = 0$. Now we can solve (4.15) to obtain following relations for the vector $\vec{k}$

$$\begin{bmatrix} k_1 \\ k_2 \\ k_3 \\ k_4 \\ k_5 \end{bmatrix} = \begin{bmatrix} 0 \\ \frac{1}{2}(\kappa_x^{eq} - \kappa_x) \\ \frac{1}{2}(\kappa_y^{eq} - \kappa_y) \\ -\frac{1}{4}(\kappa_{xx+yy}^{eq} - \kappa_{xx+yy} + \kappa_{yy-xx}^{eq} - \kappa_{yy-xx}) - u_x k_2 - u_y k_3 \\ \frac{1}{4}(\kappa_{xx+yy}^{eq} - \kappa_{xx+yy} - \kappa_{yy-xx}^{eq} + \kappa_{yy-xx}) + u_x k_2 - u_y k_3 \end{bmatrix}. \tag{4.17}$$

At this stage we will apply the relaxation mechanism for all the non-conserved moments. In (4.17) we represent k for pre-collision stage. Here we relax these moments to achieve expressions for post collision stage, such that the higher order moments (k_4, k_5) relax towards their equilibrium without effecting relaxations of lower order moments (k_2, k_3) but lower order moments relax towards equilibrium effecting the relaxations of higher order moments. Therefore we relax k such that

$$
\begin{bmatrix} k_1 \\ k_2 \\ k_3 \\ k_4 \\ k_5 \end{bmatrix} = \begin{bmatrix} 0 \\ \frac{\omega_2}{2}\left(\kappa_x^{eq} - \kappa_x\right) \\ \frac{\omega_3}{2}\left(\kappa_y^{eq} - \kappa_y\right) \\ -\frac{\omega_4}{4}\left(\kappa_{xx+yy}^{eq} - \kappa_{xx+yy} + \kappa_{yy-xx}^{eq} - \kappa_{yy-xx}\right) - \frac{u_x\omega_2}{2}\left(\kappa_x^{eq} - \kappa_x\right) - \frac{u_y\omega_3}{2}\left(\kappa_y^{eq} - \kappa_y\right) \\ \frac{\omega_5}{4}\left(\kappa_{xx+yy}^{eq} - \kappa_{xx+yy} - \kappa_{yy-xx}^{eq} + \kappa_{yy-xx}\right) + \frac{u_x\omega_2}{2}\left(\kappa_x^{eq} - \kappa_x\right) - \frac{u_y\omega_3}{2}\left(\kappa_y^{eq} - \kappa_y\right) \end{bmatrix},
\tag{4.18}
$$

where $\omega_2, \ldots, \omega_5$ are the relaxation frequencies for respective moments. It should be noted that the relaxation scheme adopted here is the cascaded one, which is evident from the (4.18). The equilibrium moments for the conserved and non-conserved moments are as follows

$$
\begin{bmatrix} m_0^{eq} \\ m_x^{eq} \\ m_y^{eq} \\ m_{xx+yy}^{eq} \\ m_{yy-xx}^{eq} \end{bmatrix} = \begin{bmatrix} T \\ Tu_x \\ Tu_y \\ aT \\ 0 \end{bmatrix}.
\tag{4.19}
$$

The equilibrium moments above are defined in form of raw moments. Here, by using (4.13) and (4.14) we transform (4.18) from central moments κ to raw moments m

$$
\begin{bmatrix} k_1 \\ k_2 \\ k_3 \\ \\ k_4 \\ \\ k_5 \end{bmatrix} = \begin{bmatrix} 0 \\ \frac{\omega_2}{2}\left(m_x^{eq} - m_x\right) \\ \frac{\omega_3}{2}\left(m_y^{eq} - m_y\right) \\ -\frac{\omega_4}{4}\left(m_{xx+yy}^{eq} - m_{xx+yy} + m_{yy-xx}^{eq} - m_{yy-xx}\right) + \left(\frac{\omega_4}{2} - \frac{\omega_2}{2}\right)u_x\left(m_x^{eq} - m_x\right) + \\ + \left(\frac{\omega_4}{2} - \frac{\omega_3}{2}\right)u_y\left(m_y^{eq} - m_y\right) \\ -\frac{\omega_5}{4}\left(m_{xx+yy}^{eq} - m_{xx+yy} - m_{yy-xx}^{eq} + m_{yy-xx}\right) + \left(\frac{\omega_5}{2} - \frac{\omega_2}{2}\right)u_x\left(m_x^{eq} - m_x\right) + \\ + \left(\frac{\omega_3}{2} - \frac{\omega_5}{2}\right)u_y\left(m_y^{eq} - m_y\right) \end{bmatrix}.
\tag{4.20}
$$

The above equation can be expressed in matrix notation such that

$$
\vec{k} = \tilde{\mathbb{M}}(\vec{m}^{eq} - \vec{m}).
\tag{4.21}
$$

From (4.11) and (4.21) we have

$$
\vec{g}^c = \vec{g} + \mathbb{K} \cdot \tilde{\mathbb{M}}(\vec{m}^{eq} - \vec{m}).
\tag{4.22}
$$

Multiplying above equation by non-orthogonal transformation matrix $\mathbb{M}$ and using

relation $m = \mathbb{M}g$ we define the new lattice Boltzmann equation for moments

$$\vec{m}^c = \vec{m} + \mathbb{M} \cdot \mathbb{K} \cdot \tilde{\mathbb{M}}(\vec{m}^{eq} - \vec{m}). \tag{4.23}$$

The term $\mathbb{M} \cdot \mathbb{K} \cdot \tilde{\mathbb{M}}$ reads

$$\mathbb{M} \cdot \mathbb{K} \cdot \tilde{\mathbb{M}} = \begin{bmatrix} 0 & 0 & 0 & 0 & 0 \\ 0 & \omega_2 & 0 & 0 & 0 \\ 0 & 0 & \omega_3 & 0 & 0 \\ 0 & (\omega_2 - \omega_4)2u_x & (\omega_3 - \omega_4)2u_y & \omega_4 & 0 \\ 0 & (\omega_2 - \omega_5)2u_x & (\omega_3 - \omega_5)2u_y & 0 & \omega_5 \end{bmatrix}. \tag{4.24}$$

From (4.13) and (4.19) we have the temperature EDF for each node

$$\begin{bmatrix} g_1^{eq} \\ g_2^{eq} \\ g_3^{eq} \\ g_4^{eq} \\ g_5^{eq} \end{bmatrix} = \begin{bmatrix} (1-a)T \\ (a - 2u_x)\frac{T}{4} \\ (a - 2u_y)\frac{T}{4} \\ (a + 2u_x)\frac{T}{4} \\ (a + 2u_y)\frac{T}{4} \end{bmatrix}, \tag{4.25}$$

where a is a free parameter.

Now we adopt the method of EPDEs using technique described in [79]. This technique enables one to recover macroscopic equations, when the lattice Boltzmann equation is rescaled and the Taylor expansion is applied. The Lattice Boltzmann Equation for temperature DF can be written as follows [96]

$$g_i(x + c_{i,x}\Delta t, y + c_{i,y}\Delta t, t + \Delta t) = g_i(x, y, t) + \Omega_i = g_i^c(x, y, t), \tag{4.26}$$

where Ω is the collision operator, in our case $\mathbb{K} \cdot \vec{k}$. The time and space shifted form of the above equation reads

$$g_i(x + c_{i,x}\Delta t/2, y + c_{i,y}\Delta t/2, t + \Delta t/2) - g_i^c(x - c_{i,x}\Delta t/2, y - c_{i,y}\Delta t/2, t - \Delta t/2) = 0. \tag{4.27}$$

The Taylor expansion of the above equation can be written as

$$\sum_{a,b,n=0}^{\infty} \frac{(\Delta t/2)^{a+b+n}}{a!\, b!\, n!} c_{ix}^a c_{iy}^b \partial_x^a \partial_y^b \partial_t^n (g_i - g_i^c(-1)^{a+b+n}) = 0. \tag{4.28}$$

From (4.13), we first transform g_i into raw moments in the above equation and using diffusive scaling $\frac{\Delta x^2}{\Delta t} = const = \epsilon$ we define the asymptotic expansion of a raw

moment

$$m_{x^m y^n} = \sum_{l=0}^{\infty} \epsilon^l m_{x^m y^n}^{(l)}, \tag{4.29}$$

which inserted into (4.28) yields

$$\sum_{a,b,n=0}^{\infty} \frac{(\epsilon)^{a+b+2n+l}}{a!\ b!\ n!} \partial_x^a \partial_y^b \partial_t^n \left(m_{x^{(\alpha+a)} y^{(\beta+b)}}^{(l)} - m_{x^{(\alpha+a)} y^{(\beta+b)}}^{c(l)} (-1)^{a+b+n} \right) = 0. \tag{4.30}$$

Next we equate the terms of equal orders of ϵ in (4.30), to recover macroscopic equations. We are interested in ϵ^3 order $(a + b + 2n + l = 3, \alpha = \beta = 0)$

$$m_0^{(3)} - m_0^{c(3)} = -\partial_t \bar{m}_0^{eq(1)} - \partial_x \bar{m}_x^{(2)} - \partial_y \bar{m}_y^{(2)}, \tag{4.31}$$

where we use the following abbreviation

$$\bar{m}_{x^m y^n} = \frac{1}{2} \left(m_{x^m y^n} + m_{x^m y^n}^c \right).$$

From (4.23) and (4.24), $m_x^{(2)}$ $m_y^{(2)}$ are calculated such that

$$\begin{aligned}
\bar{m}_x^{(2)} &= m_x^{eq(2)} + \left(\frac{1}{2} - \frac{1}{\omega_2} \right) \left(\partial_x \bar{m}_{xx}^{(1)} + \partial_y \bar{m}_{xy}^{(1)} \right) \\
\bar{m}_y^{(2)} &= m_y^{eq(2)} + \left(\frac{1}{2} - \frac{1}{\omega_3} \right) \left(\partial_x \bar{m}_{xy}^{(1)} + \partial_y \bar{m}_{yy}^{(1)} \right)
\end{aligned} \tag{4.32}$$

Substituting (4.32) into (4.31) together with equalities $m^{(0)} = m^{c(0)} = m^{eq(0)}$, $m^{(1)} = m^{c(1)} = m^{eq(1)}$ (not proved here) yields

$$\begin{aligned}
m_0^{(3)} - m_0^{c(3)} = &-\partial_t m_0^{eq(1)} - \partial_x m_x^{eq(2)} - \partial_y m_y^{eq(2)} + \left(\frac{1}{\omega_2} + \frac{1}{\omega_3} - 1 \right) \partial_{xy} m_{xy}^{eq(1)} + \\
&\left(\frac{1}{\omega_2} - \frac{1}{2} \right) \partial_{xx} m_{xx}^{eq(1)} + \left(\frac{1}{\omega_3} - \frac{1}{2} \right) \partial_{yy} m_{yy}^{eq(1)}.
\end{aligned} \tag{4.33}$$

For D_2Q_5 lattice model $m_{xy} = m_{xy}^{eq} = 0$. From (4.19), substituting $m_0 = m_0^{eq} = T$, $m_x^{eq} = Tu_x$, $m_y^{eq} = Tu_y$, $m_{xx}^{eq} = m_{yy}^{eq} = T\frac{a}{2}$ we can write the final partial differential equation

$$\frac{\partial T}{\partial t} + \frac{\partial T u_x}{\partial x} + \frac{\partial T u_y}{\partial y} = \frac{a}{2} \left(\frac{1}{\omega_2} - \frac{1}{2} \right) \frac{\partial^2 T}{\partial x^2} + \frac{a}{2} \left(\frac{1}{\omega_3} - \frac{1}{2} \right) \frac{\partial^2 T}{\partial y^2} + O(\Delta t^3). \tag{4.34}$$

The above equation can be understood as Fourier-Kirchhoff equation for anisotropic

diffusion with thermal diffusivities in x and y directions defined by

$$\alpha_x = \frac{a}{2}\left(\frac{1}{\omega_2} - \frac{1}{2}\right) \qquad \alpha_y = \frac{a}{2}\left(\frac{1}{\omega_3} - \frac{1}{2}\right) \tag{4.35}$$

In the next section we adopt the strictly similar procedure for the fluid flow problem.

4.3.2   Cascaded Lattice Boltzmann Method for Fluid Flow

Here we briefly describe the derivation of the CLBM for the fluid flow on D_2Q_9 lattice model where mass and momentum conservation rules are obliged. The non-orthogonal transformation matrix is defined as [94]

$$\mathbb{M} = \left[\vec{M}_0, \vec{M}_x, \vec{M}_y, \vec{M}_{xx+yy}, \vec{M}_{xx-yy}, \vec{M}_{xy}, \vec{M}_{xxy}, \vec{M}_{xyy}, \vec{M}_{xxyy}\right].$$

The orthogonalized transformation matrix $\mathbb{K}$ for the D_2Q_9 reads

$$\mathbb{K}^{\mathrm{T}} = \begin{bmatrix} 1 & 1 & 1 & 1 & 1 & 1 & 1 & 1 & 1 \\ 0 & -1 & -1 & -1 & 0 & 1 & 1 & 1 & 0 \\ 0 & 1 & 0 & -1 & -1 & -1 & 0 & 1 & 1 \\ -4 & 2 & -1 & 2 & -1 & 2 & -1 & 2 & -1 \\ 0 & 0 & 1 & 0 & -1 & 0 & 1 & 0 & -1 \\ 0 & 1 & 0 & -1 & 0 & 1 & 0 & -1 & 0 \\ 0 & -1 & 0 & 1 & -2 & 1 & 0 & -1 & 2 \\ 0 & 1 & -2 & 1 & 0 & -1 & 2 & -1 & 0 \\ 4 & 1 & -2 & 1 & -2 & 1 & -2 & 1 & -2 \end{bmatrix}. \tag{4.36}$$

The collision and streaming steps can be defined respectively as

$$\vec{f}^c = \vec{f} + \mathbb{K} \cdot \vec{k}(\vec{f}, \vec{f}^{eq}, \tau_1, \ldots, \tau_9), \tag{4.37}$$

$$f_i(\vec{x} + \vec{c}_i, t + 1) = f_i^c. \tag{4.38}$$

We know that the first three moments are conserved quantities (mass and momentum in x and y directions), therefore k_1, k_2, k_3 are equal to zero. Equations for the shift matrix $\mathbb{S}$ now read (skipping the first three k's)

$$\mathbb{S}\begin{bmatrix} k_4 \\ k_5 \\ k_6 \\ k_7 \\ k_8 \\ k_9 \end{bmatrix} = \begin{bmatrix} \kappa_{xx}^{eq} - \kappa_{xx} \\ \kappa_{yy}^{eq} - \kappa_{yy} \\ \kappa_{xy}^{eq} - \kappa_{xy} \\ \kappa_{xxy}^{eq} - \kappa_{xxy} \\ \kappa_{xyy}^{eq} - \kappa_{xyy} \\ \kappa_{xxyy}^{eq} - \kappa_{xxyy} \end{bmatrix}. \tag{4.39}$$

83

The shift matrix for CLBM reads

$$\mathbb{S} = \begin{bmatrix} 6 & 2 & 0 & 0 & 0 & 0 \\ 6 & -2 & 0 & 0 & 0 & 0 \\ 0 & 0 & -4 & 0 & 0 & 0 \\ -6u_y & -2u_y & 8u_x & -4 & 0 & 0 \\ -6u_x & -2u_x & 8u_y & 0 & -4 & 0 \\ 8+6(u_x^2+u_y^2) & 2(u_y^2-u_x^2) & -16u_xu_y & 8u_y & 8u_x & 4 \end{bmatrix}. \tag{4.40}$$

The equilibrium central moments $\vec{\kappa^{eq}}$ are

$$\begin{bmatrix} \kappa_{xx}^{eq} \\ \kappa_{yy}^{eq} \\ \kappa_{xy}^{eq} \\ \kappa_{xxy}^{eq} \\ \kappa_{xyy}^{eq} \\ \kappa_{xxyy}^{eq} \end{bmatrix} = \begin{bmatrix} \rho c_s^2 \\ \rho c_s^2 \\ 0 \\ 0 \\ 0 \\ \rho c_s^4 \end{bmatrix}. \tag{4.41}$$

Solving the (4.39) one can now obtain relations for the $\vec{k}$

$$\begin{bmatrix} k_4 \\ k_5 \\ k_6 \\ k_7 \\ k_8 \\ k_9 \end{bmatrix} = \begin{bmatrix} \frac{1}{12\tau_3}\left[\rho(u_x^2+u_y^2)-f_6-f_8-f_4-f_2-2(f_5+f_3+f_7+f_1-\rho c_s^2)\right] \\ \frac{1}{4\tau_4}\left[f_8+f_4-f_6-f_2+\rho(u_x^2-u_y^2)\right] \\ \frac{1}{4\tau_5}(f_7+f_3-f_1-f_5-u_xu_y\rho) \\ \frac{-1}{\tau_6}\left\{\left[f_5+f_3-f_7-f_1-2u_x^2u_y\rho+u_y(\rho-f_8-f_4-f_0)\right]/4+ \right. \\ \left. +\frac{u_x}{2}(f_7-f_1-f_5+f_3)\right\}+\frac{u_y}{2}\left(-3k_3-k_4\right)+2u_xk_5 \\ \frac{-1}{\tau_7}\left\{\left[f_3+f_1-f_5-f_7-2u_y^2u_x\rho+u_x(\rho-f_2-f_6-f_0)\right]/4+ \right. \\ \left. +\frac{u_y}{2}(f_7-f_1-f_5+f_3)\right\}+\frac{u_x}{2}\left(-3k_3+k_4\right)+2u_yk_5 \\ \frac{1}{4}\left[\frac{1}{\tau_8}\left(\rho c_s^4-\kappa_{xxyy}\right)-8k_3-6k_4(u_x^2+u_y^2)-2k_4(u_y^2-u_x^2)+\right. \\ \left. +16k_5u_xu_y-8k_6u_y-8k_7u_x\right] \end{bmatrix} \tag{4.42}$$

and use them in the relaxation step (4.37). The reader is referred to [13, 94, 268] for the detailed derivation and implementation details of the CLBM for the fluid flow.

In order to recover the Navier-Stokes equations for fluid flow, we adopt the similar methodology of EPDEs as in the previous section. The Cascaded Lattice Boltzmann Equation for the fluid flow reads

$$f_i(x+c_{i,x}\Delta t, y+c_{i,y}\Delta t, t+\Delta t) = f_i(x,y,t) + \Omega_i = f_i^c(x,y,t), \tag{4.43}$$

where Ω_i is the collision scheme for flow field. The time and space shifted form of

the above equation reads

$$f_i(x + c_{i,x}\Delta t/2, y + c_{i,y}\Delta t/2, t + \Delta t/2) - f_i^c(x - c_{i,x}\Delta t/2, y - c_{i,y}\Delta t/2, t - \Delta t/2) = 0.$$
(4.44)

The Taylor expansion of the above equation reads

$$\sum_{a,b,n=0}^{\infty} \frac{(\Delta t/2)^{a+b+n}}{a!\ b!\ n!} c_{ix}^a c_{iy}^b \partial_x^a \partial_y^b \partial_t^n (f_i - f_i^c(-1)^{a+b+n}) = 0.$$
(4.45)

Transforming f into raw moments m and applying diffusive scaling, the Taylor expansion in moment space reads

$$\sum_{a,b,n=0}^{\infty} \frac{(\epsilon)^{a+b+2n+l}}{a!\ b!\ n!} \partial_x^a \partial_y^b \partial_t^n \left(m_{x^{(\alpha+a)}y^{(\beta+b)}}^{(l)} - m_{x^{(\alpha+a)}y^{(\beta+b)}}^{c(l)}(-1)^{a+b+n} \right) = 0.$$
(4.46)

From the conditions $a + b + 2n + l = 0$ and $a + b + 2n + l = 1$ one can prove [96]

$$m_{x^\alpha y^\beta}^{(0)} = m_{x^\alpha y^\beta}^{c(0)}, \quad m_{x^\alpha y^\beta}^{(1)} = m_{x^\alpha y^\beta}^{c(1)},$$
(4.47)

i.e. for any moment the zeroth (scale invariant part) and first orders are collision invariant (they are equal to their equilibrium).

To recover the divergence free condition we put $a + b + 2n + l = 2$ and $\alpha = \beta = 0$ to obtain

$$\partial_x \bar{m}_x^{(1)} + \partial_y \bar{m}_y^{(1)} = 0$$

and after inserting appropriate equilibria $m_x^{eq} = \rho u_x$, $m_y^{eq} = \rho u_y$ we have

$$\frac{\partial \rho u_x}{\partial x} + \frac{\partial \rho u_y}{\partial y} = 0.$$

The Navier-Stokes momentum equations are obtained at ϵ^3 order ($a+b+2n+l = 3$) and below we derive the equation for u_x only ($\alpha = 1$, $\beta = 0$)

$$m_x^{(3)} - m_x^{c(3)} = -\partial_t \bar{m}_x^{(1)} - \partial_x \bar{m}_{xx}^{(2)} - \partial_y \bar{m}_{xy}^{(2)},$$

where we neglected third order derivatives and second order derivates drop out because of (4.47). The terms $\bar{m}_{xx}^{(2)}$, $\bar{m}_{xy}^{(2)}$ can be recovered from the lower order expansion and collision scheme

$$\bar{m}_{xx}^{(2)} = m_{xx}^{eq(2)} - \left(\tau - \frac{1}{2} \right) (\partial_x \bar{m}_x^{(1)} + \partial_y \bar{m}_{xxy}^{(1)})$$

$$\bar{m}_{xy}^{(2)} = m_{xy}^{eq(2)} - \left(\tau - \frac{1}{2}\right)\left(\partial_x \bar{m}_{xxy}^{(1)} + \partial_y \bar{m}_{xyy}^{(1)}\right)$$

where $\tau = \tau_4 = \tau_5$ and the final form of the EPDE is

$$-F_x^{(3)} = m_x^{(3)} - m_x^{c(3)} = -\partial_t m_x^{eq(1)} - \partial_x m_x^{eq(2)} - \partial_y m_{xy}^{eq(2)}+$$
$$+ \left(\tau - \frac{1}{2}\right)\left(\partial_{xx} m_x^{eq(1)} + \partial_{yy} m_{xyy}^{eq(1)} + 2\partial_{xy} m_{xxy}^{eq(1)}\right).$$

where F_x is a forcing term. Now after inserting equilibria

$$m_x^{eq(1)} = \rho u_x, \; m_{xx}^{eq(2)} = \rho c_s^2 + \rho u_x^2, \; m_{xy}^{eq(2)} = \rho u_x u_y, \; m_{xxy}^{eq(1)} = \rho c_s^2 u_y, \; m_{xyy}^{eq(1)} = \rho c_s^2 u_x$$

the final result is

$$\frac{\partial(\rho u_x)}{\partial t} + \frac{\partial(\rho u_x^2 + p)}{\partial x} + \frac{\partial(\rho u_x u_y)}{\partial y} =$$
$$\left(\tau - \frac{1}{2}\right)\left(\frac{\partial^2(\rho u_x)}{\partial x^2} + c_s^2 \frac{\partial^2(\rho u_x)}{\partial y^2} + 2c_s^2 \frac{\partial^2(\rho u_y)}{\partial x \partial y}\right) \tag{4.48}$$

The above equation is the incompressible Navier-Stokes equation for u_x and similarly we can obtain the equation for u_y.

4.3.3 Boundary Conditions

For different problems, different boundary conditions are needed. Basic boundary conditions for fluid flow are inlet, outlet, wall, symmetry and periodic. There are many different techniques how to implement these types of boundary conditions for the fluid flow [110, 274, 302]. For thermal problems we can have boundary conditions of first kind (Dirichlet type i.e. given temperature), second kind (Neumann type i.e. the normal derivative of temperature is given) and third kind (equal temperatures and heat fluxes on the both sides of interfaces).

In the present work, solid walls are treated with bounce-back boundary conditions located half-way, that results in no-slip conditions for velocity field and adiabatic conditions for the heat transfer

$$f_{\bar{i}}(\vec{x}_b, t+1) = f_i^c(\vec{x}_b, t), \quad g_{\bar{i}}(\vec{x}_b, t+1) = g_i^c(\vec{x}_b, t),$$

where $\vec{x}_b$ is wall adjacent fluid site, $f_{\bar{i}}$ and $g_{\bar{i}}$ correspond to DFs which characteristic velocity points in reflected direction i.e. $\vec{c}_{\bar{i}} = -\vec{c}_i$. In the case of a non-adiabatic fluid-solid interface (third kind boundary condition), no bounce-back is applied to the g_i in order to allow heat flowing through this interface.

For inlet and first kind thermal boundary conditions we use the equilibrium both

for velocity and temperature fields i.e.

$$f_i(\vec{x}_{in/d}, t) = f_i^{\text{eq}}(\rho_{\text{in}}, \vec{u}_{\text{in}}) \quad g_i(\vec{x}_{in/d}, t) = g_i^{\text{eq}}(T_{\text{in/d}}),$$

where $\vec{x}_{in/d}$ is the location of inlet or Dirichlet temperature boundary condition.

Outlet is modeled by first-order extrapolation

$$f_i(\vec{x}_{out}, t+1) = f_i^c(\vec{x}_{out} - \vec{n}, t), \quad g_i(\vec{x}_{out}, t+1) = g_i^c(\vec{x}_{out} - \vec{n}, t)$$

where $\vec{x}_{out}$ is location of the outlet, $\vec{n}$ is outer normal and i is equal to directions that are pointing to the inside of the domain.

Periodic boundaries are easy to implement because the outgoing DFs are directly shifted to the appropriate incoming DFs and symmetry boundary conditions are realized through mirroring the DFs with respect to the symmetry axis [274].

4.3.4 Physical and Lattice Units Conversions

All previous equations contain parameters and quantities expressed in lattice units. In order to relate obtained numerical results to physical units (here denoted with subscript p), we need to establish relationships between lattice and physical units. Analysis is based on dimensionless numbers appropriate for the problem solved. In our case we need Reynolds (Re), Prandtl (Pr) or Peclet (Pe) numbers to setup LBM and extract useful information from the simulations. From the previous theory we see that we have only two[4] parameters which directly occur in the equations

- ω_f - relaxation frequency for the fluid field lattice related to lattice viscosity ν.

- ω_g - relaxation frequency for the temperature field lattice related to thermal diffusivity α.

Another parameter is the number of lattice sites N used to resolve characteristic length L, which also defines the lattice step size $dx = \frac{L}{N}$. Now by knowing Re (given or computed based on characteristic velocity U and length L or time t_C and kinematic viscosity ν_p) we can compute the lattice viscosity from

$$\frac{UL}{\nu_p} = \frac{L^2}{t_C \nu_p} = Re_p = Re_{lb} = \frac{U_{lb} N}{\nu} = \frac{N^2}{t_{C,lb} \nu}, \tag{4.49}$$

where U_{lb} is characteristic velocity in lattice units which is related to the time step for the non-stationary problems and must be kept below certain value (usually equals

---

[4]Parameter a from the expressions for the g_i^{eq} has no relation to the physics and is pure numerical parameter like e.g. Courant-Friedrichs-Lewy (CFL) number.

to $0.3c_s$ i.e. subsonic flow regime for which LBM was derived) to maintain stability of the solver. $t_{C,lb}$ is the number of iterations needed for LBM to reach the physical characteristic time. The time step (i.e. physical time simulated by one iteration of the LBM algorithm) can be evaluated based on given parameters as e.g.

$$\mathrm{d}t = \frac{t_C}{t_{C,lb}} = \frac{U_{lb}L}{UN} = \frac{\nu}{\nu_p}\mathrm{d}x^2.$$

For thermal problems with forced convection we can use Prandtl number to relate thermal diffusivity in physical and lattice units

$$\frac{\nu_p}{\alpha_p} = Pr_p = Pr_{lb} = \frac{\nu}{\alpha}$$

and thermal diffusivity for solids are then defined by known ratios of fluid and solids' diffusivities.

Other quantities like velocity and temperature are then nondimensionalized

$$u_{lb} = \frac{U_{lb}}{U}u,$$

$$T_{lb} = \frac{T - T_c}{T_h - T_c},$$

where T_h and T_c are "hot" and "cold" temperatures.

4.4 Numerical Simulations

Results presented in the following text were obtained from the C code implementation of the BGK, MRT, CLBM and CTLBM using CUDA framework [59, 268] and simulations were performed with double precision on NVIDIA Geforce TITAN Z cards. Square D_2Q_5 and D_2Q_9 lattices were used. In all simulations $\omega_4 = \omega_5 = 1$. All values in the following text is expressed in lattice or non-dimensional units.

4.4.1 Advection and Diffusion of Sine Wave

First problem used to validate the proposed CTLBM is 1D advection and diffusion of the sine wave on the unit periodic domain with given advection velocity U and diffusion coefficient D. Initial condition is described by

$$\phi(x, 0) = \frac{1}{2}\left[1 + \sin\left(2\pi Kx\right)\right] \quad x \in [0, 1],$$

where K is the wave mode. PDE governing the evolution of ϕ is

$$\frac{\partial \phi}{\partial t} + \frac{\partial \phi U}{\partial x} = D \frac{\partial^2 \phi}{\partial x^2}.$$

The analytical solution to the above problem is known and reads

$$\phi_a(x,t) = \frac{1}{2} \left[1 + \exp\left(-D(2\pi K)^2 t\right) \sin\left(2\pi K \left(x - Ut\right)\right) \right].$$

Numerical solutions $\phi_n(x,t)$ are computed for $K = 1$, $U = 1$, $L = 1$ and Peclet numbers between 10^2 and 10^6. Lattice size starts with resolution of $N = 64$ and is doubled up to $N = 1024$. The solution is computed until the initial amplitude of the sine wave decrease to one half or until $t_{\text{stop}} = 100s$ of physical time for Pe $> 10^4$. In all simulations the time step was equal to $\mathrm{d}x^2$. BGK and three different MRT methods are compared, our proposed CTLBM, the Yoshida et al. [309] and the Mezrhab et al. [204]. Errors in L_∞, L_1 and L_2 norms together with measured experimental order of convergence (EOC) are given in Tables. 4.1, 4.2 and 4.3. Errors are computed as follows

$$E_\infty = \max_{x \in \{0,\ldots,N-1\}} |\phi_a(x, t_{\text{stop}}) - \phi_n(x, t_{\text{stop}})|,$$

$$E_1 = \sum_{x=0}^{N-1} |\phi_a(x, t_{\text{stop}}) - \phi_n(x, t_{\text{stop}})|,$$

$$E_2 = \sqrt{\sum_{x=0}^{N-1} |\phi_a(x, t_{\text{stop}}) - \phi_n(x, t_{\text{stop}})|^2}.$$

The EOC is then computed as

$$EOC = \frac{\ln\left(\frac{E(N_h)}{E(N_l)}\right)}{\ln\left(\frac{N_l}{N_h}\right)},$$

where $N_h > N_l$ are the consecutive lattice sizes.

Lattice thermal diffusivity was setup using Peclet number

$$\frac{UL}{\alpha_p} = \text{Pe}_p = \text{Pe}_{lb} = \frac{U_{lb}N}{\alpha},$$

where U_{lb} was set to fulfill the diffusive scaling $\mathrm{d}t = \mathrm{d}x^2$, parameter a from (4.35) is set equal to 0.66657 to improve numerical results. Plot with CTLBM and analytical solutions are presented in Fig. 4.1. In Fig. 4.2 E_∞ error for one case of the CTLBM simulation is depicted. From the obtained results we can conclude that all methods are of second order regard to the L_∞ norm and a spatial step.

N	E_∞ BGK	EOC	E_∞ CTLBM	EOC	E_∞ Mezrhab et al. [204]	EOC	E_∞ Yoshida et al. [309]	EOC
$Pe = 10^2$								
64	$2.12 \cdot 10^{-4}$		$1.96 \cdot 10^{-4}$		$3.87 \cdot 10^{-4}$		$3.16 \cdot 10^{-4}$	
128	$5.29 \cdot 10^{-5}$	1.9992	$4.90 \cdot 10^{-5}$	1.999	$9.68 \cdot 10^{-5}$	1.9975	$7.93 \cdot 10^{-5}$	1.9941
256	$1.32 \cdot 10^{-5}$	1.9997	$1.23 \cdot 10^{-5}$	1.9997	$2.42 \cdot 10^{-5}$	1.9996	$1.98 \cdot 10^{-5}$	1.9984
512	$3.31 \cdot 10^{-6}$	2.0000	$3.06 \cdot 10^{-6}$	1.9999	$6.05 \cdot 10^{-6}$	1.9998	$4.96 \cdot 10^{-6}$	1.9996
102 4	$8.27 \cdot 10^{-7}$	2.0000	$7.66 \cdot 10^{-7}$	2.0	$1.51 \cdot 10^{-6}$	2.0	$1.24 \cdot 10^{-6}$	1.9999
$Pe = 10^3$								
64	$2.13 \cdot 10^{-4}$		$2.11 \cdot 10^{-4}$		$8.33 \cdot 10^{-3}$		$3.21 \cdot 10^{-4}$	
128	$5.33 \cdot 10^{-5}$	1.9984	$5.28 \cdot 10^{-5}$	1.999	$2.08 \cdot 10^{-3}$	1.9992	$8.34 \cdot 10^{-5}$	1.9445
256	$1.33 \cdot 10^{-5}$	1.9998	$1.32 \cdot 10^{-5}$	1.9996	$5.21 \cdot 10^{-4}$	2.0001	$2.11 \cdot 10^{-5}$	1.9851
512	$3.33 \cdot 10^{-6}$	1.9999	$3.30 \cdot 10^{-6}$	1.9999	$1.30 \cdot 10^{-4}$	2.0	$5.28 \cdot 10^{-6}$	1.9963
1024	$8.32 \cdot 10^{-7}$	2.0000	$8.26 \cdot 10^{-7}$	2.0	$3.25 \cdot 10^{-5}$	2.0	$1.32 \cdot 10^{-6}$	1.9991
$Pe = 10^4$								
64	$2.16 \cdot 10^{-4}$		$2.12 \cdot 10^{-4}$		unstable		$3.26 \cdot 10^{-4}$	
128	$5.33 \cdot 10^{-5}$	2.0163	$5.35 \cdot 10^{-5}$	1.9887	$2.20 \cdot 10^{-2}$		$7.56 \cdot 10^{-5}$	2.1056
256	$1.33 \cdot 10^{-5}$	2.0010	$1.34 \cdot 10^{-5}$	1.9944	$5.50 \cdot 10^{-3}$	1.9998	$2.06 \cdot 10^{-5}$	1.8778
512	$3.33 \cdot 10^{-6}$	1.9994	$3.36 \cdot 10^{-6}$	1.9984	$1.38 \cdot 10^{-3}$	1.9999	$5.27 \cdot 10^{-6}$	1.9643
1024	$8.32 \cdot 10^{-7}$	2.0005	$8.41 \cdot 10^{-7}$	1.9996	$3.44 \cdot 10^{-4}$	2.0	$1.33 \cdot 10^{-6}$	1.9907
$Pe = 10^5$								
64	$3.89 \cdot 10^{-4}$		$3.87 \cdot 10^{-4}$		unstable		unstable	
128	$9.69 \cdot 10^{-5}$	2.0047	$9.70 \cdot 10^{-5}$	1.9954	unstable		unstable	
256	$2.42 \cdot 10^{-5}$	2.0004	$2.43 \cdot 10^{-5}$	1.998	$6.06 \cdot 10^{-3}$		$2.28 \cdot 10^{-5}$	
512	$6.05 \cdot 10^{-6}$	1.9998	$6.08 \cdot 10^{-6}$	1.9994	$1.52 \cdot 10^{-3}$	2.0	$5.98 \cdot 10^{-6}$	1.9335
1024	$1.51 \cdot 10^{-6}$	2.0002	$1.52 \cdot 10^{-6}$	1.9998	$3.79 \cdot 10^{-4}$	2.0	$1.51 \cdot 10^{-6}$	1.9838
$Pe = 10^6$								
64	$3.99 \cdot 10^{-4}$		$4.0 \cdot 10^{-4}$		unstable		unstable	
128	$1.00 \cdot 10^{-4}$	1.9969	$1.0 \cdot 10^{-4}$	1.9954	unstable		unstable	
256	$2.50 \cdot 10^{-5}$	2.0004	$2.51 \cdot 10^{-5}$	1.998	unstable		unstable	
512	$6.25 \cdot 10^{-6}$	1.9998	$6.28 \cdot 10^{-6}$	1.9994	unstable		$6.16 \cdot 10^{-6}$	
1024	$1.56 \cdot 10^{-6}$	2.0002	$1.57 \cdot 10^{-6}$	1.9998	$3.93 \cdot 10^{-4}$		$1.56 \cdot 10^{-6}$	1.9835

Tabela 4.1: E_∞ and EOC for the advection and diffusion of the sine wave.

N	E_1 BGK	EOC	E_1 CTLBM	EOC	E_1 Mezrhab et al. [204]	EOC	E_1 Yoshida et al. [309]	EOC
$Pe = 10^2$								
64	$8.62 \cdot 10^{-3}$		$7.98 \cdot 10^{-3}$		$1.58 \cdot 10^{-2}$		$1.29 \cdot 10^{-2}$	
128	$4.31 \cdot 10^{-3}$	0.9987	$3.99 \cdot 10^{-3}$	0.9987	$7.89 \cdot 10^{-3}$	0.999	$6.46 \cdot 10^{-3}$	0.994
256	$2.16 \cdot 10^{-3}$	0.9999	$2.00 \cdot 10^{-3}$	0.9998	$3.95 \cdot 10^{-3}$	0.9994	$3.23 \cdot 10^{-3}$	0.9986
512	$1.08 \cdot 10^{-3}$	0.9999	$9.99 \cdot 10^{-4}$	0.9999	$1.97 \cdot 10^{-3}$	0.9999	$1.62 \cdot 10^{-3}$	0.9996
1024	$5.39 \cdot 10^{-4}$	1.0000	$4.99 \cdot 10^{-4}$	1.0	$9.86 \cdot 10^{-4}$	1.0	$8.09 \cdot 10^{-4}$	0.9999
$Pe = 10^3$								
64	$8.68 \cdot 10^{-3}$		$8.6 \cdot 10^{-3}$		0.340		$1.31 \cdot 10^{-2}$	
128	$4.34 \cdot 10^{-3}$	1.0001	$4.31 \cdot 10^{-3}$	0.9989	0.17	1.0011	$6.8 \cdot 10^{-3}$	0.9444
256	$2.17 \cdot 10^{-3}$	0.9996	$2.15 \cdot 10^{-3}$	0.9998	$8.49 \cdot 10^{-2}$	1.0001	$3.43 \cdot 10^{-3}$	0.9857
512	$1.09 \cdot 10^{-3}$	1.0000	$1.08 \cdot 10^{-3}$	1.0	$4.24 \cdot 10^{-2}$	1.0001	$1.72 \cdot 10^{-3}$	0.9963
1024	$5.43 \cdot 10^{-4}$	1.0000	$5.38 \cdot 10^{-4}$	1.0	$2.12 \cdot 10^{-2}$	1.0	$8.61 \cdot 10^{-4}$	0.9991
$Pe = 10^4$								
64	$8.78 \cdot 10^{-3}$		$8.67 \cdot 10^{-3}$		unstable		$1.33 \cdot 10^{-2}$	
128	$4.34 \cdot 10^{-3}$	1.0153	$4.36 \cdot 10^{-3}$	0.9911	1.79		$6.17 \cdot 10^{-3}$	1.1073
256	$2.17 \cdot 10^{-3}$	1.0007	$2.19 \cdot 10^{-3}$	0.9941	0.897	0.9997	$3.35 \cdot 10^{-3}$	0.8781
512	$1.09 \cdot 10^{-3}$	0.9999	$1.1 \cdot 10^{-3}$	0.9984	0.449	1.0001	$1.72 \cdot 10^{-3}$	0.9643
1024	$5.43 \cdot 10^{-4}$	1.0002	$5.48 \cdot 10^{-4}$	0.9996	0.224	1.0	$8.65 \cdot 10^{-4}$	0.9908
$Pe = 10^5$								
64	$1.59 \cdot 10^{-2}$		$1.58 \cdot 10^{-2}$		unstable		unstable	
128	$7.89 \cdot 10^{-3}$	1.0071	$7.91 \cdot 10^{-3}$	0.9973	unstable		unstable	
256	$3.95 \cdot 10^{-3}$	1.0001	$3.96 \cdot 10^{-3}$	0.998	0.988		$3.72 \cdot 10^{-3}$	
512	$1.97 \cdot 10^{-3}$	0.9999	$1.98 \cdot 10^{-3}$	0.9994	0.494	1.0	$1.95 \cdot 10^{-3}$	0.9335
1024	$9.86 \cdot 10^{-4}$	1.0001	$9.9 \cdot 10^{-4}$	0.9998	0.247	1.0	$9.86 \cdot 10^{-4}$	0.9838
$Pe = 10^6$								
64	$1.63 \cdot 10^{-2}$		$1.63 \cdot 10^{-2}$		unstable		unstable	
128	$8.15 \cdot 10^{-3}$	0.9994	$8.17 \cdot 10^{-3}$	0.9974	unstable		unstable	
256	$4.08 \cdot 10^{-3}$	1.0001	$4.09 \cdot 10^{-3}$	0.998	unstable		unstable	
512	$2.04 \cdot 10^{-3}$	0.9999	$2.05 \cdot 10^{-3}$	0.9994	unstable		$2.01 \cdot 10^{-3}$	
1024	$1.02 \cdot 10^{-3}$	1.0001	$1.02 \cdot 10^{-3}$	0.9999	0.256		$1.02 \cdot 10^{-3}$	0.9835

Tabela 4.2: E_1 and EOC for the advection and diffusion of the sine wave.

N	E_2 BGK	EOC	E_2 CTLBM	EOC	E_2 Mezrhab et al. [204]	EOC	E_2 Yoshida et al. [309]	EOC
$\mathrm{Pe}=10^2$								
64	$1.20{\cdot}10^{-3}$		$1.11{\cdot}10^{-3}$		$2.19{\cdot}10^{-3}$		$1.79{\cdot}10^{-3}$	
128	$4.24{\cdot}10^{-4}$	1.4992	$3.92{\cdot}10^{-4}$	1.499	$7.74{\cdot}10^{-4}$	1.4984	$6.34{\cdot}10^{-4}$	1.4942
256	$1.50{\cdot}10^{-4}$	1.4998	$1.39{\cdot}10^{-4}$	1.4998	$2.74{\cdot}10^{-4}$	1.4996	$2.25{\cdot}10^{-4}$	1.4985
512	$5.30{\cdot}10^{-5}$	1.4999	$4.9{\cdot}10^{-5}$	1.4999	$9.68{\cdot}10^{-5}$	1.4999	$7.94{\cdot}10^{-5}$	1.4996
1024	$1.87{\cdot}10^{-5}$	1.5000	$1.73{\cdot}10^{-5}$	1.5	$3.42{\cdot}10^{-5}$	1.5	$2.81{\cdot}10^{-5}$	1.4999
$\mathrm{Pe}=10^3$								
64	$1.20{\cdot}10^{-3}$		$1.19{\cdot}10^{-3}$		$4.72{\cdot}10^{-2}$		$1.82{\cdot}10^{-3}$	
128	$4.26{\cdot}10^{-4}$	1.4994	$4.23{\cdot}10^{-4}$	1.4991	$1.67{\cdot}10^{-2}$	1.5006	$6.68{\cdot}10^{-4}$	1.4445
256	$1.51{\cdot}10^{-4}$	1.4998	$1.49{\cdot}10^{-4}$	1.4997	$5.89{\cdot}10^{-3}$	1.5001	$2.38{\cdot}10^{-4}$	1.4855
512	$5.33{\cdot}10^{-5}$	1.4999	$5.28{\cdot}10^{-5}$	1.4999	$2.08{\cdot}10^{-3}$	1.5	$8.45{\cdot}10^{-5}$	1.4963
1024	$1.88{\cdot}10^{-5}$	1.5000	$1.87{\cdot}10^{-5}$	1.5	$7.36{\cdot}10^{-4}$	1.5	$2.99{\cdot}10^{-5}$	1.4991
$\mathrm{Pe}=10^4$								
64	$1.22{\cdot}10^{-3}$		$1.20{\cdot}10^{-3}$		unstable		$1.84{\cdot}10^{-3}$	
128	$4.26{\cdot}10^{-4}$	1.5163	$4.28{\cdot}10^{-4}$	1.4902	0.176		$6.05{\cdot}10^{-4}$	1.6068
256	$1.51{\cdot}10^{-4}$	1.5009	$1.52{\cdot}10^{-4}$	1.4944	$6.23{\cdot}10^{-2}$	1.4998	$2.33{\cdot}10^{-4}$	1.378
512	$5.33{\cdot}10^{-5}$	1.4998	$5.38{\cdot}10^{-5}$	1.4984	$2.2{\cdot}10^{-2}$	1.5	$8.44{\cdot}10^{-5}$	1.4643
1024	$1.88{\cdot}10^{-5}$	1.5002	$1.9{\cdot}10^{-5}$	1.4996	$7.78{\cdot}10^{-3}$	1.5	$3.0{\cdot}10^{-5}$	1.4908
$\mathrm{Pe}=10^5$								
64	$2.20{\cdot}10^{-3}$		$2.19{\cdot}10^{-3}$		unstable		unstable	
128	$7.75{\cdot}10^{-4}$	1.5063	$7.76{\cdot}10^{-4}$	1.4967	unstable		unstable	
256	$2.74{\cdot}10^{-4}$	1.5004	$2.75{\cdot}10^{-4}$	1.498	$6.86{\cdot}10^{-2}$		$2.58{\cdot}10^{-4}$	
512	$9.69{\cdot}10^{-5}$	1.4999	$9.72{\cdot}10^{-5}$	1.4994	$2.42{\cdot}10^{-2}$	1.5	$9.57{\cdot}10^{-5}$	1.4335
1024	$3.42{\cdot}10^{-5}$	1.5001	$3.44{\cdot}10^{-5}$	1.4999	$8.57{\cdot}10^{-3}$	1.5	$3.42{\cdot}10^{-5}$	1.4838
$\mathrm{Pe}=10^6$								
64	$2.26{\cdot}10^{-3}$		$2.26{\cdot}10^{-3}$		unstable		unstable	
128	$8.01{\cdot}10^{-4}$	1.4985	$8.02{\cdot}10^{-4}$	1.4967	unstable		unstable	
256	$2.83{\cdot}10^{-4}$	1.5004	$2.84{\cdot}10^{-4}$	1.498	unstable		unstable	
512	$1.00{\cdot}10^{-4}$	1.4999	$1.0{\cdot}10^{-4}$	1.4994	unstable		$9.85{\cdot}10^{-5}$	
1024	$3.54{\cdot}10^{-5}$	1.5001	$3.55{\cdot}10^{-5}$	1.4999	$8.89{\cdot}10^{-3}$		$3.52{\cdot}10^{-5}$	1.4835

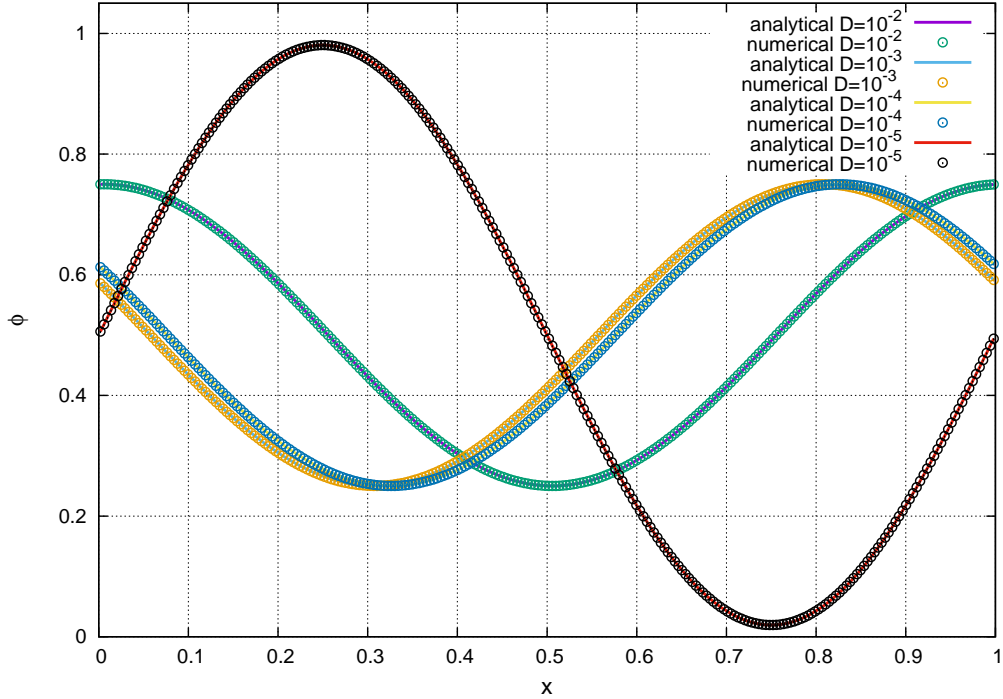Tabela 4.3: E_2 and EOC for the advection and diffusion of the sine wave.

Figura 4.1: Comparison of analytical and numerical solutions (CTLBM) of advection-diffusion of sine wave for $N = 256$, $U = 1$, $K = 1$.
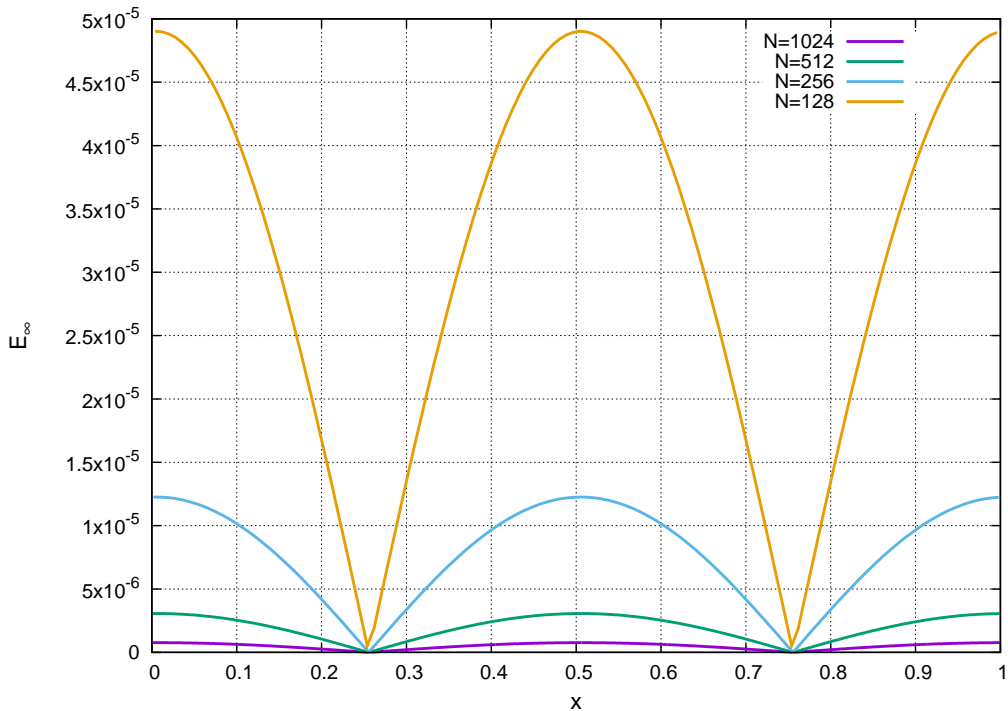
Figura 4.2: Errors of numerical solutions (CTLBM) of advection-diffusion of sine wave for Pe $=10^2$, $U = 1$, $K = 1$, $N = 128 - 1024$.

4.4.2 Forced Cooling of Cylinder with Heated Core

Next problem we want to solve is the forced convective cooling of a cylinder with a heated core. The problem involves curved boundary and we are aware that simple staircase approximation of the fluid-solid interface may produce inaccuracies, however the point here is to show performance of the CTLBM. Geometry of the problem is presented in Fig. 4.3. Core of the cylinder is kept at constant temperature $T_h = 1$. At inlet, uniform flow at $U_0 = 0.05$ and $T_c = 1/3$ is maintained. For inlet, equilibrium boundary conditions for f_i and g_i are used, outlet is modeled by extrapolation and top and bottom boundaries are periodic. For all simulations we keep Re $= 40$ and Pr $= 0.72$. Lattice viscosity is then computed from Re as

$$\nu = \frac{U_0 D}{Re},$$

where D is the number of lattice sites used to resolve the diameter of the cylinder. In our simulations we used $D = 128$. Ratios of thermal diffusivities used in simulations are $\alpha_s/\alpha_f \in \{0.5, 1, 4, 20\}$. CTLBM parameter was set to $a = \frac{2}{3}$. The simulations were run until the change in the center-line temperature was less than 10^{-6} (reached
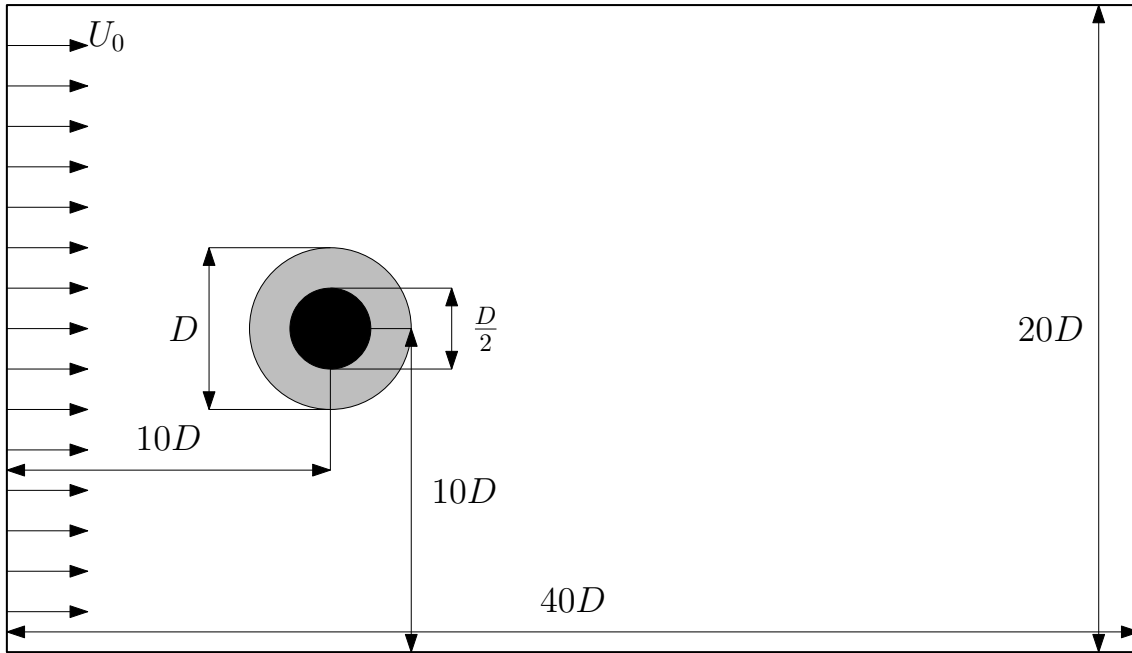
Figura 4.3: Geometry of the problem with forced cooling of the cylinder with a heated core [275].

steady-state condition). In Fig. 4.4 velocity contours and the temperature profile for the case $\alpha_s/\alpha_f = 20$ are shown. In Fig. 4.5 the interface temperature computed by the CTLBM is compared with those from literature [275]. To validate the velocity profile, normalized wake length was measured and found to be $\bar{L} = \frac{L}{D} = 2.28$ which is consistent with the experimental values from the literature [27].
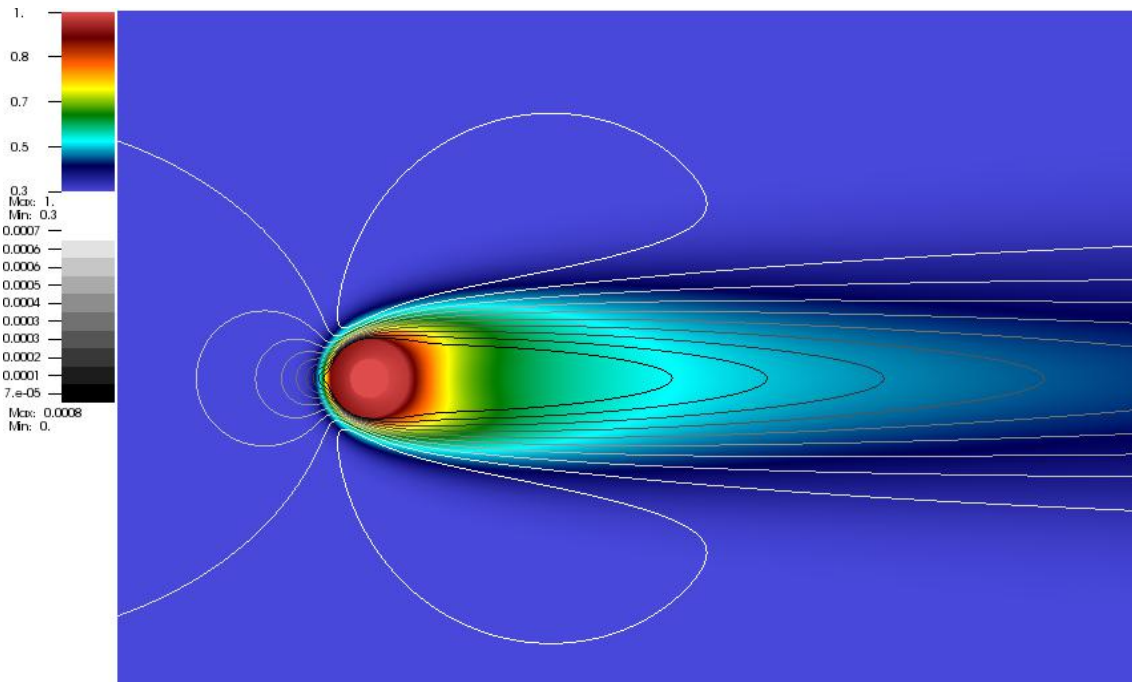
Figura 4.4: Computed temperature field around the cylinder for the $\alpha_s/\alpha_f = 20$ case, $U_0 = 0.05$, $D = 128$, $\mathrm{Re} = 40$, $\mathrm{Pr} = 0.72$, $T_h = 1$ and $T_c = 1/3$. Contours of the velocity magnitude are also rendered.
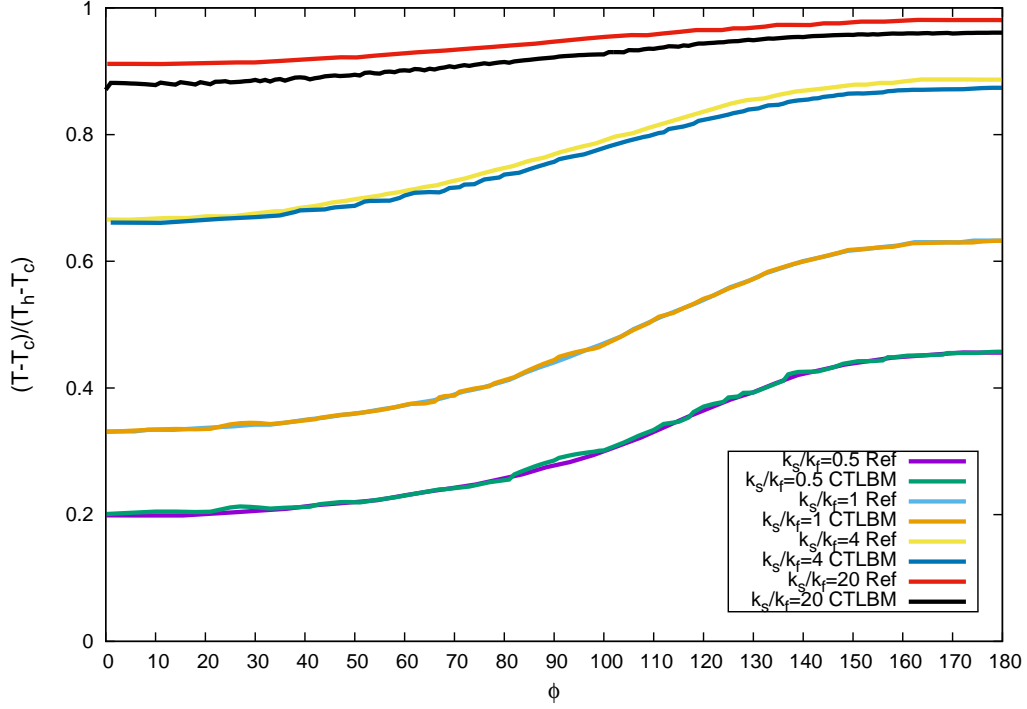
Figura 4.5: Comparison of temperature profile along the fluid-solid interface of the cylinder from the upstream stagnation point ($\phi \in [0, 180]$) with that given in [275]. Four different ratios of α_s and α_f are shown. Errors for the $\alpha_s/\alpha_f = 20$ case are less than 5%.

4.4.3   Forced Cooling of Hot Tubes

Next problem we show here is the forced convective cooling of hot tubes arranged in a row. We simulate subcritical flow regime i.e. laminar but with vortex street instabilities in order to check the numerical stability of the BGK and MRT algorithms and compare them to the proposed CTLBM. Cylinders are kept at the constant temperature $T_h = 1$ and at inlet the temperature $T_c = 1/3$ is also fixed. The Reynolds and Prandtl numbers are set to Re $= 1600^5$, Pr $= 0.72$, lattice resolution of the cylinder diameter is $D = 32$ and computational domain has resolution of $N_x = 640$ and $N_y = 128$ lattice sites per x and y directions respectively. Geometry of the problem is shown in Fig. 4.6.

---

[5]Reynolds number is defined based on D and U_0 in lattice units as in the previous section.
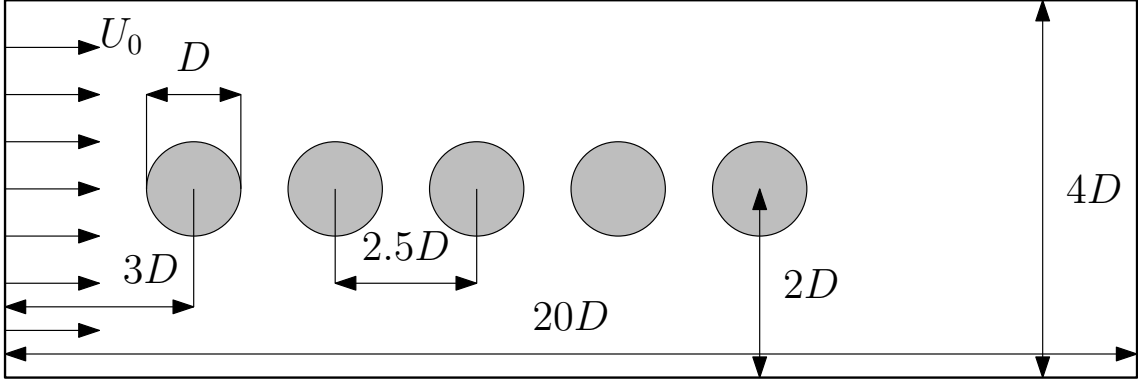
Figura 4.6: Geometry of the problem with hot tubes in a row.

Boundary conditions are the same as in the previous section, we have inlet at the left side, outlet at the right side and periodic conditions on the top and bottom of the domain. Parameter a for the CTLBM is set to $a = \frac{1}{2}$. We want to find maximal U_0 (i.e. time step) for which the computations stay numerically stable while keeping fixed lattice resolution. We started with $U_0 = 0.05$ and performed simulations down to $U_0 = 0.001$ with following results: BGK & CTLBM are numerically stable for $U_0 \leq 0.05$[6], Yoshida et al. [309] algorithm is numerically stable for $U_0 \leq 0.01$ and Mezrhab et al. [204] algorithm is numerically stable for $U_0 \leq 0.005$. For the case of Yoshida et al. and Mezrhab et al. algorithms, severe oscillatory artifacts (strong under- and over-shoots in the temperature field) occur during the simulations but the simulation can survive them. These oscillations emerged in vortexes and at the solid-fluid boundary and are related to the boundary approximations used in this work. Instant temperature fields for the case with $U_0 = 0.001$ at lattice time $t_{lb} = 6.4 \cdot 10^5$ are presented in Fig. 4.7. Time averaged temperature profiles for the same number of iterations are presented in Fig. 4.8 (physical times reached by the last iteration differ, and is the biggest for the BGK & CTLBM) and time averaged profiles for the same physical time of the last iteration are presented in Fig. 4.9 (numbers of iterations performed by the solver differ and is the lowest for the BGK & CTLBM). The characteristic time $t_{C,lb}$ is computed from (4.49) and when the physical viscosity is known (e.g. set to $\nu_p = 1.568 \cdot 10^{-5}$ m/s^2 which means that we use the air to cool the cylinders) one can also compute the physical time and characteristic time in seconds from (4.49). The U_0 in two latter cases is set to the maximal value which ensures the numerical stability for the given solver and four algorithms are compared in those figures.

As the numerical stability regarding the time step of the BGK & CTLBM in this case is the same (and limited by numerical stability of the fluid flow solver) we performed another numerical test for the case of higher Prandtl number. The following different values of parameters were used: Pr = 7.2, $U_{0,lb} = 0.01$, $t_{lb} = 8 \cdot 10^4$,

---

[6]Which is the limit for the numerical stability of the fluid flow solver.

the rest of the parameters is the same as in previous simulations. The results are depicted in Fig. 4.10.
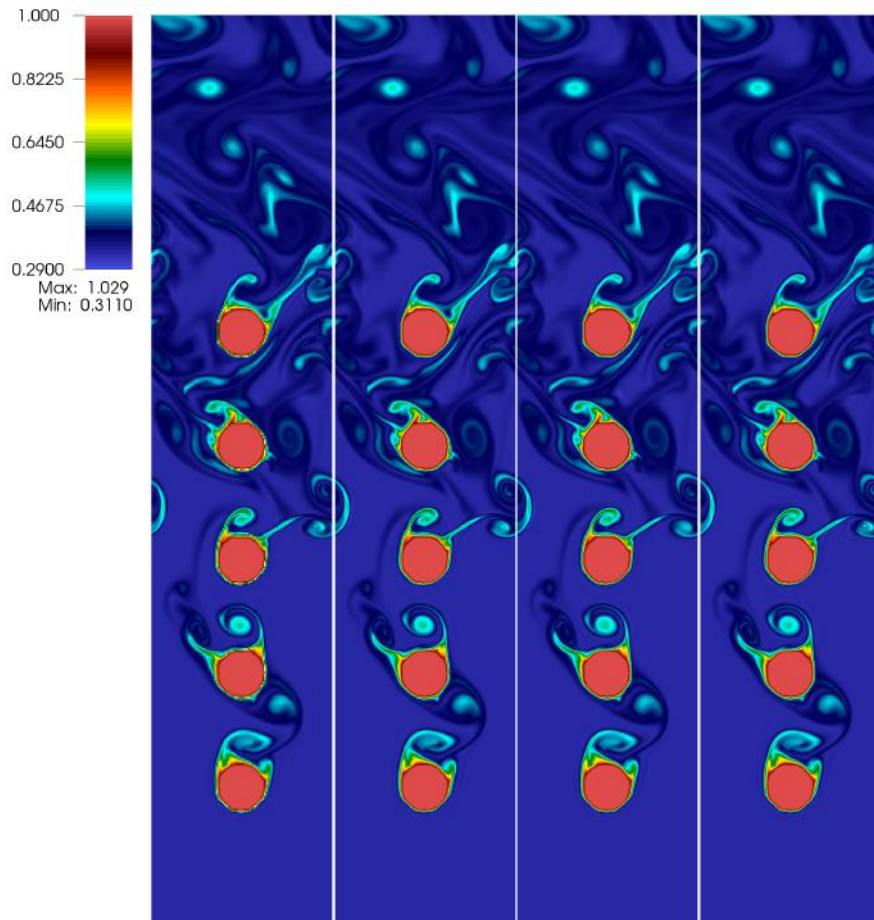

Figura 4.7: Comparison of instant temperature profiles for the different LBM algorithms. Results from left to right: BGK, CTLBM, Mezrhab et al. [204], Yoshida et al. [309]. Parameters setup: $U_0 = 0.001$, $D = 32$, Re= 1600, Pr= 0.72, $a = 0.5$, $t_{lb} = 6.4 \cdot 10^5$
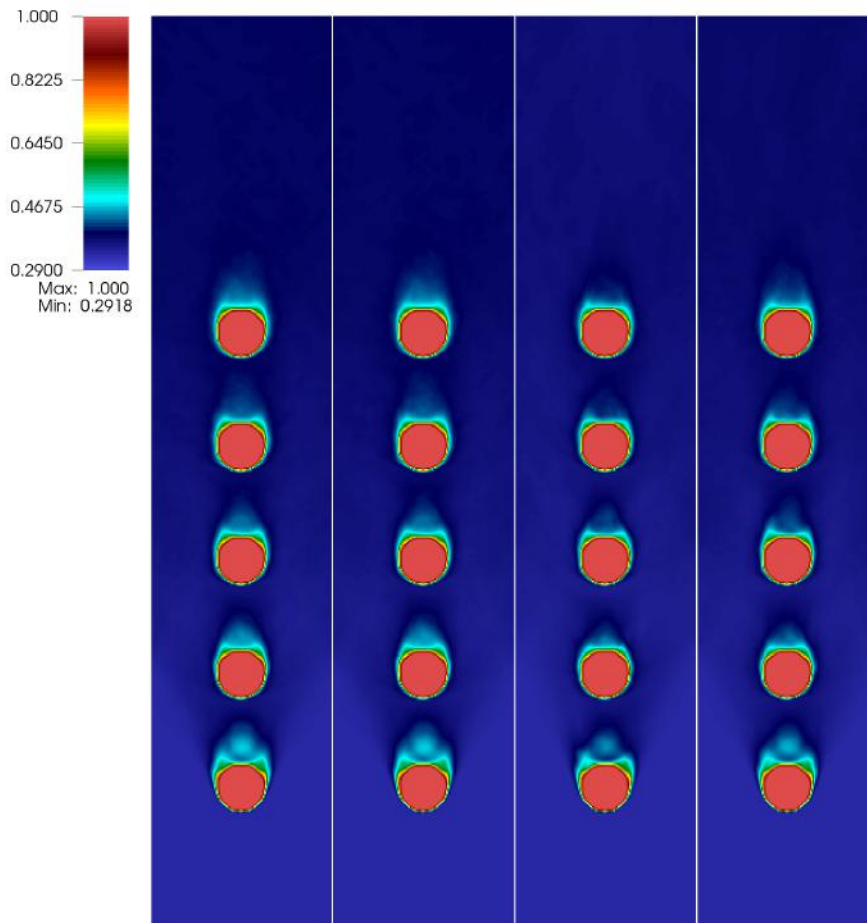
Figura 4.8: Comparison of time averaged temperature profiles for the different LBM algorithms and the same number of iterations. Results from left to right: BGK, CTLBM, Mezrhab et al. [204], Yoshida et al. [309]. Parameters setup: $D = 32$, Re= 1600, Pr= 0.72, $a = 0.5$, $t_{lb} = 6.4 \cdot 10^5$
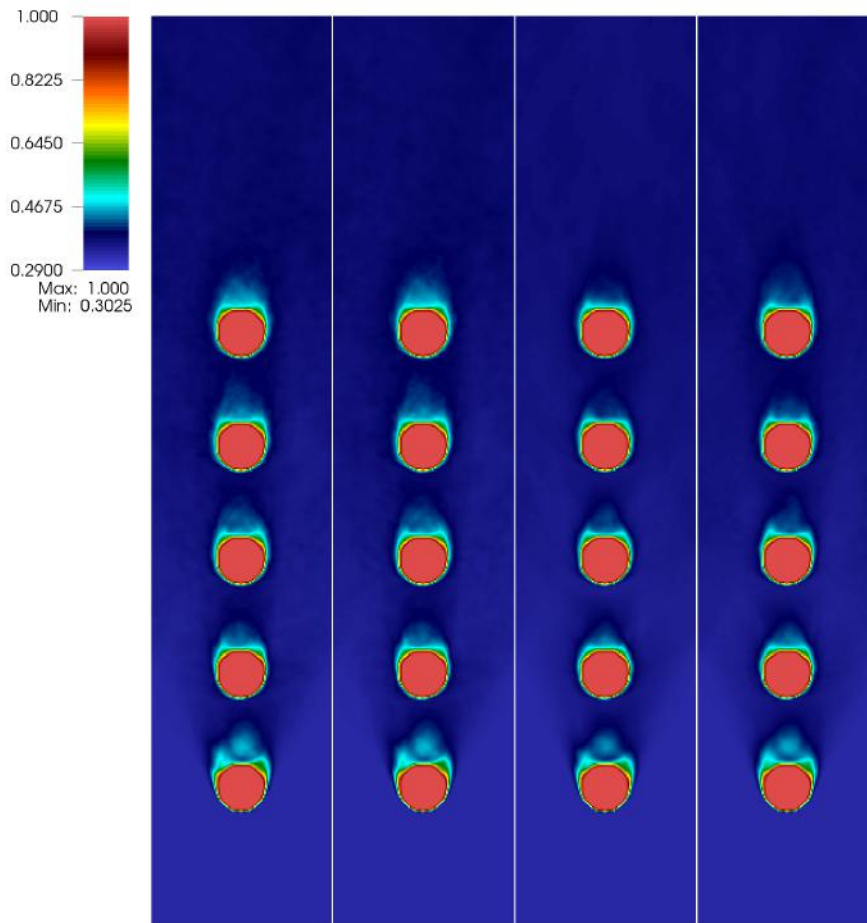
Figura 4.9: Comparison of time averaged temperature profiles for the different LBM algorithms and the same physical time of the last iteration. Results from left to right: BGK, CTLBM, Mezrhab et al. [204], Yoshida et al. [309]. Parameters setup: $D = 32$, Re= 1600, Pr= 0.72, $a = 0.5$, $t_{lb} = 100 t_{C,lb}$.
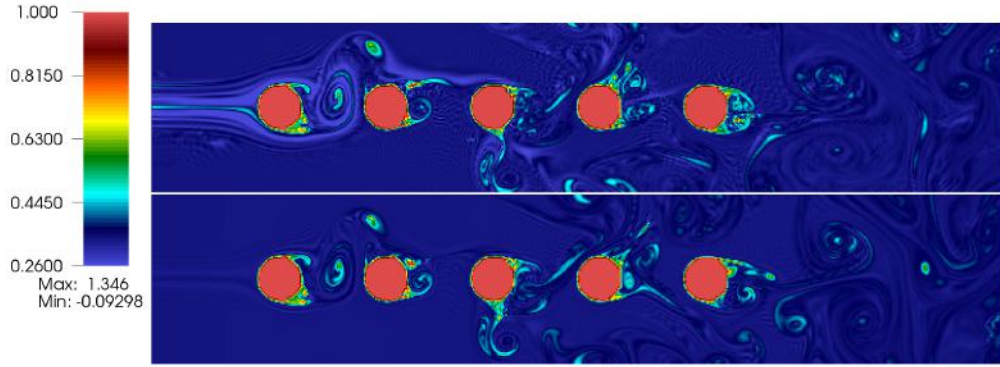
Figura 4.10: Comparison of instant temperature profiles for the BGK (top) & CTLBM (bottom) algorithms for higher Prandtl number. Parameters setup: $D = 32$, Re= 1600, Pr= 7.2, $a = 0.5$, $t_{lb} = 8 \cdot 10^8$.

4.4.4 Double shear layer flow

Motivated by the numerical stability limits of the LBM schemes from the previous subsection, we also investigated their numerical behavior in rotating flows. For this purpose the flow field is obtained by solving the well known double shear layer problem in the square domain with periodic boundary conditions. The initial conditions for lattice variables in lattice units are as follows (U_{lb} and V_{lb} are x and y components of the lattice velocity vector)

$$U_{lb}(x,y,0) = \begin{cases} U_0 \tanh(80(y/(N-1) - 0.25)) & y/(N-1) \leq 0.5 \\ U_0 \tanh(80(0.75 - y/(N-1))) & y/(N-1) > 0.5 \end{cases}$$

$$V_{lb}(x, y, 0) = 0.05 U_0 \sin(2\pi(x/(N-1) + .25))$$

$$T_{lb}(x, y, 0) = \begin{cases} 1 & \frac{1}{4} \leq y/(N-1) < \frac{3}{4} \\ 0 & \text{elsewhere} \end{cases}$$

where $x \in [0, N-1]$, $y \in [0, N-1]$, $U_0 = 0.01$, $N = 256$, $L = 1$ m, $\nu_p = 1.568 \cdot 10^{-5}$ m/s^{-2} and $Re = 16000$ together with $Pr = 72$. Simulations were performed for $t_{lb} = 2.6 \cdot 10^4$ iterations which is equal to the physical time $t = 4.058$ s. Results for all LBM schemes are depicted in Fig. 4.11.
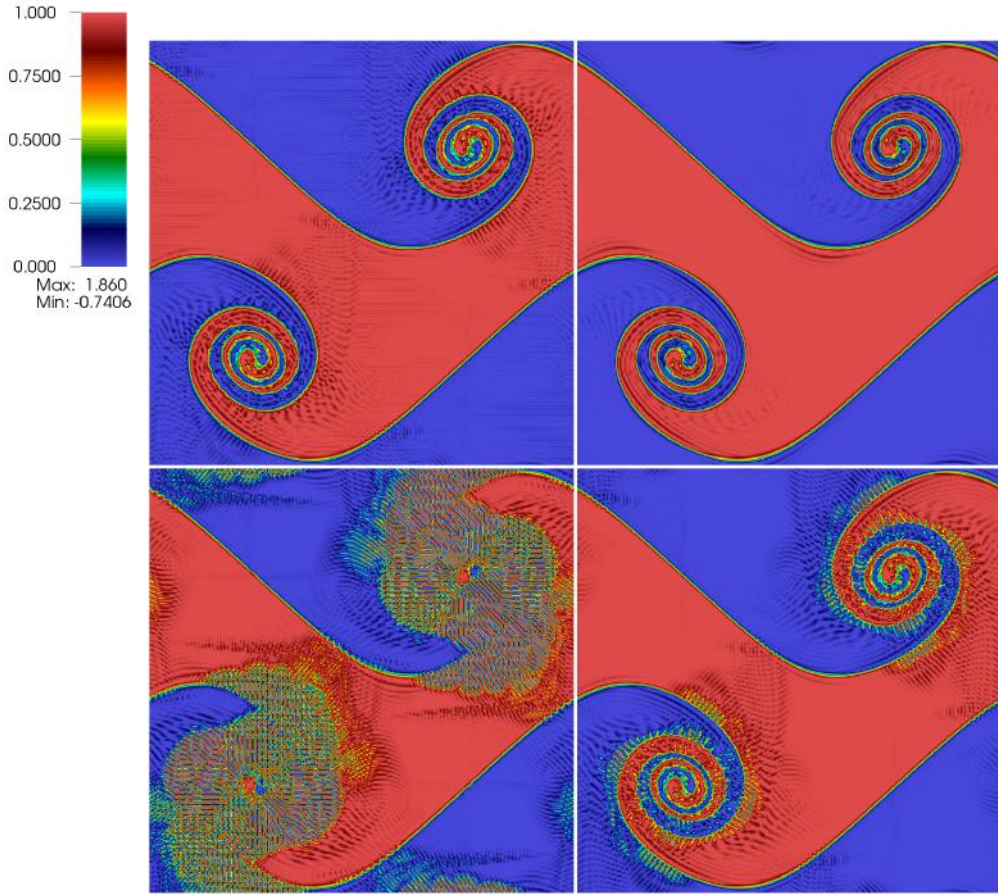

Figura 4.11: Comparison of temperature profiles for the different LBM algorithms for double shear layer flow setup. BGK (top left), CTLBM (top right), Mezrhab et al. [204] (bottom left), Yoshida et al. [309] (bottom right). Parameters setup: $N = 256$, Re= 16000, Pr= 72, $a = 0.5$, $t_{lb} = 2.6 \cdot 10^4$

4.5 Discussion

Properties of the developed CTLBM that can be drawn from the presented data for 1D simulation of advection and diffusion of the sine wave are that it can handle advective and diffusive problems on moderately resolved meshes with great accuracy even for the high Peclet number i.e. more advective than diffusive problems. Two other MRT methods studied here needed very fine resolution to become stable for $Pe \geq 10^5$, in that case the Yoshida et al. scheme were slightly better (as soon as the resolution of the lattice was fine enough to render the method stable) in terms of errors but when looking at the EOC the CTLBM achieved better results in every case studied in the Sec. 3.1. From the comparison of BGK and CTLBM one can see that for lower Pe, the CTLBM performs better than BGK and for higher Pe they perform comparable regarding the errors and EOC. From the values of E_∞ one can clearly see that all methods are of second order regard to the spatial step of the lattice. This is visualized in the Fig. 4.2 where it could be easily seen that doubling of the lattice resolution makes the maximal error four times smaller as indicated by the computed EOC.

Validation of the CTLBM for forced convection flow in 2D was performed and compared to the reference values in Sec. 3.2. Strong agreement between reference and our method is obtained even for simple staircase type of curved boundary condition and no special treatment of the conjugate fluid-solid heat transfer at the boundary of the outer cylinder as done in [226]. Nevertheless the errors in our solutions are visible only for the case of $\alpha_s/\alpha_f = 20$ and are generally less than 5%, for the case of $\alpha_s/\alpha_f = 4$ slight inconsistency in the second half of the curve is observed. The trend of the errors is mirrored when comparing the two latter cases.

Next set of simulations performed, aimed to determine the numerical stability of the methods regarding the time step for moderate Reynolds number. Performed simulations have shown enhanced stability of the method when compared to the others, thus BGK and CTLBM allows for faster simulation of convective thermal problems i.e. with less iterations we can obtain qualitatively comparable results as can be seen from the averaged temperature fields. To judge which of the BGK and CTLBM is more stable, we further increase the Prandtl number. The result is that however both methods are numerically stable, BGK amplifies more the numerical artifacts originating from the fluid solver and produce more numerical instabilities in the temperature field than the proposed CTLBM. CTLBM tends to dampen the artifacts without loosing the fine structures of the temperature field.

To show this nice property of the CTLBM for the complicated, swirling flows, we applied LBM to the double shear layer flow and investigated numerical oscillations near the hot-cold temperature interface. From the results one can see superior

property of the CTLBM, when only few oscillations are presents in the solutions, much less than in the solutions obtained by the other methods. Moreover, the solution obtained by the CTLBM has nice sharp interfaces and other fine structures are also undisturbed.

On the other hand, the CTLBM algorithm can be further enhanced by adding more accurate boundary conditions and by comprehensive analysis of a parameter influence on stability and accuracy by means of higher order equivalent PDE derivation and examination. To simulate turbulent flows, incorporation of the LES model is also possible [67]. Another enhancement can be made towards moving boundaries and more accurate boundary conditions at walls via mesh refinement [78].

4.6 Conclusion

The proposed CTLBM method was successfully tested numerically and compared to the other Lattice Boltzmann Methods for selected problems in 1D and 2D. It was shown that our CTLBM possesses higher stability and accuracy, better or comparable to the other methods widely used in LBM application in thermal problems. The proposed CTLBM also proven to be able to obtain results much faster (with less iterations) when compared to other methods. The proposed CTLBM can be very useful in a wide range of conjugate heat transfer problems and problems with phase change. Therefore our CTLBM is strongly recommended for faster and efficient simulations of heat and mass transfer problems.

Capítulo 5

Double Population Cascaded Lattice Boltzmann Method for Natural Convection Heat Transfer

5.1 Abstract

In this article, we present application of the Cascaded Thermal Lattice Boltzmann Method (CTLBM) in simulations of natural convection in differentially heated square cavity with adiabatic top and bottom walls. This classical benchmark problem is solved for wide range of Rayleigh numbers (10^6–10^{10}) and compared with data from the literature. For high Rayleigh numbers we present comparison of Nusselt number and wall shear stress distributions along hot wall with experimental and direct numerical simulation (DNS) data. Results for Rayleigh numbers up to 10^6 are also compared with previous results obtained by MRT-LBM simulations of Wang et al. The results are in good agreement with the existing ones obtained numerically and experimentally.

The material presented in this chapter has been published in the **International Journal of Thermal Sciences** as an original research paper [262].

5.2 Introduction

Lattice Boltzmann methods have established themselves as the viable alternative among numerical methods used in CFD. LBM solves the discretized Boltzmann Transport Equation (BTE) to obtain set of distribution functions (DFs), from which macroscopic quantities (density, pressure, velocity, temperature) are then obtained. The physics solved by the LBM is controlled by the form of the collision operator and chosen equilibria for the DFs. Several types of realization of collision opera-

tors have emerged [72, 77, 95, 274]. The simplest collision operator is the Single Relaxation Time (SRT) sometimes called BGK in the LBM community, after the authors Bhatnagar, Gross and Krook [21]. A large number of heat transfer and fluid flow problems solved by SRT LBM are reported in the literature [5, 230, 311]. In the SRT approach, all nonconserved moments relax to their equilibrium with the same relaxation time (due to the construction of the collision operator). SRT is based on the BGK approach [274], which could produce numerical instabilities, when the lattice resolution is insufficient [165] and also the truncation error control is limited [55, 135]. In order to increase the stability and accuracy of the LBM schemes, Multiple Relaxation Times (MRT) methods were proposed [72]. In MRT schemes collisions are performed in moment space and different moments could be relaxed with different relaxation times. MRT methods performed reasonably well and showed greater stability and accuracy compared to SRT LBM. Unfortunately the MRT methods are unstable for high Re flows and have other problems mentioned in [96]. The CLBM are methods where central moments are relaxed in a "cascaded manner" [13, 94]. CLBM was successfully used for high Re fluid flow and general heat transfer problems [84, 86, 95, 234, 244, 259, 268].

Some authors use MRT methods for the fluid flow and e.g. finite differences to solve energy equation independently [222, 286]. This approach is known as Hybrid LBM. Other approach known as Double Distribution Function (DDF) scheme was proposed by [256], here two sets of DFs are used, one for the Navier-Stokes equations and another for the energy equation. A large number of research articles appeared, which describe DDF LBM approach with SRT and MRT LBM (see e.g. [110, 165] and references therein). Recently, D_3Q_{27} DDF cascaded LBM was used for steady velocity field and solute transport in porous medium [306]. Another article describe CLBM scheme for the fluid flow and SRT LBM for the energy equation [86]. The double cascaded DDF LBM scheme for thermal problems was recently presented by the authors in [259], where CLBM-CTLBM approach was derived and applied to solve forced convection, meanwhile Fei et al. published somehow similar DDF CLBM approach applied to heat transfer [84].

In the present article we solve natural convection in a differentially heated cavity by the cascaded DDF LBM. We compare results obtained from our CTLBM code with data from literature. Flow and heat transfer in the square cavity for wide range of Rayleigh numbers have been studied by various groups and substantial research has been carried out. Various authors used finite differences, finite volumes, finite elements and pseudo-spectral methods [65, 136, 193, 198, 237, 239, 289], and also LBM [9, 74, 76, 80, 167, 184, 292]. Some of the researchers have adopted Hybrid LBM and DDF LBM [167]. The SRT [74, 76] and MRT LBM were used for laminar flow regime [9, 80, 184, 292]. Dixit et al. [74] used DDF LBM for solving internal

energy equation along with counter-slip boundary conditions together with mesh refinement and simulated high Rayleigh number flows (up to $Ra = 10^{10}$) with SRT. Recently, Jami et al. [147] published a paper where two MRT DDF LBM schemes have been used to solve natural convection up to $Ra = 10^8$. Allen and Reis derived moment based boundary conditions and incorporated them in the MRT LBM in order to solve natural convection in a square cavity [9]. Ren et al. [241] presented the CUDA implementation of DDF LBM scheme with a SRT collision operator to solve natural convection in a square cavity with solid obstacles. Wang et al. [292] used MRT LBM to qualitatively examine natural convection in square cavity up to $Ra = 10^6$ and also Rayleigh-Bénard convection. High Ra number flows in cavities with aspect ratio close or equal to 1 were studied mainly by LES and DNS e.g. [24, 251, 252].

5.2.1   Cascaded LBM for the flow field

The fluid behavior at mesoscopic scale is described by fluid particles in the framework of the Boltzmann's work and their properties at certain space and time are defined by moments $m_{\alpha\beta}$ of velocity distribution functions (DFs) $f(\mathbf{x}, \xi, t)$. The evolution of such DFs obeys Boltzmann Transport Equation which reads

$$\frac{\partial f(\mathbf{x}, \xi, t)}{\partial t} + \xi \cdot \nabla f(\mathbf{x}, \xi, t) = \Omega(f, f), \tag{5.1}$$

where ξ is the microscopic velocity, Ω is the collision operator. The spatial and temporal derivatives in BTE (5.1) are discretized, the velocity distribution functions are reduced to finite given by the desired lattice model, in our case the D_2Q_9 and D_2Q_5. Then by choosing the cascaded form of collision operator and incorporating forcing term $\tilde{F}_i$ we end up with the cascaded lattice Boltzmann equation (CLBE), which in lattice units reads

$$f_i(\mathbf{x} + \mathbf{c}_i, t + 1) = f(\mathbf{x}, t) + \mathbb{K} \cdot \mathbf{k} + \tilde{F}_i, \tag{5.2}$$

where f_i is the "velocity" distribution function linked to the ith characteristic velocity, $\mathbb{K}$ is transformation matrix, $\mathbf{k}$ is a vector of moments of f_i resulting from the cascaded collision operator. The equilibrium distribution function f_i^{eq} is defined based on the Maxwell-Boltzmann equilibrium distribution function by

$$f_i^{eq} = \rho w_i \left(1 + \frac{\mathbf{u} \cdot \mathbf{c}_i}{c_s^2} + \frac{(\mathbf{u} \cdot \mathbf{c}_i)^2}{2c_s^4} - \frac{\mathbf{u} \cdot \mathbf{u}}{2c_s^2} \right), \tag{5.3}$$

where ρ is density, c_s is the speed of sound and $\mathbf{u} = (u, v)$ is macroscopic velocity vector. For the lattice model D_2Q_9 we have $c_s = 1/\sqrt{3}$. The body force can be

modeled by different approaches, those are compared in [213] for the problem of a natural convection. We use the forcing scheme proposed by [234]. First the velocity field is modified by known force $\mathbf{\Gamma} = (\Gamma_x, \Gamma_y)$ (which is defined later),

$$u = \frac{1}{2\rho}\Gamma_x \quad v = \frac{1}{2\rho}\Gamma_y \tag{5.4}$$

then expressions for the components to be included in cascaded collisions are

$$
\begin{aligned}
F_4 &= -(\Gamma_x u + \Gamma_y v) \\
F_5 &= -(\Gamma_x u - \Gamma_y v) \\
F_6 &= \frac{1}{2}(\Gamma_x v + \Gamma_y u) \\
F_7 &= -\frac{1}{2}(u^2\Gamma_y - \Gamma_x uv) \\
F_8 &= -\frac{1}{2}(v^2\Gamma_x - \Gamma_y uv) \\
F_9 &= -(\Gamma_x uv^2 + \Gamma_y u^2 v)
\end{aligned}
\tag{5.5}
$$

and the components which are added directly to the distribution functions are

$$
\begin{aligned}
\tilde{F}_1 &= \frac{1}{9}(-\gamma_3 + \gamma_8) \\
\tilde{F}_2 &= \frac{1}{36}(-6\gamma_1 + 6\gamma_2 + 2\gamma_3 - 9\gamma_5 - 3\gamma_6 + 3\gamma_7 + \gamma_8) \\
\tilde{F}_3 &= \frac{1}{36}(-6\gamma_1 - \gamma_3 + 9\gamma_4 - 6\gamma_7 - 2\gamma_8) \\
\tilde{F}_4 &= \frac{1}{36}(-6\gamma_1 - 6\gamma_2 + 2\gamma_3 + 9\gamma_5 + 3\gamma_6 + 3\gamma_7 + \gamma_8) \\
\tilde{F}_5 &= \frac{1}{36}(-6\gamma_2 - \gamma_3 - 9\gamma_4 - 6\gamma_6 - 2\gamma_8) \\
\tilde{F}_6 &= \frac{1}{36}(6\gamma_1 - 6\gamma_2 + 2\gamma_3 - 9\gamma_5 + 3\gamma_6 - 3\gamma_7 + \gamma_8) \\
\tilde{F}_7 &= \frac{1}{36}(6\gamma_1 - \gamma_3 + 9\gamma_4 + 6\gamma_7 - 2\gamma_8) \\
\tilde{F}_8 &= \frac{1}{36}(6\gamma_1 + 6\gamma_2 + 2\gamma_3 + 9\gamma_5 - 3\gamma_6 - 3\gamma_7 + \gamma_8) \\
\tilde{F}_9 &= \frac{1}{36}(6\gamma_2 - \gamma_3 - 9\gamma_4 + 6\gamma_6 - 2\gamma_8)
\end{aligned}
\tag{5.6}
$$

where γ_i are defined as

$$\gamma_1 = \Gamma_x$$
$$\gamma_2 = \Gamma_y$$
$$\gamma_3 = 6(\Gamma_x u + \Gamma_y v)$$
$$\gamma_4 = 2(\Gamma_x u - \Gamma_x u) \tag{5.7}$$
$$\gamma_5 = \Gamma_x v + \Gamma_y u$$
$$\gamma_6 = (2 - 3u^2)\Gamma_y - 6\Gamma_x uv$$
$$\gamma_7 = (2 - 3v^2)\Gamma_x - 6\Gamma_y uv$$
$$\gamma_8 = 6((3v^2 - 2)\Gamma_x u + (3u^2 - 2)\Gamma_y v)$$

The macroscopic density ρ and macroscopic velocity $\mathbf{u}$ can be obtained as first two moments of f_i

$$\rho = \sum_i f_i,$$
$$\rho\mathbf{u} = \sum_i \mathbf{c}_i f_i. \tag{5.8}$$

We define raw moments $m_{\alpha\beta}$ and central moments $\kappa_{\alpha\beta}$ of order $\alpha + \beta$ as

$$m_{\alpha\beta} = \sum_i c_{i,x}^\alpha c_{i,y}^\beta f_i, \tag{5.9}$$

$$\kappa_{\alpha\beta} = \sum_i (c_{i,x} - u)^\alpha (c_{i,y} - v)^\beta f_i. \tag{5.10}$$

From the above one can readily see that

$$\rho = m_{00} = \kappa_{00}, \quad \rho u = m_{10}, \quad \rho v = m_{01}, \quad \kappa_{10} = \kappa_{01} = 0. \tag{5.11}$$

To perform cascaded collision we need the transformation matrix $\mathbb{K}$ and the collision vector $\mathbf{k}$. We choose following non-orthogonal moments for the flow field on the D_2Q_9 lattice (we use Einstein summation here)

$$\left\{ \sum_i f_i, c_{i,x} f_i, c_{i,y} f_i, \left(c_{i,x}^2 + c_{i,y}^2\right) f_i, \left(c_{i,x}^2 - c_{i,y}^2\right) f_i, c_{i,x} c_{i,y} f_i, c_{i,x}^2 c_{i,y} f_i, c_{i,y}^2 c_{i,x} f_i, c_{i,x}^2 c_{i,y}^2 f_i \right\}.$$

The first three moments are the conserved quantities (ρ and $\rho\mathbf{u}$). To obtain orthogonal transformation matrix [94] we use use Gram-Schmidt orthogonalization process

and eventually get

$$\mathbb{K}^T = \begin{bmatrix} 1 & 1 & 1 & 1 & 1 & 1 & 1 & 1 & 1 \\ 0 & -1 & -1 & -1 & 0 & 1 & 1 & 1 & 0 \\ 0 & 1 & 0 & -1 & -1 & -1 & 0 & 1 & 1 \\ -4 & 2 & -1 & 2 & -1 & 2 & -1 & 2 & -1 \\ 0 & 0 & 1 & 0 & -1 & 0 & 1 & 0 & -1 \\ 0 & 1 & 0 & -1 & 0 & 1 & 0 & -1 & 0 \\ 0 & -1 & 0 & 1 & -2 & 1 & 0 & -1 & 2 \\ 0 & 1 & -2 & 1 & 0 & -1 & 2 & -1 & 0 \\ 4 & 1 & -2 & 1 & -2 & 1 & -2 & 1 & -2 \end{bmatrix}. \tag{5.12}$$

The streaming step is defined by

$$f_i(\mathbf{x} + \mathbf{c}_i, t + 1) = f_i'(\mathbf{x}, t), \tag{5.13}$$

and collision step by

$$f_i'(\mathbf{x}, t) = f_i(\mathbf{x}, t) + \mathbb{K} \cdot \mathbf{k} + F_i, \tag{5.14}$$

where f_i' is the so-called post-collision velocity distribution function. The collision vector $\mathbf{k}$, has nine components $k_1, \ldots, k_9$, where k_1, k_2, k_3 vanish due to the conservation of density and momenta.

$$\mathbf{k} = \begin{bmatrix} 0, 0, 0, k_4, k_5, k_6, k_7, k_8, k_9 \end{bmatrix}^T. \tag{5.15}$$

The equilibrium central moments for the fluid flow are defined as

$$\begin{aligned} \kappa_{00} &= \kappa_{00}^{eq} = \rho, \\ \kappa_{10}^{eq} &= \kappa_{10} = 0, \\ \kappa_{01}^{eq} &= \kappa_{01} = 0, \\ \kappa_{20}^{eq} &= \rho c_s^2, \\ \kappa_{02}^{eq} &= \rho c_s^2, \\ \kappa_{11}^{eq} &= 0, \\ \kappa_{21}^{eq} &= 0, \\ \kappa_{12}^{eq} &= 0, \\ \kappa_{22}^{eq} &= \rho c_s^4. \end{aligned} \tag{5.16}$$

Cascaded collision scheme is given by the following equations for components of the $\mathbf{k}$

$$k_4 = \frac{1}{12\tau_4} \left[\rho(u^2 + v^2) - f_6 - f_8 - f_4 - f_2 - 2(f_5 + f_3 + f_7 + f_1 - \rho c_s^2) + F_4 \right],$$

$$k_5 = \frac{1}{4\tau_5} \left[f_8 + f_4 - f_6 - f_2 + \rho(u^2 - v^2) + F_5 \right],$$

$$k_6 = \frac{1}{4\tau_6} (f_7 + f_3 - f_1 - f_5 - uv\rho + F_6),$$

$$k_7 = -\frac{1}{4\tau_7} \left\{ \left[f_5 + f_3 - f_7 - f_1 - 2u^2v\rho + v(\rho - f_8 - f_4 - f_0) \right] + \right.$$
$$\left. + 2u(f_7 - f_1 - f_5 + f_3) + F_7 \right\} + \frac{v}{2} (-3k_4 - k_5) + 2uk_6,$$

$$k_8 = -\frac{1}{4\tau_8} \left\{ \left[f_3 + f_1 - f_5 - f_7 - 2v^2u\rho + u(\rho - f_2 - f_6 - f_0) \right] + \right.$$
$$\left. + 2v(f_7 - f_1 - f_5 + f_3) + F_8 \right\} + \frac{u}{2} (-3k_4 + k_5) + 2vk_6,$$

$$k_9 = \frac{1}{4} \left[\frac{1}{\tau_9} \left(\rho c_s^4 - \kappa_{xxyy} \right) - 8k_4 - 6k_5(u^2 + v^2) - 2k_5(v^2 - u^2) + \right.$$
$$\left. + 16k_6uv - 8k_7v - 8k_8u + F_9 \right]$$

$$(5.17)$$

where $\tau_{4,5,6,\dots,9}$ are the relaxation times for non-conserved moments. Relations between relaxation times and a kinematic viscosity of the fluid are following

$$\tau_5 = \tau_6 = \frac{\nu}{c_s^2} + \frac{1}{2}. \tag{5.18}$$

To achieve zero-slip at walls for half-way bounce back, we also set [84]

$$\tau_7 = \tau_8 = \frac{8\tau_5 - 1}{16\tau_5 - 8}, \tag{5.19}$$

two last relaxation times are set to $\tau_4 = \tau_9 = 1$. Two principal differences between the cascaded scheme and other MRT schemes [72] are that central moments are relaxed in the cascaded manner [13] and the cross talking among different moments are corrected [94, 96]. In order to recover the Navier-Stokes equations from the LBE, Chapmann-Enskog expansion [44], Hilbert expansion [152], Equivalent Partial Differential Equations [79] or recently emerged Maxwell iteration method [319] techniques could be used.

In every case we do Taylor expansion of the LBE, apply diffusive scaling and after lengthy algebra we eventually end up with [96, 234, 259] (with Ma being the

Mach number)

$$\frac{\partial u}{\partial x} + \frac{\partial v}{\partial y} = O(Ma^2)$$

$$\frac{\partial u}{\partial t} + \frac{\partial u^2}{\partial x} + \frac{\partial uv}{\partial y} = -\frac{\partial p}{\partial x} + \frac{1}{Re}\left(\frac{\partial^2 u}{\partial x^2} + \frac{\partial^2 u}{\partial y^2}\right) + \Gamma_x + O(Ma^3) \qquad (5.20)$$

$$\frac{\partial v}{\partial t} + \frac{\partial v^2}{\partial y} + \frac{\partial vu}{\partial x} = -\frac{\partial p}{\partial y} + \frac{1}{Re}\left(\frac{\partial^2 v}{\partial x^2} + \frac{\partial^2 v}{\partial y^2}\right) + \Gamma_y + O(Ma^3).$$

5.2.2 Cascaded LBM for the temperature field

Temperature is considered as a passive scalar obeying the advection-diffusion equation. Viscous heat dissipation and compressive work have not been considered here as their contribution in natural convection can be neglected in the cases we studied. The CTLBM is used with the D_2Q_5 lattice model. The evolution of temperature is defined by "temperature" distribution functions g_i. The discretized cascaded thermal lattice Boltzmann equation in lattice units reads

$$g(\mathbf{x} + \mathbf{c}_i, t + 1) = g(\mathbf{x}, t) + \mathbb{Q} \cdot \mathbf{q}, \qquad (5.21)$$

where $\mathbb{Q} \cdot \mathbf{q}$ is the cascaded collision scheme for the temperature field, which is similar to the collision scheme used for fluid flow but applied to temperature DFs on the separate lattice. $\mathbb{Q}$ is the orthogonal transformation matrix, and $\mathbf{q}$ is the collision vector. The streaming and collision processes are similar as before with streaming along the links and collision at nodes. The equilibrium DFs for temperature reads

$$\begin{bmatrix} g_1^{eq} \\ g_2^{eq} \\ g_3^{eq} \\ g_4^{eq} \\ g_5^{eq} \end{bmatrix} = \begin{bmatrix} (1-a)T \\ (a-2u)\frac{T}{4} \\ (a-2v)\frac{T}{4} \\ (a+2u)\frac{T}{4} \\ (a+2v)\frac{T}{4} \end{bmatrix}, \qquad (5.22)$$

where T is the temperature and a is free parameter related to the "speed of sound" (not the real one but linked to the lattice). We set $a = \sqrt{2/5}$ [84]. The moments for the temperature field for the D_2Q_5 lattice are

$$\left\{ \sum_i g_i, c_{i,x}g_i, c_{i,y}g_i, \left(c_{i,x}^2 + c_{i,y}^2\right)g_i, \left(c_{i,y}^2 - c_{i,x}^2\right)g_i \right\}.$$

The first moment $T = \sum_i g_i$ is the only conserved quantity (collisional invariant). As in previous section, we apply Gram-Schmidt orthogonalization process to obtain

the orthogonal transformation matrix $\mathbb{Q}$

$$\mathbb{Q}^{\mathrm{T}} = \begin{bmatrix} 1 & 1 & 1 & 1 & 1 \\ 0 & -1 & 0 & 1 & 0 \\ 0 & 0 & -1 & 0 & 1 \\ 4 & -1 & -1 & -1 & -1 \\ 0 & -1 & 1 & -1 & 1 \end{bmatrix}. \tag{5.23}$$

The collision step is given by

$$g_i^{'}(\mathbf{x}, t) = g_i(\mathbf{x}, t) + \mathbb{Q} \cdot \mathbf{q}, \tag{5.24}$$

and streaming step for CTLBM reads

$$g_i(\mathbf{x} + \mathbf{c}_i, t+1) = g_i^{'}(\mathbf{x}, t), \tag{5.25}$$

where $g_i^{'}$ are post collision DFs.

The cascaded relaxation scheme for the temperature DFs reads

$$
\begin{aligned}
q_1 &= 0, \\
q_2 &= \frac{1}{2\tau_{g,2}}(\kappa_{10}^{eq} - \kappa_{10}), \\
q_3 &= \frac{1}{2\tau_{g,3}}(\kappa_{01}^{eq} - \kappa_{01}), \\
q_4 &= -\frac{1}{4\tau_{g,4}}(\kappa_{20}^{eq} - \kappa_{20} + \kappa_{02}^{eq} - \kappa_{02}) - uq_2 - vq_3, \\
q_5 &= \frac{1}{4\tau_{g,5}}(\kappa_{20} - \kappa_{20}^{eq} + \kappa_{02}^{eq} - \kappa_{02}) - uq_2 + vq_3,
\end{aligned}
\tag{5.26}
$$

where $\tau_{g,2}, \tau_{g,3}, \tau_{g,4}, \tau_{g,5}$ are relaxation times for non-conserved thermal moments and again $q_1 = 0$ as it is collisional invariant and corresponds to the conserved quantity. In the cascaded scheme, lower order moments do affect the evolution of the higher order moments as can be seen from (5.26). The above scheme can be expressed in DFs and known macroscopic quantities as

$$q_2 = \frac{1}{2\tau_{g,2}}(Tu - g_3 + g_1),$$

$$q_3 = \frac{1}{2\tau_{g,3}}(Tv - g_4 + g_2),$$

$$q_4 = -\frac{1}{4\tau_{g,4}}(aT - g_1 - g_2 - g_3 - g_4) + \left(\frac{1}{2\tau_{g,4}} - \frac{1}{2\tau_{g,2}}\right)u(Tu - g_3 + g_1)+$$

$$+ \left(\frac{1}{2\tau_{g,4}} - \frac{1}{2\tau_{g,3}}\right)v(Tv - g_4 + g_2),$$

$$q_5 = \frac{1}{4\tau_{g,5}}(g_1 + g_3 - g_2 - g_4) + \left(\frac{1}{2\tau_{g,5}} - \frac{1}{2\tau_{g,2}}\right)u(Tu - g_3 + g_1)+$$

$$+ \left(\frac{1}{2\tau_{g,3}} - \frac{1}{2\tau_{g,5}}\right)v(Tv - g_4 + g_2). \tag{5.27}$$

Advection-diffusion equation for the temperature can be recovered by adopting same steps as in previous section and reads

$$\frac{\partial T}{\partial t} + \frac{\partial Tu}{\partial x} + \frac{\partial Tv}{\partial y} = \frac{a}{2}\left(\tau_{g,2} - \frac{1}{2}\right)\frac{\partial^2 T}{\partial x^2} + \frac{a}{2}\left(\tau_{g,3} - \frac{1}{2}\right)\frac{\partial^2 T}{\partial y^2} + O(\Delta t^3). \tag{5.28}$$

The thermal diffusivities can be identified once the above equation is compared with the Fourier-Kirchhoff equation

$$\alpha_x = \frac{a}{2}\left(\tau_{g,2} - \frac{1}{2}\right), \qquad \alpha_y = \frac{a}{2}\left(\tau_{g,3} - \frac{1}{2}\right). \tag{5.29}$$

Two other relaxation times are set to

$$\tau_{g,4} = \tau_{g,5} = 12\frac{1 - 2\tau_{g,2}}{1 - 12\tau_{g,2}} \tag{5.30}$$

in order to eliminate numerical slip [61].

5.2.3   Governing macroscopic equations

In present paper we study application of CTLBM in simulations of natural convection flows, which can be described by Navier-Stokes equations together with Fourier-Kirchhoff equation. The coupling between thermal and flow fields is due to the buoyancy force term added to the momentum equations. The Boussinesq approximation is employed, i.e., we have linear dependency of density on the temperature

$$\rho = \rho_0\left[1 + \beta\left(T - T_{\text{ref}}\right)\right], \tag{5.31}$$

where ρ_0 is the reference density (at the reference temperature T_{ref}) and β is the linear isobaric thermal expansion coefficient defined by

$$\beta = -\frac{1}{\rho} \left(\frac{\partial \rho}{\partial T} \right)_p. \tag{5.32}$$

The problem is then described by the following system of PDEs

$$\nabla \cdot \mathbf{u} = 0,$$
$$\frac{\partial \mathbf{u}}{\partial t} + \mathbf{u} \cdot \nabla \mathbf{u} = -\frac{1}{\rho_0} \nabla p + \nu \Delta \mathbf{u} + \Gamma, \tag{5.33}$$
$$\frac{\partial T}{\partial t} + \mathbf{u} \cdot \nabla T = \alpha \Delta T,$$

where force term Γ is given by

$$\Gamma = \mathbf{g}\beta(T - T_{\text{ref}}), \tag{5.34}$$

with $\mathbf{g}$ being the vector of gravitational acceleration. In order to compare and characterize natural convection in different systems, we need two dimensionless numbers, the Prandtl number (Pr) and Rayleigh (Ra) or Grashof (Gr) number

$$\text{Pr} = \frac{\nu}{\alpha}, \quad Ra = \frac{\beta|\mathbf{g}|\Delta T L^3}{\nu\alpha}, \quad \text{Gr} = \frac{\text{Ra}}{\text{Pr}}, \tag{5.35}$$

where L is characteristic length of the system and ΔT is temperature difference (e.g. between hot and cold walls). The characteristic velocity for natural convection flows can be defined as

$$U = \sqrt{\beta|\mathbf{g}|\Delta T L} = \sqrt{\frac{\text{Ra}}{\text{Pr}}} \frac{\nu}{L}. \tag{5.36}$$

During the computations, the Nusselt number (Nu) is also determined in order to compare our results with other authors. Two Nusselt numbers are computed

$$\text{Nu} = \frac{1}{\Delta T_{\text{lb}} L_{\text{x,lb}}} \sum_0^{L_{\text{x,lb}}} \sum_0^{L_{\text{y,lb}}} q_x(x,y) \mathrm{d}x \mathrm{d}y, \tag{5.37}$$

$$\text{Nu}_{1/2} = \frac{1}{\Delta T_{\text{lb}}} \sum_0^{L_{\text{y,lb}}} q_x\left(\frac{L_{\text{x,lb}}}{2}, y\right) \mathrm{d}y, \tag{5.38}$$

here $L_{\text{x/y,lb}}$ are number of lattice sites in x and y direction, q_x is the local heat flux in the horizontal direction, i.e.

$$q_x = \frac{u_{\text{lb}} T_{\text{lb}}}{\alpha_{\text{lb}}} - \frac{\partial T_{\text{lb}}}{\partial x} \tag{5.39}$$

and the temperature derivative is approximated by the finite differences.

In order to determine all parameters needed to perform LBM simulations, we need one more dimensionless number, namely the Mach number (Ma)

$$\text{Ma} = \frac{U}{c_s}. \tag{5.40}$$

The above system of equations can be rescaled using the following

$$\mathbf{x}^+ = \frac{\mathbf{x}}{L}, \quad t^+ = \frac{t\alpha}{L^2}, \quad \mathbf{u}^+ = \frac{\mathbf{u}L}{\alpha}, \quad p^+ = \frac{pL^2}{\rho_0\alpha^2}, \quad T^+ = \frac{T - T_{\text{ref}}}{\Delta T} \tag{5.41}$$

which results in ("+" superscripts are dropped in the following)

$$\nabla \cdot \mathbf{u} = 0,$$
$$\frac{\partial \mathbf{u}}{\partial t} + \mathbf{u} \cdot \nabla \mathbf{u} = -\frac{1}{\rho_0}\nabla p + \text{Pr}\Delta\mathbf{u} + \text{RaPr}T\mathbf{g_0}, \tag{5.42}$$
$$\frac{\partial T}{\partial t} + \mathbf{u} \cdot \nabla T = \Delta T,$$

where $\mathbf{g_0}$ is unit vector in the direction of the gravitational field. To setup parameters in lattice units, needed during the simulations, we use dimensionless numbers defined above to obtain (we can setup either the desired Ma number i.e. the time step and compute lattice viscosity or setup the lattice viscosity directly providing the resulting Ma number is small enough, say less than 0.3)

$$\nu_{\text{lb}} = \frac{\text{Ma}c_s}{L_{\text{lb}}}\sqrt{\frac{\text{Pr}}{\text{Ra}}}, \quad \alpha_{\text{lb}} = \frac{\nu_{\text{lb}}}{\text{Pr}} \tag{5.43}$$

where L_{lb} is the number of lattices used for characteristic length L. The last parameter which must be expressed in lattice units is the $\beta|\mathbf{g}|$

$$(\beta|\mathbf{g}|)_{\text{lb}} = \frac{\text{Ra}\nu_{\text{lb}}\alpha_{\text{lb}}}{L_{\text{lb}}^3\Delta T_{\text{lb}}}. \tag{5.44}$$

Some of the results (especially for Ra numbers greater than 10^9 [238]) are far away from being steady, for such flows the instant values are meaningless as the flow is chaotic. In the theory of turbulent boundary layer, the dimensionless quantities y^+, U^+ and T^+ are used in order to express the so called law of the wall [233]. These quantities are computed from the normal distance from the wall y and velocity parallel to wall v scaled by the friction velocity v_τ

$$y^+ = \frac{yv_\tau}{\nu}, \ U^+ = \frac{v}{v_\tau}, \ T^+ = \frac{T_{\text{wall}} - T}{q_w/v_\tau}, \ v_\tau = \sqrt{\nu\left(\frac{\partial v}{\partial y}\right)_{y=0}}, \ q_w = -\alpha\left(\frac{\partial T}{\partial y}\right)_{y=0}, \tag{5.45}$$

The derivatives of v and T are obtained by fitting of the third order polynomial applied to values in the vicinity of the wall.

5.2.4 Initial and boundary conditions

As the LBM solver is a transitional solver, we need to provide not only the boundary conditions but also initial conditions. The initial conditions are given by zero velocity and reference temperature

$$f_i(\mathbf{x}, 0) = f_i^{\mathrm{eq}}(\rho_{\mathrm{ini,lb}}, \mathbf{u}_{\mathrm{ini,lb}}), \; g_i(\mathbf{x}, 0) = g_i^{\mathrm{eq}}(T_{\mathrm{ini,lb}}, \mathbf{u}_{\mathrm{ini,lb}}) \forall \mathbf{x} \in [0, L_{\mathrm{x,lb}}] \times [0, L_{\mathrm{y,lb}}],$$
$$\rho_{\mathrm{ini,lb}} = 1, \; \mathbf{u}_{\mathrm{ini,lb}} = (0, 0), \; T_{\mathrm{ini,lb}} = 0.5,$$

$$(5.46)$$

where $L_{\mathrm{x,lb}}$ and $L_{\mathrm{y,lb}}$ are lattice dimensions of the computational domain.

Boundary conditions needed during the simulations are no-slip conditions for the velocity at walls, Dirichlet and adiabatic conditions for the temperature at walls. The no-slip and adiabatic conditions can be simulated by the bounce-back approach [165]

$$f_{\bar{i}}(\mathbf{x}_{\mathrm{bb}}, t + 1) = f_i'(\mathbf{x}_{\mathrm{bb}}, t), \quad g_{\bar{i}}(\mathbf{x}_{\mathrm{bb}}, t + 1) = g_i'(\mathbf{x}_{\mathrm{bb}}, t), \quad (5.47)$$

where $\mathbf{x}_{\mathrm{bb}}$ is the wall adjacent fluid site, $f_{\bar{i}}$ and $g_{\bar{i}}$ correspond to DFs which characteristic velocity points in the reflected direction i.e. $\mathbf{c}_{\bar{i}} = -\mathbf{c}_i$. This results in no-slip and/or adiabatic wall.

In the case of Dirichlet conditions (i.e. for wall with given temperature) we use "anti-bounce-back" conditions to setup the temperature of the walls

$$g_{\bar{i}}(\mathbf{x}_{\mathrm{w}}, t + 1) = -g_i(\mathbf{x}_{\mathrm{w}}, t) + \frac{a}{2}T. \quad (5.48)$$

5.3 Differentially heated square cavity

The test case for the CTLBM is the well known and well studied differentially heated square cavity. The cavity's top and bottom walls are insulated, left and right walls are kept at different temperatures (the left wall is the hot wall, see Fig. 5.1). The fluid inside the cavity is heated up by the hot wall and rise due to buoyancy forces, while it is cooled down by the cold wall and descends which produces various flow patterns inside the cavity. To compare our results with other authors' results we will measure the maximal horizontal and vertical velocity (u_{max} and v_{max}) at mid-cross-sections (vertical and horizontal ones) together with their positions along that cross-section (y_{max} and x_{max}) and two Nusselt numbers defined earlier. This problem was extensively studied by many authors [65, 74, 76, 80, 167, 184, 193, 237, 289, 292]
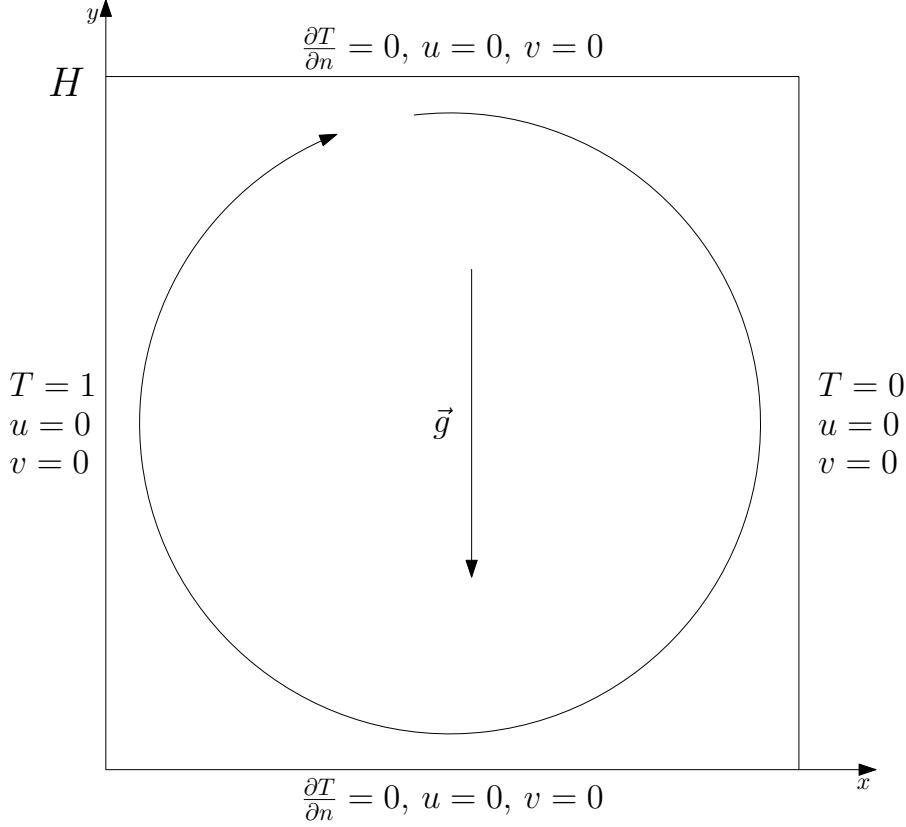
Figura 5.1: Differentially heated cavity geometry and boundary conditions.

and data provided by them will be used for comparison for the Rayleigh numbers up to 10^{10}.

5.3.1 Numerical simulations setup

The natural convection in a square cavity of height H was simulated for the range of Ra $= 10^3$–10^{10}. The flow in 2D is laminar up to Ra $\sim 1.82 \cdot 10^8$ [238], for Ra numbers above Ra $= 10^9$ the flow is fully chaotic. To setup the LBM solver, we have to choose the Prandtl number (equal to 0.71 in all simulations, i.e. the air filled cavity), the Rayleigh number, and the Mach number. Temperature difference in lattice units was equal to 1 with $T_{\text{hot,lb}} = 1$ and $T_{\text{cold,lb}} = 0$. Initial temperature was set to $T_{\text{ini,lb}} = 0.5$. Initial velocity field is set to zero $\mathbf{u}_{\text{ini,lb}} = (0,0)$. The number of lattice size in x and y direction $L_{x,lb} = L_{y,lb} = N$ were varied from 64 to 1024 (or 2048 for Ra$= 10^7 - 10^8$). We also performed simulations with different Mach numbers (Ma=0.01, 0.05, 0.1, 0.15) to examine behavior of quantities under study, when the time step is increased.

For Ra$= 10^3, \ldots, 10^8$, the computations were performed until the following con-

ditions were met:

$$\frac{\sum_{x,y} |\mathbf{u}(x, y, t + 1000) - \mathbf{u}(x, y, t)|_{L_2}}{\sum_{x,y} |\mathbf{u}(x, y, t)|_{L_2}} < 10^{-10}$$

$$\max_{x,y} |T(x, y, t + 1000) - T(x, y, t)| < 10^{-6}$$

$$(5.49)$$

i.e. we seek steady state by checking L_2 norm of velocity and L_∞ norm of temperature fields.

5.3.2 Grid convergence of the solutions

First we check the grid convergence of the solutions for different Ra numbers and Mach numbers. Ma number is related to the time step of the simulations and also to the compressibility error [68]. To measure the errors we compare solutions on several grids with reference solution (grid with $N = 1024$ or in case of Ra$= 10^7$ and Ra$= 10^8$ with $N = 2048$). To compute L_2-velocity and L_∞-density/temperature norms we interpolate values from fine grid to the coarse grids using cubic interpolation. Results are summarized in Tabs. 5.1-5.4, where n denotes order of the convergence. From the tables one can observe that for small Mach number the orders are close or above 2.0 except for the pressure field for the two smallest Ra numbers. With increasing Mach number the order of convergence for pressure field becomes lower, with lowest values for low Ra numbers. The errors are also increasing with increased Ra numbers.

5.3.3 Convergence of hydrodynamical quantities and Nusselt numbers

Next we study behavior of averaged Nusselt numbers $N_{1/2}$ and Nu, maximal velocities in x and y directions $u_{\max}$ and $v_{\max}$ at vertical and horizontal mid-lines, together with their locations. The values and positions are obtained by first fitting velocity to the quadratic function in the vicinity of node with maximal value and then this function is used to compute maximal values and their positions. Results are summarized in Tabs. 5.5-5.8. Asymptotic values (denoted by "$N = \infty$") are obtained by least-square fit of the 3rd order polynomial function as done in [292]. Comparison of asymptotic values for different Ma numbers are summarized in Tab. 5.9. The most sensitive are components of maximal horizontal and vertical velocity, while their positions are not very sensitive the the increasing time step. With increasing Ma, the maximal velocities tend to be over predicted while Nu numbers have opposite trend and are under predicted in the most cases. Asymptotic quantities for the Ma$= 0.01$ will be compared with results from the literature in the next section.

Tabela 5.1: Natural convection in a square cavity: grid convergence for Ma = 0.01.

N	$|T|_{L_\infty}$	$|P|_{L_\infty}$	$|\mathbf{u}|_{L_2}$
Ra= 10^3			
64	$1.745\cdot10^{-4}$	$1.101\cdot10^{-2}$	$1.670\cdot10^{-3}$
128	$4.437\cdot10^{-5}$	$2.730\cdot10^{-3}$	$4.110\cdot10^{-4}$
256	$1.120\cdot10^{-5}$	$9.000\cdot10^{-4}$	$9.663\cdot10^{-5}$
512	$2.578\cdot10^{-6}$	$2.768\cdot10^{-4}$	$1.957\cdot10^{-5}$
768	$9.201\cdot10^{-7}$	$9.085\cdot10^{-5}$	$5.593\cdot10^{-6}$
n	2.0908	1.8583	2.2587
Ra= 10^4			
64	$6.730\cdot10^{-4}$	$3.645\cdot10^{-2}$	$2.529\cdot10^{-3}$
128	$1.608\cdot10^{-4}$	$8.018\cdot10^{-3}$	$6.418\cdot10^{-4}$
256	$3.710\cdot10^{-5}$	$2.478\cdot10^{-3}$	$1.528\cdot10^{-4}$
512	$7.464\cdot10^{-6}$	$7.429\cdot10^{-4}$	$3.113\cdot10^{-5}$
768	$2.272\cdot10^{-6}$	$2.421\cdot10^{-4}$	$8.474\cdot10^{-6}$
n	2.2627	1.9425	2.2536
Ra= 10^5			
64	$2.597\cdot10^{-3}$	$9.753\cdot10^{-2}$	$6.796\cdot10^{-3}$
128	$6.448\cdot10^{-4}$	$1.837\cdot10^{-2}$	$1.803\cdot10^{-3}$
256	$1.501\cdot10^{-4}$	$3.910\cdot10^{-3}$	$4.338\cdot10^{-4}$
512	$2.974\cdot10^{-5}$	$9.645\cdot10^{-4}$	$8.784\cdot10^{-5}$
768	$7.796\cdot10^{-6}$	$2.987\cdot10^{-4}$	$2.289\cdot10^{-5}$
n	2.2954	2.2787	2.2494
Ra= 10^6			
64	$7.983\cdot10^{-3}$	$2.202\cdot10^{-1}$	$2.400\cdot10^{-2}$
128	$2.131\cdot10^{-3}$	$4.806\cdot10^{-2}$	$6.172\cdot10^{-3}$
256	$5.182\cdot10^{-4}$	$8.384\cdot10^{-3}$	$1.498\cdot10^{-3}$
512	$1.034\cdot10^{-4}$	$1.460\cdot10^{-3}$	$3.004\cdot10^{-4}$
768	$2.683\cdot10^{-5}$	$3.945\cdot10^{-4}$	$7.718\cdot10^{-5}$
n	2.2502	2.5284	2.2639
Ra= 10^7			
64	$2.987\cdot10^{-2}$	$4.308\cdot10^{-1}$	$1.200\cdot10^{-1}$
128	$7.133\cdot10^{-3}$	$1.247\cdot10^{-1}$	$3.080\cdot10^{-2}$
256	$1.861\cdot10^{-3}$	$2.255\cdot10^{-2}$	$7.688\cdot10^{-3}$
512	$4.551\cdot10^{-4}$	$3.888\cdot10^{-3}$	$1.827\cdot10^{-3}$
768	$1.864\cdot10^{-4}$	$1.431\cdot10^{-3}$	$7.374\cdot10^{-4}$
1024	$9.227\cdot10^{-5}$	$6.943\cdot10^{-4}$	$3.577\cdot10^{-4}$
n	2.0606	2.3642	2.0824

Tabela 5.2: Natural convection in a square cavity: grid convergence for Ma = 0.05.

N	$|T|_{L_\infty}$	$|P|_{L_\infty}$	$|\mathbf{u}|_{L_2}$
Ra= 10^3			
64	$2.125 \cdot 10^{-4}$	$5.645 \cdot 10^{-3}$	$1.724 \cdot 10^{-3}$
128	$6.274 \cdot 10^{-5}$	$2.035 \cdot 10^{-3}$	$4.221 \cdot 10^{-4}$
256	$1.932 \cdot 10^{-5}$	$8.196 \cdot 10^{-4}$	$1.011 \cdot 10^{-4}$
512	$5.579 \cdot 10^{-6}$	$2.725 \cdot 10^{-4}$	$2.118 \cdot 10^{-5}$
768	$1.912 \cdot 10^{-6}$	$9.070 \cdot 10^{-5}$	$6.096 \cdot 10^{-6}$
n	1.8515	1.5992	2.2336
Ra= 10^4			
64	$6.592 \cdot 10^{-4}$	$1.533 \cdot 10^{-2}$	$2.730 \cdot 10^{-3}$
128	$1.618 \cdot 10^{-4}$	$5.414 \cdot 10^{-3}$	$6.898 \cdot 10^{-4}$
256	$4.130 \cdot 10^{-5}$	$2.155 \cdot 10^{-3}$	$1.746 \cdot 10^{-4}$
512	$9.769 \cdot 10^{-6}$	$7.073 \cdot 10^{-4}$	$3.976 \cdot 10^{-5}$
768	$2.925 \cdot 10^{-6}$	$2.354 \cdot 10^{-4}$	$1.152 \cdot 10^{-5}$
n	2.134	1.6176	2.1557
Ra= 10^5			
64	$2.660 \cdot 10^{-3}$	$3.368 \cdot 10^{-2}$	$7.557 \cdot 10^{-3}$
128	$6.305 \cdot 10^{-4}$	$7.985 \cdot 10^{-3}$	$1.930 \cdot 10^{-3}$
256	$1.449 \cdot 10^{-4}$	$2.653 \cdot 10^{-3}$	$4.813 \cdot 10^{-4}$
512	$2.893 \cdot 10^{-5}$	$8.254 \cdot 10^{-4}$	$1.061 \cdot 10^{-4}$
768	$7.650 \cdot 10^{-6}$	$2.715 \cdot 10^{-4}$	$2.947 \cdot 10^{-5}$
n	2.3107	1.8631	2.1866
Ra= 10^6			
64	$8.858 \cdot 10^{-3}$	$8.786 \cdot 10^{-2}$	$2.468 \cdot 10^{-2}$
128	$2.208 \cdot 10^{-3}$	$1.667 \cdot 10^{-2}$	$6.323 \cdot 10^{-3}$
256	$5.195 \cdot 10^{-4}$	$3.695 \cdot 10^{-3}$	$1.523 \cdot 10^{-3}$
512	$1.034 \cdot 10^{-4}$	$9.342 \cdot 10^{-4}$	$3.202 \cdot 10^{-4}$
768	$2.686 \cdot 10^{-5}$	$2.939 \cdot 10^{-4}$	$8.654 \cdot 10^{-5}$
n	2.2894	2.2408	2.2322
Ra= 10^8			
64	$1.228 \cdot 10^{-1}$	$6.947 \cdot 10^{-1}$	$5.363 \cdot 10^{-1}$
128	$2.744 \cdot 10^{-2}$	$1.408 \cdot 10^{-1}$	$2.152 \cdot 10^{-1}$
256	$6.816 \cdot 10^{-3}$	$2.539 \cdot 10^{-2}$	$7.045 \cdot 10^{-2}$
512	$1.632 \cdot 10^{-3}$	$5.084 \cdot 10^{-3}$	$1.722 \cdot 10^{-2}$
1024	$3.254 \cdot 10^{-4}$	$9.575 \cdot 10^{-4}$	$3.411 \cdot 10^{-3}$
n	2.1191	2.3797	1.8236

Tabela 5.3: Natural convection in a square cavity: grid convergence for Ma = 0.1.

N	$|T|_{L_\infty}$	$|P|_{L_\infty}$	$|\mathbf{u}|_{L_2}$
Ra$= 10^3$			
64	$2.640{\cdot}10^{-4}$	$4.990{\cdot}10^{-3}$	$1.757{\cdot}10^{-3}$
128	$8.756{\cdot}10^{-5}$	$1.986{\cdot}10^{-3}$	$4.363{\cdot}10^{-4}$
256	$3.225{\cdot}10^{-5}$	$8.263{\cdot}10^{-4}$	$1.080{\cdot}10^{-4}$
512	$1.029{\cdot}10^{-5}$	$2.750{\cdot}10^{-4}$	$2.380{\cdot}10^{-5}$
768	$3.456{\cdot}10^{-6}$	$9.134{\cdot}10^{-5}$	$6.943{\cdot}10^{-6}$
n	1.6862	1.5513	2.1856
Ra$= 10^4$			
64	$6.759{\cdot}10^{-4}$	$1.277{\cdot}10^{-2}$	$2.877{\cdot}10^{-3}$
128	$1.817{\cdot}10^{-4}$	$5.118{\cdot}10^{-3}$	$7.626{\cdot}10^{-4}$
256	$5.275{\cdot}10^{-5}$	$2.127{\cdot}10^{-3}$	$2.133{\cdot}10^{-4}$
512	$1.585{\cdot}10^{-5}$	$7.069{\cdot}10^{-4}$	$5.494{\cdot}10^{-5}$
768	$5.378{\cdot}10^{-6}$	$2.355{\cdot}10^{-4}$	$1.679{\cdot}10^{-5}$
n	1.8947	1.5493	2.0191
Ra$= 10^5$			
64	$2.634{\cdot}10^{-3}$	$2.332{\cdot}10^{-2}$	$7.966{\cdot}10^{-3}$
128	$6.203{\cdot}10^{-4}$	$6.706{\cdot}10^{-3}$	$2.088{\cdot}10^{-3}$
256	$1.464{\cdot}10^{-4}$	$2.505{\cdot}10^{-3}$	$5.606{\cdot}10^{-4}$
512	$3.120{\cdot}10^{-5}$	$8.100{\cdot}10^{-4}$	$1.364{\cdot}10^{-4}$
768	$8.611{\cdot}10^{-6}$	$2.685{\cdot}10^{-4}$	$4.017{\cdot}10^{-5}$
n	2.2573	1.7234	2.0797
Ra$=10^6$			
64	$9.132{\cdot}10^{-3}$	$5.989{\cdot}10^{-2}$	$2.515{\cdot}10^{-2}$
128	$2.222{\cdot}10^{-3}$	$1.202{\cdot}10^{-2}$	$6.493{\cdot}10^{-3}$
256	$5.219{\cdot}10^{-4}$	$3.089{\cdot}10^{-3}$	$1.660{\cdot}10^{-3}$
512	$1.048{\cdot}10^{-4}$	$8.712{\cdot}10^{-4}$	$3.844{\cdot}10^{-4}$
768	$2.741{\cdot}10^{-5}$	$2.818{\cdot}10^{-4}$	$1.104{\cdot}10^{-4}$
n	2.2921	2.0921	2.1386

Tabela 5.4: Natural convection in a square cavity: grid convergence for Ma = 0.15.*-
the reference solution for Ra= 10^3 is the one with $N = 768$.

N	$|T|_{L_\infty}$	$|P|_{L_\infty}$	$|\mathbf{u}|_{L_2}$
Ra= 10^3*			
64	$3.118 \cdot 10^{-4}$	$4.744 \cdot 10^{-3}$	$1.782 \cdot 10^{-3}$
128	$1.127 \cdot 10^{-4}$	$1.908 \cdot 10^{-3}$	$4.453 \cdot 10^{-4}$
256	$4.163 \cdot 10^{-5}$	$7.462 \cdot 10^{-4}$	$1.086 \cdot 10^{-4}$
512	$1.017 \cdot 10^{-5}$	$1.853 \cdot 10^{-4}$	$1.928 \cdot 10^{-5}$
n	1.6251	1.5390	2.1626
Ra= 10^4			
64	$7.154 \cdot 10^{-4}$	$1.198 \cdot 10^{-2}$	$3.035 \cdot 10^{-3}$
128	$2.079 \cdot 10^{-4}$	$5.040 \cdot 10^{-3}$	$8.515 \cdot 10^{-4}$
256	$7.111 \cdot 10^{-5}$	$2.126 \cdot 10^{-3}$	$2.595 \cdot 10^{-4}$
512	$2.421 \cdot 10^{-5}$	$7.073 \cdot 10^{-4}$	$7.165 \cdot 10^{-5}$
768	$8.196 \cdot 10^{-6}$	$2.357 \cdot 10^{-4}$	$2.247 \cdot 10^{-5}$
n	1.7324	1.5258	1.9194
Ra= 10^5			
64	$2.613 \cdot 10^{-3}$	$1.967 \cdot 10^{-2}$	$8.344 \cdot 10^{-3}$
128	$6.219 \cdot 10^{-4}$	$6.295 \cdot 10^{-3}$	$2.274 \cdot 10^{-3}$
256	$1.533 \cdot 10^{-4}$	$2.460 \cdot 10^{-3}$	$6.525 \cdot 10^{-4}$
512	$3.485 \cdot 10^{-5}$	$8.047 \cdot 10^{-4}$	$1.703 \cdot 10^{-4}$
768	$1.023 \cdot 10^{-5}$	$2.678 \cdot 10^{-4}$	$5.202 \cdot 10^{-5}$
n	2.1851	1.6602	1.9917
Ra= 10^6			
64	$9.262 \cdot 10^{-3}$	$4.934 \cdot 10^{-2}$	$2.566 \cdot 10^{-2}$
128	$2.232 \cdot 10^{-3}$	$1.046 \cdot 10^{-2}$	$6.821 \cdot 10^{-3}$
256	$5.260 \cdot 10^{-4}$	$2.888 \cdot 10^{-3}$	$1.858 \cdot 10^{-3}$
512	$1.072 \cdot 10^{-4}$	$8.506 \cdot 10^{-4}$	$4.635 \cdot 10^{-4}$
768	$2.845 \cdot 10^{-5}$	$2.780 \cdot 10^{-4}$	$1.387 \cdot 10^{-4}$
n	2.2825	2.0163	2.0520

Tabela 5.5: Natural convection in a square cavity: convergence of Nusselt numbers and maximal velocities and their positions for Ma = 0.01.*- values omitted from the fit.

N	u_{max}	y	v_{max}	x	Nu	$Nu_{1/2}$
Ra= 10^3						
64	3.65629	0.81329	3.69244	0.17875	1.10912	1.11825
128	3.65234	0.81330	3.69499	0.17856	1.11344	1.11790
256	3.65076	0.81327	3.69623	0.17846	1.11561	1.11782
512	3.65008	0.81326	3.69684	0.17840	1.11670	1.11780
768	3.64986	0.81325	3.69704	0.17837	1.11706	1.11779
1024	3.64975	0.81325	3.69714	0.17836	1.11724	1.11779
∞	3.64945	0.81324	3.69744	0.17832	1.11778	1.11778
Ra= 10^4						
64	16.17183	0.82244	19.59757	0.11966	2.23155	2.25000
128	16.17603	0.82292	19.61129	0.11930	2.23710	2.24609
256	16.17919	0.82309	19.61943	0.11909	2.24069	2.24513
512	16.18114	0.82316	19.62376	0.11898	2.24269	2.24489
768	16.18185	0.82318	19.62524	0.11894	2.24338	2.24485
1024	16.18222	0.82320	19.62601	0.11892	2.24373	2.24483
∞	16.18340	0.82323	19.62830	0.11886	2.24481	2.24481
Ra= 10^5						
64	34.43644	0.85271	68.82944	0.06626	4.52089*	4.55751
128	34.56981	0.85370	68.67551	0.06604	4.51241	4.53036
256	34.65174	0.85419	68.64584	0.06597	4.51489	4.52379
512	34.69525	0.85441	68.63845	0.06592	4.51774	4.52217
768	34.71022	0.85448	68.63699	0.06590	4.51892	4.52187
1024	34.71780	0.85451	68.63646	0.06589	4.51955	4.52177
∞	34.74050	0.85461	68.63500	0.06585	4.52160	4.52160
Ra= 10^6						
64	66.31031	0.85079	222.45383	0.03807	8.82095	8.82671
128	65.10217	0.84961	220.82891	0.03775	8.97848	9.05081
256	64.87421	0.84966	220.58087	0.03778	8.84599	8.88117
512	64.83188	0.84976	220.55092	0.03778	8.82159	8.83898
768	64.82778	0.84981	220.55138	0.03777	8.81996	8.82861
1024	64.82770	0.84983	220.55338	0.03777	8.82173	8.82605
∞	64.83190	0.84990	220.56600	0.03775	8.82522	8.82522
Ra= 10^7						
64	166.86413*	0.86819	659.33366*	0.02152	17.68625	17.82338
128	154.37172	0.87314	704.65400*	0.02125	16.78495	16.85144
256	149.84663	0.87812	700.20230	0.02128	16.57263	16.60530
512	148.84643	0.87921	699.45001	0.02130	16.52722	16.54344
768	148.68581	0.87934	699.36131	0.02131	16.52130	16.53209
1024	148.63414	0.87937	699.33808	0.02130	16.52006	16.52814
2048	148.59562	0.87937	699.33198	0.02130	16.52031	16.52435
∞	148.58000	0.87940	699.32400	0.02130	16.52310	16.52320

Tabela 5.6: Natural convection in a square cavity: convergence of Nusselt numbers and maximal velocities and their positions for Ma = 0.05.

N	u_{max}	y	v_{max}	x	Nu	$Nu_{1/2}$
Ra= 10^3						
64	3.65665	0.81328	3.69282	0.17875	1.10913	1.11822
128	3.65250	0.81329	3.69526	0.17856	1.11343	1.11789
256	3.65087	0.81327	3.69648	0.17846	1.11559	1.11782
512	3.65016	0.81325	3.69708	0.17840	1.11668	1.11780
768	3.64994	0.81324	3.69729	0.17838	1.11704	1.11780
1024	3.64983	0.81324	3.69739	0.17837	1.11722	1.11780
∞	3.64952	0.81322	3.69769	0.17834	1.11776	1.11780
Ra= 10^4						
64	16.17599	0.82239	19.60140	0.11965	2.23160	2.25005
128	16.17785	0.82289	19.61313	0.11930	2.23709	2.24608
256	16.18028	0.82307	19.62094	0.11909	2.24066	2.24510
512	16.18190	0.82315	19.62516	0.11898	2.24265	2.24485
768	16.18250	0.82318	19.62661	0.11894	2.24334	2.24480
1024	16.18281	0.82319	19.62734	0.11892	2.24369	2.24479
∞	16.18380	0.82323	19.62950	0.11886	2.44760	2.24476
Ra= 10^5						
64	34.41572	0.85241	68.82834	0.06623	4.52098	4.55757
128	34.56839	0.85362	68.67820	0.06604	4.51233	4.53026
256	34.65212	0.85415	68.64821	0.06596	4.51480	4.52369
512	34.69677	0.85439	68.64098	0.06591	4.51764	4.52207
768	34.71213	0.85447	68.63961	0.06590	4.51882	4.52177
1024	34.71990	0.85451	68.63911	0.06589	4.51946	4.52167
∞	34.74360	0.85462	68.63800	0.06586	4.52153	4.52153
Ra= 10^6						
64	66.04260	0.84973	222.11650	0.03804	8.98358	9.05594
128	65.08150	0.84926	220.81599	0.03774	8.84599	8.88116
256	64.87265	0.84952	220.59140	0.03778	8.82147	8.83886
512	64.83385	0.84971	220.56106	0.03778	8.81984	8.82849
768	64.83106	0.84979	220.56111	0.03777	8.82083	8.82658
1024	64.83161	0.84983	220.56288	0.03777	8.82160	8.82592
∞	64.83940	0.84994	220.57600	0.03774	8.82508	8.82509
Ra= 10^8						
256	364.92262	0.93898	2236.44327	0.01201	30.64091	30.70105
512	329.87857	0.93039	2224.82989	0.01199	30.31308	30.34281
1024	323.67959	0.92808	2222.93528	0.01200	30.23916	30.25396
2048	322.47709	0.92791	2222.57050	0.01200	30.22461	30.23200
∞	321.61300	0.92790	2222.48000	0.01200	30.22360	30.22460

Tabela 5.7: Natural convection in a square cavity: convergence of Nusselt numbers and maximal velocities and their positions for Ma = 0.1.

N	u_{max}	y	v_{max}	x	Nu	$Nu_{1/2}$
Ra= 10^3						
64	3.65710	0.81326	3.69364	0.17875	1.10908	1.11821
128	3.65281	0.81326	3.69604	0.17857	1.11336	1.11790
256	3.65113	0.81324	3.69724	0.17847	1.11552	1.11784
512	3.65039	0.81323	3.69784	0.17840	1.11660	1.11783
768	3.65016	0.81322	3.69803	0.17838	1.11696	1.11783
1024	3.65004	0.81322	3.69813	0.17837	1.11714	1.11783
∞	3.64971	0.81321	3.69842	0.17833	1.11768	1.11783
Ra= 10^4						
64	16.18093	0.82231	19.60712	0.11964	2.23155	2.24998
128	16.18089	0.82285	19.61779	0.11930	2.23698	2.24596
256	16.18246	0.82305	19.62528	0.11909	2.24052	2.24496
512	16.18365	0.82314	19.62936	0.11897	2.24249	2.24470
768	16.18411	0.82317	19.63077	0.11894	2.24318	2.24465
1024	16.18435	0.82318	19.63148	0.11892	2.24353	2.24463
∞	16.18510	0.82322	19.63360	0.11886	2.44600	2.24460
Ra= 10^5						
64	34.41215	0.85219	68.83653	0.06622	4.52068	4.55722
128	34.57100	0.85354	68.68623	0.06603	4.51203	4.52995
256	34.65772	0.85413	68.65651	0.06596	4.51449	4.52338
512	34.70392	0.85440	68.64961	0.06591	4.51734	4.52177
768	34.71980	0.85449	68.64833	0.06589	4.51852	4.52147
1024	34.72782	0.85453	68.64791	0.06588	4.51915	4.52137
∞	34.75230	0.85466	68.64700	0.06584	4.52123	4.52123
Ra= 10^6						
64	65.95183	0.84877	222.06853	0.03802	8.98417	9.05652
128	65.08016	0.84901	220.84664	0.03773	8.84559	8.88075
256	64.88160	0.84941	220.62340	0.03778	8.82108	8.83846
512	64.84803	0.84971	220.59182	0.03777	8.81942	8.82807
768	64.84712	0.84983	220.59150	0.03777	8.82039	8.82615
1024	64.84854	0.84989	220.59309	0.03776	8.82116	8.82548
∞	64.86070	0.85009	220.60600	0.03773	8.82460	8.82460

Tabela 5.8: Natural convection in a square cavity: convergence of Nusselt numbers and maximal velocities and their positions for Ma = 0.15.

N	u_{max}	y	v_{max}	x	Nu	$Nu_{1/2}$
Ra= 10^3						
64	3.65770	0.81322	3.69494	0.17876	1.10898	1.11822
128	3.65327	0.81323	3.69730	0.17858	1.11324	1.11794
256	3.65152	0.81321	3.69849	0.17848	1.11539	1.11788
512	3.65075	0.81319	3.69908	0.17842	1.11647	1.11788
768	3.65051	0.81318	3.69928	0.17839	1.11683	1.11788
∞	3.65005	0.81316	3.69967	0.17834	1.11755	1.11789
Ra= 10^4						
64	16.18671	0.82223	19.61542	0.11963	2.23138	2.24981
128	16.18484	0.82280	19.62520	0.11930	2.23675	2.24574
256	16.18555	0.82302	19.63237	0.11909	2.24027	2.24472
512	16.18630	0.82312	19.63629	0.11897	2.24224	2.24445
768	16.18662	0.82316	19.63765	0.11893	2.24292	2.24440
1024	16.18678	0.82317	19.63833	0.11892	2.24327	2.24438
∞	16.18730	0.82322	19.64040	0.11886	2.24433	2.24434
Ra= 10^5						
64	34.41439	0.85201	68.85101	0.06620	4.52017	4.55667
128	34.57930	0.85348	68.70022	0.06601	4.51153	4.52943
256	34.66913	0.85414	68.67088	0.06595	4.51399	4.52287
512	34.71688	0.85444	68.66425	0.06590	4.51683	4.52126
768	34.73329	0.85453	68.66309	0.06588	4.51801	4.52097
1024	34.74155	0.85458	68.66270	0.06587	4.51865	4.52087
∞	34.76680	0.85471	68.66200	0.06583	4.52100	4.52100
Ra= 10^6						
64	65.91483	0.84796	222.09400	0.03801	8.98376	9.05609
128	65.09141	0.84874	220.90094	0.03773	8.84490	8.88005
256	64.90330	0.84938	220.67544	0.03777	8.82039	8.83776
512	64.87526	0.84979	220.64249	0.03777	8.81870	8.82735
768	64.87624	0.84994	220.64178	0.03776	8.81966	8.82542
1024	64.87871	0.85002	220.64318	0.03776	8.82043	8.82475
∞	64.89440	0.85027	220.65600	0.03773	8.82380	8.82380

Tabela 5.9: Natural convection in a square cavity: Mach number influence on Nu and $\mathbf{u}_{\max}$.

Ma	u_{max}	y	v_{max}	x	Nu	$Nu_{1/2}$
Ra= 10^3						
0.01	3.64945	0.81324	3.69744	0.17832	1.11778	1.11778
0.05	3.64952	0.81322	3.69769	0.17834	1.11776	1.11780
0.1	3.64971	0.81321	3.69842	0.17833	1.11768	1.11783
0.15	3.65005	0.81316	3.69967	0.17834	1.11755	1.11789
Ra= 10^4						
0.01	16.1834	0.823230	19.6283	0.118860	2.24481	2.24481
0.05	16.1838	0.823231	19.6295	0.118862	2.44760	2.24476
0.1	16.1851	0.823223	19.6336	0.118862	2.44600	2.24460
0.15	16.1873	0.823223	19.6404	0.118856	2.24433	2.24434
Ra= 10^5						
0.01	34.7405	0.854610	68.635	0.0658500	4.52160	4.52160
0.05	34.7436	0.854621	68.638	0.0658644	4.52153	4.52153
0.1	34.7523	0.854656	68.647	0.0658441	4.52123	4.52123
0.15	34.7668	0.854712	68.662	0.0658313	4.52100	4.52100
Ra= 10^6						
0.01	64.8319	0.849900	220.566	0.0377500	8.82522	8.82522
0.05	64.8394	0.849944	220.576	0.0377445	8.82508	8.82509
0.1	64.8607	0.850091	220.606	0.0377313	8.82460	8.82460
0.15	64.8944	0.850268	220.656	0.0377349	8.82380	8.82380

5.3.4 Comparison with benchmark solutions and other numerical methods

The asymptotic values computed with Ma= 0.01 are compared with literature values by different authors and methods in Tabs. 5.11-5.12. Up to Ra= 10^6 we can observe excellent agreement with precise values by Le Quéré [237–239] obtained by the pseudo spectral method and also with Wang et al. [292] obtained by the incompressible version of MRT LBM. For the Rayleigh numbers above 10^6 our results are still the same or very close to the ones obtained by Le Queré and other authors. In Tab. 5.13 are averaged values for high Ra numbers, obtained in the following way: we performed 10^8 iterations with Ma= 0.05, the results in the table are averaged values from the last $5 \cdot 10^7$ iterations. We obtained different values of velocity components for Ra= 10^9 while their positions and Nusselt numbers are consistent with other authors. For the case of Ra= 10^{10} the situation is the same, except position of the $v_{\max}$ reported by Dixit [74] (but this could be typo in the original text). The Nusselt numbers obtained from CTLBM simulation is very close to the values given by Le Quéré and Dixit.

From the computation point of view, the number of iterations needed to achieve steady state prescribed earlier is also of interest. The summary is given in the Tab. 5.10 and it can be seen from the values there that increasing resolution twice also

Tabela 5.10: Natural convection in a square cavity: number of iterations needed to reach steady state.

N	Ra$= 10^3$	Ra$= 10^4$	Ra$= 10^5$	Ra$= 10^6$	Ra$= 10^7$
Ma$= 0.01$					
64	663000	1406000	1961000	3570000	7193000
128	1296000	2780000	3810000	6965000	14265000
256	2528000	5410000	7325000	13388000	27631000
512	4910000	10513000	14000000	25557000	53103000
768	7238000	15483000	20408000	37222000	58791000
1024	9522000	13483000	26643000	48564000	76547000
Ma$= 0.05$					Ra$= 10^8$
64	141000	302000	602000	1116000	unstable
128	278000	595000	1189000	2198000	4663000
256	542000	1163000	2322000	4293000	9481000
512	1056000	2264000	4520000	8348000	17884000
768	1557000	3339000	6664000	12304000	25987000
1024	2051000	4396000	8773000	16193000	33887000
Ma$= 0.1$					
64	73000	156000	310000	570000	-
128	143000	307000	612000	1130000	-
256	279000	599000	1196000	2211000	-
512	544000	1167000	2331000	4305000	-
768	803000	1722000	3438000	6350000	-
1024	1057000	2268000	4528000	8361000	-
Ma$= 0.15$					
64	50000	106000	210000	387000	-
128	97000	208000	415000	766000	-
256	190000	407000	812000	1500000	-
512	369000	792000	1582000	2922000	-
768	544000	1169000	2334000	4310000	-
1024	unstable	1540000	3074000	5677000	-

approximately doubles the iterations count. Situation is the same with increasing Ra number, where increasing Ra by one order causes double increase in iterations. The numerical code was implemented in NVIDIA CUDA framework [59] and ran on different GPUs. The highest MLUPS (Million Lattice Updates Per Second) was achieved on NVIDIA TESLA K40 and NVIDIA GEFORCE TITAN Z cards; 1056 MLUPS and 869 MLUPS respectively are the average performance of the GPUs.

5.3.5 Results for high Rayleigh numbers

Averaged vertical velocities and temperature profiles at different vertical positions are compared in Fig. 5.2. From the figures one can clearly see formation of the thin boundary layers, with steep gradients of velocity and temperature.

The local Nusselt number at hot wall and the wall shear stress distributions for Ra$= 10^8$–10^{10} are presented in Fig. 5.3. The comparison of experimental data by Tian et al. [282] and King [162] are presented in Fig. 5.4 together with data from Le Quéré and Behnia [238]. We can observe good agreement for both Nusselt number and shear stress values along hot wall.

In Fig. 5.5 dimensionless velocities and temperatures are reported in wall units defined earlier, we can observe a clue of the universal profile up to $y^+ = 5$ for the vertical velocities and up to $y^+ = 11$ for the temperature within the near-wall region.

Temperature stratification for different Ra numbers is plotted in Fig. 5.6 and also reported in Tab. 5.14, where we give its numerical values defined as

$$S_T = \frac{\partial T}{\partial y}(0.5, 0.5)$$

where T and y are dimensionless.

Tabela 5.11: Natural convection in a square cavity: comparison with literature.

ref.	u_{max}	y	v_{max}	x	$Nu_{1/2}$	Nu/Nu_0
Ra= 10^3						
CTLBM	3.64945	0.81324	3.69744	0.17832	1.11778	1.11778
Le Quéré [239]	3.6494	0.813	3.6974	0.178	1.1178	1.1178[†]
Wang [292]	3.6494	0.8132	3.6974	0.1783	1.1178	1.1178
Dixit [74]	3.6529	0.8125	3.682	0.17183	1.118	1.121
Kuznik [167]	3.636	0.809	3.686	0.174	-	-
Mezrhab [204]	3.667	-	3.714	-	-	1.112
Dubois [80]	3.649	0.814	3.697	0.176	-	1.117
Li [184]	3.664	0.81	3.699	0.18	-	1.207
D'Orazio [76]	3.6532	0.8125	3.7006	0.1797	-	1.117
VahlDavis1983 [65]	3.649	0.813	3.697	0.178	1.118	1.118
Ra= 10^4						
CTLBM	16.1834	0.82323	19.6283	0.11886	2.24481	2.24481
Le Quéré [239]	16.183	0.823	19.629	0.119	2.245	2.245[†]
Wang [292]	16.1834	0.8232	19.6278	0.1189	2.2447	2.2447
Dixit [74]	16.163	0.828	19.569	0.125	2.256	2.286
Kuznik [167]	16.167	0.821	19.597	0.12	-	-
Mezrhab [204]	16.202	-	19.644	-	-	2.241
Dubois [80]	16.188	0.822	19.632	0.119	-	2.243
Li [184]	16.351	0.82	19.589	0.12	-	2.2528
D'Orazio [76]	16.237	0.8203	19.6803	0.1172	-	2.235
VahlDavis [65]	16.178	0.823	19.617	0.119	2.243	2.243
Ra= 10^5						
CTLBM	34.7405	0.85461	68.635	0.06585	4.5216	4.52160
Le Quéré [239]	34.75	0.855	68.64	0.066	4.523	4.522[†]
Wang [292]	34.743	0.8546	68.6318	0.06588	4.5214	4.5213
Dixit [74]	35.521	0.8554	68.655	0.0664	4.519	4.5463
Kuznik [167]	34.962	0.854	68.578	0.067	-	-
Mezrhab [204]	34.805	-	68.63	-	-	4.519
Dubois [80]	34.748	0.856	68.652	0.065	-	4.517
Li [184]	35.703	0.855	68.536	0.065	-	4.535
D'Orazio [76]	34.8225	0.8529	68.7122	0.0637	-	4.504
VahlDavis [65]	34.73	0.855	68.59	0.066	4.519	4.519
Ra= 10^6						
CTLBM	64.8319	0.8499	220.566	0.03775	8.8252	8.8252
Le Quéré [237]	64.83	0.85	220.6	0.038	8.825	8.825[†]
Wang [292]	64.8277	0.8498	220.5506	0.03779	8.8256	8.8247
Contrino [58]	64.8334	0.8499	220.5644	0.0378	8.8252	8.8252
Dixit [74]	64.186	0.8496	219.866	0.0371	8.5074	8.805
Kuznik [167]	64.133	0.86	220.537	0.038	-	-
Mezrhab [204]	64.793	-	219.663	-	-	8.817
Dubois [80]	64.842	0.849	220.669	0.037	-	8.806
D'Orazio [76]	64.8679	0.8529	221.1869	0.0392	-	8.767
VahlDavis1983 [65]	64.63	0.85	219.36	0.0379	8.799	8.8

Tabela 5.12: Natural convection in a square cavity: comparison with literature cont.

ref.	$u_{\max}$	y	$v_{\max}$	x	$Nu_{1/2}$	Nu/Nu_0
Ra= 10^7						
CTLBM	148.58	0.8794	699.324	0.0213	16.5231	16.5232
Le Quéré [237]	148.58	0.879	699.236	0.021	16.523	16.523[†]
Contrino [58]	148.5852	0.8793	699.3224	0.0213	16.5231	16.5231
Dixit [74]	164.236	0.851	701.922	0.02	16.79[†]	-
Kuznik [167]	148.768	0.881	702.029	0.02	16.408	-
Mezrhab [204]	148.4	-	998.3	-	-	16.51
Mayne [198]	145.2666	0.8845	703.2526	0.0215	16.3869[†]	-
Wan [289]	143.56	0.922	714.48	0.022	-	16.656
Ra= 10^8						
CTLBM	321.613	0.9279	2222.48	0.012	30.2236	30.2246
Le Quéré [237]	321.9	0.928	2222.0	0.012	30.225	30.225[†]
Contrino [58]	321.9063	0.9279	2222.3279	0.012	30.2251	30.2251
Dixit [74]	389.877	0.937	2241.374	0.0112	30.506[†]	-
Kuznik [167]	321.457	0.94	2243.36	0.121	28.819[†]	-
Mezrhab [204]	305.332	-	2169.562	-	-	30.033
Mayne [198]	283.0689	0.9455	2223.4424	0.013	29.6256[†]	-
Wan [289]	296.71	0.93	2259.08	0.012	-	31.486
Markatos [193]	514.3	0.941	1812	0.0135	-	32.045

Tabela 5.13: Natural convection in a square cavity: comparison with literature cont.

ref.	$u_{\max}$	y	$v_{\max}$	x	$Nu_{1/2}$	Nu/Nu_0
Ra= 10^9						
CTLBM	491.56	0.911	7040.9422	0.0064	54.8217	54.7531
Le Quéré [238]	-	-	-	-	54.6	-
Dixit [74]	503.24	0.966	6820.07	0.0064	57.35[†]	-
Barakos [16]	-	-	-	-	-	60.1
Henkes1991 [130]	-	-	-	-	-	59.5
Ra= 10^{10}						
CTLBM	1252	0.97	22290	0.0034	99.836	100.2
Le Quéré [238]	-	-	-	-	100	-
Dixit [74]	2323	0.940233	21463	0.49072	103.663[†]	-
Markatos [193]	2323	0.9625	16890	0.0055	-	156.85
Barakos [16]	-	-	-	-	-	134.6
Henkes1991 [130]	-	-	-	-	-	133.4
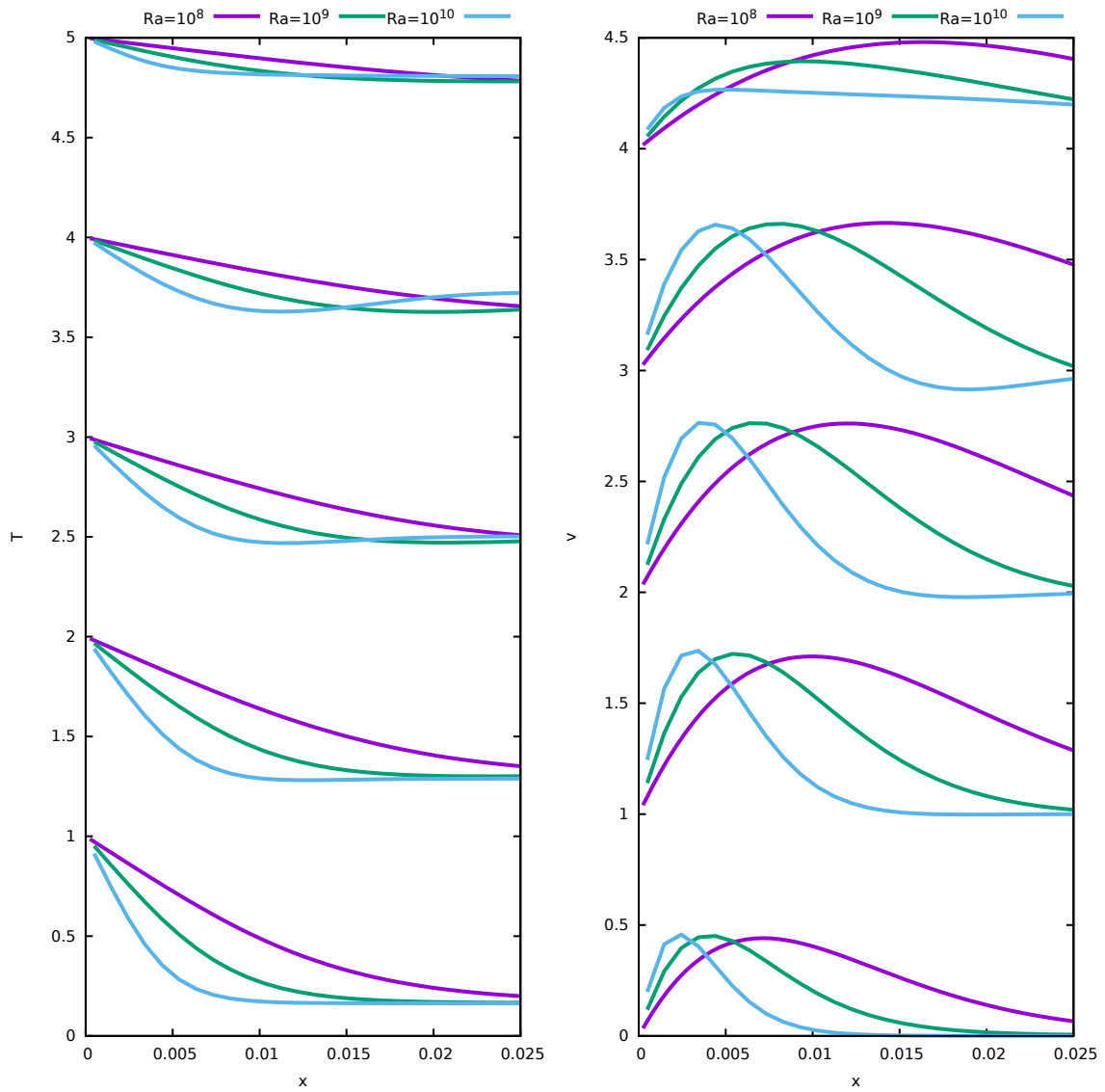
Figura 5.2: Averaged temperature (left) and vertical velocity (right) profiles at different positions $y = 0.1, 0.3, 0.5, 0.7, 0.9$ and Ra=$10^8, 10^9, 10^{10}$.

Tabela 5.14: Averaged temperature stratification for Ra=$10^8, 10^9, 10^{10}$.

Ra	10^8	10^9	10^{10}
S_T	0.9872	0.9996	1.0123
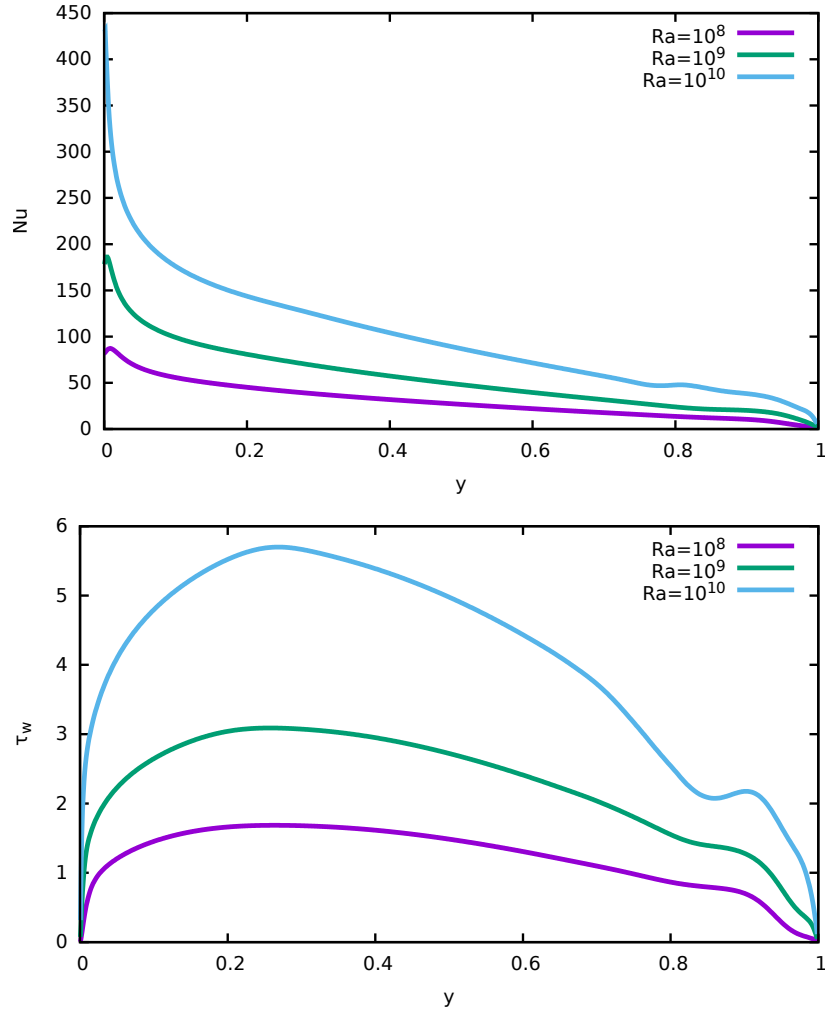
Figura 5.3: Local Nusselt number along hot wall (top) and dimensionless wall shear stress (bottom) profiles.

5.4 Conclusions

The CTLBM was applied to natural convection in differentially heated cavity. From the presented results it is clear that CTLBM can deliver accurate solutions. The performed grid convergence tests showed that the method is of second order. It turned out that CTLBM gives results which agree with benchmark solutions computed by other authors. For the high Ra regime, the Nusselt number and wall shear stress distributions along the hot wall are in good agreement with experimental and DNS data.
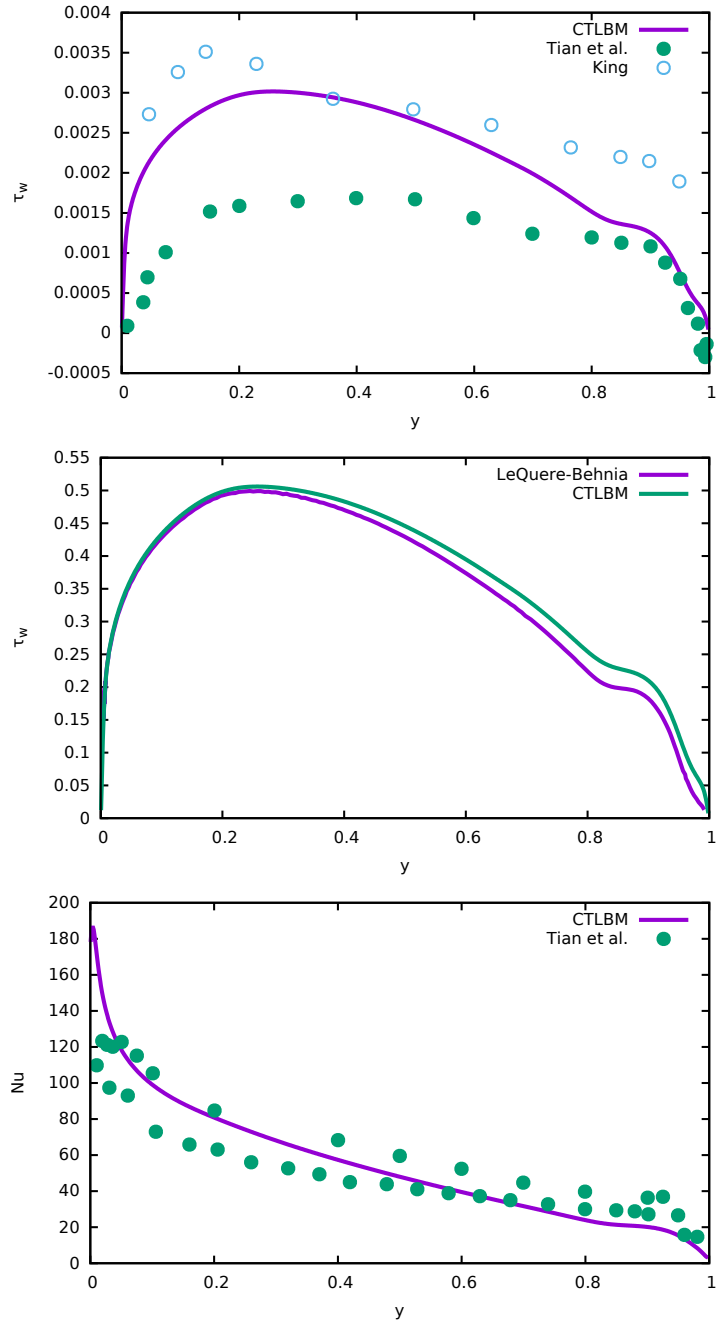
Figura 5.4: Wall shear stress and Nusselt number along hot wall for Ra= 10^9 compared to experimental data of Tian et al. [282] and King [162] (top & bottom) and wall shear stress DNS data by Le Queré and Behnia [238] (center, $\tau_w = \text{Ra}^{-1/4} \partial v / \partial x$).
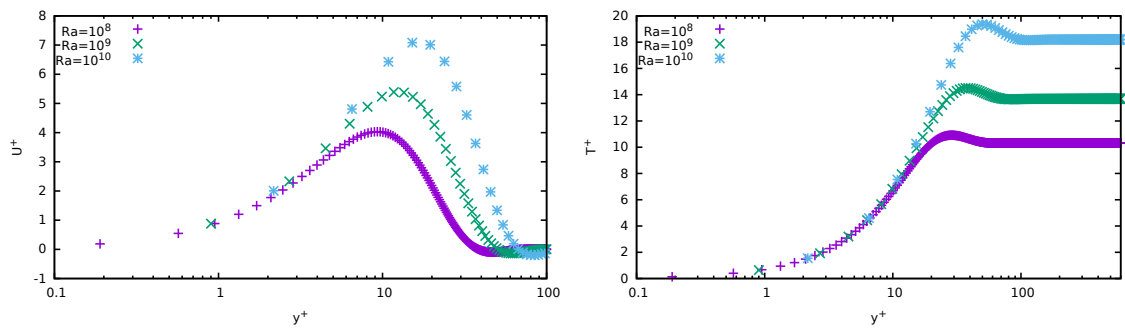
Figura 5.5: Dimensionless velocity U^+ (left) and temperature T^+ (right) in wall units y^+ for the three highest Ra numbers.
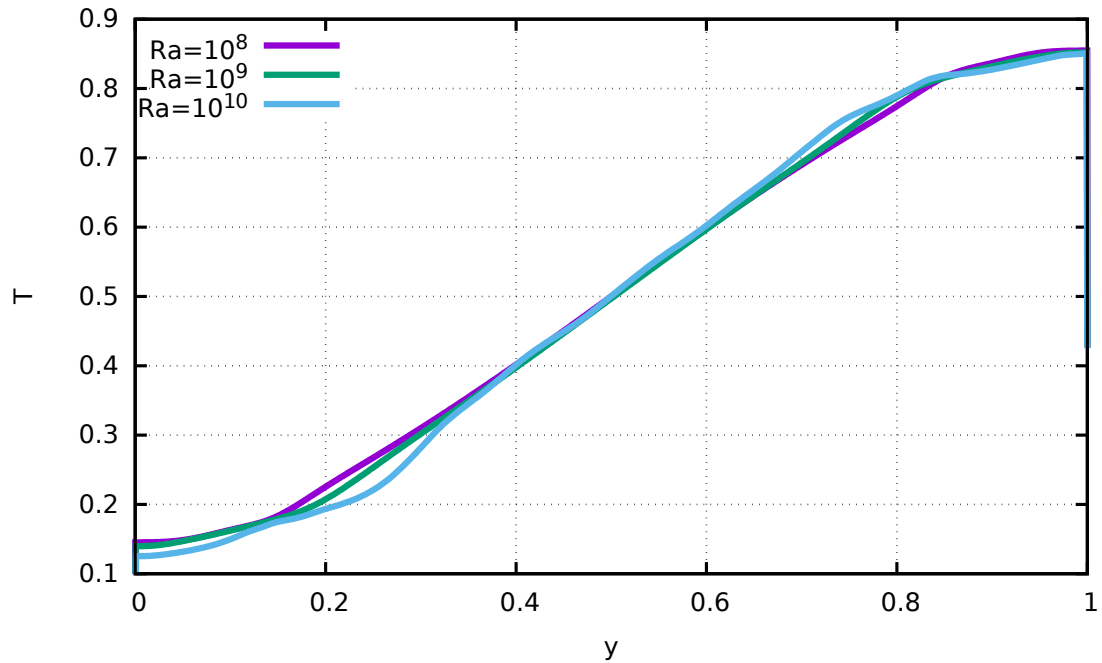
Figura 5.6: Averaged temperature stratification along the mid-width of the cavity.

135

Capítulo 6

Cascaded Lattice Boltzmann Method Application in Forced and Natural Convection From Hot Tube Banks

Robert Straka, **Keerti Vardhan Sharma** and Frederico Wanderley Tavares

6.1 Abstract

Lattice Boltzmann Method is applied to forced and natural convection heat transfer from the tube banks. Hot tubes are cooled by flowing or passive air. Two Reynolds numbers (Re=80 and Re=1600) and two Rayleigh numbers (Ra=10^3 and Ra=10^5) of the corresponding heat transfer regime are studied. The method itself is based on the recently derived cascaded collision operator not only for the fluid flow but also for the temperature field. Using this method and moderate space resolution of the lattice we were able to obtain stable and bounded simulations for the non-trivial geometry.
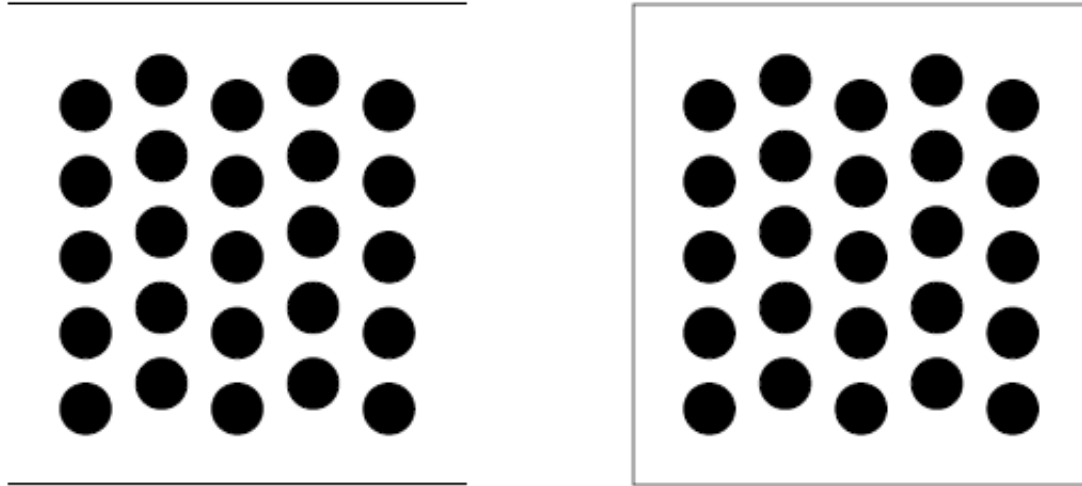
Figura 6.1: Geometry of the channel with hot tube banks for forced convection (left) and adiabatic enclosure with hot tube banks for natural convection (right)

6.2 Forced Convection
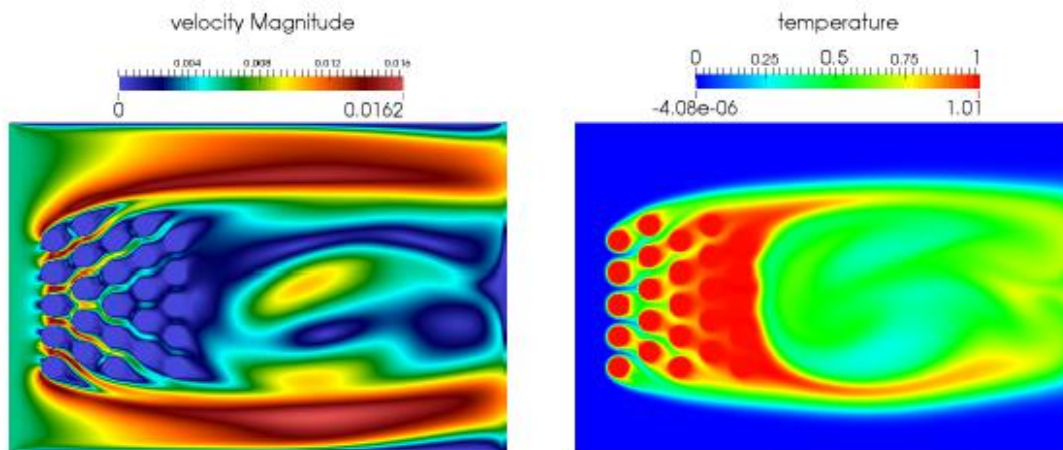
Figura 6.2: Instant velocity magnitude for forced cooling of hot tube banks in the channel at Re=80, Pr=0.71 at lattice time $t^+ = 25.10^4$ (left), Instant temperature for forced cooling of hot tube banks in the channel at Re=80, Pr=0.71 at lattice time $t^+ = 25.10^4$ (left).
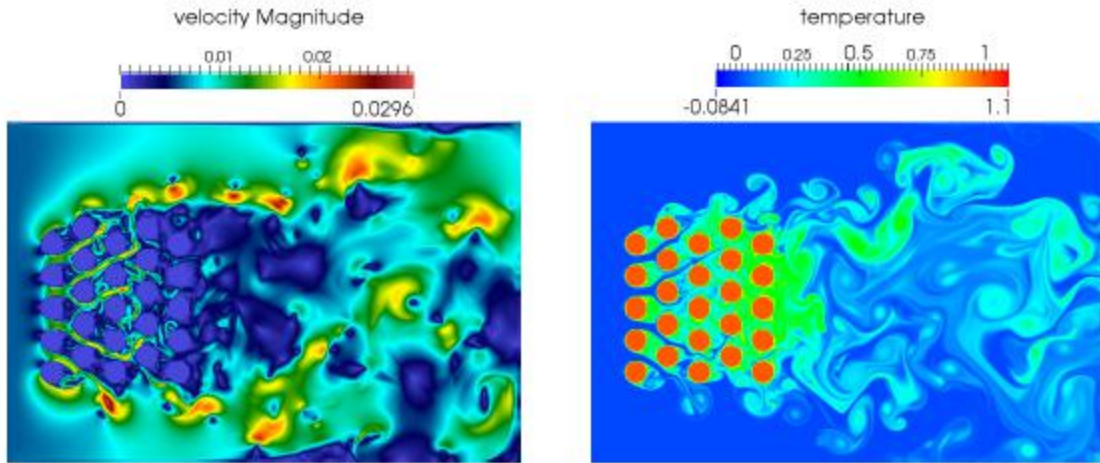
Figura 6.3: Instant velocity magnitude for forced cooling of hot tube banks in the channel at Re=1600, Pr=0.71 at lattice time $t^+ = 25.10^4$ (left), Instant temperature for forced cooling of hot tube banks in the channel at Re=1600, Pr=0.71 at lattice time $t^+ = 25.10^4$ (left).

6.3   Natural Convection
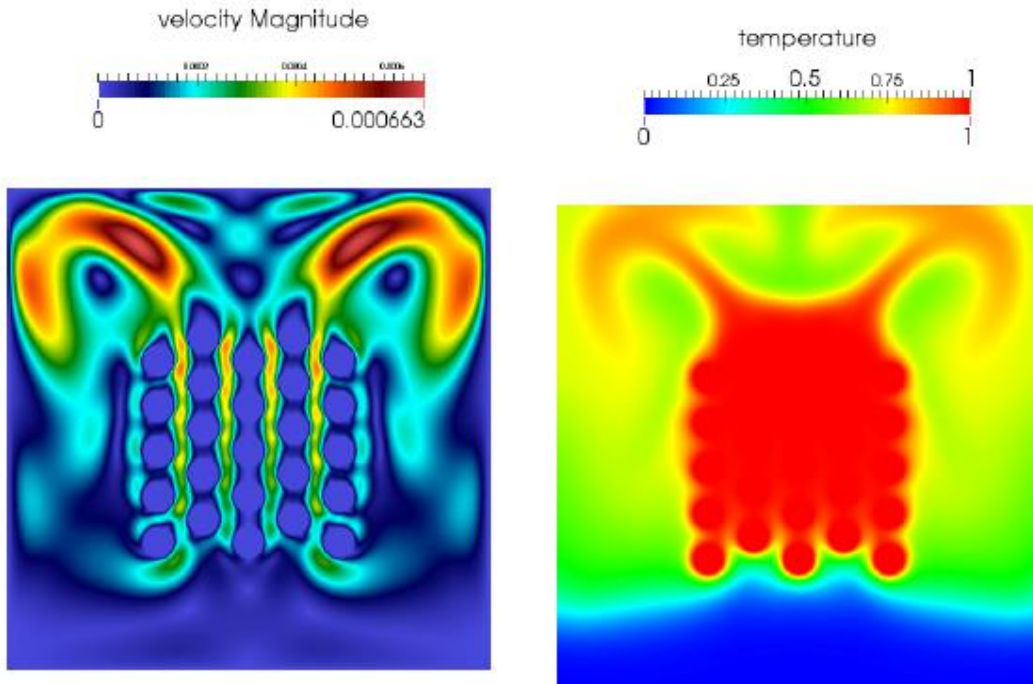
Figura 6.4: Instant velocity magnitude for natural convection from hot tube banks in the channel at Ra=10^3, Pr=0.71 at lattice time $t^+ = 25.10^4$ (left), Instant temperature for natural convection from hot tube banks in the channel at Ra=10^3, Pr=0.71 at lattice time $t^+ = 25.10^4$ (left).
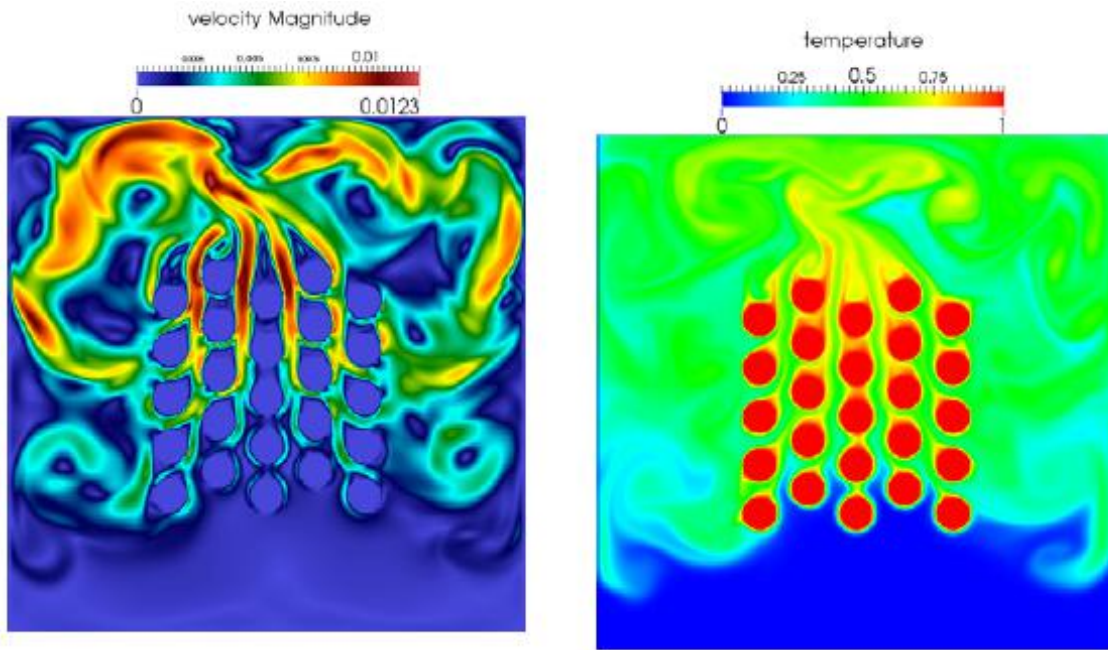
Figura 6.5: Instant velocity magnitude for natural convection from hot tube banks in the channel at Ra=10^5, Pr=0.71 at lattice time $t^+ = 25.10^4$ (left), Instant temperature for natural convection from hot tube banks in the channel at Ra=10^5, Pr=0.71 at lattice time $t^+ = 25.10^4$ (left).

Capítulo 7

Application of Lattice Boltzmann Method in Pore Scale Modeling

7.1 Motivation

After successfully achieving the main goal of the PhD (development and implementations of the Double Population Cascaded LBM scheme), we intended to start working in the direction of its applications in porous media fluid flow. Therefore, we selected a real world porous rocks with industrial importance to simulate flux through porous media. We developed a systematic study in which we first studied the imaging techniques using micro-CT of porous rocks for reliable simulations of fluid flow. Motivated by the idea of manipulating microscopic properties that could be captured by LBM, we decided to alter the microstructural properties of porous rocks using lasers and performed pore scale modeling in the laser-treated rocks samples using cascaded lattice Boltzmann method. It was for the first time that lasers were used to induce microscopic changes in porous rocks. The obtained results are promising and clearly show that lasers can be used to alter microstructural and microscopic transport behavior of micro-nanodevices used in microfluidics, electronics, etc. Lattice Boltzmann simulations suggested that pulsed laser beams can open new pores and enhace pore connectivity enhancing the permeability, i.e. making it easier for the fluid to flow through the improved pore-network.

7.2 Laser-Induced Alteration of Microstructural and Microscopic Transport Properties in Porous Materials: Experiment, Modeling and Analysis

7.2.1 Abstract

Porous materials are of great importance in various industrial applications. Microscopic modifications in the pore structures of these materials can change their functional behavior. We treat Indiana limestone by lasers to modify its pore structures microscopically. Microcomputed tomography (micro-CT) of the treated samples reveal that pulsed Nd:YAG laser with energy 330 mJ increases open porosity of limestone by 15% and almost doubles the total porosity. This laser increases the limestone pore connectivity by 460%. High power CO_2 laser increases the open porosity by 20% but it reduces the pore connectivity of limestone. Our findings show that pulsed laser beams induce high increase in porosity and connectivity. 3D pore scale modeling using Cascaded lattice Boltzmann method (CLBM) on a D_3Q_{27} model shows that regions treated by pulsed Nd:YAG lasers exhibit enhanced fluid transport efficiency compared to untreated regions. The obtained results successfully demonstrate that lasers can be used to induce a well controlled heat transfer in porous materials directly enhancing their morphometric characteristics and microscopic fluid transport behavior.

The material presented in this work has been published in ***Materials & Design*** as an original research paper [260].

7.2.2 Introduction

Porous materials are complex arrangement of grains (matrix) with voids (pores). The behavior of fluid flow in the complex structures depends strongly on the pore connectivity and porosity. Fluid transport efficiency of these materials is directly related to the degree of complexity of the pore structures. Tuning of macroscopic fluid transport efficiency can be achieved by modifying the rock pore structure on a large scale. This has become a common practice to stimulate, control and enhance the fluid flow efficiency in many large scale applications [14]. Rock drilling, acidification, formation fracturing are some of the methods used to modify the pore structure of the porous rocks for various field scale applications [109, 166]. The drawback with such techniques is that they are harmful to the environment and ecosystems [57]. The techniques used for field scale applications are not appropriate to induce changes

141

in the morphometric properties of micro-sizes porous materials supporting microscale fluid flows, i.e. fluid flows through micro devices such as filters, catalysts, microfluidics and biological flows. This is supported by the fact that micro devices contain very small porous volume which require microscopic changes in order to increase microscopic transport efficiency. In microfluidic devices, where polymers are used due to their porous structure [300, 301], the performance of such micro devices can be tuned by modifying polymer's pore structure. Therefore, to cause microscopic modifications in pore structures we need to look for techniques which can manipulate the pore geometry microscopically without destroying, damaging and changing the functional prospects of the structures.

In this article, we propose to manipulate the pore structures microscopically with lasers. As far as we know, this is the first time that lasers have been used to modify rock's surface pore structures microscopically. Very interestingly, laser is the most environment friendly and well behaved heat source with well controlled intensity and power. The core motivation of this paper is to study microscale laser beam-rock interaction (in terms of morphometric properties and permeability) for lasers with different wavelengths and energy. We perform quantitative morphometric analysis using micro-CT and pore scale fluid flow simulations using CLBM to study the microscopic impact of lasers on rocks. In a separate study, the authors have studied the alteration of wettability in limestone using lasers [261].

Pore scale modeling is the most reliable way to characterize the microscopic fluid flow behavior in porous media [255, 313]. Thanks to the micro-CT imaging of the porous rock, exact and accurate pore structures' 3D images can be generated by the X-Ray tomography. Lattice Boltzmann method (LBM) is the favourite choice to simulate fluid flow in porous media at the pore scale. This claim is supported by the fact that complex boundary conditions associated with porous materials are naturally incorporated in the LBM using bounce-back boundary condition formulation [117, 227]. The overall structure of this paper is as follows: A homogeneous Indiana limestone core sample was cut into small pieces. Three samples's surfaces were treated by sweeps from three lasers of different wavelengths and power. Some area was left untreated on each of the three samples. Afterwards, micro-CT scans were performed to characterize the local pore structure properties of each sample. 3D tomographic images were generated for all samples. Next, many Volume of Interest (VOIs) were selected from the treated and untreated regions of all samples to study the microscopic modifications in morphometric properties of the rock. Finally, pore scale modeling of fluid flow was performed using LBM in the selected VOIs from untreated and treated regions.

This study is first of its kind which investigates the effect of laser induced temperature on porosity and microscopic fluid flow efficiency in porous materials. The results

142

obtained from this study possess great implications for applications which involve microscopic fluid flow in complex geometry, e.g. biological flows, water treatment processes, catalysis, etc. The impact of this research can be extended to macroscale applications. On macroscale, the proposed technique may be used to open clogged pores, e.g reducing Skin effect and enhance the fluid flow in the vicinity of the wellbore of oil wells. Depending on the thermal conductivity of the porous material, microfractures can be created by well controlled laser power without weakening the strength of wellbore formation. It should be noted that present study focuses on inducing microscopic changes instead of using lasers for rock drilling.

7.2.3 Materials and methods

Materials

The present study employed an Indiana Limestone core plug of 37 mm diameter with porosity 13.33% and permeability 244 mD. The chemical composition of Indiana limestone has been provided in Tab. 7.1. It is a well known real world porous material with a huge scope in industrial applications. Indiana limestone are inexpensive, readily available, homogeneous and outcrops of a large number of oil producing fields. Moreover, several carbonate rocks are used by the petroleum industry as standard porous media for laboratory experiments. The another benefit of the present study is that the findings of this study can be compared with data derived from experiments conducted using real oil reservoir cores.

Tabela 7.1: Chemical composition of Indiana Limestone [26].

$CaCO_3$	$MgCO_3$	Al_2O_3	SiO_2
97.3%	0.4%	0.5%	1.7%

Microcomputed tomography experiment

Microcomputed tomography imaging of the limestone samples have been conducted for an intensive morphometric analysis. The system used in this work is X-Ray micro-CT Skyscan model 1173 (Bruker, Belgium). The equipment has X-ray source operating in a range of 40 to 130 kV and its detection system consists of a flat-panel sensor operating with a maximum matrix of 2240x2240. For acquisition process of sample, the 18 μm pixel size has been used, voltage was set at 130 kV with a current of 61 μA, and an additional copper filter of 0.5 mm thickness was used. To perform an analysis on the structure of the pores connected before and after laser treatment, digital rock analysis of the regions of interest were performed with software CT analyzer v1.15.4. It allows the analysis of different parameters in micro-CT dataset.

A size distribution is calculated from the pore network. For morphometric analysis, we need binarized image in which each pixel needs to become either black or white, this is called segmentation.

We chose to use the global segmentation for a range from 0 to 255. Global segmentation is the simplest method to separate the image into two categories (background and object). This separation is carried out by scanning the image point by point, and identifying them as points of the object or of the background according to a threshold. The Fig. 7.9 has been provided to demonstrate the binarization process and the threshold histogram for value 60 applied in this study for Indiana limestone. A closed pore in a 3D analysis is the empty space which is totally surrounded on all sides by solid matrix. An open pore is defined as any space located between solid objects, which has any 3D connection with the space outside. On the other hand, total porosity is the volume of all open and closed pores, as a percent of the total volume. Euler analysis provides a measure of connectivity density, indicating the number of redundant connections between rock-matrix structures per unit volume. Rock-matrix connectivity can contribute significantly to structure strength [223]. The connectivity and connectivity density is calculated by CTanalyzer software using Euler number correlation. With 3D image analysis by micro-CT a true 3D thickness of minerals can be measured which is model-independent. Local thickness for a point in solid is defined as the diameter of the largest sphere which fulfills two conditions: (1) the sphere encloses the point (but the point is not necessarily the center of the sphere); (2) the sphere is entirely bounded within the solid surfaces. The illustration of rock-matrix thickness and separation has been shown in Fig. 7.1. 3D distances calculated by adjusting spheres within the structure facilitate evaluation of thickness and the average separation. The mean diameter of the spheres represent the thickness of the object, and the standard deviation of the diameter represents the variability in the thickness of the object. The method for these calculations begins with "skeletonization"identifying the medial axes of all structures. Then, the "ball-adjusted"local thickness measurement is made for all voxels located along this axis [240]. Any region of a binarized object can be characterized by the thickness distribution, which is an important tool in the characterization of complex structures.
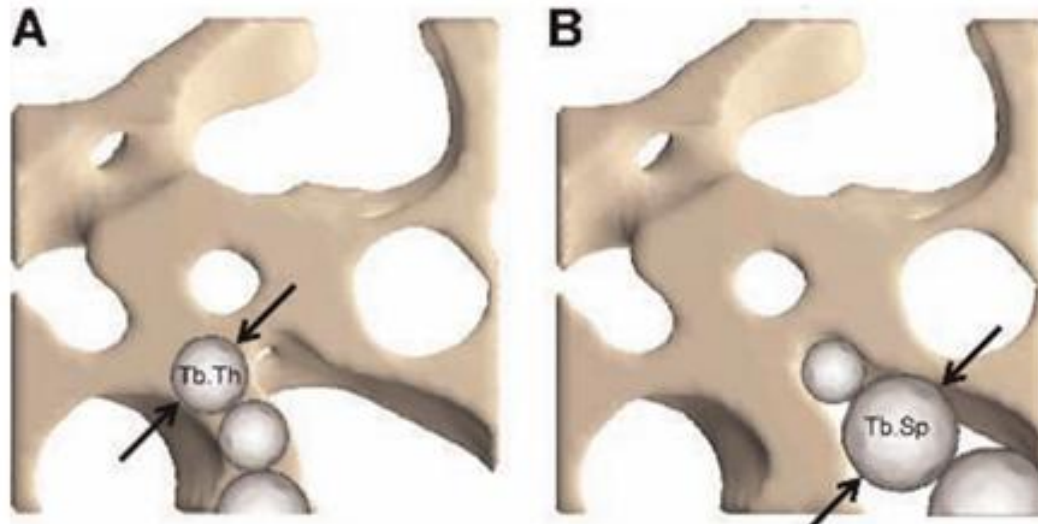
Figura 7.1: Schematic representation of algorithm used for direct 3D method for calculating rock-matrix thickness (figure A) and separation (figure B). The distances are computed by fitting spheres inside the structure or inside the background. T_bT_h represent the trabecular (rock-matrix) thickness and T_bS_p trabecular (rock-matrix) separation [25].

Homogeneity analysis of Indiana limestone core plug

We carried out microcomputed tomography imaging of the whole core plug to study its homogeneity beforehand. The core plug is 60 mm high with 37 mm diameter. To ascertain homogeneity of the core plug we have adopted two strategies. One is quantitative analysis of the tomographic images of whole sample. In this method, we check for pore distribution of each tomographic slice. Grayscale pore distribution of slices from top, middle and bottom region of the core sample are shown in Fig. 7.2(d). Second approach is quantitatively more intensive.
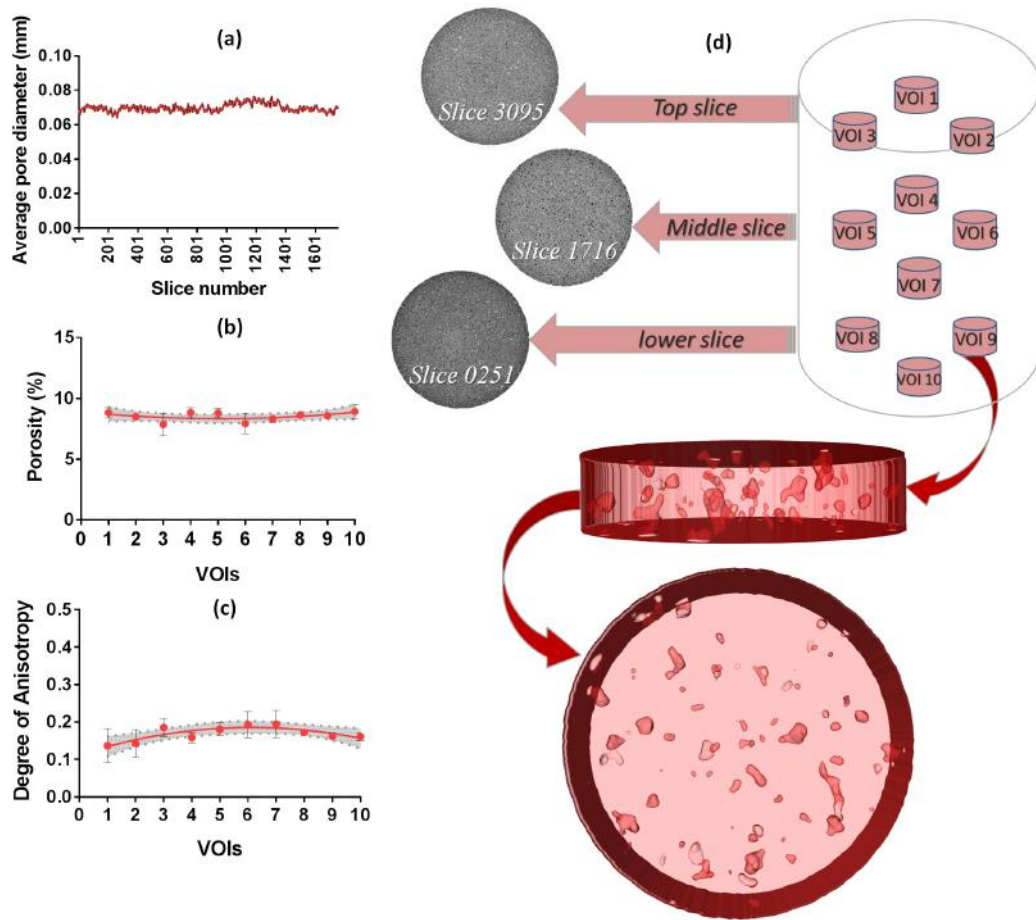
Figura 7.2: (a): Average pore diameter of the slices of original sample obtained by micro-CT (b): Porosity comparison of all VOIs chosen from various locations in the original core plug. (c): Degree of anisotropy (DA) comparison of all 10 VOIs chosen from Indiana limestone core plug (d): Locations of the VOIs selected from the core sample, and 3D representation of pore distribution network of one VOI of 5 *mm* diameter.
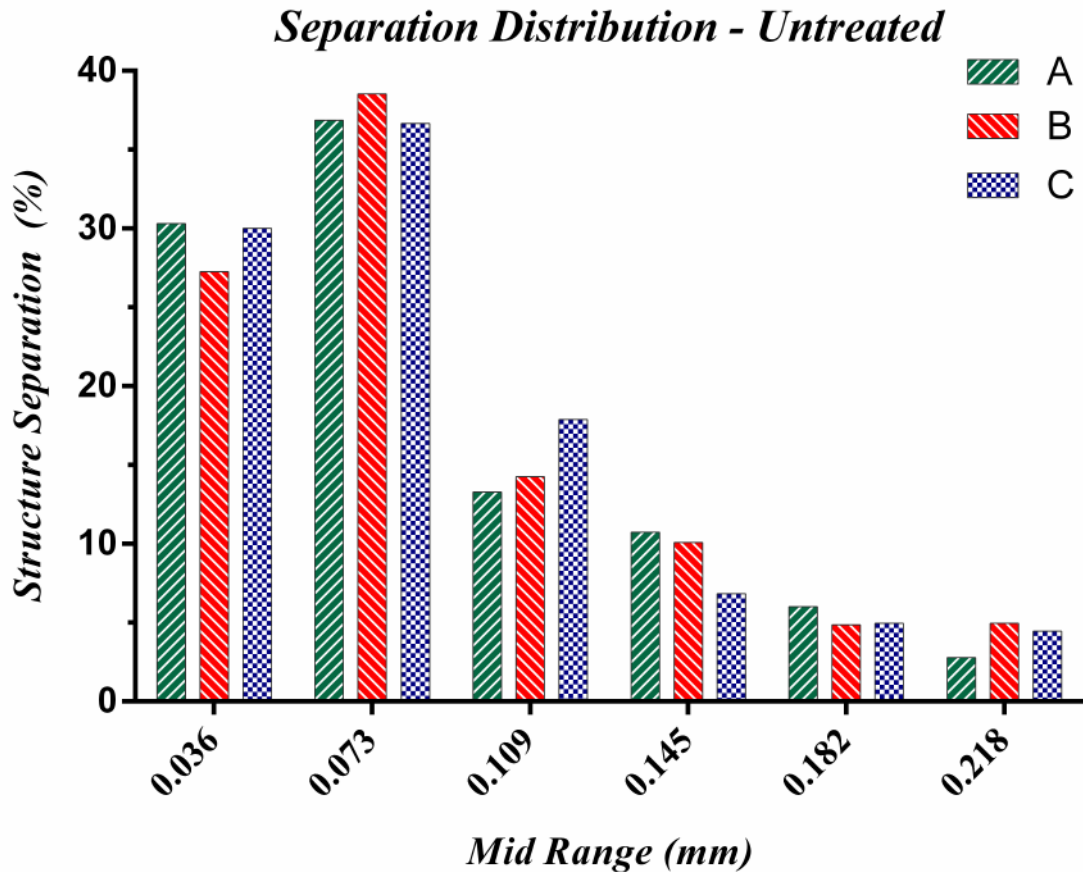
Figura 7.3: Separation distribution of untreated samples A, B and C, respectively, after cutting the core plug. The x-axis represents the mid-range in mm and y-axis represents the structure separation distribution as percent volume. It is evident that rock-matrix separation of larger portion of the total volume have smaller range and are approximately the same for samples A, B and C.

Detailed tomographic analysis was carried out for 10 VOIs distributed all over the core plug, see Fig. 7.2(d). Average pore diameter, total porosity and degree of anisotropy were determined for all marked VOIs by using CT analyzer. The CTanalyzer software computes the degree of anisotropy using the mean intersection length (MIL). It is calculated by laying a line through the 3D volume containing binarized objects and dividing the length of that line by the number of times it intercepts the solid phase. Test lines should cross the center of the binarized spheres in the image and the length distribution should cover all randomly distributed 3D angles. Any asymmetry in the MILs in relation to the 3D angle will represent the anisotropy of the sample. The results are shown in Fig. 7.2 (a), (b) and (c). The results (a) show that all slices demonstrated approximately similar average pore diameter signaling a trend towards homogeneity. Advancing further for porosity evaluation, it is evident from plot (b) that all VOIs have approximately the same porosity value. The third plot (c) represents the degree of anisotropy (DA) of the

core plug. A rock is considered to be isotropic for $DA < 1$ [249]. All VOIs show DA values between $0.1 - 0.2$, which still is very small and can be approximated to 0. Therefore, the results obtained by quantitative tomographic analysis ascertain the homogeneity and isotropicity of the core plug. After cutting the core plug into few pieces, we chose three samples; A, B, and C. The rock-matrix separation distribution of each untreated sample (after cutting) have been shown in Fig. 7.3.
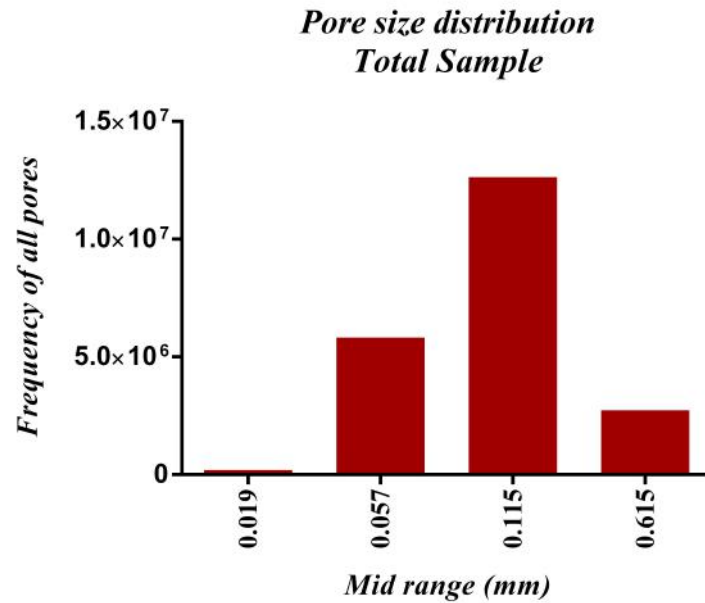
Figura 7.4: Pore size distribution of Indiana limestone core plug.

The Fig. 7.4 shows the pore size distribution of the original Indiana limestone core plug. Which is in great agreement with the average pore diameter values calculated slice per slice in Fig. 7.2(a).

Laser treatment of Indiana limestone surfaces

The homogeneity analysis presented in Section 2.3 shows that Indiana limestone core plug is a homogeneous and isotropic porous rock. This analysis helped us in making an important decision regarding laser treatments which is described later in the text. We cut the core plug into some pieces. Then the samples were mounted on a mobile sample holder platform and were exposed to laser beams one by one. The rock holder platform moved horizontally from one end to another and after one horizontal sweep the laser was turned off. The platform height was changed (upwards or downwards) by the size of the beam spot diameter. Afterwards, the next horizontal sweep was made in the direction opposite of the first scan. We followed this process until the desired area was treated. Since in the present study we are interested in microscopic modifications only, thanks to the homogeneity of the rock,

we decided to treat some area of the samples with laser, deliberately leaving some area untreated for comparison purposes. Laser specifications and other important parameters are provided in Tab. 7.2.

Tabela 7.2: Laser treatment specifications for Sample A, B and C.

Specifications	Sample A	Sample B	Sample C
Laser Type	Nd:YAG	Nd:YAG	CO_2
Wavelength	266 nm	532 nm	10.6 μm
Radiation Type	Pulsed	Pulsed	Continuous
Pulse Duration	43 ns	43 ns	NA
Power Used	27 $mJ/Pulse$	330 $mJ/Pulse$	4 W
Beam Spot Diameter	12 mm	12 mm	6 mm
Repetition Rate	10 Hz	10 Hz	NA
Fluence (Deposited Energy)	0.023 J/cm^2	0.291 J/cm^2	14.154 J/cm^2
Penetration Depth	0.4 mm	0.75 mm	0.7 mm, 0.8 5 mm (hole)
Exposure Period	2 s	2 s	2 s, 3-4 s (hole)
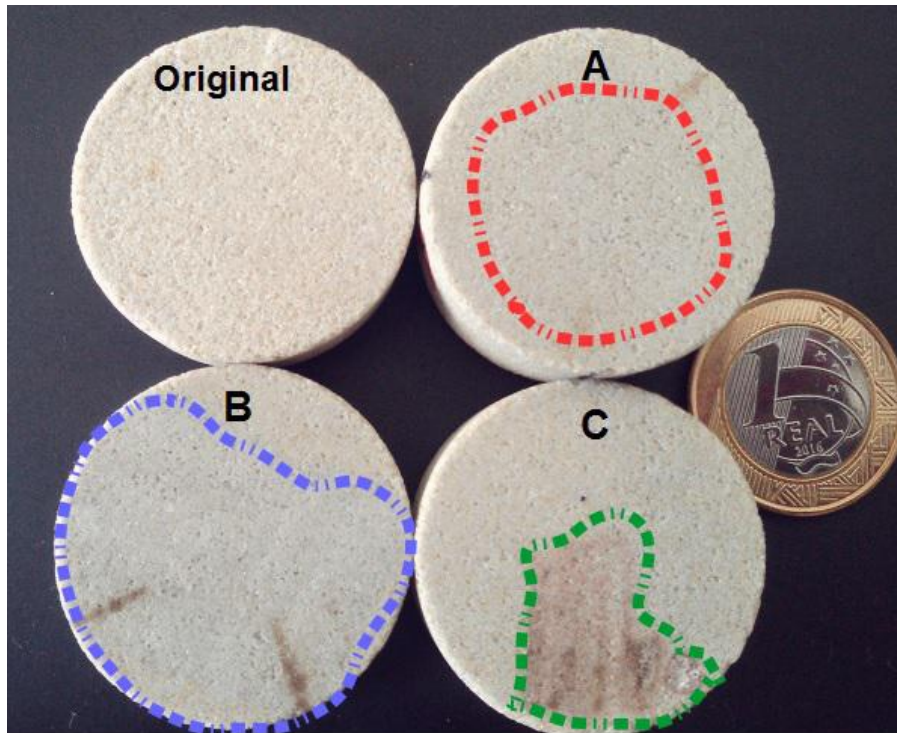
Figura 7.5: Image of untreated and laser treated limestone samples. The area within dotted boundaries represent laser treated region. The diameter of each sample is 37 mm.

Volume of Interest (VOI) preparation

To perceive microscopic changes in morphometric quantities and fluid transport properties in top surface of samples it is unnecessary to analyse the whole volume of the

samples. Quantitative analysis of tomographic data for large samples is extremely memory demanding and require very sophisticated computational resources. VOIs and representative element volumes help in reducing the computational cost of the morphometric analysis and pore scale numerical schemes [215, 255, 313]. Various VOIs were selected from each of the untreated and laser treated region co-existing on samples A, B and C, respectively. In order to quantify and perceive the differences caused by laser treatment, 3D tomographic images will be used for morphometric and fluid transport efficiency analysis. Therefore, for best visualization of microscopic changes in surfaces we selected top 50 slices of samples' tomographic images forming these VOIs. We assured the fact that the physical thickness of 50 slices is larger than the laser-rock interaction depth (see Tab. 7.2) for all three cases. In total, 8 VOIs were selected from untreated and treated regions (see Fig. 7.6), respectively, from all three samples.
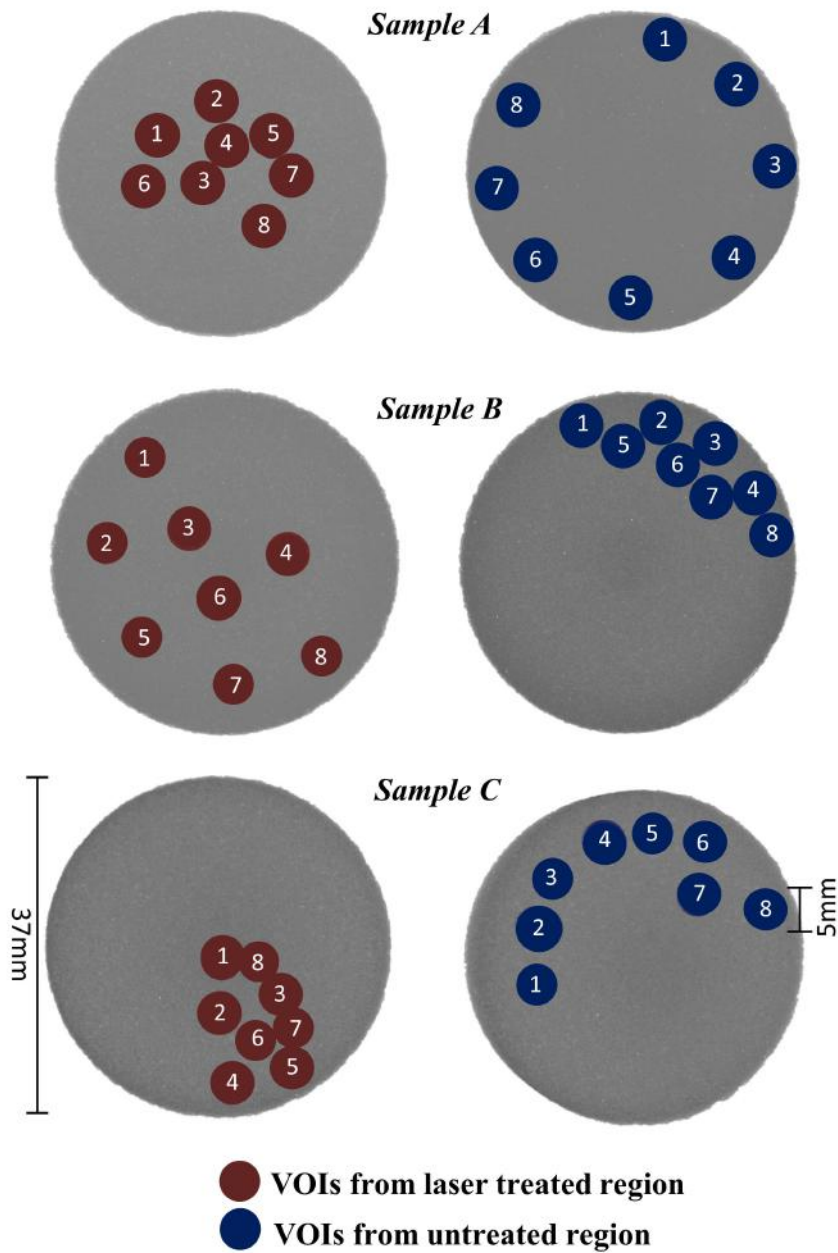
Figura 7.6: Locations of VOIs in laser treated and untreated region for samples A, B and C. Each VOI is circular, 1 mm thick and has diameter of 5 mm.

7.2.4 Cascaded Lattice Boltzmann Method for Fluid Flow

Fluid are treated as fictitious particles in lattice Boltzmann simulations (LBM). These particle move on a spatial arrangement called lattice model. The particles'

evolution in the space is defined by velocity distribution function f. In this study to solve fluid flow through porous media we have used a 3D LBM with cascaded collision operator [95, 96, 259]. The D_3Q_{27} model for the fluid flow which stands for 3 dimensions and 27 characteristic velocities is depicted in Fig. 7.7.
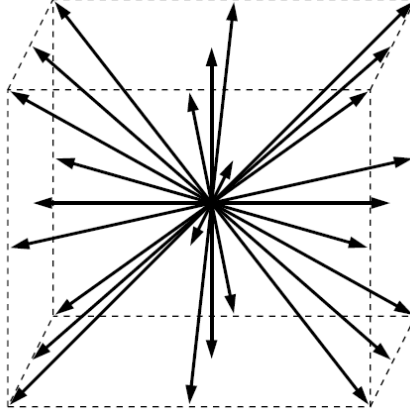
Figura 7.7: Characteristic velocities for the D_3Q_{27} lattice model used in the 3D simulations.

Mass and momentum are conserved quantities and can be computed from distribution functions through the two first moments as

$$\rho = \sum_i f_i, \qquad \rho\vec{u} = \sum_i f_i \vec{c}_i, \tag{7.1}$$

where ρ is the macroscopic density, $\vec{c}_i$ is the i-th lattice characteristic velocity and $\vec{u}$ is the macroscopic velocity. The evolution equation for the distribution function is called Lattice Boltzmann Equation, which written in dimensionless form reads

$$f_i(\vec{x} + \vec{c}_i, t+1) = f_i^c = f_i(\vec{x}, t) + \mathbb{K} \cdot (\vec{f}^{eq} - \vec{f}), \tag{7.2}$$

where $\mathbb{K}$ is the general collision matrix, super-script c denotes so called post-collisional state, f^{eq} is the equilibrium distribution function vector. The right hand side of the equation is called "collision" and the left hand side describes the update rule "called streaming". The matrix $\mathbb{K}$ determines the collision model used. The

equilibrium distribution function f_i^{eq} is function of macroscopic conserved quantities ρ and $\vec{u}$. In the cascaded LBM, the collision is performed in the space of central moments, i.e. raw moments shifted by the macroscopic velocity $\vec{u} = (u, v, w)$. The raw moments $m_{\alpha\beta\gamma}$ and central moments $\kappa_{\alpha\beta\gamma}$ of order $\alpha + \beta + \gamma$ are defined by

$$
\begin{aligned}
m_{\alpha\beta\gamma} &= \sum_i c_{i,x}^\alpha c_{i,y}^\beta c_{iz}^\gamma f_i, \\
\kappa_{\alpha\beta\gamma} &= \sum_i (c_{i,x} - u)^\alpha (c_{i,y} - v)^\beta (c_{i,z} - w)^\gamma f_i,
\end{aligned}
\tag{7.3}
$$

By definition we have following identities

$$
\begin{aligned}
m_{000} &= \rho, \quad m_{100} = \rho u, \quad m_{010} = \rho v, \quad m_{001} = \rho w \\
\kappa_{000} &= \rho, \quad \kappa_{100} = \kappa_{010} = \kappa_{001} = 0
\end{aligned}
\tag{7.4}
$$

i.e. first raw moments are conserved quantities (they are also collisional invariants i.e., they do not change in collisions).

In every iteration of the LBM, we have to compute macroscopic variables, central moments, perform collision, convert central moments back to distribution functions and perform streaming step together with application of the boundary conditions. The cascaded collision scheme in central moment space reads [96]

$$
\kappa_{200}^c - \kappa_{020}^c = \left(1 - \frac{1}{\tau_1}\right)\left(\kappa_{200} - \kappa_{020}\right) - 3\rho\left(1 - \frac{1}{2\tau_1}\right)\left(u^2 D_x u - v^2 D_y v\right)
\tag{7.5}
$$

$$
\kappa_{200}^c - \kappa_{002}^c = \left(1 - \frac{1}{\tau_1}\right)\left(\kappa_{200} - \kappa_{002}\right) - 3\rho\left(1 - \frac{1}{2\tau_1}\right)\left(u^2 D_x u - w^2 D_z w\right)
\tag{7.6}
$$

$$
\begin{aligned}
\kappa_{200}^c + \kappa_{002}^c + \kappa_{002}^c &= \frac{\rho}{\tau_2} + \left(1 - \frac{1}{\tau_2}\right)\left(\kappa_{200} + \kappa_{020} + \kappa_{002}\right) \\
&\quad - 3\rho\left(1 - \frac{1}{2\tau_2}\right)\left(u^2 D_x u + v^2 D_y v + w^2 D_z w\right)
\end{aligned}
\tag{7.7}
$$

$$
\kappa_{120}^c + \kappa_{102}^c = \left(1 - \frac{1}{\tau_3}\right)\left(\kappa_{120} + \kappa_{102}\right)
\tag{7.8}
$$

$$
\kappa_{120}^c - \kappa_{102}^c = \left(1 - \frac{1}{\tau_4}\right)\left(\kappa_{120} - \kappa_{102}\right)
\tag{7.9}
$$

$$
\kappa_{201}^c = \left(1 - \frac{1}{\tau_5}\right)\kappa_{111}
\tag{7.10}
$$

$$
\kappa_{220}^c - 2\kappa_{202}^c + \kappa_{022}^c = \left(1 - \frac{1}{\tau_6}\right)\left(\kappa_{220} - 2\kappa_{202} + \kappa_{022}\right)
\tag{7.11}
$$

$$\kappa_{220}^c + \kappa_{202}^c - 2\kappa_{022}^c = \left(1 - \frac{1}{\tau_6}\right)\left(\kappa_{220} + \kappa_{202} - 2\kappa_{022}\right) \tag{7.12}$$

$$\kappa_{220}^c + \kappa_{202}^c + \kappa_{022}^c = \left(1 - \frac{1}{\tau_7}\right)\left(\kappa_{220} + \kappa_{202} + \kappa_{022}\right) + \frac{\rho}{3\tau_7} \tag{7.13}$$

$$\kappa_{211}^c = \left(1 - \frac{1}{\tau_8}\right)\kappa_{211} \tag{7.14}$$

$$\kappa_{221}^c = \left(1 - \frac{1}{\tau_9}\right)\kappa_{221} \tag{7.15}$$

$$\kappa_{222}^c = \left(1 - \frac{1}{\tau_{10}}\right)\kappa_{222} + \frac{\rho}{27\tau_{10}} \tag{7.16}$$

The moments not shown here can be obtained from the above formulas by permuting the indices. The spatial derivatives $D_x u$, $D_y v$, $D_z w$ included in the collisions decrease numerical artifacts originating from the finiteness of the velocity set and can be obtained locally as [96]

$$D_x u = -\frac{1}{2\rho\tau_1}\left(2\kappa_{200} - \kappa_{020} - \kappa_{002}\right) - \frac{1}{2\rho\tau_2}\left(\kappa_{200} + \kappa_{020} + \kappa_{002} - \rho\right) \tag{7.17}$$

$$D_y v = D_x u + \frac{3}{2\rho\tau_1}\left(\kappa_{200} - \kappa_{020}\right) \tag{7.18}$$

$$D_z w = D_x u + \frac{3}{2\rho\tau_1}\left(\kappa_{200} - \kappa_{002}\right) \tag{7.19}$$

The parameters present in the equations are relaxation times $\tau_1, \ldots, \tau_{10}$, only the τ_1 is related to the only physical parameter describing the simulated fluid i.e., the kinematic viscosity, the relation between τ_1 and kinematic viscosity in lattice units is following

$$\nu = \frac{1}{3}\left(\tau_1 - \frac{1}{2}\right). \tag{7.20}$$

Other τ's has no influence on the leading order of the solution, but has some influence on the accuracy and stability of the method [96] and we set them to unity in our numerical simulations. The conserved quantities are collisional invariants and thus have relaxation times equal to zero.

7.2.5 LBM boundary conditions for porous media

Bounce back boundary conditions have been used at the solid surfaces of the porous media to fulfill no-slip condition. Bounce back can be realized by following collision

step at boundary nodes

$$f_{\bar{i}}(\vec{x}_b, t+1) = f_i^c(\vec{x}_b, t), \qquad (7.21)$$

where bar over the index i means opposite direction i.e. $\vec{c}_{\bar{i}} = -\vec{c}_i$ [147]. From microscopic point of view this means that when a fluid particle coming from a lattice node approaches a solid node of the wall, it is reflected on a halfway between the lattice sites back to the same lattice node it originally came from.

For the inlet and outlet, pressure boundary conditions (anti-bounce back approach [99, 100]) were used, where pressure is related to the density by lattice equation of state

$$\rho = 3p \qquad (7.22)$$

and the conditions for the unknown distributions at the boundary sites read

$$f_{\bar{i}}(\vec{x}_b, t+1) = -f_i^c(\vec{x}_b, t) + 2\omega_i \rho_{in/out} \left[1 + \frac{9\left(\vec{c}_i \cdot \vec{u}_{in/out}\right)^2}{2} - \frac{3\vec{u}_{in/out}^2}{2} \right], \qquad (7.23)$$

where $\vec{x}_b$ is the position vector of the boundary lattice site, ω_i are weights for the links [96], $\rho_{in/out}$ are densities at inlet and outlet, readily computed from the known pressure difference as

$$\rho_{in} = 1 + \frac{3\Delta p}{2}, \quad \rho_{out} = 1 - \frac{3\Delta p}{2} \qquad (7.24)$$

and $\vec{u}_{in/out}$ are lattice velocities at inlet and outled, computed by extrapolation [145]

$$\vec{u}_{in/out} = \vec{u}(\vec{x}_b) + \frac{1}{2}\left[\vec{u}(\vec{x}_b) - \vec{u}(\vec{x}_{b+1})\right], \qquad (7.25)$$

where $\vec{x}_{b+1}$ is the interior site next to the boundary site in the inward normal direction.

For more details on boundary conditions and their implementation we point the reader to the excellent monograph [165].

Values used in LBM simulations are as follows; the kinematic viscosity of water $\nu = 10^{-6} m^2/s$, pressure difference $\Delta p = 120 kPa$, dimensions of the REV sample were $D = 5mm$ (diameter) and $H = 1mm$ (height) with spatial step $\Delta x = 2\cdot10^{-6}m$. It should be noted that we perform pore scale fluid flow by solving Navier-Stokes equations to check for non-zero velocity field in the connected pores. In order to simulate pore scale fluid flow in our samples we have used a 3D LBM with cascaded collision operator [96, 259].

7.3 Results and discussions

7.3.1 Laser beam-rock interaction

Laser can be considered as a heat source with controlled power and intensities. When a laser beam is incident on the rock surface it induces high temperature zone in the rock, especially in the exposed region depending on the thermal conductivity of the rock. Heat affected zone in a rock with lower thermal conductivity such as limestone is always limited to the laser exposure area [92, 104, 265]. It has been shown that rock with higher thermal conductivity such as berea sandstone has larger heat affected zone, and this wide range of temperature distribution weakens the rock which is not desirable either for microscale applications or in the wellbore region [104]. Due to the low thermal conductivity of limestone rock, laser treatment induces high temperature in a very limited zone modifying the pore structures by melting solid grains, vaporizing cementation, without weakening the rock so much. This is evident in Fig. 7.5, for Nd:YAG laser (266 nm) which has very low fluence, the treated surface does not show much visible changes. When we treat the surface with another laser (Nd:YAG 532 nm) with high fluence, the solid grains of limestone are heated inducing a notable change in the color of the surface. But for the CO_2 laser, due to its very high continuous fluence, the laser beam caused melting and then vaporization of the rock grains creating a small hole. In Fig. 7.5, for sample C, one hole with white lime powder ($CaCO$) can be noticed in the right bottom corner of the closed dotted region. This white lime powder hole was created when CO_2 laser beam was incident at this point for longer time period (3 s) inducing chemical changes and rock vaporization. Limestones do have very low amounts of clay and quartz present. Laser induced temperature can cause quartz crystals to expand and clay to dehydrate. This expansion of quartz crystals can induce microfractures, and water released during dehydration increases the volume and pressure inside pores prompting those pores to break [104, 265]. Therefore, the porosity and permeability in limestones can be changed by heating, vaporization and inducing micro-fractures in limestone rocks.

7.3.2 Surface pore network properties of laser treated limestone

The 3D reconstruction of samples' surfaces obtained by micro-CT are shown in Fig. 7.8. Area within the dotted boundary represents laser treated region. The impact of lasers on the surfaces are clearly visible. Sample B, which was treated by high fluence Nd:YAG laser, shows more pores present on the surface. For sample C, holes can be seen in the region treated by CO_2 laser. This is because CO_2 laser (due to its

very high fluence) induced very high temperature which created holes and pores. To establish clear microscopic impact of lasers on morphometric properties of samples A, B and C, we chose a threshold value of 60 for segmentation. Considering the pore size distribution of Indiana limestone and our tomographic setup specifications, e.g. pixel size, etc., this value of threshold is appropriate to capture smaller pores, which is our principal objective in the present study. In this way, new smaller or micro-pores induced by lasers would be identified efficiently. The histogram and pore distribution for a fixed threshold value have been shown in Fig. 7.9. It is clearly evident that pore distribution for all VOI from untreated regions of samples A, B and C are approximately the same which proves the homogeneity of our sample. VOIs chosen from laser treated regions of sample A, B, and C show enhanced pore distribution. And it is also evident that laser with higher fluence creates more new pores compare to a laser with lower fluence. The impact of laser treatments on rock-matrix thickness and separation is shown in Fig. 7.10. In case of sample A, low fluence Nd:YAG laser caused minute changes in thickness distribution of the rock but the rock matrix separation was increased slightly enhancing the porosity. For sample B, treated by high fluence Nd:YAG laser, thickness distribution was shifted towards larger range. The volume of rock-matrix with small separation were reduced and separation with a wider range were induced increasing the porosity significantly.
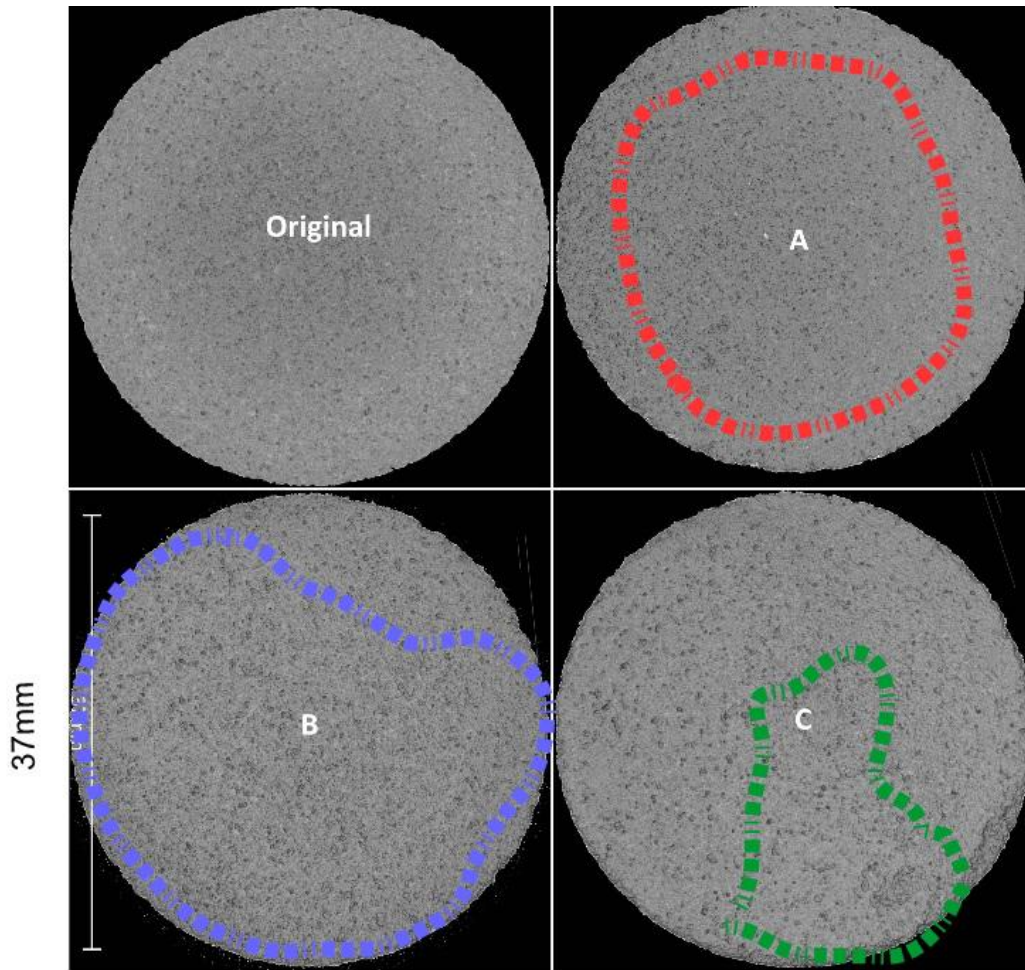
Figura 7.8: 3D reconstruction of surfaces (grayscale, top view) of samples by tomography. Original sample and samples treated by Nd:YAG laser (A) 266 nm, Nd:YAG laser 532 nm (B), CO_2 laser (C), with laser treated area enclosed by dotted boundary. It is evident that low fluence laser (sample A) does not create visible changes compared to original. High fluence pulsed laser (sample B) shows more pores compared to sample A and original sample. On the other hand, for CO_2 laser (sample C), hole and big pores can be seen.

That also suggests that this laser increased the pore diameter along with creation of new wide pores. The continuous wave CO_2 laser increased the thickness distribution and separation significantly for larger range. This is evident in Fig. 7.5 where holes can be noticed. The results for sample C show that the rock matrix became thicker. The hole with lime powder created by CO_2 laser contribute to the high separation distribution peak (after treatment) for sample C.
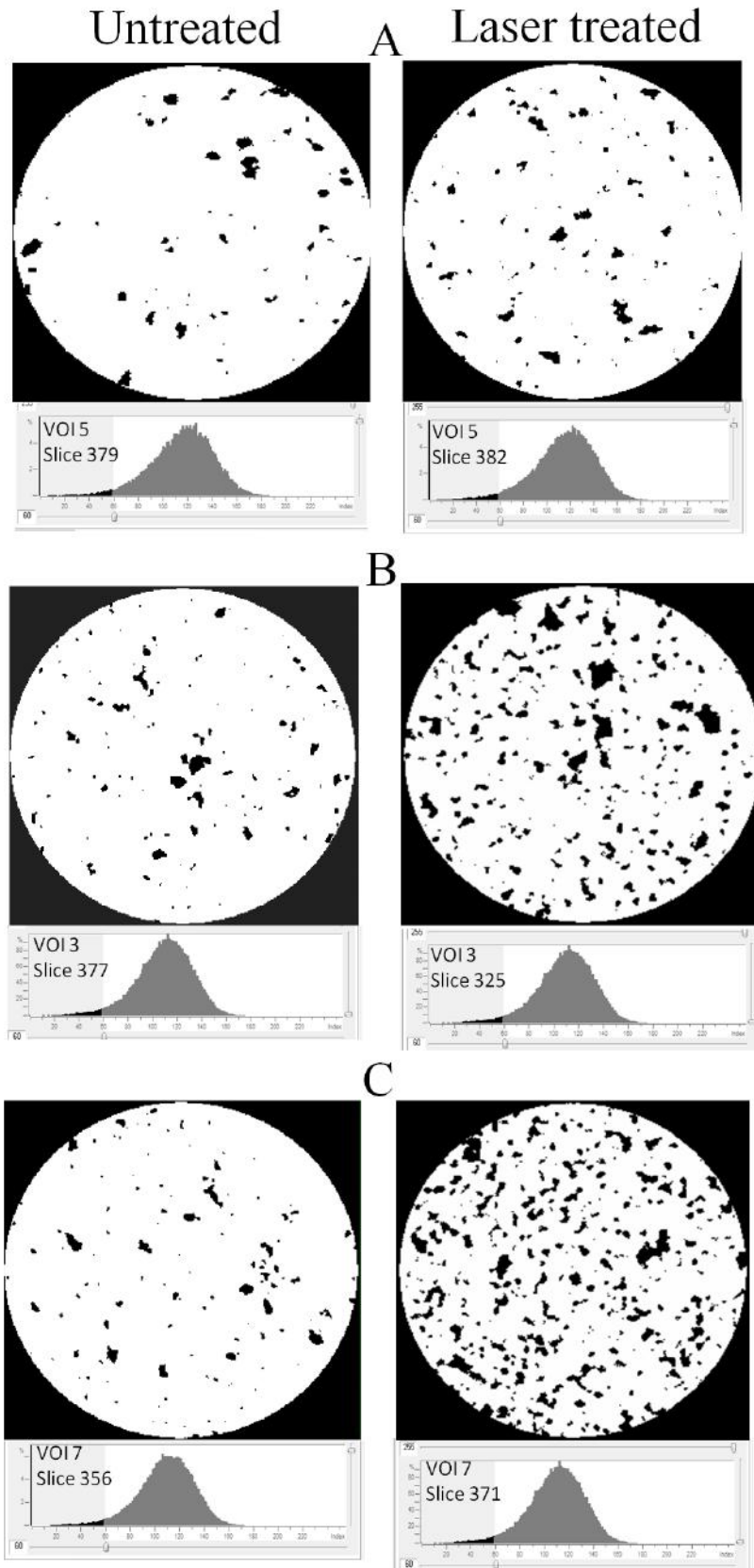
Figura 7.9: Binarized pore distribution network (2D cuts from 3D volume) of VOIs from samples A, B and C, and respective histograms (obtained from 3D volume) for the threshold value of 60.
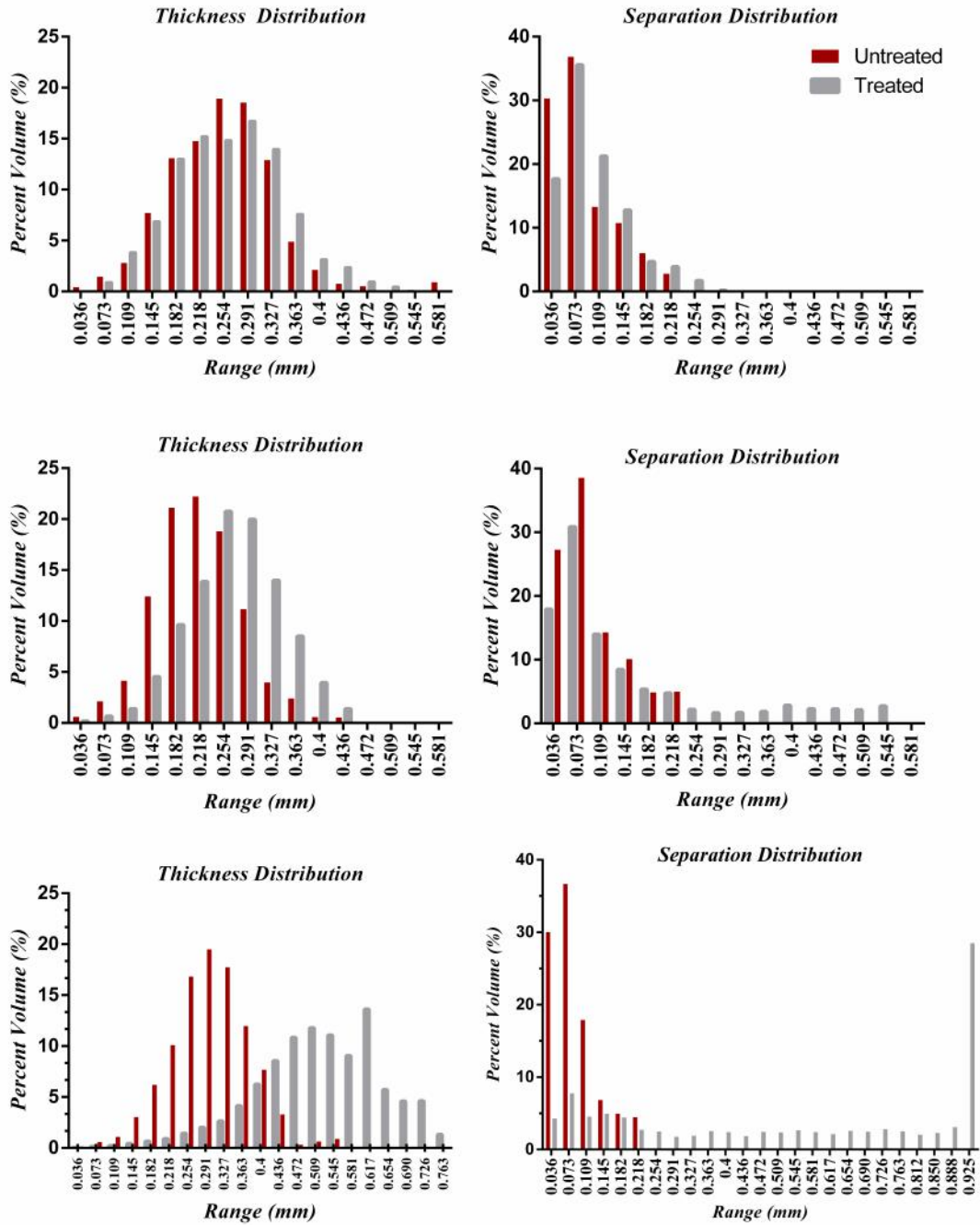
Figura 7.10: Rock-matrix thickness and separation distribution for original and laser treated region of sample A, B and C. Red color represents rock matrix data for untreated (original) region and gray color represents laser treated region.

The quantitative morphometric analysis for samples A, B and C is shown in Fig. 7.11. The results represent the average of morphometric quantities of all VOI's chosen from the laser treated and untreated region, respectively. We can observe in the results that the total porosity was increased after laser treatment for all cases. The trends show that lasers with higher fluence generate more pores. Nd:YAG laser with 266 nm (sample A) did not induce temperature high enough to cause

160

significant heating of the rock grains and cementation. It only caused some heating of rock which resulted in the slight increase in the porosity possibly due to some microfractures caused by thermal shocks. High fluence Nd:YAG laser operating at 532 nm (sample B) induced temperature high enough to cause thermal shocks and ablation of the rock grains and cementation. It increased the porosity quite significantly. The pulsed irradiation of high fluence Nd:YAG laser can deliver very high energy instantly to the rock grains facilitating ablation of the grains and cementation. For CO_2 laser, the temperature induced by very high fluence caused a large scale evaporation of rock grains and cementation. Continuous irradiation from this laser gradually increased the temperature resulting in the melting of the cementation and evaporation. This higher degree of evaporation is the reason behind creation of holes contributing significantly in the porosity of sample C. Connectivity density is a 3-D connectivity index, it is a measure of the degree to which a structure is multiply connected. The Euler number is a characteristic of a three-dimensional structure that is topologically invariant. It is calculated based on the maximum number of branches that can be cut without separating the structure from its surroundings in 3D. Sample A, which was treated by low fluence Nd:YAG laser, showed a minute increase in the connectivity.
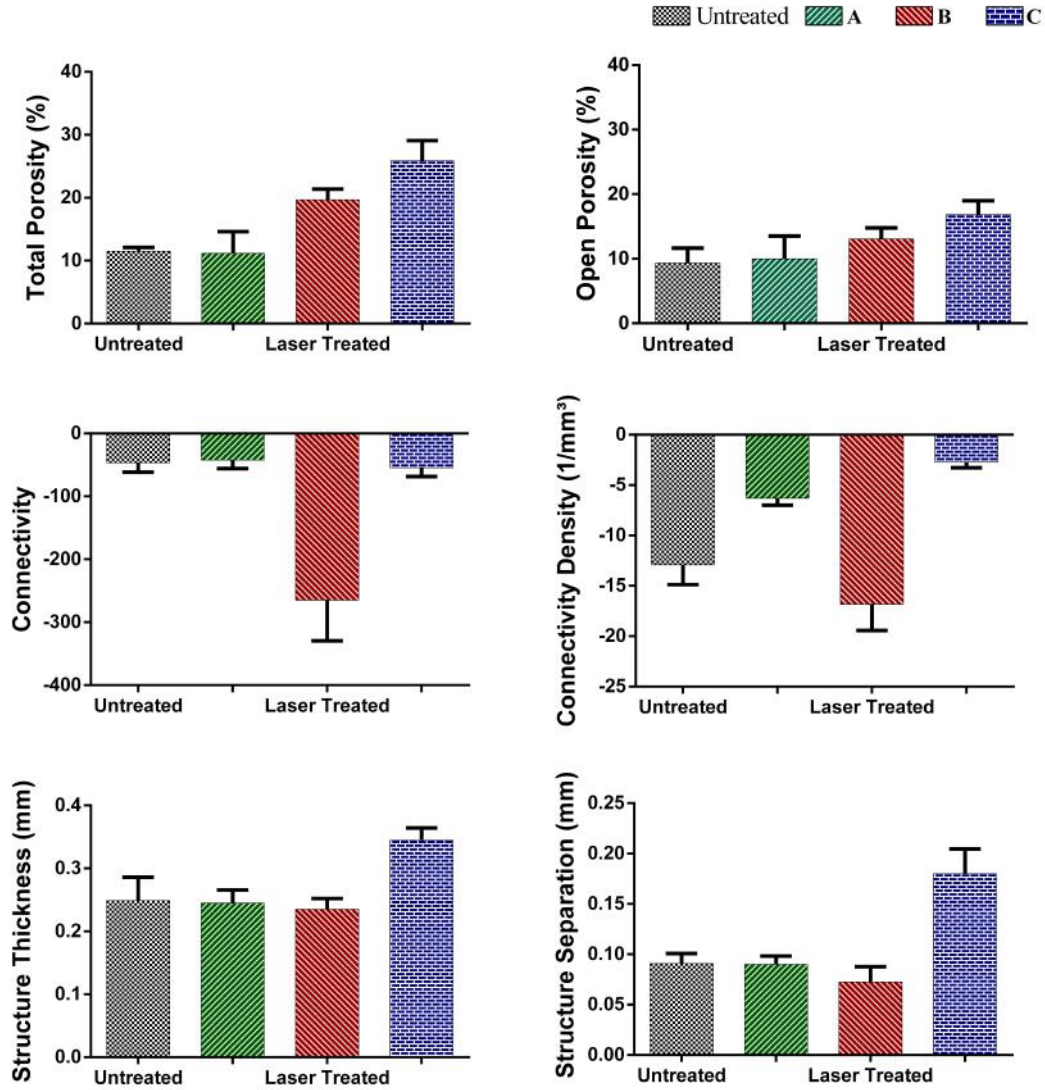
Figura 7.11: Morphological modifications caused by the laser in the total pore-network structures and their comparisons with the original (untreated) ones. A, B and C represent the samples treated by laser A, B and C, respectively.

Treatment from high fluence Nd:YAG laser (Sample B) induced a phenomenal increase in the pore connectivity and connectivity density. Surprisingly, continuous wave CO_2 laser which has very high fluence reduced the pore connectivity and connectivity density quite significantly. CO_2 laser increased porosity remarkably but a significant decrease in connectivity suggests that melting caused by laser increased the rock-matrix thickness reducing the connectivity (excluding the hole region). But on the contrary, pulsed Nd:YAG lasers caused ablation, opening of more pores, microfractures and no holes. It is clearly evident from the results that a moderately powered Nd:YAG laser (sample B) is more appropriate to modify the microscopic surface properties. 3D pore distribution network of untreated and treated VOIs have been provided in Fig. 7.12. The pink contours (bubble like shapes) are pores.
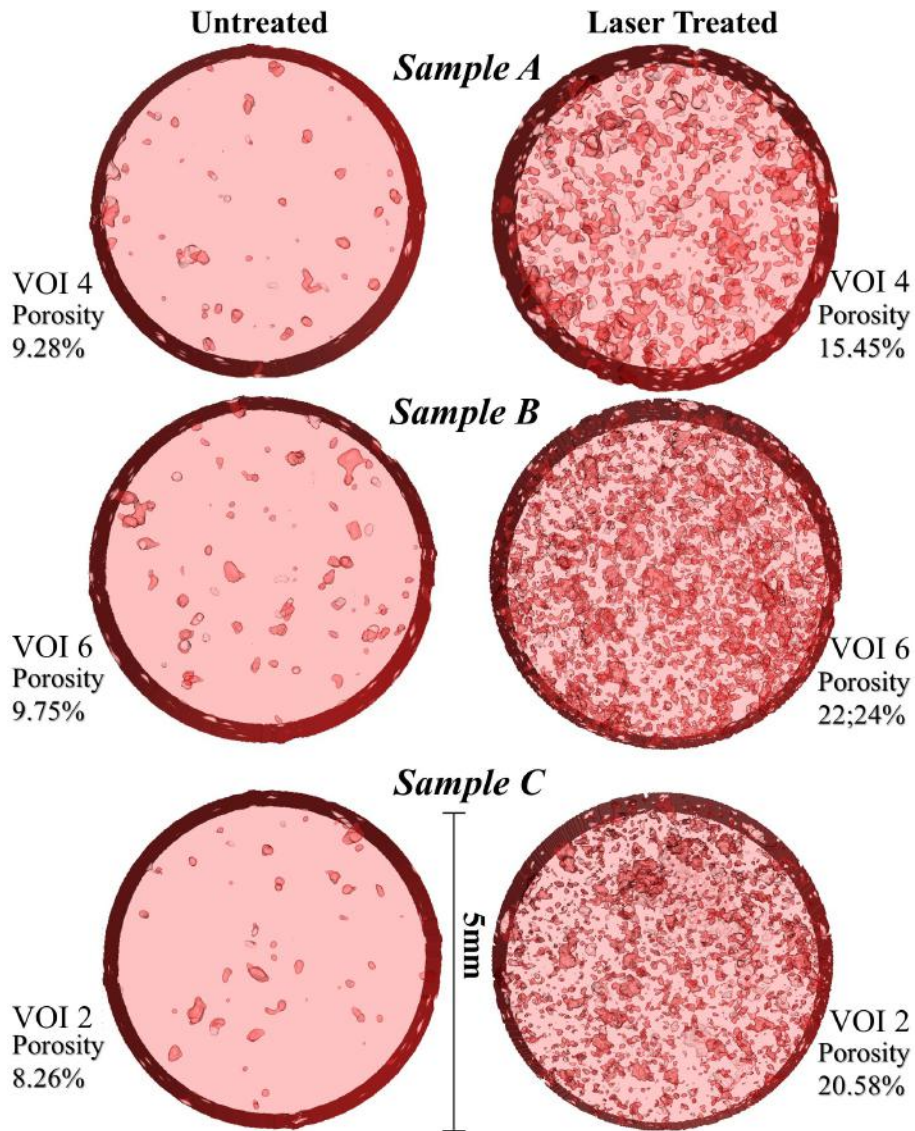
Figura 7.12: Tomographic pore network of VOIs chosen from samples A, B, and C (see Fig. 7.6 for VOI locations). All VOIs have been produced with an identical binarization process with a threshold of 60, as described in earlier section. Each VOI has a diameter of 5 mm and is 1 mm thick. Laser treated VOIs clearly show enhanced porosity.

7.3.3   Pore scale water flow simulations by CLBM

Pore scale fluid flow simulations were carried out to visualize the improvements in the microscopic fluid transport efficiency induced by lasers. Non-zero flow field was calculated using cascaded lattice Boltzmann method. 3D plots of flow field in untreated and laser treated regions have been shown in Fig. 7.13. VOIs were selected from untreated and laser treated region of each sample, see Fig. 7.6. We have shown the results for few VOIs in Fig. 7.13 which represent the common trend followed by majority of the VOIs. VOIs representing untreated regions of all samples demonstrated zero velocity field (no flow) for the pixel resolution (18 μm) and

threshold (60) used in the X-ray tomographic setup. Laser treated region of sample A (treated by a low fluence Nd:YAG 266 nm laser) showed few connected pore regions supporting non-zero velocity. The non-zero velocity has been represented by blue (online/ color print) or in black (black and white print). The results indicate that the low fluence laser created some new and wider pores with some degree of connectivity. Laser treated region of sample B, which was treated by high fluence Nd:YAG 532 nm laser, demonstrated big clusters of connected and widened pores supporting the fluid flow. This laser treatment significantly enhanced the microscopic fluid transport efficiency. The widened pores may consist of new connected pores which can support the fluid flow and old pores with increased diameter due to temperature effect. On the other hand, laser treated region of sample C, treated by continuous wave CO_2 laser, showed zero velocity field. That suggests that CO_2 laser did improve the porosity but it did not stimulate the occurence of pores wide enough to support the fluid flow.
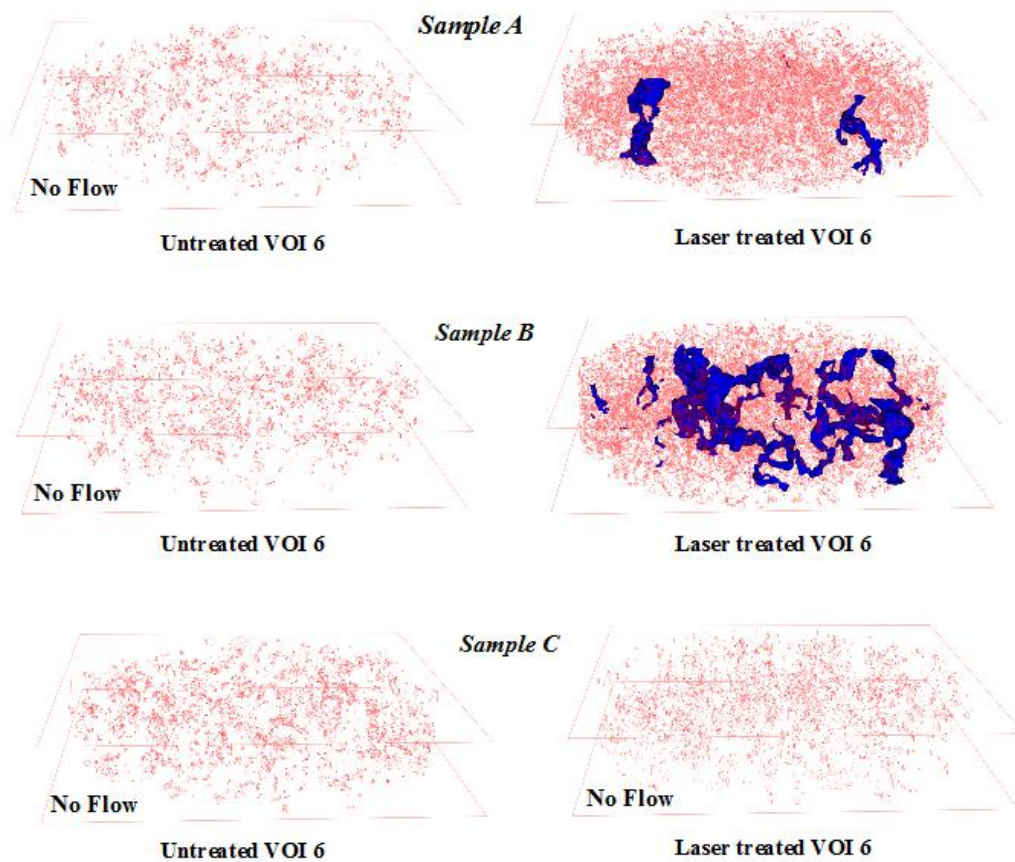
Figura 7.13: Pore scale fluid flow simulations to determine pore regions supporting non-zero velocity field in untreated and laser treated region of samples A, B and C using CLBM.

This is why no blue spot is present for laser treated sample C. CO_2 laser treated region also showed very poor pore connectivity. It can be understood that an increase in porosity does not always mean an increase in the permeability. To increase permeability along with porosity one have to (1) induce more new pores, (2) create micro-fractures connecting those new and old pores and (3) increase the pore diameter of the old and new pores.

7.4 Conclusions

We successfully demonstrated that lasers can be used to induce microscopic changes in pore structures of porous materials directly influencing their microscopic fluid transport efficiency. To assure the importance of the present study we chose a real world porous material (Indiana limestone) which has a wide range of industrial ap-

plications. We showed that temperature induced by the lasers changed the porosity by instant thermal shocks and ablation in the cases of pulsed Nd:YAG lasers, and by melting and evaporation in the case of continuous wave CO_2 laser. Our findings show that the higher the fluence, the higher the induced porosity. Another important finding is that an increase in porosity does not always mean an increase in pore connectivity or permeability. Thermal shocks and ablation by short pulses proves to be the most efficient mechanism in increasing the porosity, pore size and pore connectivity. On the contrary, continuous heating of Indiana limestone by very high fluence CO_2 laser reduces the pore connectivity. Therefore, we can conclude that degree of microscopic changes in morphometry and fluid transport efficiency of porous material depend on thermal properties such as thermal conductivity and diffusivity, fluence of the laser and most importantly operating mode of laser (pulsed or continuous irradiation). We recommend the use of ultra-short pulse lasers of high fluence to achieve large penetration depth in near wellbore regions to increase the fluid transport efficiency microscopically.

Capítulo 8

General Conclusions and Suggestions for Future Research

An efficient and stable double population cascaded lattice Boltzmann scheme (named as CTLBM) was developed and tested. The literature review presented in Chapter 2 shows that previous DDF LBM schemes consisted of BGK and MRT collision operators, which in some cases such as complex flows, i.e. turbulent flows, produced numerical instabilities. Therefore, to correct the DDF LBM schemes from this defect, CTLBM was proposed. In this approach, other collision schemes were replaced by cascaded collision schemes and implemented on two separate lattice models, simultaneously. Preserving Galilean invariance, the developed scheme increased the stability of the LBM schemes and produced results in agreement with the literature, and in some cases even better. Some important conclusions of this work are listed below.

8.1 Consistency

Consistency analysis is highly important to make sure that the proposed LBM scheme is second order correct in space and first-order correct in time. In Chapter 3, the method of equivalent partial differential equations (EPDE) was applied to the cascaded lattice Boltzmann equations (LBE) to recover N-S equations. Detailed derivation of recovery of N-S and F-K equations are presented for various collision operators. Results showed that double population cascaded LBM scheme successfully recovered the N-S equations, second-order correct in space and first-order correct in time. Therefore, the proposed method is consistent with the N-S equations.

8.2   Numerical Stability and Accuracy

The theoretical development of the double population cascaded LBM scheme has been presented in Chapter 4. The flow field equations were solved on a D_2Q_9 lattice model and temperature equation was solved on a D_2Q_5 lattice model. The scheme was applied to solve advection-diffusion of the sine wave. It is evident from the results that CTLBM produced accurate results when compared with the analytical solution of the advection-diffusion equation. The CTLBM was also compared against other collision LBM schemes such as BGK and MRT developed by other authors. The CTLBM produced stable and accurate results for high Peclet (Pe) number cases where BGK and MRT schemes were unstable. The proposed method was then applied to simulate forced convection and rotating flows. CTLBM produced stable and bounded numerical results for flow past heated cylinder and forced cooling of an array of heated tubes. For rotating flows (double shear layer flow) CTLBM showed better stability compared to two different MRT collision schemes and simple BGK scheme.

In Chapter 5, a force term was added to the CTLBM to simulate natural convection heat transfer. A systematic theoretical development has been presented in the chapter prior to the numerical implementation. The method was used to simulate natural convection in a differentially heated square cavity with adiabatic top and bottom walls. The results obtained were compared with the benchmarking solutions available in the literature. CTLBM performed well and produced accurate and stable results in various flow regimes. Laminar (Ra$< 10^6$), transitional ($10^6 < Ra < 10^8$) and turbulent flows (Ra$> 10^8$) were successfully simulated and results were compared with experimental and numerical data available in the literature. It can be noticed from the literature that very few groups have implemented simple LBM approaches to simulate turbulent flows. Therefore, one of the highlights of this work is that CTLBM, unlike other LBM approaches, does not require any special treatment such as mesh refinement, non-uniform meshing, turbulence modeling, etc. to produce stable and accurate solutions. To improve the accuracy of the proposed method to fourth-order, high order accuracy analysis of the cascaded LBM has been presented in Appendix A. The initial results are promising and the work has been submitted for publication.

8.3   Porous Media Fluid Flow Applications

In LBM, fluid flow through porous media can be studied in two different ways, (1) pore scale approach and (2) REV approach. In Chapter 7, the pore scale appro-

ach has been adopted to simulate fluid flow in limestone porous rocks. 3-D images of limestone rocks were generated using micro-CT imaging technique followed by segmentation and binarization. Cascaded LBM was then successfully applied to simulate fluid flow in the 3-D geometry.

During the course of the application, some interesting findings were discovered. It was found that pulsed irradiation from lasers can induce porosity and pore connectivity enhancement in porous rocks (presented in Chapter 7). The work developed in Chapter 7 was then extended to study the physicochemical (fluid-rock interaction) properties of porous rocks, which is of great interest. It was concluded that laser irradiation induces alteration of wettability properties in porous rocks (presented in Appendix B). In Appendix C, representative elementary volume analysis has been presented for reliable numerical simulations in porous media. To simulate fluid flows of industrial interests, it is necessary to first characterize the REV which could represent the whole sample. Since our future research plans are to implement cascaded collision scheme to study thermal multiphase flows in porous media, we have developed a procedure to define REV for efficient and accurate simulations, which is presented in Appendix C.

8.4 Future Research Suggestions

It is evident from the literature that due to the simplicity of BGK and MRT collision operators they have been used quite extensively to simulate complex fluid flows. Use of advanced collision operators such as cascaded, entropic and cumulants is very scarce in the literature. Therefore, there exists a great potential to study complex fluid flows using advanced collision schemes for further increase in the accuracy of the existing numerical schemes and better prediction of flow properties. Thermal flow problems with phase transition, separation, and multiphase multicomponent flow problems can be solved using double population cascaded LBM scheme. One needs a separate LBE for each component and an appropriate phase interaction scheme. The scheme by Shan-Chen [258] is the most popular multiphase multicomponent approach which can be incorporated into the CTLBM through a correct definition of forcing term.

Referências Bibliográficas

[1] R. M. A. Abdulmazeed, A. Datar, S. V. Bhoraskar, and V. N. Bhoraskar. Surface modification of polymers by atomic oxygen using ECR plasma. *Nucl. Instrum. Methods Phys. Res.*, B 258:345–351, 2007. doi: 10.1016/j.nimb.2007.01.230.

[2] T. Abe. Derivation of the lattice Boltzmann method by means of the discrete ordinate method for the Boltzmann equation. *Journal of Computational Physics*, 131:241, 1997. doi: 10.1006/jcph.1996.5595.

[3] A. Adrover and M. Giona. A predictive model for permeability of correlated porous media. *Chemical Engineering Journal*, 64:7–19, 1996. doi: 10.1016/s0923-0467(96)03084-9.

[4] A. R. M. N. Afrooz, D. Das, C. J. Murphy, and P. Vikesland. Co-transport of gold nanospheres with single-walled carbon nanotubes in saturated porous media. *Water Research*, 99:7–15, 2016. doi: 10.1016/j.watres.2016.04.006.

[5] C. K. Aidun and J. R. Clausen. Lattice-Boltzmann method for complex flows. *Annual Review of Fluid Mechanics*, 42:439–472, 2010. doi: 10.1146/annurev-fluid-121108-145519.

[6] H. Aksulu, D. Hamso, S. Strand, T. Puntervold, and T. Austad. Evaluation of low-salinity enhanced oil recovery effects in sandstone: Effects of the temperature and pH gradient. *Energ. Fuel*, 26:3497–3503, 2012. doi: 10.1021/ef300162n.

[7] H. S. Al-Hadhrami and M. J. Blunt. Thermally induced wettability alteration to improve oil recovery in fractured reservoirs. *SPE Res. Eva. Engg.*, pages 179–186, 2001. doi: 10.2118/59289-ms.

[8] F. J. Alexander, S. Chen, and J. D. Sterling. Lattice Boltzmann thermohydrodynamics. *Physical Review E*, 47(4), 1993. doi: 10.1103/physreve.47.r2249.

[9] R. Allen and T. Reis. Moment-based boundary conditions for lattice Boltzmann simulations of natural convection in cavities. *Progress in Computational Fluid Dynamics*, 16(4):216–231, 2016. doi: 10.1504/pcfd.2016.077296.

[10] S. Ansumali and I. V. Karlin. Consistent lattice Boltzmann method. *Physical Review Letters*, 95:260605, 2005. doi: 10.1103/physrevlett.95.260605.

[11] S. Arcidiacono, I. V. Karlin, J. Mantzaras, and C. E. Frouzakis. Lattice Boltzmann model for the simulation of multicomponent mixtures. *Phys. Rev. E*, 76:046703, 2007. doi: 10.1103/physreve.76.046703.

[12] P. Asinari. Asymptotic analysis of multiple-relaxation-time lattice Boltzmann schemes for mixture modeling. *Computers and mathematics with applications*, 55:1392–1407, 2008. doi: 10.1016/j.camwa.2007.08.006.

[13] P. Asinari. Generalized local equilibrium in the cascaded lattice Boltzmann method,. *Physical Review E*, 78:016701, 2008. doi: 10.1103/physreve.78.016701.

[14] M. Bakhtbidar and M. Abdideh. The effect of laser irradiation on rock permeability enhancement to improve oil recovery, session: Reservoir studies. In *79 EAGE Conference and Exhibition*, 2017.

[15] K. Balasubramanian, F. Hayot, and W. F. Saam. Darcy's law from lattice-gas hydrodynamics. *Physical Review A*, 36:2248, 1987. doi: 10.1103/physreva.36.2248.

[16] G. Barakos, E. Mitsoulis, and D. Assimacopoulos. Natural convection flow in a square cavity revisited: laminar and turbulent models with wall functions. *International Journal of Numerical Methods in Fluids*, 18:695–719, 1994. doi: 10.1002/fld.1650180705.

[17] A. Bartoloni, C. Battista, S. Cabasino, P. S. Paolucci, J. Pech, R. Sarno, G. M. Todesco, M. Torelli, W. Tross, P. Vicini, R. Benzi, N. Cabibbo, F. Massaioli, and R. Tripiccione. LBE simulations of Rayleigh-Be/'nard convection. *International Journal of Modern Physics C*, 4(5):993–1006, 1993.

[18] R. Benzi and S. Succi. Two-dimensional turbulence with the lattice Boltzmann equation. *J. Phys. A*, 23:1–5, 1990. doi: 10.1088/0305-4470/23/1/001.

[19] R. Benzi, S. Succi, and M. Vergassola. The lattice Boltzmann equation: theory and application. *Physics Reports*, 222, No. 3:145–197, 1992. doi: 10.1016/0370-1573(92)90090-m.

[20] M. H. Berg, S. Llic, D. Bartls, W. B. Joekar, and V. Niasar. Kinetics of low salinity flooding effect. *SPE Journal*, 165255:8–20. doi: 10.2118/165255-pa.

[21] P. L. Bhatnagar, E. P. Gross, and M. Krook. A model for collision processes in gases i: Small amplitude processes in charged and neutral one-component systems. *Phys. Rev. E*, 94:511–525, 1954. doi: 10.1103/physrev.94.511.

[22] J. P. Boon. Statistical mechanics and hydrodynamics of lattice gas automata: an overview. *Physica D*, 47:3–8, 1991. doi: 10.1016/0167-2789(91)90272-b.

[23] F. Bosch, S. S. Chikatamarla, and I. V. Karlin. Entropic multirelaxation lattice boltzmann models for turbulent flows. *Physical Review E*, 92(4):043309, 2015. doi: 10.1103/physreve.92.043309.

[24] C. Bosshard, A. Dehbi, M. Deville, E. Leriche, R. Puragliesi, and A. Soldati. Large eddy simulation of the differentially heated cubic cavity flow by the spectral element method. *Computers & Fluids*, 86:210–227, 2013. doi: 10.1016/j.compfluid.2013.07.007.

[25] M. L. Bouxsein, S. K. Boyd, B. A. Christiansen, R. E. Guldberg, K. J. Jepsen, and R. Muller. Guidelines for assessment of bone microstructure in rodents using micro–computed tomography. *Journal of bone and mineral research*, 25(7):1468–1486, 2010. doi: 10.1002/jbmr.141.

[26] R. S. Boyton. *Chemistry and Technology of lime and limestone.* New York, Wiley, 1980.

[27] M. Braza, P. Chassaing, and H. H. Minh. Numerical study and physical analysis of the pressure and velocity fields in the near wake of a circular cylinder. *Journal of Fluid Mechanics*, 165:79–130, 1986. doi: 10.1017/s0022112086003014.

[28] A. D. Brent, V. R. Voller, and K. Reid. Enthalpy-porosity technique for modeling convection–diffusion phase change: application to the melting of a pure metal. *Numerical Heat Transfer*, 13:297–318, 1988. doi: 10.1080/10407788808913615.

[29] J. Cai and X. Huai. Study on fluid–solid coupling heat transfer in fractal porous medium by lattice Boltzmann method. *Applied Thermal Engineering*, 30: 715–723, 2010. doi: 10.1016/j.applthermaleng.2009.12.001.

[30] A. Cancelliere, C. Chang, E. Foti, D. H. Rothman, and S. Succi. The permeability of a random medium: comparison of simulation with theory. *Physics of Fluids A*, 2:2085–2088, 1990. doi: 10.1063/1.857793.

[31] N. Cao, S. Chen, S. Jin, and D. Martinez. Physical symmetry and lattice symmetry in the lattice Boltzmann method. *Physical Review E*, 55(1), 1997. doi: 10.1103/physreve.55.r21.

[32] Y. A. Cengel. *Heat Transfer: A Practical Approach 2nd Edition.* Mcgraw-Hil, 2002.

[33] S. Chakraborty and D. Chatterjee. An enthalpy-based hybrid lattice-Boltzmann method for modelling solid–liquid phase transition in the presence of convective transport. *J. Fluid Mech.*, 592:155–175, 2007. doi: 10.1017/s0022112007008555.

[34] X. Chan and H. Chen. Lattice Boltzmann model for simulating flows with multiple phases and components. *Phys. Rev. E*, 47:1815–1819, 1993. doi: 10.1103/physreve.47.1815.

[35] X. Chan and G. D. Doolen. Multicomponent lattice-Boltzmann model with interparticle interaction. *J. Stat. Phys.*, 81:379–393, 1995. doi: 10.1007/bf02179985.

[36] C. Chang, C-H Liu, and C-A Lin. Boundary conditions for lattice Boltzmann simulations with complex geometry flows. *Computers & Mathematics with Applications*, 58(5):940–949, 2009. doi: 10.1016/j.camwa.2009.02.016.

[37] Q. Chang and J. I. D. Alexander. Application of the lattice Boltzmann method to two-phase Rayleigh–Benard convection with a deformable interface. *Journal of Computational Physics*, 212:473–489, 2006. doi: 10.1016/j.jcp.2005.05.031.

[38] S. C. Chang. A critical analysis of the modified equation technique of Warming and Hyett. *J. Comput. Phys.*, 86:107–126, 1990. doi: 10.1016/0021-9991(90)90093-g.

[39] D. Chatterjee. An enthalpy-based thermal lattice Boltzmann model for non-isothermal systems. *EPL*, 86:14004, 2009. doi: 10.1209/0295-5075/86/14004.

[40] C-K. Chen, T-S. Yen, and Y-T. Yang. Lattice Boltzmann method simulation of backward-facing step on convective heat transfer with field synergy

principle. *International Journal of Heat and Mass Transfer*, 49:1195–1204, 2006. doi: 10.1016/j.ijheatmasstransfer.2005.08.027.

[41] H. Chen. H-theorem and generalized semi-detailed balance condition for lattice gas system. *Journal of Statistical Physics*, 81(1–2):347–408, 1995. doi: 10.1007/bf02179983.

[42] H. Chen, S. Chen, and W. H. Matthaeus. Recovery of Navier-Stokes equations using a lattice-gas Boltzmann method. *Physical Review A*, 45(8), 1992. doi: 10.1103/physreva.45.r5339.

[43] H. Chen, C. Teixeira, and K. Molvig. Digital physics approach to computational fluid dynamics: Some basic theoretical features. *International Journal of Modern Physics C*, 8(4), 1997. doi: 10.1142/s0129183197000576.

[44] S. Chen and G. D. Doolen. Lattice Boltzmann method for fluid flows. *Annual Review in Fluid Mechanics*, 30:329–64, 1998. doi: 10.1146/annurev.fluid.30.1.329.

[45] S. Chen and Z. Tian. Simulation of thermal micro-flow using lattice Boltzmann method with langmuir slip model. *International Journal of Heat and Fluid Flow*, 31:227–235, 2010. doi: 10.1016/j.ijheatfluidflow.2009.12.006.

[46] S. Chen, Z-S. Chen, L. C. Harrison, and G. D. Doolen. Optimal initial condition for lattice-gas hydrodynamics. *Physical Review A*, 39:2725, 1989. doi: 10.1103/physreva.39.2725.

[47] S. Chen, M. Lee, K. H. Zhao, and Gary D. Doolen. A lattice gas model with temperature. *Physica D*, 37:42–59, 1989. doi: 10.1016/0167-2789(89)90116-4.

[48] S. Chen, H. Chen, D. Martinez, and W. Matthaeus. Lattice Boltzmann model for simulation of magnetohydrodynamics. *Physical Review Letters*, 67(27), 1991. doi: 10.1103/physrevlett.67.3776.

[49] S. Chen, K. Diemer, G. D. Doolen, K. Eggert, C. Fu, S. Gutman, and B. J. Travis. Lattice gas automata for flow through porous media. *Physica D*, 47:72–84, 1991. doi: 10.1016/0167-2789(91)90281-d.

[50] S. Chen, Z. Liu, C. Zhang, Z. He, Z. Tian, B. Shi, and C. Zheng. A novel coupled lattice Boltzmann model for low Mach number combustion simulation. *Applied Mathematics and Computation*, 193:266–284, 2007. doi: 10.1016/j.amc.2007.03.087.

[51] Y. Chen, H. Ohashi, and M. Akiyama. Thermal lattice Bhatnagar-Gross-Krook model without nonlinear deviations in macrodynamic equations. *Physical Review E*, 50(4):2776–2783, 1994. doi: 10.1103/physreve.50.2776.

[52] Y. Chen, H. Ohashi, and M. Akiyama. Two-parameter thermal lattice BGK model with a controllable Prandtl number. *Journal of Scientific Computing*, 12(2), 1997.

[53] P. Cheng. Heat transfer in geothermal systems. *Advances in Heat Transfer*, 4: 1–105, 1978. doi: 10.1016/s0065-2717(08)70085-6.

[54] X. Chi, Y. Li, H. Addy, G. Addy, Y. Choo, T. Shih, and H. Chen. A comparative study using CFD to predict iced airfoil aerodynamics. *43rd AIAA Aerospace Sciences Meeting and Exhibit*, 43:1371–1382, 2005. doi: 10.2514/6.2005-1371.

[55] B. Chopard, J.-L. Falcone, and J. Latt. The lattice Boltzmann advection-diffusion model revisited. *The European Physical Journal Special Topics*, 171(1):245–249, 2009. doi: 10.1140/epjst/e2009-01035-5.

[56] T. J. Chung. *Computational fluid dynamics*. Cambridge University Press, 2010. doi: 10.1017/cbo9780511780066.

[57] T. Colborn, C. Kwiatkowski, K. Schultz, and M. Bachran. Natural gas operations from a public health perspective. *Human and Ecological Risk Assessment: an International Journal*, 17(5):1039–1056, 2015. doi: 10.1080/10807039.2011.605662.

[58] D. Contrino, P. Lallemand, P. Asinari, and L.-S. Luo. Lattice-Boltzmann simulations of the thermally driven 2d square cavity at high rayleigh numbers. *Journal of Computational Physics*, 275:257–272, 2014. doi: 10.1016/j.jcp.2014.06.047.

[59] NVIDIA Corporation. *NVIDIA CUDA C Programming Guide v6.5*, 2014. URL https://docs.nvidia.com/cuda/cuda-c-programming-guide/#abstract.

[60] W. P. Crowley. *Journal of Computational Physics*, 1:471, 1967.

[61] S. Cui, N. Hong, B. Shi, and Z. Chai. Discrete effect on the halfway bounce-back boundary condition of multiple-relaxation-time lattice boltzmann model for convection-diffusion equations. *Physical Review E*, 93(4):043311, 2016. doi: 10.1103/physreve.93.043311.

[62] J. Dahlburg, D. Montgomery, and G. D. Doolen. Noise and compressibility in lattice-gas fluids. *Physical Review A*, 36:1471, 1987. doi: 10.1103/physreva.36.2471.

[63] O. Dardis and J. McCloskey. Lattice Boltzmann scheme with real numbered solid density for the simulation of flow in porous media. *Physical Review E*, 57:4834–4837, 1998. doi: 10.1103/physreve.57.4834.

[64] O. M. O. de Araujo, K. V. Sharma, A. S. Machado, T. M. P. Santos, C. G. Ferreira, R. Straka, F. W. Tavares, and R. T. Lopes. Representative elementary volume in limestone sample. *Journal of Instrumentation*, 13 (C):10003, 2018. doi: 10.1088/1748-0221/13/10/c10003.

[65] G. de Vahl Davis. Natural convection of air in a square cavity: a bench mark numerical solution. *International Journal for numerical methods in fluids*, 3(3):249–264, 1983. doi: 10.1002/fld.1650030305.

[66] G. DeFabritis, A. Mancini, and S. Succi. Mesoscopic models of liquid/solid phase transitions. *International Journal of Modern Physics C*, 9:1405–1415, 1998. doi: 10.1142/s0129183198001278.

[67] N. Delbosc, J. L. Summers, A. I. Khan, N. Kapur, and C. J. Noakes. Optimized implementation of the lattice Boltzmann method on a graphics processing unit towards real-time fluid simulation. *Computers and Mathematics with Applications*, 67(2):462–475, 2014. doi: 10.1016/j.camwa.2013.10.002.

[68] P. J. Dellar. Bulk and shear viscosities in lattice Boltzmann equations. *Physical Review E*, 64, 2001. doi: 10.1103/physreve.64.031203.

[69] A. Amiri Delouei, M. Nazari, M. H. Kayhani, and S. Succi. Non-newtonian unconfined flow and heat transfer over a heated cylinder using the direct-forcing immersed boundary–thermal lattice Boltzmann method. *Physical Review E*, 89:053312, 2014. doi: 10.1103/physreve.89.053312.

[70] D. d'Humieres. Generalized lattice-Boltzmann equations. *Prog. Aeronaut. Astronaut.*, 159:450–458, 1992. doi: https://doi.org/10.2514/5.9781600866319.0450.0458.

[71] D. d'Humieres, I. Ginzburg, M. Krafczyk, P. Lallemand, and L-S. Luo. Multiple-relaxation-time lattice Boltzmann models in three dimensions. *Philosophical Transactions of Royal Society of London*, 360:437–451, 2002. doi: 10.1098/rsta.2001.0955.

[72] D. D'Humières. Generalized lattice-Boltzmann equations. *Progress in Astronautics and Aeronautics*. doi: 10.2514/5.9781600866319.0450.0458.

[73] D. D'Humières, I. Ginzburg, M. Krafczyk, P. Lallemand, and LI-Shi Luo. Multiple-relaxation-time lattice Boltzmann models in three dimensions. *Philosophical Transactions of the Royal Society of London. Series A: Mathematical, Physical and Engineering Sciences*, 360(1792):437–51, 2002. doi: 10.1098/rsta.2001.0955.

[74] H. N. Dixit and V. Babu. Simulation of high rayleigh number natural convection in a square cavity using the lattice Boltzmann method. *International Journal of Heat and Mass Transfer*, 49:727–739, 2006. doi: 10.1016/j.ijheatmasstransfer.2005.07.046.

[75] A. D'Orazio and S.Succi. Simulating two-dimensional thermal channel flows by means of a lattice Boltzmann method with new boundary conditions. *Future Generation Computer Systems*, 20:935–944, 2004. doi: 10.1016/j.future.2003.12.005.

[76] A. D'Orazio, M. Corcione, and G. P. Celata. Application to natural convection enclosed flows of a lattice boltzmann BGK model coupled with a general purpose thermal boundary condition. *International Journal of Thermal Sciences*, 43:575–586, 2004. doi: 10.1016/j.ijthermalsci.2003.11.002.

[77] B. Dorschner, F. Bosch, S. S. Chikatamarla, K. Boulouchos, and I. V. Karlin. Entropic multi-relaxation time lattice Boltzmann model for complex flows. *Journal of Fluid Mechanics*, 801:623–651, 2016. doi: 10.1017/jfm.2016.448.

[78] B. Dorschner, N. Frapolli, S. S. Chikatamarla, and I. V. Karlin. Grid refinement for entropic lattice Boltzmann models. *Physical Review E*, 94(5):053311, 2016. doi: 10.1103/physreve.94.053311.

[79] F. Dubois. Equivalent partial differential equations of a lattice Boltzmann scheme. *Computers and mathematics with applications*, 55:1441–1449, 2008. doi: 10.1016/j.camwa.2007.08.003.

[80] F. Dubois, C-A Lin, and M. M. Takitek. Anisotropic thermal lattice Boltzmann simulation of 2d natural convection in a square cavity. *Computers and Fluids*, 124:278–287, 2016. doi: 10.1016/j.compfluid.2015.10.015.

[81] J. G. M. Eggels and J. A. Somers. Numerical simulation of free convective flow using the lattice Boltzmann scheme. *J. Heat Fluid Flow*, 16:357, 1995. doi: 10.1016/0142-727x(95)00052-r.

[82] R. A. Escobar, S. S. Ghai, M. S. Jhon, and C. H. Amon. Multi-length and time scale thermal transport using the lattice Boltzmann method with application to electronics cooling. *International Journal of Heat and Mass Transfer*, 49:97–107, 2006. doi: 10.1016/j.ijheatmasstransfer.2005.08.003.

[83] K. Fei, W. H. Chen, and C. W. Hong. Microfluidic analysis of CO2 bubble dynamics using thermal lattice-Boltzmann method. *Microfluidics and Nanofluidics*, 5:119–129, 2008. doi: 10.1007/s10404-007-0232-x.

[84] L. Fei and K. H. Luo. Cascaded lattice Boltzmann method for incompressible thermal flows with heat sources and general thermal boundary conditions. *Computers and Fluids*, 165:89–95, 2018. doi: 10.1016/j.compfluid.2018.01.020.

[85] L. Fei and K. H. Luo. Cascaded lattice boltzmann method for thermal flows on standard lattices. *International Journal of Thermal Sciences*, 132: 368–377, 2018. doi: 10.1016/j.ijthermalsci.2018.06.017.

[86] L. Fei and K.H. Luo. Thermal cascaded lattice Boltzmann method. *arXiv preprint*, 2016. URL http://arxiv.org/abs/1610.07114.

[87] M. A. Ferno, M. Torsvik, S Haugland, and A. Graue. Dynamic laboratory wettability alteration. *Energy and Fuels*, 24:395–3958, 2010. doi: 10.1021/ef1001716.

[88] O. Fillipova and D. Hanel. A novel lattice BGK approach for low Mach number combustion. *Journal of Computational Physics*, 158:139–160, 2000. doi: 10.1006/jcph.1999.6405.

[89] E. G. Flekkoy and H. J. Hermann. Lattice Boltzmann models for complex fluids. *Physica A: Statistical Mechanics and its Applications*, 199:1–11, 1993. doi: 10.1016/0378-4371(93)90091-h.

[90] U. Frisch. Relation between the lattice Boltzmann equation and the Navier-Stokes equations. *Physica D*, 47:231–232, 1991. doi: 10.1016/0167-2789(91)90293-i.

[91] U. Frisch, B. Hasslacher, and Y. Pomeau. Lattice-gas automata for the Navier-Stokes equation. *Physical Review Letters*, 56(14), 1986. doi: 10.1103/physrevlett.56.1505.

[92] B. Gahan, R. Parker, R. Graves, S. Batarseh, C Reed, Z Xu, H Figueroa, and N Skinner. Laser drilling: Drilling with the power of light - phase one: Fe-

asibility study. Technical report, Topical Report Cooperative Agreement No. DEFC26-00NT40917, 2001.

[93] D. Gao, Z. Chen, and L. Chen. A thermal lattice Boltzmann model for natural convection in porous media under local thermal non-equilibrium conditions. *International Journal of Heat and Mass Transfer*, 70:979–989, 2014. doi: 10.1016/j.ijheatmasstransfer.2013.11.050.

[94] M. Geier. *Ab initio derivation of the cascaded lattice Boltzmann automaton*. phdthesis, University of Freiburg, 2006. URL https://freidok.unifreiburg.de/data/2860/.

[95] M. Geier, A. Greiner, and J. G. Korvink. Cascaded digital lattice Boltzmann automata for high Reynolds number flow. *Physical Review E*, 73(6):066705, 2006. doi: 10.1103/physreve.73.066705.

[96] M. Geier, M. Schonherr, A. Pasquali, and M. Krafczyk. The Cumulant lattice Boltzmann equation in three dimensions: theory and validation. *Comput. Math. Appl.*, 70(4):507–547, 2015. doi: 10.1016/j.camwa.2015.05.001.

[97] J. Ghazanfarian and A. Abbassi. Heat transfer and fluid flow in microchannels and nanochannels at high Knudsen number using thermal lattice-Boltzmann method. *Physical Review E*, 82:026307, 2010. doi: 10.1103/physreve.82.026307.

[98] I. Ginzburg and D. d'Humieres. Local second-order boundary methods for lattice Boltzmann models. *Journal of Statistical Physics*, 84:927–971, 1996. doi: 10.1007/bf02174124.

[99] I. Ginzburg, F. Verhaeghe, and D. d'Humieres. Two-relaxation-time lattice boltzmann scheme: About parametrization, velocity, pressure and mixed boundary conditions. *Communications in Computational Physics*, 3(2): 427–478, 2008.

[100] I. Ginzburg, F. Verhaeghe, and D. d'Humieres. Study of simple hydrodynamic solutions with thetwo-relaxation-times lattice boltzmann scheme. *Communications in Computational Physics*, 3(2):519–581, 2008.

[101] F. Golse and L. Saint-Raymond. The Navier-Stokes limit of the Boltzmann equation. *C. R. Acad. Sci. Paris Serie*, 333(9):897–902, 2001. doi: 10.1016/s0764-4442(01)02136-x.

[102] F. Golse and L. Saint-Raymond. The Navier-Stokes limit of the Boltzmann equation for bounded collision kernels. *Invent. Math.*, 155:81–161, 2004.

[103] G. Gonnella, A. Lamura, and V. Sofonea. Lattice Boltzmann simulation of thermal nonideal fluids. *Physical Review E*, 76:036703, 2007. doi: 10.1103/physreve.76.036703.

[104] R. M. Graves, S. Batarseh, R. A. Parker, and B. C. Gahan. Temperatures induced by high power lasers: Effects on reservoir rock strength and mechanical properties. *SPE/ISRM 78154*, Rock Mechanics Conference, Irving, Texas, 2002.

[105] D. Griffiths and J. Sanz-Serna. On the scope of the method of modified equations. *SIAM Journal on Scientific and Statistical Computing*, 7, 1986. doi: 10.1137/0907067.

[106] M. Gross, R. Adhikari, M. E. Kates, and F. Varnik. Thermal fluctuations in the lattice Boltzmann method for nonideal fluids. *Physical Review E*, 82: 056714, 2010. doi: 10.1103/physreve.82.056714.

[107] D. Grunau, S. Chen, and K. Eggert. A lattice Boltzmann model for multiphase fluid flows. *Phys. Fluids A*, 5:2557–2562, 1993. doi: 10.1063/1.858769.

[108] A. K. Gunstensen and D. H. Rothman. A lattice-gas model for three immiscible fluids. *Physica D*, 47:47–52, 1991. doi: 10.1016/0167-2789(91)90278-h.

[109] J. Guo, B. Gou, K. Wang, J. Ren, and J. Zeng. An optimal design of network-fracture acidification for ultra-deep gas wells in the lower permian strata of the western sichuan basin. *Natural Gas Industry B*, 2017. doi: 10.1016/j.ngib.2017.09.012.

[110] Z. Guo and C. Shu. *Lattice Boltzmann Method and its applications in engineering*. World Scientifc, 2013. doi: 10.1142/8806.

[111] Z. Guo and T. S. Zhao. Lattice Boltzmann model for incompressible flows through porous media. *Physical Review E*, 66:036304, 2002. doi: 10.1103/physreve.66.036304.

[112] Z. Guo and T. S. Zhao. A lattice Boltzmann model for convection heat transfer in porous media. *Numerical Heat Transfer, Part B*, 42(2):157–177, 2005. doi: 10.1080/10407790590883405.

[113] Z. Guo, B. Shi, and C. Zheng. A coupled lattice BGK model for the Boussinesq equations. *International Journal for Numerical Methods in Fluids*, 39: 325–342, 2002. doi: 10.1002/fld.337.

[114] Z. Guo, C. Zheng, B. Shi, and T. S. Zhao. Thermal lattice Boltzmann equation for low Mach number flows: Decoupling model. *Physical Review E*, 75: 036704, 2007. doi: 10.1103/physreve.75.036704.

[115] N. Gupta, R. Chaitanya, and S. C. Mishra. Lattice Boltzmann method applied to variable thermal conductivity conduction and radiation problems. *Journal of Thermophysics and Heat Transfer*, 20(4), 2006. doi: 10.2514/1.20557.

[116] F. Hajabdollahi, K. N. Premnath, and S. W. J. Welch. Cascaded lattice Boltzmann method based on central moments for axisymmetric thermal flows including swirling effects. *International Journal of Heat and Mass Transfer*, 128:999–1016, 2019. doi: 10.1016/j.ijheatmasstransfer.2018.09.059.

[117] H. Hammou, I. Ginzburg, and M. Boulerhcha. Two-relaxation times lattice boltzmann schemes for solute transport in unsaturated water flow, with a focus on stability. *Advances in Water Resources*, 34:779–793, 2011. doi: 10.1016/j.advwatres.2011.04.008.

[118] X. Han, H. Fang, G. He, and D. Rebile. Effects of roughness and permeability on solute transfer at the sediment water interface. *Water Research*, 129: 39–50. doi: 10.1016/j.watres.2017.10.049.

[119] J. Hardy and Y.Pomeau. *J. Math Phys*, 13:1042, 1972.

[120] J. Hardy, Y.Pomeau, and O. de Pazzis. *J. Math Phys*, 14:1746, 1973.

[121] J. Hardy, O. de Pazzis, and Y. Pomeau. *Phys. Rev. A*, 13:1949, 1976.

[122] S. Harris. Approach to equilibrium in a moderately dense discrete velocity gas. *The Physics of Fluid*, 9:1328, 1966. doi: 10.1063/1.1761848.

[123] X. He and L-S. Luo. A priori derivation of the lattice Boltzmann equation. *Physical Review E*, 55(6), 1997. doi: 10.1103/physreve.55.r6333.

[124] X. He and L-S. Luo. A priori derivation of the lattice Boltzmann equation. *Physical Review E*, 55(6), 1997. doi: 10.1103/physreve.55.r6333.

[125] X. He, L-S. Luo, and M. Dembo. Some progress in lattice Boltzmann method. part 1. nonuniform mesh grids. *Journal of Computational Physics*, 129: 357–363, 1996. doi: 10.1006/jcph.1996.0255.

[126] X. He, Q. Zou, L-S. Luo, and M. Dembo. Analytic solution of simple flows and analysis of nonslip boundary conditions for the lattice Boltzmann BGK model. *Journal of Statistical Physics*, 87:115, 1997. doi: 10.1007/bf02181482.

[127] X. He, S. Chen, and G. D. Doolen. A novel thermal model for the lattice Boltzmann method in incompressible limit. *Journal of Computational Physics*, 146:282–300, 1998. doi: 10.1006/jcph.1998.6057.

[128] X. He, X. Shan, and G. D. Doolen. A discrete Boltzmann equation model for non-ideal gases. *Physical Review E*, 57(R13), 1998. doi: 10.1103/phys-reve.57.r13.

[129] X. He, S. Chen, and R. Zhang. A lattice Boltzmann scheme for incompressible multiphase flow and its application in simulation of Rayleigh-Taylor instability. *J. Comput. Phys.*, 152:642–663, 1999. doi: 10.1006/jcph.1999.6257.

[130] R. A. W. M. Henkes, F. F. van der Vlugt, and C. J. Hoogendoorn. Natural convection flow in a square cavity calculated with low-Reynolds-number turbulence models. *International Journal of Heat and Mass Transfer*, 4: 1543–1557, 1991. doi: 10.1016/0017-9310(91)90258-g.

[131] F. J. Higueira, S. Succi, and R. Benzi. Lattice gas dynamics with enhanced collisions. *Europhysics Letters*, 9(4):345–349, 1989. doi: 10.1209/0295-5075/9/4/008.

[132] D. Hilbert. Mathematical problems. *Bulletin of American Mathematical Society*, 8(10):437–51, 1902. doi: 10.1090/s0002-9904-1902-00923-3.

[133] C. W. Hirt. Heuristic stability theory for finite-difference equations. *Journal of Computational Physics 2, 339-355*, 1968. doi: 10.1016/0021-9991(68)90041-7.

[134] J-R Ho, C-P Kuo, and W-S Jiaung. Study of heat transfer in multilayered structure within the framework of dual-phase-lag heat conduction model using lattice Boltzmann method. *International Journal of Heat and Mass Transfer*, 46:55–69, 2003. doi: 10.1016/s0017-9310(02)00260-0.

[135] D. J. Holdych, D. R. Noble, J. G. Georgiadis, and R. O. Buckius. Truncation error analysis of lattice Boltzmann methods. *Journal of Computational Physics*, 193(2):595–619, 2004. doi: 10.1016/j.jcp.2003.08.012.

[136] M. Hortmann, M. Peric, and G. Scheuerer. Finite volume multigrid prediction of laminar natural convection : benchmark solutions. *International Journal for Numerical Methods in Fluids*, 11(2):189–207, 1990. doi: 10.1002/fld.1650110206.

[137] S. Hou, Q. Zou, S. Chen, G. D. Doolen, and A. C. Cogley. Simulation of cavity flow by the lattice Boltzmann method. *Journal of Computational Physics*, 118:329, 1995. doi: 10.1006/jcph.1995.1103.

[138] S. Hou, X. Shan, Q. Zou, G. D. Doolen, and W. E. Soll. Evaluation of two lattice Boltzmann models for multiphase flows. *J. Comput. Phys.*, 138: 695–713, 1997. doi: 10.1006/jcph.1997.5839.

[139] R. Huang and H. Wu. An immersed boundary-thermal lattice Boltzmann method for solid–liquid phase change. *Journal of Computational Physics*, 277:305–319, 2014. doi: 10.1016/j.jcp.2014.08.020.

[140] G. Hurwitz, G. R. Guillen, and E. M. V. Hoek. Probing polyamide membrane surface charge, zeta potential, wettability, and hydrophilicity with contact angle measurements. *Journal of Membrane Science*, 349:349–357, 2010. doi: 10.1016/j.memsci.2009.11.063.

[141] T. Ihle and D.M. Kroll. Thermal lattice-Boltzmann method for non-ideal gases with potential energy. *Computer Physics Communications*, 129: 1–12, 2000. doi: 10.1016/s0010-4655(00)00087-4.

[142] T. Inamuro, M. Yoshino, and F. Ogino. A non-slip boundary condition for lattice Boltzmann simulations. *Physics of Fluids*, 7(12):2928–2930, 1995. doi: 10.1063/1.868766.

[143] T. Inamuro, N. Konishi, and F. Ogino. A galilean invariant model of the lattice Boltzmann method for multiphase fluid flows using free-energy approach. *Comput. Phys. Commun.*, 129:32–45, 2000. doi: 10.1016/s0010-4655(00)00090-4.

[144] T. Inamuro, M. Yoshino, H. Inoue, R. Mizuno, and F. Ogino. A lattice Boltzmann method for a binary miscible fluid mixture and its application to a heat-transfer problem. *Journal of Computational Physics*, 179:201–215, 2002. doi: 10.1006/jcph.2002.7051.

[145] S. Izquierdo and N. Fueyo. Characteristic nonreflecting boundary conditions for open boundaries in lattice boltzmann methods. *Physical Review E*, 78 (4):046707, Oct 2008. doi: 10.1103/PhysRevE.78.046707. URL https://link.aps.org/doi/10.1103/PhysRevE.78.046707.

[146] M. Jami, A. Mezrhab, M. Bouzidi, and P. Lallemand. Lattice Boltzmann method applied to the laminar natural convection in an enclosure with a heat-generating cylinder conducting body. *International Journal of Thermal Sciences*, 46:38–47, 2007. doi: 10.1016/j.ijthermalsci.2006.03.010.

[147] M. Jami, F. Moufekkir, A. Mezrhab, J. P. Fontaine, and M. Bouzidi. New thermal MRT lattice Boltzmann method for simulations of convective flows. *International Journal of Thermal Sciences*, 100:98–107, 2016. doi: 10.1016/j.ijthermalsci.2015.09.011.

[148] H. K. Jeong, H. S. Yoon, M. Y. Ha, and M. Tsutahara. An immersed boundary-thermal lattice Boltzmann method using an equilibrium internal energy density approach for the simulation of flows with heat transfer. *Journal of Computational Physics*, 229:2526–2543, 2010. doi: 10.1016/j.jcp.2009.12.002.

[149] W. Jiaung, J. Ho, and C. Kuo. Lattice Boltzmann method for the heat conduction problem with phase change. *Numerical Heat Transfer, Part B*, 39:167–187, 2001. doi: 10.1080/10407790150503495.

[150] G. Juncu. The influence of the physical properties ratios on the conjugate heat transfer from a drop. *Heat and Mass Transfer*, 35:251–257, 1999. doi: 10.1007/s002310050321.

[151] M. Junk and W. A. Yong. Rigorous Navier-Stokes limit of the lattice Boltzmann equation. *Asympt. Anal.*, 35:165–185, 2003.

[152] M. Junk, A. Klar, and L. Luo. Asymptotic analysis of the lattice Boltzmann equation. *J. Comput. Phys.*, 210:676–704, 2005. doi: 10.1016/j.jcp.2005.05.003.

[153] G. Kaehler and A. J. Wagner. Derivation of hydrodynamics for multi-relaxation time lattice Boltzmann using the moment approach. *Communications in Computational Physics*, 13, No.3:614–628, 2013. doi: 10.4208/cicp.451011.260112s.

[154] D. Kandhai, D. J-E. Vidal, A. G. Hoekstra, H. Hoefsloot, P. Iedema, and P. M. A. Sloot. Lattice-Boltzmann and finite-element simulations of fluid flow in a smrx static mixer reactor. *International Journal of Numerical Methods in Fluids*, 31:1019–1033, 1999. doi: 10.1002/(sici)1097-0363(19991130)31:6¡1019::aid-fld915¿3.0.co;2-i.

[155] S. K. Kang and Y. A. Hassan. A direct-forcing immersed boundary method for the thermal lattice Boltzmann method. *Computers and Fluids*, 49: 36–45, 2011. doi: 10.1016/j.compfluid.2011.04.016.

[156] I. V. Karlin, A. Ferrante, and H. C. Öttinger. Perfect entropy functions of the lattice Boltzmann method. *Europhysics Letters*, 47:182–188, 1999. doi: 10.1209/epl/i1999-00370-1.

[157] I. V. Karlin, D. Sichau, and S. S. Chikatamarla. Consistent two population lattice Boltzmann model for thermal flows. *Physical Review E*, 88(6): 063310, 2013. doi: 10.1103/physreve.88.063310.

[158] N. S. Kasalkova, P. Slecpicka, Z. Colska, and V. Svorick. *Wettability and other surface properties of modified polymers.* Intechopen, 2015. doi: 10.5772/60824.

[159] Y. Keehm. *Computational rock physics: Transport properties in porous media and applications.* Ph.d. dissertation, Stanford University, 2003.

[160] GH. R. Kefayati, S. F. Hosseinizadeh, M. Gorji, and H. Sajjad. Lattice Boltzmann simulation of natural convection in an open enclosure subjugated to water/copper nanofluid. *International Journal of Thermal Sciences*, 52:91–101, 2012. doi: 10.1016/j.ijthermalsci.2011.09.005.

[161] T. Y. Kim and S. W. Baek. Analysis of combined conductive–radiative heat transfer in a two-dimensional rectangular enclosure using the discrete ordinate method. *International Journal of Heat and Mass Transfer*, 34(9): 2265–2273, 1991.

[162] K. J. King. *Turbulent Natural Convection in Rectangular Air Cavities.* PhD thesis, University of London, 1989.

[163] J. M. V. A. Koleman. A simple lattice Boltzmann scheme for Navier-Stokes fluid flow. *Europhysics Letters*, 15(6):603–607, 1991.

[164] J. Koplik and T. Lasseter. One- and two-phase flow in network models of porous media. *Chem. Eng. Comm.*, 26:285–95, 1985.

[165] T. Kruger, H. Kusumaatmaja, A. Kuzmin, O. Shardt, G. Silva, and E. M. Viggen. *The Lattice Boltzmann Method: Principles and Practice.* Springer International Publishing Switzerland, 2017. doi: 10.1007/978-3-319-44649-3.

[166] F. Kuchuk, D. Biryukov, and T. Fitzpatrick. Fractured-reservoir modeling and interpretation. *SPE Journal*, 20(5), 2015. doi: 10.2118/176030-PA.

[167] F. Kuznik, J. Vareilles, G. Rusaouen, and G. Krauss. A double-population lattice Boltzmann method with non-uniform mesh for the simulation of natural convection in a square cavity. *International Journal of Heat and Fluid Flow*, 28:862–870, 2007. doi: 10.1016/j.ijheatfluidflow.2006.10.002.

[168] A. J. C. Ladd. Numerical simulations of particulate suspensions via a discretized boltzmann equation: Part1: theoretical foundation. *Journal of Fluid Mechanics*, 271:285–309, 1994. doi: 10.1017/s0022112094001771.

[169] A. J. C. Ladd. Numerical simulations of particulate suspensions via a discretized boltzmann equation: Part2. numerical results. *Journal of Fluid Mechanics*, 271:311–339, 1994. doi: 10.1017/s0022112094001783.

[170] J. Lai, B. Sunderland, J. Xue, S. Yan, W. Zhao, M. Folkard, B. D. Michael, and Y. Wang. Study on hydrophilicity of polymer surfaces improved by plasma treatment. *Applied Surface Science*, 252:3375–3379, 2006. doi: 10.1016/j.apsusc.2005.05.038.

[171] P. Lallemand and L-S. Luo. Theory of the lattice Boltzmann method: Dispersion, dissipation, isotropy, Galilean invariance, and stability. *Physical Review E*, 61(6), 2000. doi: 10.1103/physreve.61.6546.

[172] P. Lallemand and L-S. Luo. Hybrid finite-difference thermal lattice Boltzmann equation. *International Journal of Modern Physics B*, 17(1/2): 41–47, 2003. doi: 10.1142/s0217979203017060.

[173] P. Lallemand and L-S. Luo. Theory of the lattice Boltzmann method: Acoustic and thermal properties in two and three dimensions. *Physical Review E*, 68:036706, 2003. doi: 10.1103/physreve.68.036706.

[174] P. Lallemand and Li-Shi Luo. Theory of the lattice Boltzmann method: Dispersion, dissipation, isotropy, Galilean invariance, and stability. *Physical Review E*, 61(6), 2000. doi: 10.1103/physreve.61.6546.

[175] P. Lavallee, J. P. Boon, and A. Noullez. Boundaries in lattice gas flows. *Physica D*, 47:233–240, 1991. doi: 10.1016/0167-2789(91)90294-j.

[176] J. Lawrence, L. Hao, and H. R. Chew. On the correlation between nd:yag laser-induced wettability characteristics modification and osteoblast cell bioactivity on a titanium alloy. *Surface and Coatings Technology*, 200: 5581–5589, 2006. doi: 10.1016/j.surfcoat.2005.07.107.

[177] P. D. Lax. Hyperbolic systems of conservation laws ii. *Communications on Pure and Applied Mathematics, Vol X, 537-566*, 1957. doi: 10.1002/cpa.3160100406.

[178] P. D. Lax and B. Wedroff. Systems of conservation laws. *Communications on Pure and Applied Mathematics, Vol. XIII, 217-237*, 1960. doi: 10.2172/4244712.

[179] A. Lerat and R. Peyret. Noncentered schemes and shock propagation problems. *Computers and Fluids, Vol. 2, pp. 35-52*, 1974. doi: 10.1016/0045-7930(74)90004-8.

[180] L. Li, R. Mei, and J. F. Klausner. Boundary conditions for thermal lattice Boltzmann equation method. *Journal of Computational Physics*, 237: 366–395, 2013. doi: 10.1016/j.jcp.2012.11.027.

[181] L. Li, C. Chen, R. Mei, and J. F. Klausner. Conjugate heat and mass transfer in the lattice Boltzmann equation method. *Physical Review E*, 89(4): 043308, 2014.

[182] Q. Li and A. J. Wagner. Symmetric free-energy-based multicomponent lattice Boltzmann method. *Physical Review E*, 76, 2007. doi: 10.1103/physreve.76.036701.

[183] Q. Li, Y. L. He, Y. Wang, and W. Q. Tao. Coupled double-distribution-function lattice Boltzmann method for the compressible Navier-Stokes equations. *Physical Review E*, 76, 2007. doi: 10.1103/physreve.76.056705.

[184] Z. Li, Y. Mo, and Y. Zhang. Lattice Boltzmann method simulation of 3-D natural convection with double mrt model. *International Journal of Heat and Mass Transfer*, 94:222–238, 2016. doi: 10.1016/j.ijheatmasstransfer.2015.11.042.

[185] P-L Lions and M. Masmoudi. From the Boltzmann equations to the equations of incompressible fluid mechanics: Parts i and ii. *Arch. Rat. Mech. Anal.*, 158:173–211, 2001.

[186] C-H Liu, K-H Lin, H-C Mai, and C-A Lin. Thermal boundary conditions for thermal lattice Boltzmann simulations. *Computers & Mathematics with Applications*, 59:2178–2193, 2010. doi: 10.1016/j.camwa.2009.08.043.

[187] H. B. Luan, H. Xu, L. Chen, Y. L. Feng, Y. L. He, and W. Q. Tao. Coupling of finite volume method and thermal lattice Boltzmann method and its application to natural convection. *Int. J. Numer. Meth. Fluids*, 2011. doi: 10.1002/fld.2685.

[188] L. Luo and S. S. Girimaji. Theory of the lattice Boltzmann method: Two-fluid model for binary mixtures. *Physical Review E*, 67, 2003. doi: 10.1103/physreve.67.036302.

[189] L-S. Luo. Unified theory of lattice Boltzmann models for nonideal gases. *Physical Review Letters*, 81(8), 1998. doi: 10.1103/physrevlett.81.1618.

[190] L. S. Luo. Some recent results on discrete velocity models and ramifications for lattice Boltzmann equation,. *Computer Physics Communications*, 129 (1/3):63–74, 1999. doi: 10.1016/s0010-4655(00)00093-x.

[191] R. S. Maier, R. S. Bernard, and D. W. Grunau. Boundary conditions for the lattice Boltzmann method. *Physics of Fluids*, 8:1788, 1996. doi: 10.1063/1.868961.

[192] Z. Malinowski, T. Telejko, B. Hadala, A. Cebo-Rudnicka, and A. Szajding. Dedicated three dimensional numerical models for the inverse determination of the heat flux and heat transfer coefficient distributions over the metal plate surface cooled by water. *International Journal of Heat and Mass Transfer*, 75:347–361, 2014. doi: 10.1016/j.ijheatmasstransfer.2014.03.078.

[193] N. C. Markatos and K. A. Pericleous. Laminar and turbulent natural convection in an enclosed cavity. *International Journal of Heat and Mass Transfer*, 27(5):755–772, 1984. doi: 10.1016/0017-9310(84)90145-5.

[194] N. S. Martys and H. Chen. Simulation of multicomponent fluids in complex three dimensional geometries by the lattice Boltzmann method. *Physical Review E*, 53:743–750, 1996. doi: 10.1103/physreve.53.743.

[195] N. S. Martys, J. G. Hagedorn, D. Goujon, and J. E. Devaney. Large scale simulations of single and multi-component flow in porous media. *Proceedings of SPIE, The International Society for Optical Engineering*, 3772: 205–213, 1999.

[196] A. De Masi, R. Esposito, and J. L. Lebowitz. Incompressible Navier-Stokes and Euler limits of the Boltzmann equation. *Comm. Pure Appl. Math*, 42:1189, 1989. doi: 10.1002/cpa.3160420810.

[197] F. Massaioli, R. Benzi, and S. Succi. Exponential tails in two-dimensional Rayleigh-Benard convection. *Europhysics Letters*, 21:305–310, 1993. doi: 10.1209/0295-5075/21/3/009.

[198] D. A. Mayne, A. S. Usmani, and M. Crapper. h-adaptive finite element solution of high Rayleigh number thermally driven cavity problem. *International Journal of Numerical Methods for Heat & Fluid Flow*, 10(6):598–615, 2000. doi: 10.1108/09615530010347187.

[199] M. E. McCracken and J. Abraham. Multiple-relaxation-time lattice-Boltzmann model for multiphase flow. *Physical Review E*, 71, 2005. doi: 10.1103/physreve.71.036701.

[200] G. R. McGuire and J. L. Morris. A class of second-order accurate methods for the solution of systems of conservation laws. *J. Comput. Phys. 11, 531-549*, 1973. doi: 10.1016/0021-9991(73)90136-8.

[201] G. R. McNamara and G. Zanetti. Use of the Boltzmann equation to simulate lattice-gas automata. *Physical Review Letters*, 1988. doi: 10.1007/bf01386051.

[202] G. R. McNamara, A. L. Garcia, and B. J. Alder. Stabilization of thermal lattice Boltzmann models. *Journal of Statistical Physics*, 81(1/2), 1995. doi: 10.1007/bf02179986.

[203] A. Mezrhab, M. Bouzidi, and P. Lallemand. Hybrid lattice-Boltzmann finite-difference simulation of convective flows. *Computers and Fluids*, 33:623–641, 2004. doi: 10.1016/j.compfluid.2003.05.001.

[204] A. Mezrhab, M. A. Moussaoui, M. Jami, H. Naji, and M. Bouzidi. Double MRT thermal lattice Boltzmann method for simulating convective flows. *Physics Letters A*, 374:3499–3507, 2010. doi: 10.1016/j.physleta.2010.06.059.

[205] W. Miller. The lattice Boltzmann method: a new tool for numerical simulation of the interaction of growth kinetics and melt flow. *Journal of Crystal Growth*, 230:263–269, 2001. doi: 10.1016/s0022-0248(01)01353-7.

[206] W. Miller and S. Succi. A lattice Boltzmann model for anisotropic crystal growth from melt. *Journal of Statistical Physics*, 107:173–186, 2002.

[207] W. Miller, S. Succi, and D. Manutti. Lattice Boltzmann model for anisotropic liquid–solid phase transition. *Physical Review Letters*, 86:3578–3581, 2001. doi: 10.1103/physrevlett.86.3578.

[208] S. C. Mishra and A. Lankadasu. Transient conduction–radiation heat transfer in participating media using the lattice Boltzmann method and the discrete transfer method. *Numerical Heat Transfer, Part A*, 47:935–954, 2005. doi: 10.1080/10407780590921935.

[209] S. C. Mishra and H. K. Roy. Solving transient conduction and radiation heat transfer problems using the lattice Boltzmann method and the finite volume method. *Journal of Computational Physics*, 223:89–107, 2007. doi: 10.1016/j.jcp.2006.08.021.

[210] S. C. Mishra, P. Talukdar, D. Trimis, and F. Durst. Computational efficiency improvements of the radiative transfer problems with or without conduction—a comparison of the collapsed dimension method and the discrete transfer method. *International Journal of Heat and Mass Transfer*, 46 (16):3083–3095, 2003. doi: 10.1016/s0017-9310(03)00075-9.

[211] S. C. Mishra, A. Lankadasu, and K. N. Beronov. Application of the lattice Boltzmann method for solving the energy equation of a 2-D transient conduction–radiation problem. *Int. J. of Heat and Mass Transfer*, 48: 3648–3659, 2005. doi: 10.1016/j.ijheatmasstransfer.2004.10.041.

[212] S. C. Mishra, H. Poonia, R. Vernekar, and A. K. Das. Lattice Boltzmann method applied to radiative transport analysis in a planar participating medium. *Heat Transfer Engineering*, 35(14–15):1267–1278, 2014. doi: 10.1080/01457632.2013.876806.

[213] A. A. Mohamad and A. Kuzmin. A critical evaluation of force term in lattice Boltzmann method, natural convection problem. *International Journal of Heat and Mass Transfer*, 53(5):990–996, 2010. doi: 10.1016/j.ijheatmasstransfer.2009.11.014.

[214] A. A. Mohamad, M. El-Ganaoui, and R. Bennacer. Lattice Boltzmann simulation of natural convection in an open ended cavity. *International Journal of Thermal Sciences*, 48:1870–1875, 2009. doi: 10.1016/j.ijthermalsci.2009.02.004.

[215] P. Mohammadmoradi and A. Kantzas. Petrophysical characterization of porous media starting from micro-tomographic images. *Advances in Water Resources*, 94:200–216, 2016. doi: 10.1016/j.advwatres.2016.05.009.

[216] B. Mondal and S. C. Mishra. Simulation of natural convection in the presence of volumetric radiation using the lattice Boltzmann method. *Numerical Heat Transfer, Part A*, 55(1):18–41, 2008. doi: 10.1080/10407780802603121.

[217] A. Montessori, P. Prestininzi, M. La Rocca, and S. Succi. Lattice Boltzmann approach for complex nonequilibrium flows. *Physical Review E*, 92, 2015.

[218] F. Mugele, B. Bera, A. Cavalli, I. Siretanu, A. Maestro, M. Duits, M. Cohen-Stuart, Dirk van den Ende, I. Stocker, and I. Collins. Ion adsorption-induced wetting transition in oil-water-mineral systems. *Scientific Reports*, 5:10519, 2015. doi: 10.1038/srep10519.

[219] J. V. Nicolini, C. H. Ferraz, and C. P. Borges. Effect of seawater ionic composition modified by nanofiltration on enhanced oil recovery in Berea sandstone. *Fuel*, 203:222–232, 2017. doi: 10.1016/j.fuel.2017.04.120.

[220] P. Nithiarasu, K. N. Seetharamu, and T. Sundararajan. Natural convection heat transfer in a fluid saturated variable porosity medium. *International Journal of Heat and Mass Transfer*, 40:3955–3967, 1997. doi: 10.1016/s0017-9310(97)00008-2.

[221] X. D. Niu, C. Shu, and Y. T. Chew. A thermal lattice Boltzmann model with diffuse scattering boundary condition for micro thermal flows. *Computers and Fluids*, 36:273–281, 2007. doi: 10.1016/j.compfluid.2005.11.007.

[222] C. Obrecht, F. Kuznik, B. Tourancheau, and J.-J. Roux. Multi-GPU implementation of a hybrid thermal lattice Boltzmann solver using the TheLMA framework. *Computers & Fluids*, 80:269–275, 2013. doi: 10.1016/j.compfluid.2012.02.014.

[223] A. Odgaard and H.J.G. Gundersen. Quantification of connectivity in cancellous bone, with special emphasis on 3-d reconstructions. *Bone*, 14(2): 173–182, 1993. doi: 10.1016/8756-3282(93)90245-6.

[224] F. Oulehle and J. Hruska. Rising trends of dissolved organic matter in drinking-water reservoirs as a result of recovery from acidification in the ore mts., Czech Republic,. *Environmental Pollution*, 157:3433–3439, 2009. doi: 10.1016/j.envpol.2009.06.020.

[225] B. J. Palmer and D. R. Rector. Lattice Boltzmann algorithm for simulating thermal flow in compressible fluids. *Journal of Computational Physics*, 161:1–20, 2000. doi: 10.1006/jcph.2000.6425.

[226] G. Pareschi, N. Frapolli, S. S. Chikatamarla, and I. V. Karlin. Conjugate heat transfer with the entropic lattice Boltzmann method. *Physical Review E*, 94, 2016. doi: 10.1103/physreve.94.013305.

[227] A. Pazdniakou and P.M. Alder. Dynamic permeability of porous media by the lattice boltzmann method. *Advances in Water Resources*, 2013. doi: 10.1016/j.advwatres.2013.06.001.

[228] Y. Peng, C. Chu, and Y. T. Chew. Simplified thermal lattice Boltzmann model for incompressible thermal flows. *Physical Review E*, 68:026701, 2003. doi: 10.1103/physreve.68.026701.

[229] Y. Peng, C Shu, and Y. T. Chew. A 3D incompressible thermal lattice Boltzmann model and its application to simulate natural convection in a cubic cavity. *Journal of Computational Physics*, 193:260–274, 2003. doi: 10.1016/j.jcp.2003.08.008.

[230] D. A. Perumal and A. K. Dass. A review on the development of lattice Boltzmann computation of macro fluid flows and heat transfer. *Alexandria Engineering Journal*, 54(4):955–971, 2015. doi: 10.1016/j.aej.2015.07.015.

[231] W. Pfleging, M. Bruns, A. Welle, and S. Wilson. Laser-assisted modification of polystyrene surfaces for cell culture applications. *Applied Surface Science*, 253:9177–9184, 2007. doi: 10.1016/j.apsusc.2007.05.047.

[232] F. Pirani, A. Angelini, S. Ricciardi, F. Frascella, and E. Descrovi. Laser-induced anisotropic wettability on azopolymeric micro-structures. *Applied Physics Letters*, 110:101603, 2017. doi: 10.1063/1.4978260.

[233] S. B. Pope. *Turbulent Flows*. Cambridge University Press, 2000. doi: 10.1017/cbo9780511840531.

[234] K. N. Premnath and S. Banerjee. Incorporating forcing terms in cascaded lattice Boltzmann approach by method of central moments. *Physical Review E*, 80, 2009. doi: 10.1103/physreve.80.036702.

[235] Y. H. Qian. Simulating thermohydrodynamics with lattice BGK model. *Journal of Scientific Computing*, 8(3), 1993. doi: 10.1007/bf01060932.

[236] Y. H. Qian, D. D'Humières, and P. Lallemand. Lattice BGK models for Navier-Stokes equation. *Europhysics Letters*, 17 (6):479–484, 1992. doi: 10.1209/0295-5075/17/6/001.

[237] P. Le Quéré. Accurate solutions to the square thermally driven cavity at high Rayleigh number. *Computers & Fluids*, 20(1):29–41, 1991. doi: 10.1016/0045-7930(91)90025-d.

[238] P. Le Quéré and M. Behnia. From onset of unsteadiness to chaos in a differentially heated square cavity. *Journal of Fluid Mechanics*, 359:81–107, 1998. doi: 10.1017/s0022112097008458.

[239] P. Le Quéré and T. A. de Roquefort. Computation of natural convection in twodimensional cavities with Chebyshev polynomials. *Journal of Computational Physics*, 57:210–228, 1985. doi: 10.1016/0021-9991(85)90043-9.

[240] E. Remy and E. Thiel. Medial axis for chamfer distances: computing look-up tables and neighbourhoods in 2d or 3d. *Pattern Recognition Letters*, 23 (6):649–661, 2002. doi: 10.1016/S0167-8655(01)00141-6.

[241] Q. Ren and C.L. Chan. Natural convection with an array of solid obstacles in an enclosure by lattice Boltzmann method on a CUDA computation platform. *International Journal of Heat and Mass Transfer*, 93:273–285, 2016. doi: 10.1016/j.ijheatmasstransfer.2015.09.059.

[242] R. D. Richtmyer. Technical Report 63-2, NCAR Tech. Notes, 1962.

[243] R. D. Richtmyer and K. W. Morton. *Difference methods for initial value problems.* Wiley, New York, 1967.

[244] A. D. Rosis. Nonorthogonal central-moments-based lattice Boltzmann scheme in three dimensions. *Physical Review E*, 95:13310, 2017. doi: 10.1103/physreve.95.013310.

[245] D. H. Rothman. Cellular automaton fluids: A model for flow in porous media. *GEOPHYSICS*, 53(4):509–518, 1988. doi: 10.1190/1.1442482.

[246] M. Rywotycki, A. Szajding, Z. Malinowski, T. Telejko, A. Goldasz, and M. Benes. The influence of burner locations in the heating furnace on the charge temperature field. *Archives of Metallurgy and Materials*, 60(3):1981–1985, 2015. doi: 10.1515/amm-2015-0336.

[247] H. Safari, M. H. Rahimian, and M. Krafczyk. Extended lattice Boltzmann method for numerical simulation of thermal phase change in two-phase fluid flow. *Physical Review E*, 88:013304, 2013. doi: 10.1103/physreve.88.013304.

[248] M. Salehi, S. J. Johnson, and J. T. Liang. Mechanistic study of wettability alteration using surfactants with applications in naturally fractured reservoirs. *Langmuir*, 24:3950–3958, 2008. doi: 10.1021/la802464u.

[249] H. Saroglou. Engineering behaviour of anisotropic and heterogeneous layered rocks. In *Proc. of IAEG Conf. "Global view of Engineering Geology and the Environment"At: 721-731*, 2013.

[250] A. Scagliarini, L. Biferale, M. Sbragaglia, K. Sugiyama, and F. Toschi. Lattice boltzmann methods for thermal flows: Continuum limit and applications to compressible rayleigh–taylor systems. *Physics of Fluids*, 22:055101, 2010. doi: 10.1063/1.3392774.

[251] F. Sebilleau, R. Issa, S. Lardeau, and S. P. Walker. Direct Numerical Simulation of an air-filled differentially heated square cavity with Rayleigh numbers up to. *International Journal of Heat and Mass Transfer*, 123: 297–319, 2018. doi: 10.1016/j.ijheatmasstransfer.2018.02.042.

[252] A. Sergent, S. Xin, P. Joubert, P. Le Quéré, J. Salat, and F. Penot. Resolving the stratification discrepancy of turbulent natural convection in differentially heated air-filled cavities Part i: reference solutions using Chebyshev spectral methods. *International Journal of Heat and Fluid Flow*, 39:1–14, 2013. doi: 10.1016/j.ijheatfluidflow.2012.08.008.

[253] T. Seta and K. Kono. Thermal lattice Boltzmann thermal method for liquid-gas two-phase flows in two dimensions. *JSME International Journal*, 47 (3), 2004.

[254] T. Seta, E. Takegoshi, and K. Okui. Lattice Boltzmann simulation of natural convection in porous media. *Mathematics and Computers in Simulation*, 72:195–200, 2006. doi: 10.1016/j.matcom.2006.05.013.

[255] S. M. Shah, F. Gray, J. P. Crawshaw, and E. S. Boek. Micro-computed tomography pore-scale study of flow in porous media: Effect of voxel resolution. *Advances in Water Resources*, 95:276–287, 2015. doi: 10.1016/j.advwatres.2015.07.012.

[256] X. Shan. Solution of Rayleigh–Benard convection using a lattice Boltzmann method. *Physical Review E*, 55:2780, 1997.

[257] X. Shan and H. Chen. Lattice Boltzmann model for simulating flows with multiple phase and components. *Physical Review E*, 47:1815–1819, 1993. doi: 10.1103/physreve.47.1815.

[258] X. Shan and H. Chen. Lattice Boltzmann model for simulating flows with multiple phases and components. *Physical Review E*, 47:1815, 1993. doi: 10.1103/physreve.47.1815.

[259] K. V. Sharma, R. Straka, and F. W. Tavares. New cascaded thermal lattice Boltzmann method for simulations of advection-diffusion and convective heat transfer. *International Journal of Thermal Sciences*, 117:259–277, 2017. doi: 10.1016/j.ijthermalsci.2017.04.020.

[260] K. V. Sharma, O. M. O. de Araujo, J. V. Nicolini, R. Straka, H. C. Ferraz, R. T. Lopes, and F. W. Tavares. Laser-induced alteration of microstructural and microscopic transport properties in porous materials: Experi-

ment, modeling and analysis. *Materials and Design*, 155:307–316, 2018. doi: 10.1016/j.matdes.2018.06.002.

[261] K. V. Sharma, J. V. Nicolini, O. M. O. de Araujo, R. Straka, H. C. Ferraz, R. T. Lopes, and F. W. Tavares. Laser-induced wettability alteration in limestone rocks. *Materials Today Communications*, 17:332–340, 2018. doi: 10.1016/j.mtcomm.2018.09.012.

[262] K. V. Sharma, R. Straka, and F. W. Tavares. Natural convection heat transfer modeling by the cascaded thermal lattice Boltzmann method. *International Journal of Thermal Sciences*, 134:552–564, 2018. doi: 10.1016/j.ijthermalsci.2018.08.033.

[263] M. Soe, G. Vahala, P. Pavlo, L. Vahala, and H. Chen. Thermal lattice Boltzmann simulations of variable Prandtl number turbulent flows. *Physical Review E*, 57(4), 1998. doi: 10.1103/physreve.57.4227.

[264] V. Sofonea and R. F. Sekerka. Diffuse-reflection boundary conditions for a thermal lattice Boltzmann model in two dimensions: Evidence of temperature jump and slip velocity in microchannels. *Physical Review E*, 71: 066709, 2005. doi: 10.1103/physreve.71.066709.

[265] W. H. Somerton. *Thermal Properties and Temperature Related Behavior of Rock/Fluid System*. Elsevier, Science Publication B. V., Amsterdam, the Netherlands, 1992.

[266] M. A. A. Spaid and F. R. Phelan. Lattice Boltzmann methods for modeling microscale flow in fibrous porous media,. *Physics of Fluids*, 9:2468–2474, 1997. doi: 10.1063/1.869392.

[267] J. D. Sterling and S. Chen. Stability analysis of lattice Boltzmann methods. *Journal of Computational Physics*, 123:196, 1996. doi: 10.1006/jcph.1996.0016.

[268] R. Straka. Numerical simulations of heat transfer in packed beds by two population thermal lattice Boltzmann method. *Mechanics and Industry*, 17(2):203–214, 2016. doi: 10.1051/meca/2015071.

[269] R. Straka, K. V. Sharma, D. Svyetlichnyy, and F. W. Tavares. Cascaded lattice Boltzmann method application in forced and natural convection. *Journal of Physics: Conference Series*, 1101:012040, 2018. doi: 10.1088/1742-6596/1101/1/012040.

[270] G. Strang. Accurate partial difference methods. *Numerische Mathematik 6,*, pages 37–46, 1964. doi: 10.1007/bf01386051.

[271] S. Succi, E. Foti, and F. Higuera. Three-dimensional flows in complex geometries with the lattice Boltzmann method. *Europhysics Letters*, 10(5):433, 1989. doi: 10.1209/0295-5075/10/5/008.

[272] S. Succi, H. Chen, C. Teixeira, G. Bella, A. De Maio, and K. Molvig. An integer lattice realization of a Lax scheme for transport processes in multiple component fluid flows. *Journal of Computational Physics*, 152:493–516, 1999. doi: 10.1006/jcph.1999.6242.

[273] S. Succi, I. Karlin, and H. Chen. Colloquium: role of the H-theorem in lattice Boltzmann hydrodynamic simulations. *Review of Modern Physics*, 74(4): 1203–1220, 2002. doi: 10.1103/revmodphys.74.1203.

[274] M. C. Sukop and D. T. Thorne Jr. *Lattice Boltzmann modeling: An introduction for geoscientists and engineers*. Springer-Verlag, New York, 2006. doi: 10.1007/3-540-27982-2.

[275] B. Sunden. Conjugated heat transfer from circular cylinders in low reynolds number flow. *International Journal of Heat and Mass Transfer*, 23(10): 1359–1367, 1980. doi: 10.1016/0017-9310(80)90210-0.

[276] M. R. Swift, E. Orlandini, W. R. Osborn, and J. M. Yeomans. *Physical Review E*, 54:5041, 1996.

[277] G. H. Tang, W. Q. Tao, and Y. L. He. Thermal boundary condition for the thermal lattice Boltzmann equation. *Physical Review E*, 72:016703, 2005. doi: 10.1103/physreve.72.016703.

[278] A. Tarokh, A. A. Mohamad, and L. Jiang. Simulation of conjugate heat transfer using the lattice Boltzmann method. *Numerical Heat Transfer, Part A: Applications*, 63(3):159–178, 2013. doi: 10.1080/10407782.2012.725009.

[279] C. Teixeira. Incorporating turbulence models into the lattice-Boltzmann method. *International Journal of Modern Physics C*, 9(8):1159–1175, 1998. doi: 10.1142/s0129183198001060.

[280] C. Teixeira, H. Chen, and D. M. Freed. Multi-speed thermal lattice Boltzmann method stabilization via equilibrium under-relaxation. *Computer Physics Communications*, 129:207–226, 2000. doi: 10.1016/s0010-4655(00)00108-9.

[281] Y. Tian, J. Du, W. Han, X. Zu, X. Yuan, and W. Zheng. Thermal conductivity of vitreous silica from molecular dynamics simulations: The effects of force field, heat flux and system size. *Journal of Chemical Physics*, 146 (5):054504, 2017. doi: 10.1063/1.4975162.

[282] Y. S. Tian and T. G. Karayiannis. Low turbulence natural convection in an air filled square cavity part i: the thermal and fluid flow fields. *International Journal of Heat and Mass Transfer*, 43:849–866, 2000. doi: https://doi.org/10.1016/S0017-9310(99)00199-4.

[283] Z-W Tian, C. Zou, H-J Liu, Z-L Guo, Z-H Liu, and C-G Zheng. Lattice Boltzmann scheme for simulating thermal micro-flow. *Physica A:*, 385: 59–68, 2007. doi: 10.1016/j.physa.2007.01.021.

[284] K. Vafai. Convective flow and heat transfer in variable porosity media. *Journal of Fluid Mechanics*, 147:233–259, 1984. doi: 10.1017/s002211208400207x.

[285] G. Vahala, P. Pavlo, L. Vahala, and N. Martys. Thermal lattice Boltzmann models for compressible flows. *International Journal of Modern Physics C*, 9(8):1247–1261, 1998.

[286] F. Verhaeghe, B. Blanpain, and P. Wollants. Lattice Boltzmann method for double-diffusive natural convection. *Physical Review E*, 75(4):046705, 2007. doi: 10.1103/physreve.75.046705.

[287] V. R. Voller and C. Prakash. A fixed grid numerical modeling methodology for convection–diffusion mushy region phase change problems. *International Journal of Heat and Mass Transfer*, 30:1709–1719, 1987. doi: 10.1016/0017-9310(87)90317-6.

[288] A. J. Wagner. Thermodynamic consistency of liquid-gas lattice Boltzmann simulations. *Physical Review E*, 74, 2006. doi: 10.1103/physreve.74.056703.

[289] D. C. Wan, B. S. V. Patnaik, and G. W. Wei. A new benchmark quality solution for the buoyancy-driven cavity by discrete singular convolution. *Numerical Heat Transfer: Part B: Fundamentals*, 40(3):199–228, 2001. doi: 10.1080/104077901752379620.

[290] J. Wang, M. Wang, and Z. Li. A lattice Boltzmann algorithm for fluid–solid conjugate heat transfer. *International Journal of Thermal Sciences*, 46: 228–234, 2007. doi: 10.1016/j.ijthermalsci.2006.04.012.

[291] J. Wang, M. Wang, and Z. Li. A lattice Boltzmann algorithm for fluid solid conjugate heat transfer,. *International Journal of Thermal Sciences*, 46: 228–234, 2007. doi: 10.1016/j.ijthermalsci.2006.04.012.

[292] J. Wang, D. Wang, P. Lallemand, and L.-S. Luo. Lattice Boltzmann simulations of thermal convective flows in two dimensions. *Computers & Mathematics with Applications*, 65(2):262–286, 2013. doi: 10.1016/j.camwa.2012.07.001.

[293] M. Wang, H. Jihuan, Y. Jianyong, and P. Ning. Lattice Boltzmann modeling of the effective thermal conductivity for fibrous materials. *International Journal of Thermal Sciences*, 46:848–855, 2007. doi: 10.1016/j.ijthermalsci.2006.11.006.

[294] X. D. Wang, X. F. Peng, J. F. Lu, T. Liu, and B. X. Wang. Contact angle hysteresis on rough solid surfaces. *Heat Transfer - Asian Research*, 33: 201–210, 2004. doi: 10.1002/htj.20013.

[295] R. F. Warming and B. J. Hyett. The modified equation approach to the stability and accuracy analysis of finite-difference methods. *Journal of Computational Physics 14, 159-179*, 1974. doi: 10.1016/0021-9991(74)90011-4.

[296] M. Watari. Velocity slip and temperature jump simulations by the three-dimensional thermal finite-difference lattice Boltzmann method. *Physical Review E*, 79:066706, 2009. doi: 10.1103/physreve.79.066706.

[297] M. Watari and M. Tsutahara. Two-dimensional thermal model of the finite-difference lattice Boltzmann method with high spatial isotropy. *Physical Review E*, 67:036306, 2003. doi: 10.1103/physreve.67.036306.

[298] M. Watari and M. Tsutahara. Possibility of constructing a multispeed Bhatnagar-Gross-Krook thermal model of the lattice Boltzmann method. *Physical Review E*, 70:016703, 2004. doi: 10.1103/physreve.70.016703.

[299] R. N. Wenzel. Resistance of solid surfaces to wetting by water. *Industrial Engineering Chemistry*, 28(8):988–994, 1936. doi: 10.1021/ie50320a024.

[300] G. M. Whitesides. The origins and the future of microfluidics. *Nature*, 442 (7101):368–373, 2006. doi: 10.1038/NATURE05058.

[301] G. M. Whitesides and S. K. Sia. Microfluidic devices fabricated in poly (dimethylsiloxane) for biological studies. *Electrophoresis*, 24(21):3563–3576, 2003. doi: 10.1002/ELPS.200305584.

[302] D. A. Wolf-Gladrow. *Lattice-gas cellular automata and lattice Boltzmann models – An introduction.* Springer, 2005. doi: 10.1007/b72010.

[303] C.-Y. Wu and N.-R. Ou. Transient two-dimensional radiative and conductive heat transfer in a scattering medium. *International Journal of Heat and Mass Transfer*, 37:2675–2686, 1994. doi: 10.1016/0017-9310(94)90384-0.

[304] Z. Yand and Wen-An Yong. Validity of the Chapman–Enskog expansion for a class of hyperbolic relaxation systems. *Journal of Differential Equations*, 2015. doi: 10.1016/j.jde.2014.12.024.

[305] N. N. Yanenko and Yu I. Shokin. First differential approximation method and approximate viscosity of difference schemes. *Physics of Fluids 12, II-28*, 1969. doi: http://dx.doi.org/10.1063/1.1692451.

[306] X. Yang, Y. Mehmani, W. A. Perkins, A. Pasquali, M. Schonherr, K. Kim, M. Perego, M. L. Parks, N. Trask, M. T. Balhoff, M. C. Richmond, M. Geier, M. Krafczyk, L.-S. Luo, A. M. Tartakovsky, and T.D. Scheibe. Intercomparison of 3D pore-scale flow and solute transport simulation methods. *Advances in Water Research*, 95:176–189, 2016. doi: 10.1016/j.advwatres.2015.09.015.

[307] J. Yong, F. Chen, Q. Yang, and X. Hou. Femtosecond laser controlling wettability of solid surfaces. *Soft Matter*, 46, 2015. doi: 10.1039/c5sm02153g.

[308] Wen-An Yong, W. Zhao, and L. Luo. Theory of the lattice Boltzmann method: Derivation of macroscopic equations via the maxwell iteration. *Physical Review E*, 93, 2016. doi: 10.1103/physreve.93.033310.

[309] H. Yoshida and M. Nagaoka. Multiple-relaxation-time lattice Boltzmann model for the convection and anisotropic diffusion equation. *Journal of Computational Physics*, 229(20):7774–9, 2010. doi: 10.1016/j.jcp.2010.06.037.

[310] D. Yu, R. Mei, L. Luo, and W. Shyy. Viscous flow computations with the method of lattice Boltzmann equation. *Progress in Aerospace Sciences*, 39:329–367, 2003. doi: 10.1016/s0376-0421(03)00003-4.

[311] D. Yu, R. Mei, L.-S. Luo, and W. Shyy. Viscous flow computations with the method of lattice Boltzmann equation. *Progress in Aerospace Sciences*, 39:329–367, 2003. doi: 10.1016/s0376-0421(03)00003-4.

[312] H. Yu. *Lattice Boltzmann equation simulations of turbulence, mixing, and combustion.* phdthesis, Texas A & M University, 2006.

URL http://oaktrust.library.tamu.edu/bitstream/handle/1969.1/3081/etd-tamu-2004C-AERO-Yu.pdf.

[313] C. Yuan, B. Chareyre, and F. Darve. Pore-scale simulations of drainage in granular materials: Finite size effects and the representative elementary volume. *Advances in Water Resources*, 95:109–124, 2015. doi: 10.1016/j.advwatres.2015.11.018.

[314] W. W. Yuen and E. E. Takara. Analysis of combined conductive-radiative heat transfer in a two-dimensional rectangular enclosure with gray medium. *Journal of Heat Transfer*, 11(2):468–474, 1988. doi: 10.1115/1.3250509.

[315] G. Zanetti. Counting hydrodynamic modes in lattice gas automata. *Physica D*, 47:30–35, 1991.

[316] R. Zhang and H. Chen. Lattice Boltzmann method for simulations of liquid-vapor thermal flows. *Physical Review E*, 67:066711, 2003. doi: 10.1103/physreve.67.066711.

[317] R. Zhang, X. Shan, and H. Chen. Efficient kinetic method for fluid simulation beyond the Navier-Stokes equation. *Physical Review E*, 74, 2006. doi: 10.1103/physreve.74.046703.

[318] B. Zhao, C. W. MacMinn, and R. Juanes. Wettability control on multiphase flow in patterned microfluidics. *PNAS*, 113(37):10251–10256, 2016. doi: 10.1073/pnas.1603387113.

[319] W. Zhao and W-A. Yong. Maxwell iteration for the lattice Boltzmann method with diffusive scaling. *Physical Review E*, 95, 2017. doi: 10.1103/physreve.95.033311.

[320] H. W. Zheng, C. Shu, and Y. T. Chew. A lattice Boltzmann model for multiphase flows with large density ratio. *J. Comput. Phys.*, 218:353–371, 2006. doi: 10.1016/j.jcp.2006.02.015.

[321] Q. Zou and X. He. On pressure and velocity boundary conditions for the lattice Boltzmann BGK model. *Physics of Fluids*, 9:1591, 1997. doi: 10.1063/1.869307.

Apêndice A

Accuracy Analysis of the Cascaded Lattice Boltzmann Method

(Robert Straka, **Keerti Vardhan Sharma** and Frederico Wanderley Tavares)

A.1   Abstract

We analyze higher order error terms (greater than second order) in the cascaded lattice Boltzmann method (CLBM) for one conservation law – the advection-diffusion equation. To inspect behavior of the error terms we derived an equivalent finite difference equation (EFDE). The EFDE is obtained from the recurrence formulas of the lattice Boltzmann equations for the CLBM and is subsequently analyzed by standard analytical techniques. We have found relations of the relaxation times which could cancel some of the higher order terms, making the method more accurate. The detailed derivation of the EFDE and higher order terms' pre-factors are the main results of this paper. Despite the fact that our approach is different from the other techniques used in the LBM community (i.e. the Chapman-Engskog expansion, equivalent partial differential equations or the Maxwell iteration), we believe that it is highly related to what is really being solved by the numerical programs run by computers.
This work has been submitted to **Physical Review E**.

Apêndice B

Laser-Induced Wettability Alteration in Limestone Rocks

Keerti Vardhan Sharma, J. V. Nicolini, O. M. O. de Araujo, R. Straka, H. C. Ferraz, R. T. Lopes, F. W. Tavares

B.1   Abstract

Alteration of wettability is pre-eminent in improving the efficiency of various industrial applications related to the materials such as metals, polymers, and rocks. We demonstrate wettability alteration in limestone porous rocks using different lasers with different wavelengths and energy. In addition to the chemical changes induced in rocks, laser treatments with different fluence modify the surface roughness of limestone differently. Pulsed Nd:YAG laser (330 mJ/pulse) reduced the surface roughness of limestone from 12.22 μm to 10.10 μm. For ultrapure water/air interface, all laser treated limestone surfaces exhibited increased contact angle. Especially, for seawater/air, pulsed Nd:YAG laser increased the contact angle substantially, from 56.75° to 106.6°, changing the surface from hydrophilic to hydrophobic. For crude oil/ultrapure water interface, increase in contact angles were reported for all laser treated limestone samples. But for crude oil/seawater interface, limestone treated with pulsed Nd:YAG laser exhibited a reduced contact angle of oil/limestone, from 29.4° to 13.3°, making the surface even more oleophobic.
This work has been Published in ***Materials Today Communications*** as an original research paper [261].

B.2   Introduction

Materials such as minerals (porous rocks), metals, polymers, biological tissues, etc. are of great importance to many industrial applications and processes. The characteristic behavior of these materials, from the physico-chemical point of view, can be readily understood by analyzing the dynamics of their interaction with different fluids or chemicals. The characteristics of fluid-solid interactions can be efficiently understood by determining wetting behavior of the materials involved [158, 294]. Alteration of wettability by changing chemical composition and surface topology of the materials is a common practice which is used to modify the performance efficiency of these materials [307, 318].

The surface topology can be modified by creating micro-structures or patterns on these materials [232, 307]. And chemical composition can be changed by exposing these surfaces to chemicals, heat, etc [7, 218]. Isotropic and anisotropic wettability was induced on azopolymeric micro-structures and polystyrene surfaces using laser [231, 232]. The anisotropic wettability means that wettability is different in different direction. And when wetting behavior of the material is independent of spatial positions or directions, the wettability is called isotropic. Wettability characteristics of titanium alloy were altered using Nd:YAG laser [176]. Femtosecond pulsed laser was used to control wettability of solid surfaces [307]. Microwave-induced argon plasma was used to change the surface properties of polycarbonate (PC), polypropylene (PP), polyethylene (PET) [170]. Atomic oxygen using ECR plasma was used to modify the surface properties of polymers such as polymide and flourinated ethylene propylene [1]. Therefore, it is quite evident from the literature that lasers have been frequently used to modify the surface structures and alter wettability of metals, various polymers, and other solid surfaces.

For hydrocarbon reservoirs, or minerals such as limestone, sandstone, no scientific study shows the application of lasers to tune the wettability. Ion-adsorption and surfactant injection techniques have been frequently used to alter the wettability in rocks and in naturally fractured reservoir [4, 6, 118, 218, 248]. Dynamic laboratory wettability alteration was performed for outcrop chalk using aging method, in which dynamic aging was carried out with continuous injection of crude oil [87]. Thermal methods have also been used to tune the wetting behavior of fractured reservoir. In this technique, hot water was injected into the reservoir to cause chemical changes and to increase the oil recovery [7]. The wettability altering techniques used in hydrocarbon industry applications are motivated by the increased oil recovery (IOR) and are harmful to the environment [224]. Lasers can only induce changes in wettability in the regions of exposure, e.g. near wellbore region, microfluidic devices, particular surfaces in core plugs used in laboratory evaluation of reservoirs etc.

In this article, we propose use of lasers to alter the wettability of porous rocks. To the best of our knowledge, the only application of lasers related to porous rock is to increase the permeability by drilling holes through rocks for IOR purpose [14, 104]. We propose much elaborated use of lasers which changes the microscopic and macroscopic wetting behavior by changing surface topography of porous rocks. We recently showed that laser can be used to cause microscopic changes in the morphometric properties of porous rocks [260]. In present work, we present surface treatment of three limestone samples by means of three types of laser irradiation with different wavelength and potential. Pulsed Nd:YAG (532 nm), pulsed Nd:YAG with second harmonic generation (266 nm), and continuous wave carbon dioxide laser (10.6 μm) have been used to treat the limestone surface. We perform Surface profilometry experiment and confocal laser scanning microscopy experiments to study the surface roughness of the laser processed limestone rock samples. After quantifying the surface's topological modifications caused by lasers, we move to characterize the fluid-solid interaction to quantify the altered wettability. We measure contact angles in the laser treated area with black oil, seawater and ultrapure water by drop shape analysis for each sample, and compare them with the contact angles measured in untreated regions. In section 2, we present the limestone's chemical composition and zeta potential, the detailed specifications of lasers used in this study, the details regarding laser treatment, specifications of equipments used, and methodology to measure surface roughness and contact angle. In section 3, we discuss the impact of lasers on surface roughness, and contact angles for air/water, air/seawater, oil/water and oil/seawater systems.

B.3 Materials and Methods

B.3.1 Limestone's surface roughness characterization

To characterize the limestone surfaces morphologically we performed surface profilometry experiment on each laser treated and non-treated area of samples A, B and C. DektakXT Stylus profilometer Vision64 from BRUKER was used to measure the average roughness. This equipment works on the principal of registering hills and valleys to measure the roughness of the surface. We place samples on the platform and take measurements by scanning the sample by the probe horizontally. The procedure of cutting and polishing rock samples can cause different roughness in different directions. Therefore, to enhance the accuracy and reliability of our roughness estimation experiment, we measure roughness in three different directions.

B.3.2   3D imaging and topography characterization

ZEISS LSM 800, the confocal laser scanning microscope (CLSM), was used to analyze the surfaces of the original and laser treated limestone samples. 3D surface topography and surface pore structures were analyzed for all samples by using this experiment. CLSM provides the precise three dimensional imaging and analysis of materials' surface.

B.3.3   Wettability (contact angle) measurements

The contact angle measurement was performed in order to observe the wetting behavior of laser treated surfaces. Static contact angle of ultrapure water and seawater was assessed by the sessile drop method using a goniometer (Dataphisics OCA 15). A droplet of each liquid $(1\mu L)$ was delivered onto limestone surface and a static image of the droplet was taken. SCA software (Dataphisics) was used to calculate the contact angle, see Fig. B.1(a). Contact angle measurement of crude oil onto limestone surface under water was performed in the same equipment, using the pendant-drop method, as shown in Fig. B.1(b). A droplet of crude oil was delivered through the U shaped needle, being collected at the surface of the limestone rock. After reaching the equilibrium configuration, a static image of the droplet was taken and the equipment software calculated the contact angle. All the analysis, the measurements were performed at three different points of the rock surface to obtain the average contact angle value. All the experiments were performed at room temperature.
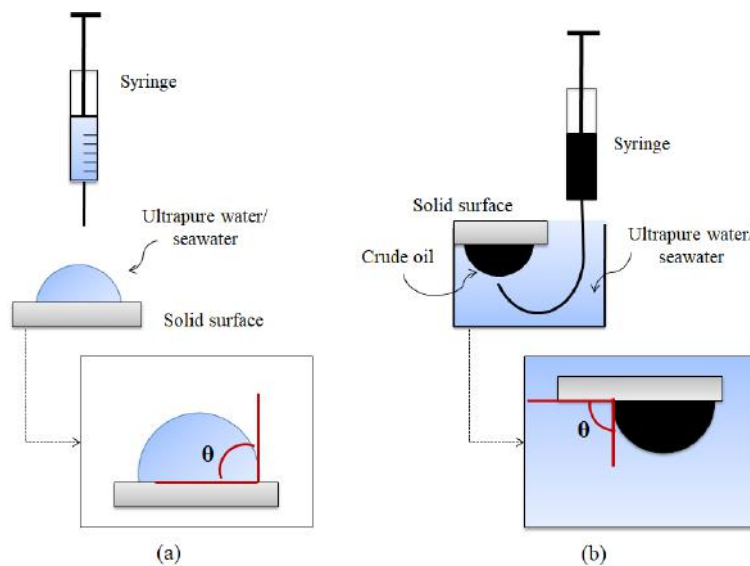

Figura B.1: Schematic diagram of contact angle measurements: (a) air/water system and (b) oil/water system.

B.4 Results and discussions

B.4.1 Laser treated limestone's properties

To manipulate the wettability properties of the limestone rock, a process was needed which could change the surface roughness. The benefit of using laser is that its power can be tuned according to our interest therefore giving us the total control over up to what degree we want to change the surface properties physically. When parameters such as power, energy density are not set and monitored properly, lasers can cause irreparable damages to the rock sample e.g., burning, breaking, creating holes etc. [104]. The performance and consequences of the laser processing of limestone depends on the thermal diffusivity and conductivity of the material.

For sample A, see Fig. 7.5A, for which the energy density is very low, there were no major visible changes on the surface. That shows that laser A irradiation was not able to heat up the matrix grains sufficiently to cause visible topological and chemical changes. Laser B, which has higher fluence, see Fig. 7.5B, induces visible changes on the limestone surface. Limestone which initially had brighter white surface turned dark gray due to the laser exposure. Laser C, which is the highest continuous power and longest wavelength used in the present study, caused greater changes on the surface and some matrix burning was noticed, see Fig. 7.5C. Where CO_2 laser irradiation was incident for longer period holes with white CaCO powder were created as a result [260].

B.4.2 Surface roughness

Wenzel studied the relationship between surface roughness and wettability in 1936 and concluded that changes in surface roughness might enhance the wettability caused by the chemistry of the surface [299]. Wenzel statement can be described by:

$$cos\theta_m = r(cos\theta_Y) \tag{B.1}$$

where θ_m is the measured contact angle, θ_Y is the Young contact angle and r is the roughness factor. Roughness factor is the ratio between the actual and treated solid surface area. Roughness measurements for original and laser treated limestone samples are provided in Fig. B.2. Roughness was measured in three different directions, as can be seen in left part of Fig. B.2. It is evident from the results that Nd:YAG 266nm (laser A) increases the surface roughness of the limestone and r factor according to Eq.(B.1). For each scan the roughness was increased for laser treated regions. Results also show that surface roughness is different in different directions of the measurements. The very interesting finding

of this experimental study is that treatment by Nd:YAG 532nm (laser B) reduces the surface roughness of the limestone. Quantitatively, the reduction in contact angle values after Nd:YAG 532nm laser indicates a reduction of the roughness factor, towards the smoother surface. CO_2 laser increases the limestone's roughness slightly, mostly due to the holes. Fig. B.2 represents the comparison charts of surface roughness in different directions for all samples. One may ask about the different y scale (roughness) for sample A. Roughness of original (untreated) regions for sample B and C are almost identical. But for sample A, untreated regions demonstrate higher roughness compared to the untreated ones of samples B and C. This can be supported by the fact that sample B and C were better polished compared to sample A. This difference does not make any unwanted impact on the findings related to lasers' effect on surface roughness because all untreated regions in each sample demonstrate equal roughness. Roughness were measured at four different locations in treated and untreated regions, respectively. Measurement performed at one location is expressed as one scan, see Fig. B.2. The average surface roughness of laser treated sample A measured by surface profilometry is 18.14 μm and surface roughness of the laser treated sample B is 10.10 μm.
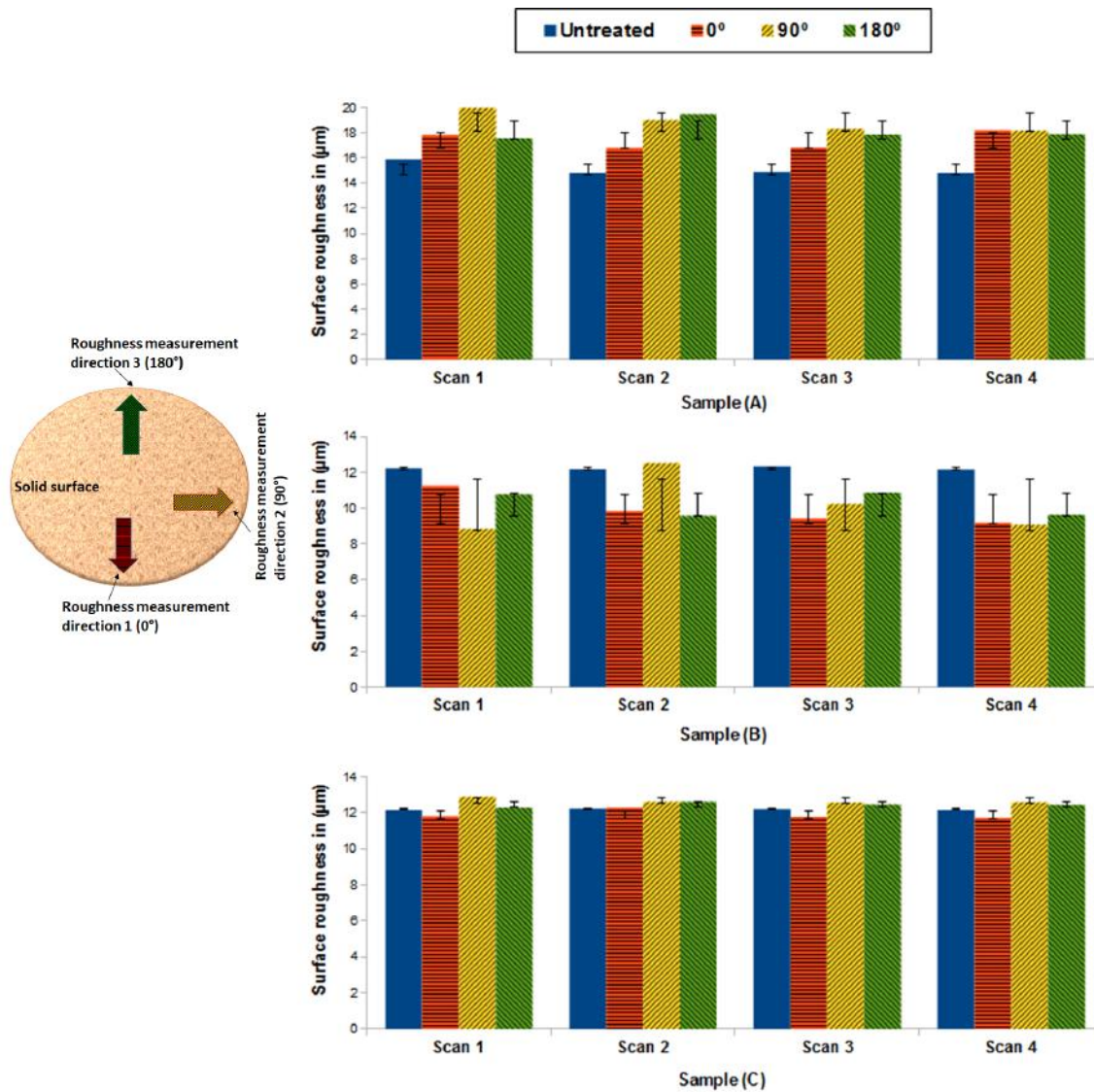
Figura B.2: Limestone surface roughness comparisons for samples A, B and C. Roughness was measured in laser treated and untreated regions at four different locations, respectively (4 scans) in three different directions as shown in the left. One scan means one particular location in treated or untreated regions

B.4.3 Limestone's 3D imaging and topographical analysis

Surface roughness test by means of the surface profilometry is done by a probe which touches the surface and notes the valleys and hills. The probe can touch the surface and move in a straight line. Therefore, to characterize the topography of the surfaces, we choose the method of CLSM. By means of CLSM, we are able to perform 3D imaging of a relatively bigger area compared to a point in one go, and moreover, with clear roughness distribution of the surface. The topography imaging of all the samples are presented in Fig. B.3.
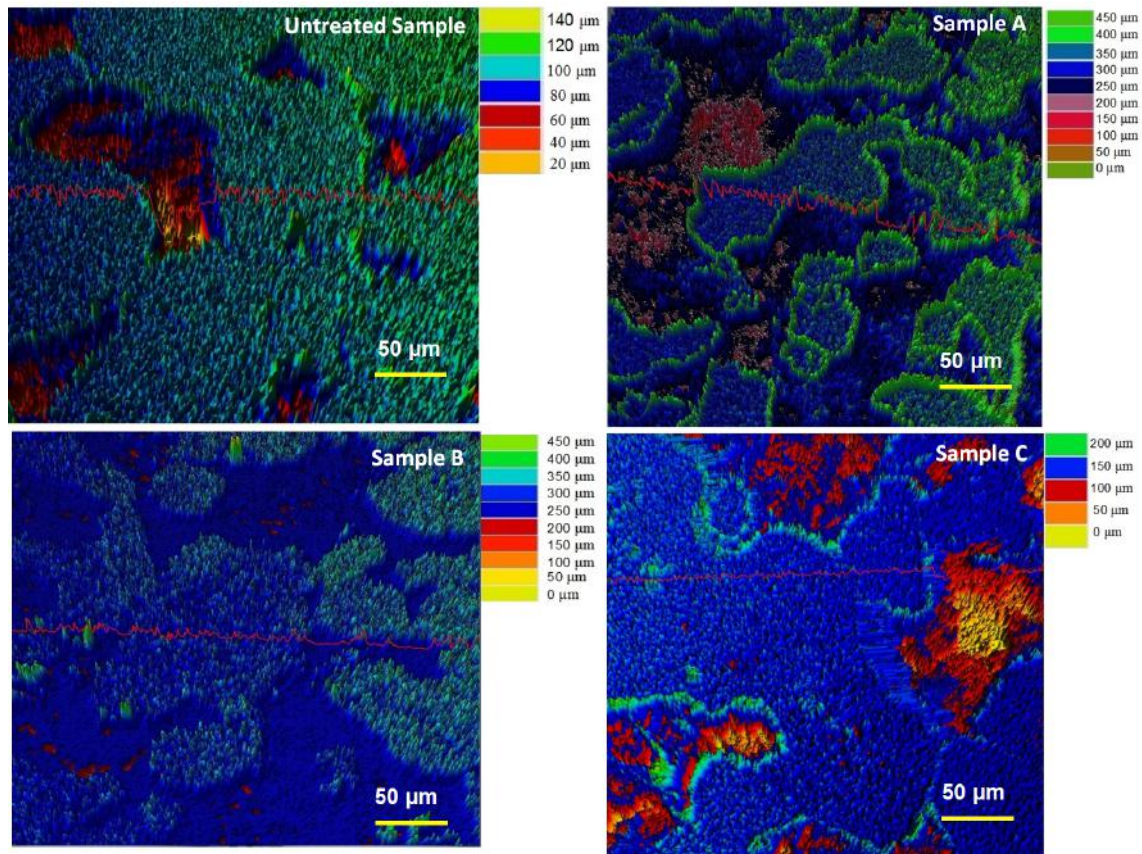
Figura B.3: Topographical images of untreated and laser treated samples A, B and C, obtained by confocal laser scanning microscopy. It is evident that laser treated sample A demonstrates highly rough topographical profile, while laser treated sample B shows smoother roughness profile. Leaving the holes aside (seen as red-yellow valleys in sample C), the roughness profile of original sample is approximately identical to the roughness profile of sample C. Laser A increses the surface roughness, while laser B reduces the roughness, and laser C did not have significant effect on roughness in mildly treated areas.

For sample A, clusters of green peaks (400-450 μm) surrounding green-blue peaks (350-400 μm) are evident. The high roughness of the surface can be easily seen in Fig. B.3. For sample B, which is treated by higher potential 532 nm pulsed Nd:YAG laser, the microscopic analysis shows that the peak heights are decreased, reducing the roughness. For sample B, the peaks are of the order of 250 μm - 350 μm. The red zigzag lines superimposed on the images are the average surface roughness profiles, and it is clearly evident that the surface roughness profile of sample A is more turbulent compared to the red-line profile for sample B. It is seen that laser processing of limestone with the pulsed wavelength of 532 nm and 330 mJ power reduces the roughness of the limestone surface. Sample C, which is treated by the CO_2 laser, demonstrates more valleys created by the high continuous power of the laser irradiation. After analysing the results one may notice that surface roughness of sample A's untreated regions is higher than the surface roughness of untreated

regions of samples B and C. While the roughness of untreated regions of samples B and C is approximately the same. This difference could be caused by the polishing procedure of the samples. Laser A, delivered shocks to the already rough surface increasing the roughness even further. Laser A can induce porosity enhancement but without significant connectivity among those surface pores [260]. For sample B, pulsed laser B induced great increase in porosity and surface pore connectivity through ablation and stronger thermal shocks creating a huge connected network of surface pores, see Ref. [260]. This development could justify the decrease in the surface roughness. While for sample C, laser C caused heating and evaporation of the surface rock grains without any severe impact on the surface roughness. The one important outcome that can be drawn from above results is that pulsed lasers induce notable changes in the surface roughness compared to continuous wave laser. Moreover, there seem to exist one inverse relation between surface roughness and pore connectivity such that the greater the surface pore connectivity the lower will be the roughness. This is evident in the Fig. B.3, for sample C, where large area is homogeneously covered in blue (connected pore network) with lower surface roughness.

B.4.4   Aqueous Solution/Air Interface Wettability

The contact angle measurement was performed in order to observe the wetting behavior of laser treated limestone surface. The variation of contact angle is listed in Table B.1. Fig. B.4 and B.5 represent the contact angle of ultrapure water and seawater solution onto original and laser treated samples with pulsed Nd:YAG – 266 nm (sample A), pulsed Nd:YAG – 532 nm (sample B) and CO_2 laser– 10.6 μm (sample C). It can be observed that different types of laser processing affects the contact angles differently. For ultrapure water, the contact angle was increased for all laser treatment cases. For Nd:YAG – 532 nm (sample B), the higher variation was observed for both ultrapure water and for seawater. Contact angle in seawater solution was higher compared to the contact angle of ultrapure water. Seawater solution consists of several ions. These ions could play a role through interaction with charged surface of limestone. According to the results of contact angle, original surface is hydrophilic. For sample treated by pulsed Nd:YAG – 532 nm (sample B), the surface has become hydrophobic. From Fig. B.6, the relationship between surface roughness and wettability is evident for the sample treated with laser B (sample B), because the reduction of the roughness caused by the laser led to the increase of the observed contact angle. Surface treated by pulsed Nd:YAG-532 nm laser demonstrates the lowest roughness and great increase in contact angle compared to the original value for both ultrapure water and seawater. Fig.B.7

shows a schematic and possible hypothesis for these changes in hydrophilicity. In the original limestone surface, with the roughness, and later deposition of liquid (water or seawater), there is the formation of microvoids that imprison air. With treatment by pulsed Nd:YAG 532 nm, the surface became less rough, and without the presence of microvoids with air, the water molecules are more strongly structured at the interface. This improving the ability of water molecules to form hydrogen bonds [140], and in turn, produce stronger interactions between water and the solid surface. With seawater, these interactions are weakened at the interface, because cations interact with the negatively charged surface, and water molecules change orientation close to the interface.

Tabela B.1: Contact angle measurements for original and laser treated limestone surfaces for Air/Aqueous solution interface.

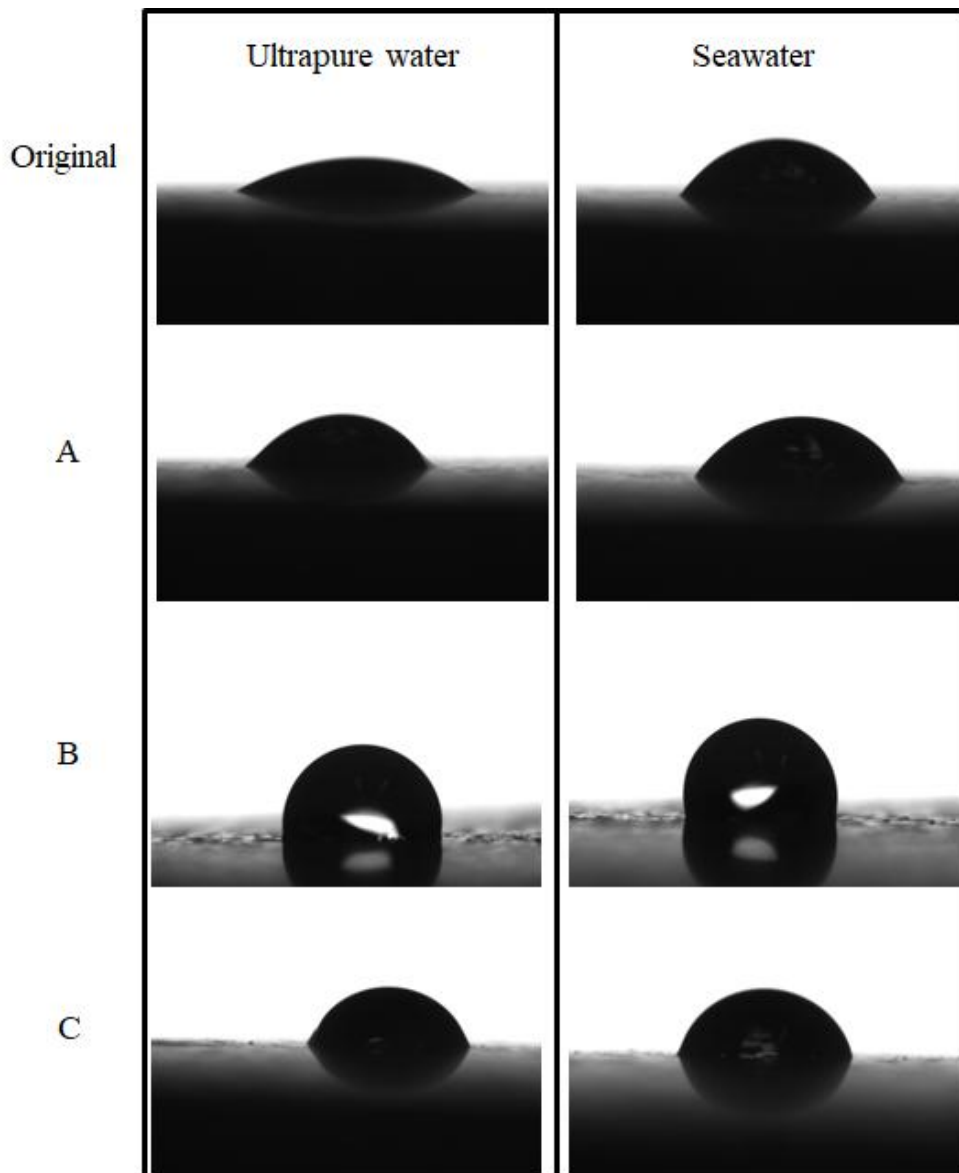| | Ultra-Pure Water | | Seawater Solution | |
	Contact Angle°	Error	Contact Angle°	Error
Original	31.35	3.89	56.75	2.3
Sample A	54.25	4.03	48.05	0.78
Sample B	99.55	0.64	106.6	0.85
Sample C	72.45	1.1	77.6	0.99

Figura B.4: Contact angle for aqueous solution/air interface for original and laser treated samples A, B and C.
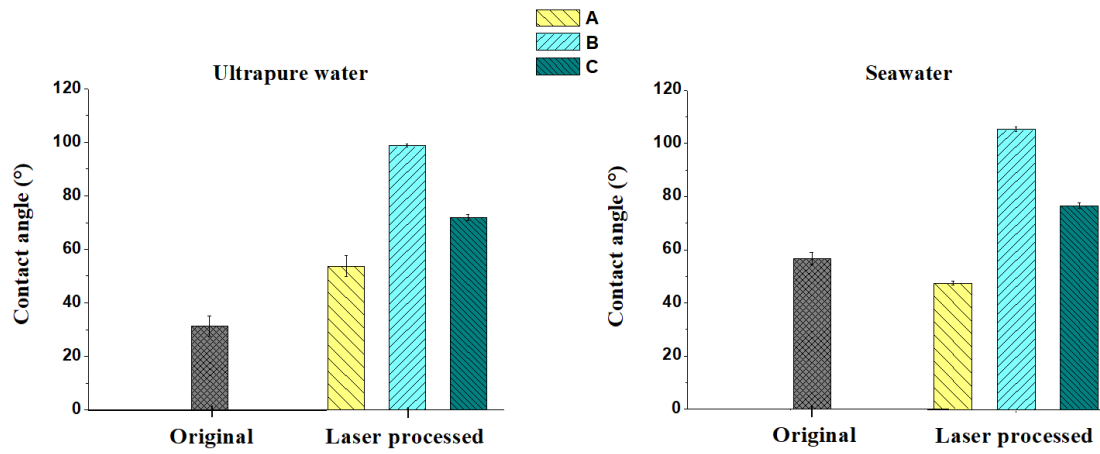
Figura B.5: Contact angle comparison for aqueous solution/air interface for original and laser treated samples A, B and C.
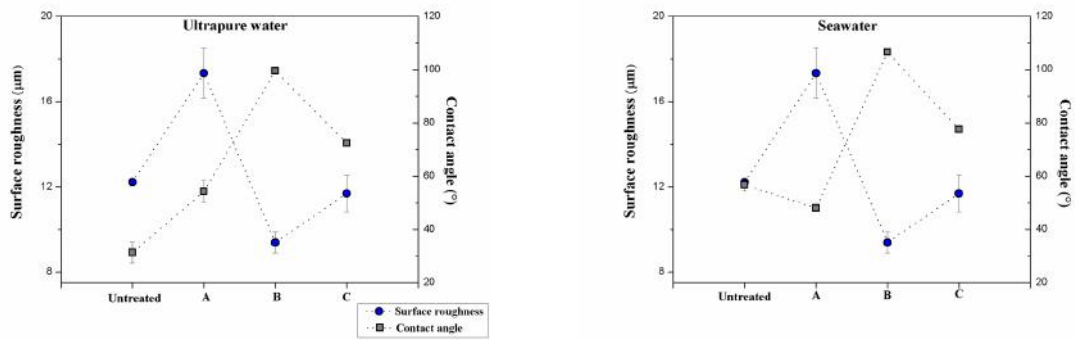

Figura B.6: Relation between contact angle and surface roughness for original and laser treated samples A, B and C for ultrapure water/air interface (left) and Seawater/air interface (right).
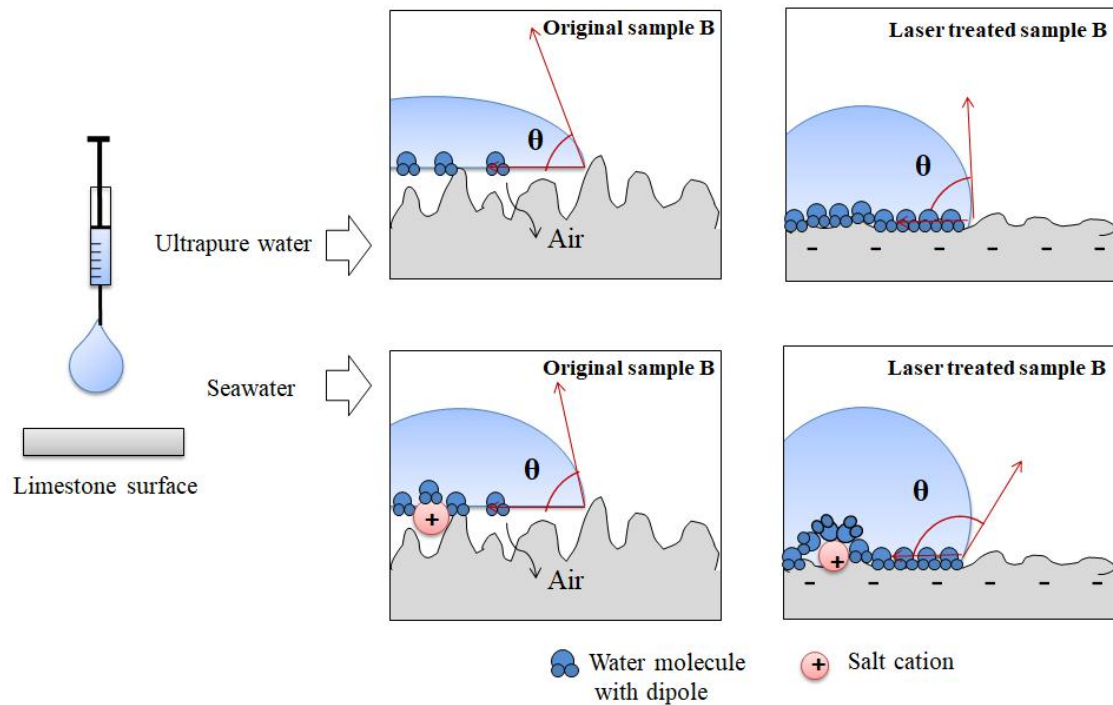
Figura B.7: Schematic representation of interfacial interaction at interface water/-limestone in original surface and after treatment from pulsed Nd:YAG 532 nm laser (sample B).

B.4.5 Oil/Aqueous Solution Interface Wettability

The effect of laser processing on limestone wettability was also evaluated through the measurement of the contact angle of the crude oil at limestone surface immersed in ultrapure water and seawater. The results are shown in Table B.2 and Fig. B.8 and B.9. According to the results, ultrapure water in the original regions promotes low contact angles, which implies higher oil recoveries. These results are related to the effect of low salinity water, increasing the repulsion forces between the oil and the limestone surface, resulting in the expansion of the electric double layer [219]. In this way, adhesion strength points become fractions and the contact angle decreases towards a water-wet surface. The opposite effect is observed for the contact angle of the original surface in seawater, where the attraction forces between the oil and sea water are strong, given the contraction of the double electric layer, as a result of the high ionic strength [20]. Fig. B.10 represents this phenomenon. With the laser treatment, changes in the contact angle are observed. All treatment promoted increased contact angle of oil in ultrapure water, indicating a more oil-wet surface. For seawater, treatment B was efficient in increasing the contact angle of oil, suggesting changes towards higher oil recovery. These results may well be related to the inter connectivity of limestone pores after laser treatments. It is proven that 532 nm Nd:YAG laser promoted enhanced pore connectivity as well as

porosity in limestone [260]. The results of the contact angle in seawater indicate higher recoveries, possibly due to the increase of the pore imbibition by the water given active capillary forces and subsequent thickening of the water film. This result is of great importance, because in limestone reservoirs, the injection of seawater is a common practice, and a treatment with laser B would improve the wettability of the rock by the seawater and further improve the efficiency of enhanced oil recovery.

Tabela B.2: Contact angle measurements for original and laser treated limestone surface for Oil/Aqueous solution interface.

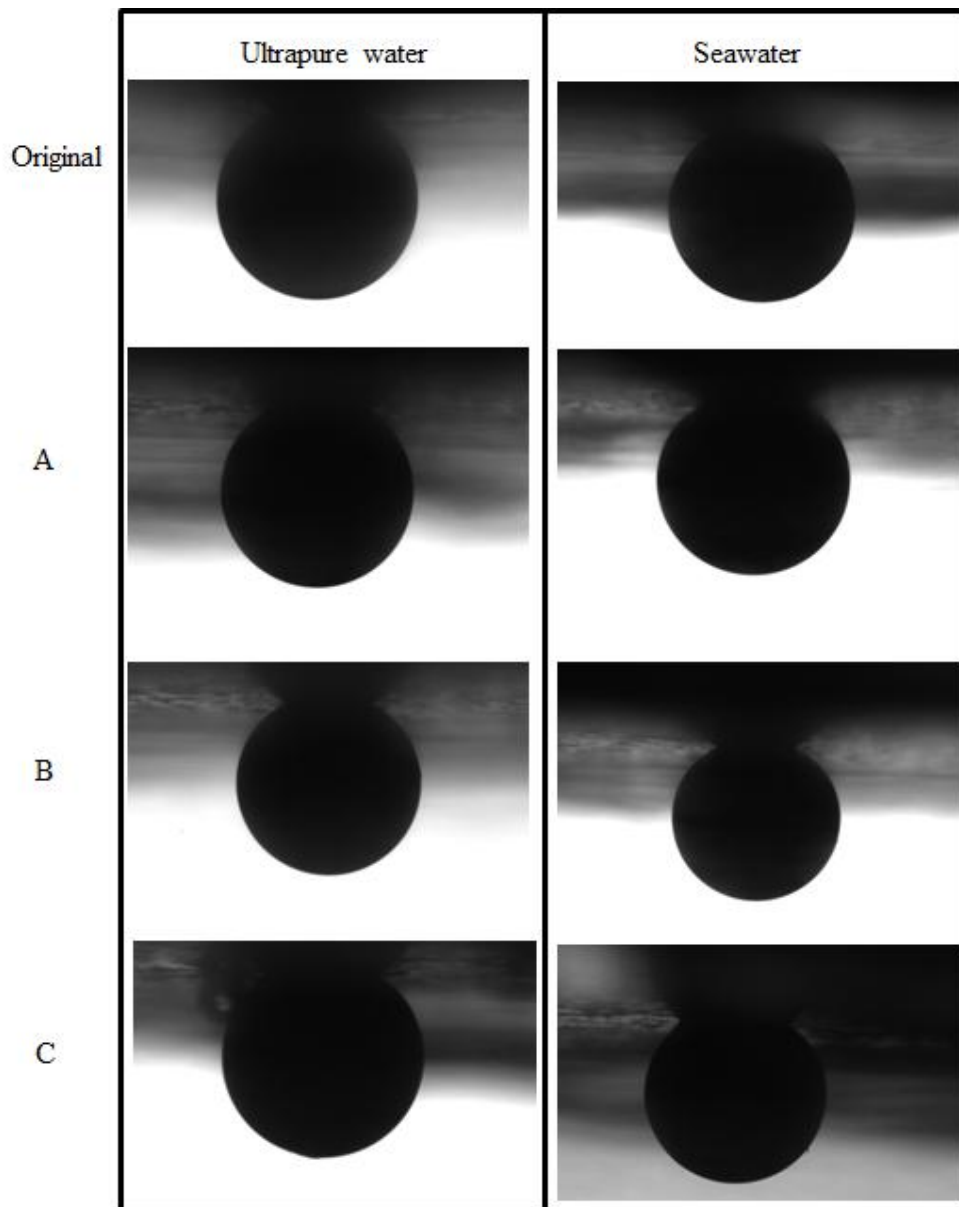| | Ultra-Pure Water | | Seawater Solution | |
	Contact Angle°	Error	Contact Angle°	Error
Original Sample	12.5	0.1	29.4	1.10
Sample A	30.4	0.5	30	0.90
Sample B	24.2	0.70	13.3	0.40
Sample C	34.7	0.07	29.85	0.07

Figura B.8: Contact angle for oil/aqueous solution interface for original and laser treated samples A, B and C.
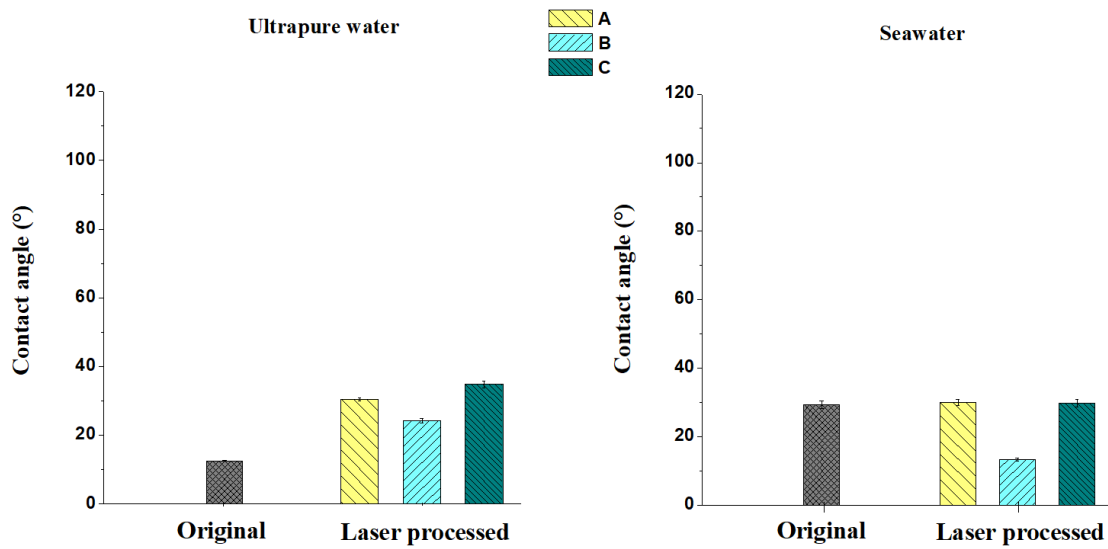
Figura B.9: Contact angle comparison for Oil/aqueous solution interface for original and laser treated samples A, B and C.
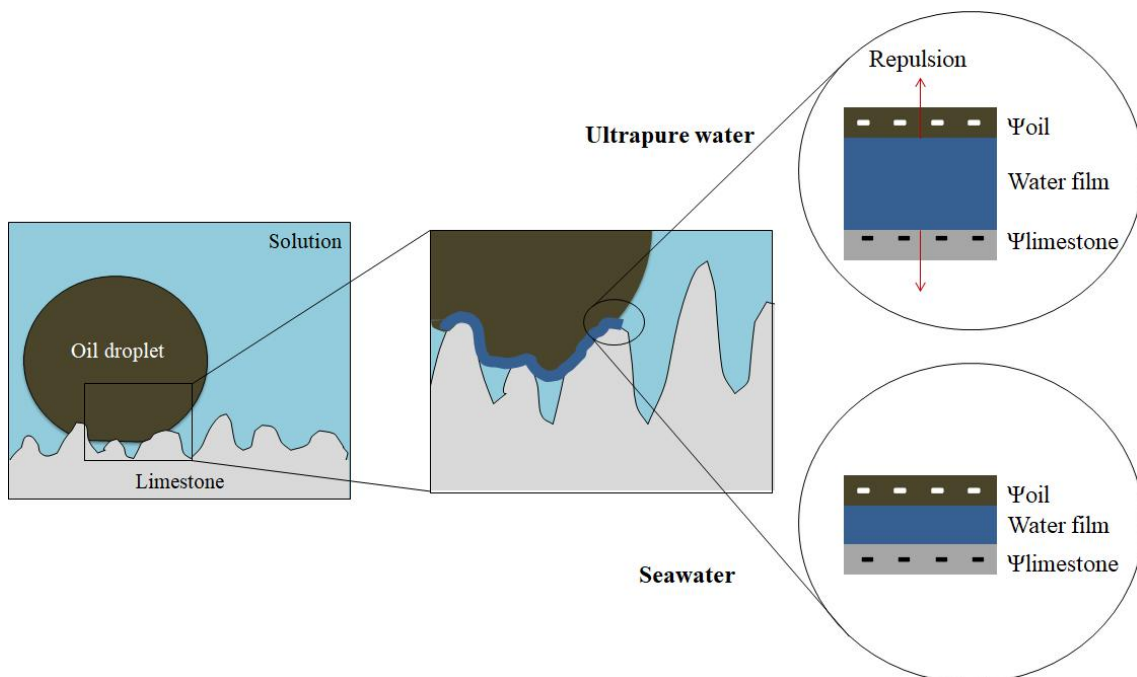

Figura B.10: Schematic representation of crude oil wettability onto limestone for ultrapure water and seawater imbibition.

B.5   Conclusions

We successfully used lasers to alter the wettability of limestone porous rocks. The results show that pulsed lasers cause notable effects on the limestone rocks' physical properties. The surface roughness of limestone is reduced by the pulsed Nd:YAG 532

nm laser treatment by 2 μm. For aqueous solutions/air wettability, laser treatment of limestone transform the surface from hydrophilic to strongly hydrophobic. Pulsed Nd:YAG 532 nm laser induced the maximum hydrophobicity. For crude oil/ultra-pure water system, all laser treatments induce higher contact angle for crude oil, i.e. the surface became more oil-wet after laser treatment. The results obtained for laser treated limestone for crude oil/seawater wettability are eminently interesting from EOR point of view. The results show that treatment by pulsed Nd:YAG laser reduced the contact angle on seawater side, i.e., the surface became highly oleophobic after treatment. It clearly suggests that laser treated limestone assists in increasing the sweeping efficiency of oil for seawater injection. We strongly believe that the proposed technique can be used to alter the wettability in the near wellbore region and in microfluidic devices.

Apêndice C

Representative Elementary Volume in Limestone Sample

O. M. O. de Araujo, **Keerti Vardhan Sharma**, A. S. Machado, T. M. P. Santos, C. G. Ferreira, R. Straka, F. W. Tavares, and R. T. Lopes.

C.1 Abstract

The study of fluid flow through porous media with complex characteristics is of great relevance in applications related to exploration of oil and gas reserves. With growth of computer simulation combined with the use of reconstructed images it became increasingly common to use a representative volume, popularly known as REV. The use of a REV is necessary since the total volume of reconstructed image is too heavy to be loaded into simulation software, increasing data processing time and in some cases making total volume simulation impracticable. However, when investigating different rocks types, some main issues are addressed related to REV, such as how reliable is representative volume compared to the total sample volume. Quantitative and qualitative results such as porosity and permeability vary with the region chosen for the REV as well as configuration of pore connected vary depending on region, showing the importance in choosing a region so that REV represents total results of the sample.
This work has been Published in **_Journal of Instrumentation_** as an original research paper [64]. The full text of the paper can be downloaded from https://doi.org/10.1088/1748-0221/13/10/C10003